INNOVATIVE DESIGN OF FRP COMPOSITE MEMBERS COMBINED WITH CONCRETE

by

NIKOLA DESKOVIC

Diploma in Civil Engineering, University of Split, Croatia
(1988)

M.Sc. in Civil Engineering, Massachusetts Institute of Technology
(1991)

SUBMITTED TO THE DEPARTMENT OF CIVIL AND ENVIRONMENTAL ENGINEERING IN PARTIAL FULFILLMENT OF THE REQUIREMENTS FOR THE DEGREE OF

DOCTOR OF PHILOSOPHY IN CIVIL ENGINEERING

at the

MASSACHUSETTS INSTITUTE OF TECHNOLOGY

April 1993

Signature of Author_____

Department of Civil and Environmental Engineering
April, 1993

Certified by_____

Thanasis C. Triantafillou
Thesis Supervisor

Accepted by_____

Eduardo Kausel
Chairman, Departmental Graduate Committee

INNOVATIVE DESIGN OF FRP COMPOSITE MEMBERS COMBINED WITH CONCRETE

by

Nikola Deskovic

Submitted to the Department of Civil and Environmental Engineering on April 30, 1993 in partial fulfillment of the requirements for the degree of Doctor of Philosophy in Civil Engineering

Abstract

The thesis develops a basic understanding of the mechanical behavior of an innovative design concept involving the combination of fiber reinforced plastic (FRP) components with concrete. According to the new concept, glass fiber reinforced plastic (GFRP) box beams are combined with a concrete layer in the compression zone and a thin carbon fiber reinforced plastic (CFRP) sheet in the tension zone, to result in low cost, low weight and high performance elements with pseudo-ductile characteristics. The method maximizes system performance using materials by combination, and can be thought as a better way of producing structural members based on pultrusion. A design procedure is presented, based on given strength, stiffness and ductility constraints. Comparisons with plain GFRP sections illustrate that the material cost reductions achieved with the proposed design can be as low as 50%. Analytical procedures describing the response in short term, creep, fatigue and temperature-related conditions are developed and appropriate material behavior models are adopted. The basic mechanical behavior characteristics of the proposed concept are verified experimentally on two series of hybrid FRP-concrete beams subjected to three and four point bending under static, sustained and dynamic loading. The analysis agrees quite well with the experiments, and it is concluded that the strength, the stiffness as well as the ductility of the new elements can be predicted in a reliable manner in both short and long term loading configurations. The results show that for typical load ranges the creep deformations over a period of 100 years are of the same order as the short term ones, while in fatigue the deformations increase by about 50% after 10^7 cycles.

Thesis Supervisor: Thanasis C. Triantafillou

Title: Assistant Professor of Civil and Environmental Engineering

To my loving parents:

Mojim roditeljima, koji su mi svojom podrskom i ljubavlju omogucili sve sto sam ostvario, na cemu cu im zauvijek ostati zahvalan, sa zeljom da cu uvijek opravdati ukazano mi povjerenje.

Acknowledgments

I would like to express my profound gratitude to Professor Thanasis Triantafillou, my thesis supervisor, for his expert and invaluable guidance as well as his financial support throughout the course of this thesis, his abundant help, his never ending patience and at last his sincere friendship.

The experimental work was partially supported by a grant from the Swiss Federal Laboratories for Materials Testing and Research (EMPA). I would like to thank Professor Urs Meier, for having provided the opportunity to perform the essential experimental program at the EMPA (Swiss Federal Laboratories for Materials Testing and Research) as well as his expert advice, financial support and encouragement during my stay in Dübendorf.

I deeply appreciate the effort of Professor Lorna Gibson, Professor Jerome Connor and Professor Frederick McGarry, who as members of my Ph.D. Thesis Committee provided crucial comments and gave important directions.

Many thanks are due to Mrs. Helga Eissler, Martin Deuring, Heinz Meier, Gregor Schwegler and Richard Nordstrom who introduced me to the facilities at the EMPA and whose help and friendship I deeply appreciate. I would also like to thank Dr. Reto Cantieni, Manfred Waldvogel, René Menet, Heiner Liphuner, Mr. Jaene, Trindler and Krebs for their technical assistance at the EMPA, as well as Mr. Musch and Rolf Bandhauer from Huber&Suhner.

I can not thank enough to all my good friends from the Department of Civil and Environmental Engineering: Nikolaos Plevris, Hayat Tazir, Bidjan Gaherman, Charis Gantes, Adrian Eterovic, Boris Ivanovic, Gebran Karam, Alexander Gamota, all the members of the soccer team Cosmos and all the others that I have unintentionally forgotten.

At last but certainly not least, I would like to express my warmest thanks to my mother, Dora, my brother Zarko, my whole family and my fiancé Katja, whose love and encouragement constituted a priceless support.

Table of Contents

List of Figures

List of Tables

List of Symbols

A	=	constant;
	=	area of cross section;
A_{CFRP}	=	cross sectional area of CFRP sheet;
a	=	empirical constant;
	=	location of neutral axis when in concrete;
	=	crack length;
a_i	=	empirical constants;
B	=	first moment of inertia;
	=	constant;
b	=	width of cross section;
	=	empirical constant;
C	=	compliance;
c	=	depth of concrete layer;
D	=	flexural rigidity;
	=	stiffness matrix of multilayered composite;
D_L	=	material constant;
D_T	=	material constant;
d	=	depth of webs;
	=	empirical constant;
d_a	=	thickness of adhesive layer;
d_F	=	fiber direction;
d_{ij}	=	elements of composite stiffness matrix;
E_F	=	Young's modulus of fiber;
$E_{F\parallel}$	=	Young's modulus of fiber in fiber direction;
$E_{F\perp}$	=	Young's modulus of fiber perpendicular to fiber direction;
E_M	=	Young's modulus of matrix;
E_M^o	=	transformed Young's modulus of matrix;
E_c	=	Young's modulus of concrete;
E_i	=	Young's modulus of wall i;
E_w	=	Young's modulus of webs;
E_{wT}	=	transverse Young's modulus of webs;
$\overline{E}_{x,y}$	=	average elastic modulus of composite in x or y direction;
E_o^x	=	initial elastic modulus of material x;

E_1 = Young's modulus of GFRP bottom flange;

E_{1T} = transverse Young's modulus of GFRP bottom flange;

E_2 = Young's modulus of CFRP laminate;

E_3 = Young's modulus of top GFRP flange;

$E_{\|}$ = elastic modulus of lamina in fiber direction;

$E_{\perp}$ = elastic modulus of lamina perpendicular to fiber direction;

F_{BF} = tensile force in bottom flange;

F_{BW} = tensile force in GFRP web (bottom);

F_C = compressive force in concrete layer;

F_{Cc} = compressive force in concrete layer when neutral axis in concrete;

F_{Ct} = tensile force in concrete layer when neutral axis in concrete;

F_{CC} = tensile force in CFRP sheet;

F_{TF} = force in GFRP top flange;

F_{TW} = compressive force in GFRP web (top);

f = frequency;
= empirical constant;

$f_{GFRP\text{-}fl}$ = function describing the stress-strain relationship of the GFRP flange;

$f_{GFRP\text{-}web}$ = function describing the stress-strain relationship of the GFRP web;

$f_{concrete}$ = function describing the stress-strain relationship of concrete;

$f_c^{'}$ = compressive strength of concrete;

$f_t^{'}$ = tensile strength of concrete;

f_1 = principal tensile stress;
= empirical function resulting from variation analysis;

f_2 = empirical function resulting from variation analysis;

G_{II} = strain energy release rate;

G_{IIC} = critical strain energy release rate at interface;

G_M = shear modulus of matrix;

G_c = shear modulus of concrete;

G_w = shear modulus of webs;

$\overline{G}_{xy}$ = average shear modulus of composite;

G_1 = shear modulus of GFRP flange;

$G_{\#}$ = shear modulus of unidirectional laminate;

$G_{\#}^{o}$ = initial shear modulus of unidirectional laminate;

H = material constant;

h_g = height of GFRP cross section;

I = moment of inertia;

I_i = moment of inertia of wall i;

K = constant;

K_s = shear coefficient;

k = constant;

k_f = buckling coefficient;

k_l = load case factor;

k_1 = cross section aspect ratio constant;

k_2 = ratio of ultimate moment to moment at CFRP fracture;

L = span length;
= complement probability (1-P);

M = bending moment;

M_b = moment at buckling of top GFRP flange;

M_c = moment at shear failure of concrete layer;

M_{el} = moment in elastic response region;

M_o = sustained moment;

M_i = calculated moment, at increment i;

M_{st} = short term response moment;

M_u = ultimate bending moment;

M_0 = moment from external forces;

M_2 = bending moment at failure of CFRP;

m = empirical constant;
= geometric constant;

m_1 = moment from virtual unit force;

m'' = empirical constant;

N = number of cycles;

N_F = fatigue life;

n = empirical constant;
= geometric constant;

n_c = concrete-web modular ratio;

n_1 = bottom flange-web modular ratio;

n_2 = CFRP-web modular ratio;

n_3 = top flange-web modular ratio;

P = applied load in three-point bending tests;

P_s = service load;

P_u = ultimate load;

P_o = external force;

P_1 = virtual unit force;

Q = shear rigidity;

S_C = characteristic stress level;

S_{max} = ratio between maximum stress applied and strength;

S_{min} = ratio between minimum stress applied and strength;

T = temperature;

T_o = initial temperature;
= total time;

t = time;

t_l = laminate layer thickness;

t_w = thickness of webs;

t_o = elapsed creep time;

t_1 = thickness of GFRP bottom flange;

t_2 = thickness of CFRP flange;

t_3 = thickness of GFRP top flange;

U = strain energy;

u_{ij} = ij -th displacement component;

$u_{\Delta T}$ = relative temperature deformation;

u_1 = equilibrating beam bottom fiber deformation;

u_2 = equilibrating FRP deformation;

V = shear force;

V_F = fiber volume fraction;

V_{GFRP} = ultimate shear force for GFRP shear fracture;

V_c = ultimate shear force for concrete shear failure;

V_u = ultimate shear force;

v = flexural deflection;

W_{ext} = external work;

W_F = fiber weight fraction;

w = shear deflection;

x = horizontal beam axis;

x_{con} = centroid of concrete normal force;

x_n = depth of neutral axis at failure;

x_{web} = centroid of web normal force;

y = depth of elastic neutral axis from top of GFRP webs;

y_c = distance from top compressive fiber;

y_u = depth of neutral axis at failure from top of GFRP section;

α = empirical constant;
= weight factor;

$\alpha_{F\|}$ = thermal expansion coefficient of fiber parallel to its axis;

$\alpha_{F\perp}$ = thermal expansion coefficient of fiber perpendicular to its axis;

α_M = thermal expansion coefficient of matrix;

$\alpha_{x\theta}$ = thermal expansion coefficient of laminate in θ direction;

$\alpha_{\|}$ = thermal expansion coefficient of unidirectional laminate parallel to fibers;

$\alpha_{\perp}$ = thermal expansion coefficient of unidirectional laminate perpendicular to fibers;

α_1 = thermal expansion coefficient of beam;

α_2 = thermal expansion coefficient of FRP;

β_1 = concrete rectangular stress block factor;

γ = shear strain;

γ_M = specific weight of matrix;

γ_c = correction factors for concrete content;

γ_{cp} = correction factors for initial moist curing;

γ_h = correction factors for average thickness of the member;

γ_{la} = correction factors for loading age;

γ_s = correction factors for slump;

$\gamma_{v/s}$ = volume-surface ratio;

γ_α = correction factors for air content;

γ_λ = correction factors for relative humidity;

γ_ψ = correction factors for fine aggregate percentage;

Δ = displacement in three-point bending;

Δ_{max} = maximum allowable displacement;

ε_F^* = fiber ultimate strain;

ε_M^* = matrix ultimate strain;

ε_c = strain in concrete top fiber;

ε_c^u = ultimate compressive strain of concrete;

ε_{cr} = creep strain in concrete;

ε_e = endurance strain in concrete;

ε_{fat} = fatigue strain;

ε_g = GFRP strain;

ε_i = strain in GFRP-concrete interface;

ε_{sh} = concrete shrinkage strain;

ε_{shu} = ultimate concrete shrinkage strain;

ε_{st} = short term strain;

ε_{tot} = total fatigue strain in concrete;

ε_x = strain in material x;

ε_x^{eff} = effective concrete strain in material x;

ε_x^{st} = real strain in material x;

ε_x^{o} = initial strain in material x;

$\varepsilon_o^{"}$ = empirical material parameter;

ε_o^{i} = initial strain in i-th iteration;

ε_1 = strain in bottom of GFRP bottom flange;

ε_{1t} = strain in top of GFRP bottom flange;

ε_1^{*} = tensile failure strain of GFRP;

ε_2 = strain in CFRP sheet;

ε_{2i} = initial strain in CFRP sheet;

ε_2^{*} = tensile failure strain of CFRP;

ε_3 = strain in bottom of GFRP top flange;

θ = arbitrary angle;
= angle of rotation;

θ_{ij} = ij-th component of rotation;

κ = curvature;

ν_L = longitudinal Poisson's ratio;

ν_M = matrix Poisson's ratio;

ν_T = transverse Poisson's ratio;

ν_c = concrete Poisson's ratio;

ν_w = web Poisson's ratio;

ν_1 = flange Poisson's ratio;

$\nu_{\perp\parallel}$ = fiber Poisson's ratio in fiber direction;

$\nu_{\parallel\perp}$ = fiber Poisson's ratio perpendicular to fiber direction;

$\overline{\nu}_{xy}$ = average Poisson's ratio of composite;

ξ = constant;

ρ_F = fiber density;

σ = normal stress;

σ_F^* = fiber tensile strength;

σ_M^* = matrix tensile strength;

σ_{bf}^* = GFRP flange buckling strength;

σ_m = empirical material parameter;

σ_{max} = maximum stress level during cycling,

σ_ε = empirical material parameter;

σ_x = stress in material x;

$\sigma_{\Delta T}$ = stress in CFRP due to temperature change;

σ_1 = stress in bottom of GFRP bottom flange;

σ_2 = stress in CFRP;

σ_2^* = laminate tensile strength;

σ_3 = GFRP top flange stress;

τ = shear stress;

τ_{bw}^* = web shear buckling strength;

$\tau_{concrete}^I$ = maximum concrete shear stress when neutral axis within GFRP;

$\tau_{concrete}^{II}$ = maximum concrete shear stress when neutral axis within concrete;

τ_{fw}^* = web shear fracture strength;

τ_{max} = maximum web shear stress;

τ_{web}^I = maximum GFRP shear stress when neutral axis within GFRP;

τ_{web}^{II} = maximum GFRP shear stress when neutral axis within concrete;

τ_o = shear stress generated by external;

τ_1 = shear stress generated by virtual unit load;

τ_θ = shear stress at angle θ;

φ_c = creep coefficient of concrete;

φ_{ul} = ultimate concrete creep coefficient;

φ_x = creep coefficient of material x;

ϕ = stiffness reduction factor;

ϕ^u = ultimate curvature;

ϕ^* = curvature at CFRP fracture.

ψ = empirical constant; and

ω = constant.

Chapter 1

INTRODUCTION

1.1 Fiber Reinforced Plastics in Structures

The evolution of fiber reinforced plastics is basically an extension of man's curiosity and his continuing search for the performance of materials with better physical and chemical properties. Fiber reinforced composites have been used by man for a very long time. The first to be used were naturally occurring composites, such as wood. The issue was to use materials that would perform more efficiently in their specific application. Today engineers make artificial fiber composite materials using glass, carbon or aramid fibers, bonded together with a matrix such as epoxy resin. By combining fibers and plastic matrix a bulk material is produced with a strength and stiffness close to that of the fibers and with the chemical resistance of the plastic. In advanced composites, the fibers are oriented at high volume fractions in the directions of stress. Among the properties of interest to engineers of fiber reinforced plastics (FRP) are high tensile strength, low weight, resistance to corrosion, high fatigue strength and high damping (Hull 1981). Fiber composites offer unique advantages for solving many civil engineering problems in areas where conventional materials do not perform well. Such areas include corrosive environments and structural elements required to have high strength/weight ratio.

Potential applications of FRP in structural engineering include: (a) lightweight structural components such as framing and bridges (e.g., McCormick 1978, Starr 1983, Sims et al. 1987, Bakeri 1989, Bank and Mosallam 1990, and Plecnik et al. 1990); (b) strengthening of existing structural members and reinforcement of new ones with nonprestressed or prestressed epoxy-bonded FRP sheets (e.g., Meier 1987b, Kaiser 1989, Saadatmanesh and Ehsani 1989, Deskovic 1991, Meier and Kaiser 1991, Meier and Deuring 1991, Triantafillou and Deskovic 1991, Triantafillou and Plevris 1991, Meier et al. 1992, Plevris and Triantafillou 1992, Triantafillou and Deskovic 1992, Triantafillou et al. 1992); (c) high-strength lightweight cables for cable-supported bridges (e.g., Meier 1987a, Aminian and White 1988, Burgoyne 1988, Plecnik et al. 1989, and Kim and Meier 1991) and tendons in prestressed elements (e.g., Rubinsky and Rubinsky 1954, Kaifasz 1960,

Somes 1963, Rehm and Franke 1974, Preis and Bell 1986, Waaser and Wolff 1986, Gerritse et al. 1987, Tanigaki et al. 1988, Budelmann et al. 1990, Iyer and Anigol 1991, Kakihara et al. 1991, and Zoch et al. 1991); (d) composite rods as reinforcement in concrete structures, offering corrosion immunity and providing non-conductive/magnetic fields (e.g., Fujisaki et al. 1987, Brown and Bartholomew 1990, Faza and GangaRao 1990, and Pleimann 1991); (e) rehabilitation of historic structures and shear walls in masonry with externally applied (and prestressed) FRP sheets (Schwegler 1992, Triantafillou and Fardis 1993); and (f) other applications such as storage tanks, pipes and stabilization of soils as well as retaining walls.

The drawback of composites is often associated with the involving and expensive production requirements. On the other hand, manufacture of composite materials by automated processes can produce today high quality components at a relatively low labor cost. One such process is pultrusion, in which fibers are pulled through a heated die into which resin is injected, and a fully cured member is produced with good dimensional stability. Typical member cross sections made by the pultrusion process are shown in Figure 1.1, the only requirement being the constant cross sectional dimensions.

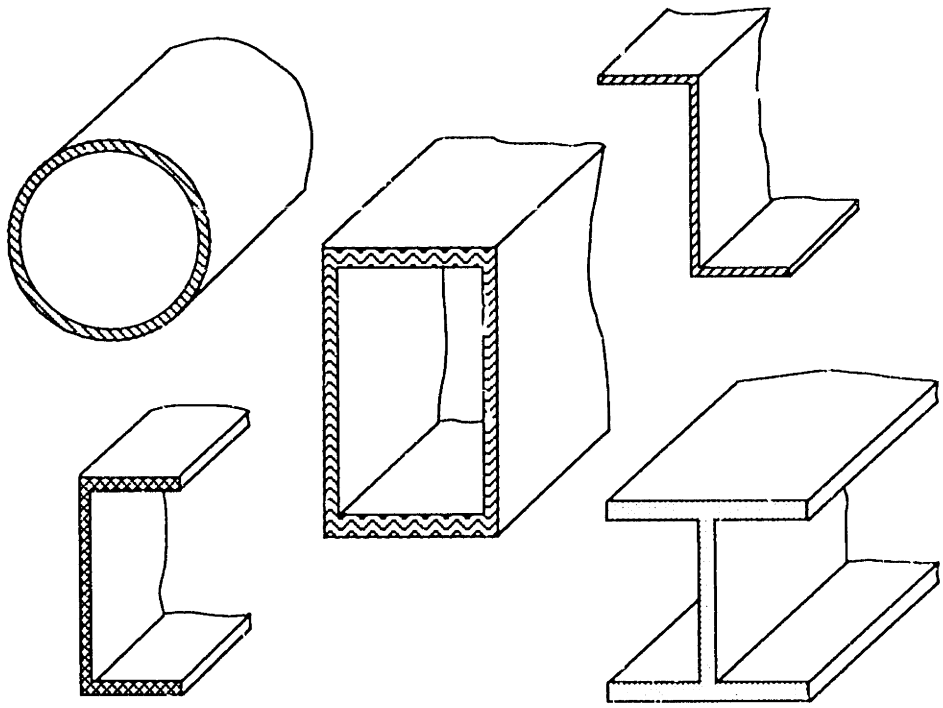

Figure 1.1 Standard pultruded members.

Pultrusion is a fast-growing process for manufacturing FRP structural members, and a great awareness among engineers of how the features of pultruded products can be

translated into cost saving benefits has made the method quite popular. However, until significant further developments take place in manufacturing technology linked to innovative designs to enable more efficient, reliable and cost effective structures to be produced, composite materials will hardly take their place in construction alongside traditional materials such as concrete, steel and wood.

This thesis presents in detail how composite materials can be combined with a low-cost construction material, concrete, to result in new concepts for the design of lightweight, corrosion immune and yet inexpensive beams with excellent damping and fatigue properties. The behavior in short and long term loading configurations is investigated. The proposed concept lends itself to low cost prefabrication of high performance structural elements, with a high potential of use in both today's construction of specialized composite structures and tomorrow's buildings and bridges formed out of modular systems.

1.2 New Design Concepts Using Materials by Combination

Consider, for instance, the case of a glass fiber reinforced plastic (GFRP) pultruded beam section. Thin walled box sections are the most efficient for beams (e.g., Ashby 1989), and are, in fact, very commonly used in structural applications for pultruded profiles. However, they suffer from some disadvantages, including the following:

(i) the compressive flange is considerably weaker than the tensile flange, because GFRP has a compressive strength of about half its tensile strength and because of local buckling phenomena (Banks and Rhodes 1983, Holmes and Just 1983);

(ii) failure is usually catastrophic without warning, as composite materials are linear elastic to failure; and

(iii) the design is usually governed by stiffness (because of the relatively low stiffness of GFRP), resulting in a need for excessive use of composite material to satisfy certain stiffness requirements.

In view of the above, the motivation for the subject discussed in this thesis was nucleated with the desire to create a novel and more efficient design of composite box sections, driven by the following considerations:

(i) The compression stresses in the section should be carried by a material with the highest compressive strength and stiffness to cost ratio, and hence, the GFRP flange could be eliminated and substituted by a layer of concrete.

(ii) Another composite material with a failure strain less than that of GFRP could be added to the section's tension zone, so that it will be the first element to fail giving some warning of an imminent collapse (pseudo-ductility). Since this element will be part of a flange, it should preferably possess a high stiffness, too, to increase the section's rigidity. An externally epoxy-bonded thin layer of unidirectional carbon fiber reinforced plastic (CFRP) appears to be the best candidate material for this purpose. Selection of this material will also enhance the member's fatigue and creep behavior, given that unidirectional CFRP has an excellent response to fatigue loading and is practically creep-free.

(iii) Since the proposed design involves casting of concrete, part of the cross section should be used as formwork for the wet concrete, to minimize fabrication costs.

Developments in the area of composite material systems linked to innovative designs of components using fiber reinforced plastics (FRP) in combination with concrete can enable more efficient, reliable and effective structures to be produced. These components possess many desirable mechanical behavior characteristics such as corrosion resistance, electromagnetic transparentness, high stiffness and strength, while maintaining a low weight. The main features of the new concept proposed here for hybrid sections can be summarized as follows: the concrete layer substitutes the GFRP compressive flange of traditional pultruded box sections, thus reducing the materials cost and increasing the stiffness; and the bottom flange is made by a combination of two composites (GFRP and CFRP), one failing in tension earlier than the other (and, possibly, in a gradual manner), serving the role of a "sensor" which indicates an imminent collapse (pseudo-ductile response).

The proposed concept for hybrid FRP-concrete elements can be thought of as a better way of designing composite profiles using materials by combination and placing them exactly where they perform best. Optimum combination of materials in structural design is increasingly becoming a necessity as well as an indispensable part of the structural engineer's response to the pressure for more durable and lightweight premanufactured components. Interesting applications of the proposed scheme may be found in the improvement of today's FRP pultruded members as well as in the construction of lightweight prefabricated or in situ cast bridge and/or floor decks.

A schematic illustration of hybrid FRP-concrete cross sections for beams in both building and bridge applications is given in Figure 1.2. Note that the top concrete layer is encased in a GFRP channel with wall thickness just equal to that required to carry the wet concrete and transfer the interface shear. Furthermore, a very good bond between the

concrete and the GFRP can be achieved either by the use of epoxy adhesives or by providing the GFRP-concrete surface with mechanical deformations, or, finally, by a combination of the two.

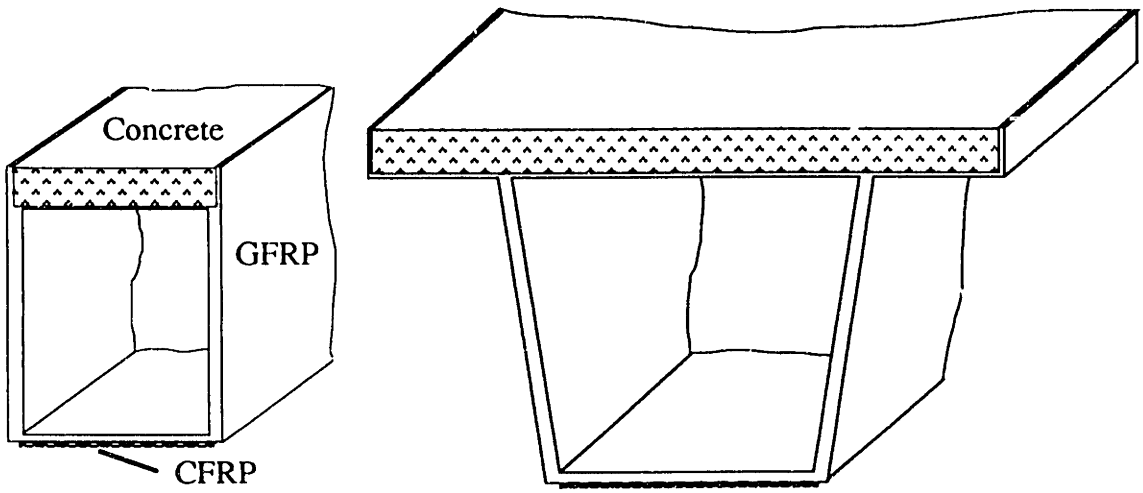

Figure 1.2 Proposed hybrid members.

The research of this thesis concentrates on the structural behavior and performance of this innovative hybrid FRP concrete beam system. It proposes design methodologies optimizing shape and material to be used in structural applications. The long term behavior addressing issues such as creep, fatigue, temperature and shrinkage effects is described. Exploiting the benefits of the proposed concept it appears that the technique can be implemented efficiently in the production of structural elements. The relatively high cost of production can be offset by the advantages in performance this system provides. As mentioned earlier, high stiffness and low weight, high corrosion and fatigue resistance, electromagnetic neutrality etc. are sufficient factors to justify the high material cost. It should be mentioned that the cost of FRP materials would decrease if its production were to increase. The high cost today is basically a result of the fabrication organization. The author believes that in future the production of FRP materials will increase and they will be used more widely in all engineering branches, including structural engineering.

1.3 Organization of the Thesis

The present work is organized in eight chapters, with the main emphasis given in Chapters 3, 4, 5, 6 and 7 in which both the analytical and experimental work are described and the innovative hybrid beam design concept is presented.

After the introduction given in this chapter, Chapter 2 is devoted to a brief review of existing structural applications with fiber reinforced plastics and composite construction in general. This review describes the FRP applications in: a) corrosive environments, b) electomagnetic interference circumstances and c) bridges. A general description of composite construction is included and the implication to hybrid elements is given.

The short term analysis of the new concept of hybrid elements is presented in Chapter 3. The assumptions made in the analysis are defined and nonlinear material models are chosen. Several failure mechanisms are considered: a) concrete crushing, b) CFRP rupture, c) GFRP tension failure, d) beam shear failure, e) interface debonding, f) GFRP web shear buckling and g) lateral instability. In addition, stiffness and deflection response relations are derived. A simplified failure analysis is proposed and a design methodology for FRP-concrete elements is developed. A design example is also given. Finally, a computer program for the nonlinear analysis of the hybrid member is presented.

In Chapter 4 the analysis for the prediction of the long term response of the hybrid beam is developed. A shrinkage model for concrete is adopted for the shrinkage analysis. Creep models for concrete and GFRP are defined for the creep analysis and a computer program taking material nonlinearity and creep effects into account is presented. The residual response of the beam after being subjected to a creep history is analyzed. Models characterizing fatigue behavior of concrete and GFRP are adopted and incorporated in the fatigue analysis of the hybrid beam. A computer program conducting the fatigue response analysis is presented including the capability for residual strength computation. The temperature impact onto the beam is also investigated and the analysis accounting for temperature-related deformations is derived. Special consideration is given to the CFRP-GFRP interface.

Chapter 5 describes the manufacturing process and design procedures followed in the production of the hybrid beams. The choice of geometric parameters is presented. Two types of hybrid beams, small scale beams with pultruded polyester GFRP profiles and large scale filament wound beams with an epoxy matrix, were chosen for the experimental program. The filament winding process used is described in detail. The setups for static, creep and fatigue tests on the hybrid beams produced are also given.

The parameters introduced in Chapters 3 and 4 for the characterization of short and long term material models are calibrated in Chapter 6. Experimental results from specimen tests are used to calibrate the proposed models for concrete, GFRP and CFRP. Apart from the short term response of the above materials, the creep and fatigue properties of concrete and GFRP are examined and modeled.

In Chapter 7 the experimental verification of the analysis presented earlier is described. First, the short term response of hybrid beams is evaluated on eighteen small and three large scale beams. A finite element model is generated and analyzed for the large scale beams to enhance experimental and analytical results. Experiment and analytical predictions are compared. Second, the creep response of the large scale hybrid beams is examined. Experimental results from 24 hour and 6 month creep tests (two each) are obtained and compared to the analytically computed values. Also, a parametric study on the residual response of hybrid beams is conducted. Third, the fatigue response of two large scale beams is tested and compared to analytical results. The effect of creep is also considered in the analysis. Furthermore, the residual response of one beam after fatigue is determined analytically and verified with experiment.

Finally, Chapter 8 summarizes the main findings that have come out of the research work. Conclusions regarding the performance of hybrid beams and the efficiency of the analytical tools developed are given. A discussion on the possible improvements of the proposed method is presented and recommendations regarding future investigation expanding the presented research work are given.

Chapter 2

BACKGROUND

2.1 General

The use of composite materials in the construction industry is currently represented in very modest quantities, but drawing the analogy to other industries the role of composites should increase in the future drastically. The aerospace, automotive, boating and sporting-equipment industries have incorporated composites in many products. Composite materials have been used to produce products such as satellite elements, aircraft, boat hulls, car bodies, windsurf boards and many others. Initially, in these industries, the use of composites in structural applications was mostly confined to secondary systems and/or in conjunction with other materials such as steel, aluminum or wood. Recently, the aerospace industry has begun to consider composites for primary load-bearing components. It is therefore acceptable to anticipate this initiative to expand into the structural world of civil engineering, as well. In fact, the construction and transportation industries have already introduced this concept, but to a limited extent. Specialized building systems, usually implemented for their corrosion resistance or electromagnetic transparency (e.g., to prevent interference with electromagnetic signals to antennas or satellite dishes) were placed in the market. As in other industries, many of the systems introduced are for secondary structures such as platforms, ladders and walkways. The main reason for these limitations was set by the high price of composites. A completely new philosophy behind the applicability of composites in construction practice was created with the development of cheap production alternatives. Structural products such as pultruded beam sections which are currently available in the market represent a good starting point in this process. But even here, the latter are mostly used as secondary elements and are being applied only for very specialized purposes in environmentally critical locations of some damaged structures. Moreover, in the applications encountered here the design is not optimized, since adequate analysis is often too involving. Therefore, it is important to stimulate the practicing engineer with improved concepts of applications of pultruded sections, using the beneficial properties of the latter and substituting deficiencies with better designs. This was attempted in this thesis. The future outlook foresees a

design code with specifications, very much similar to those frequently used in conventional materials such as steel , concrete or wood structures.

Among the most important features required for a possible breakthrough of composite structures are their superior performance and reduction in cost. The latter appears to be even more important considering today's economy and shrinking budgets. The savings in cost can be achieved through their increased durability (life-cycle), larger live load carrying capacity (due to lower dead weight) and easier construction methods. The life-cycle cost reduction will become increasingly important as maintenance and inspection costs increase and initial costs become a smaller fraction of the total investment. In addition, composites that offer higher strength, stiffness and fatigue life at a lower weight could reduce even the construction costs of structures where dead load forms a significant part of the structural load. For instance, the savings (due to lower dead load) in the foundation costs of a bridge can be substantial, or the increase of the load carrying capacity with the same dead weight can upgrade a bridge load rating. Composites may also strengthen their role in the market through the ability to incorporate embedded sensors. The demand for smart structures providing the possibility of nondestructive evaluation is growing. The cost of continuously monitoring composite materials may be less than that of monitoring conventional materials such as wood or concrete. All these considerations give an insight in the vast possibilities offered by composite materials and thus explain the need for more research work in this field, to provide a better understanding of their behavior in future civil engineering applications. An attempt to accomplish a small part of this effort is carried out in the research presented in this thesis.

2.2 Applications of Composite Elements in Structures

Today's bridges and structures are mainly made of traditional construction materials such as steel, concrete and timber. At the same time the existing infrastructure of the world's most developed countries is rapidly becoming inadequate. It is estimated that about 60% of the output of America's steel industry is going into replacement products (Mallinson 1974). Another drastic figure shows that only in the US about one half of the approximately 600,000 highway bridges are in need of replacement or rehabilitation (Klaiber et al. 1987). The deterioration of structures built forty or fifty years ago, an increase in the loads they have to carry and the importance of aesthetics are just some of the sources for technological innovation in structural engineering. Therefore, the increasing

demands on the performance and properties of building materials is triggering the development of new materials such as advanced composites. In addition, innovative design approaches, combining these materials are gaining importance in the attempt to meet these challenges.

As a result of the above it can be concluded that there is a large potential in the 1990s and beyond for advanced composite materials in structural engineering as they gain acceptance as substitutes to conventional materials. Profiles of glass fiber reinforced plastics are now used in many sectors of the construction industry. 'I', box, and plate profile sections are standard "off-the-shelf" structural elements which can be manufactured continuously by pultrusion. Chapter 5 gives further details on the pultrusion process. Some other applications of composites are in situations where an aggressive environment imposes strict requirements on the materials to be used. Examples are platforms for chemical storage tanks, beams for roof supports in aluminum manufacturing implants, walkways in chemical processing environments, water/wastewater plants, offshore oil platforms, zinc plating lines and others. To highlight the latter a few examples are given next.

In the UK five different pultruded profiles have been used in a 16000 m^2 floor suspended under the A19 Tees road bridge near Middlesborough. It contains 250 tons of pultruded material (Hollaway 1990). A large six-cell cooling tower installation in Forth Worth, Texas represents a further example for the application of composite profiles. Here, all the primary structural elements (columns, beams and lintels) were constructed with pultruded sections. Nearly half a mile of FRP beams went into construction of the twin cooling towers at the Grand River Dam 1000 MW coal fired power plant in Chouteau, Oklahoma (Figure 2.1).

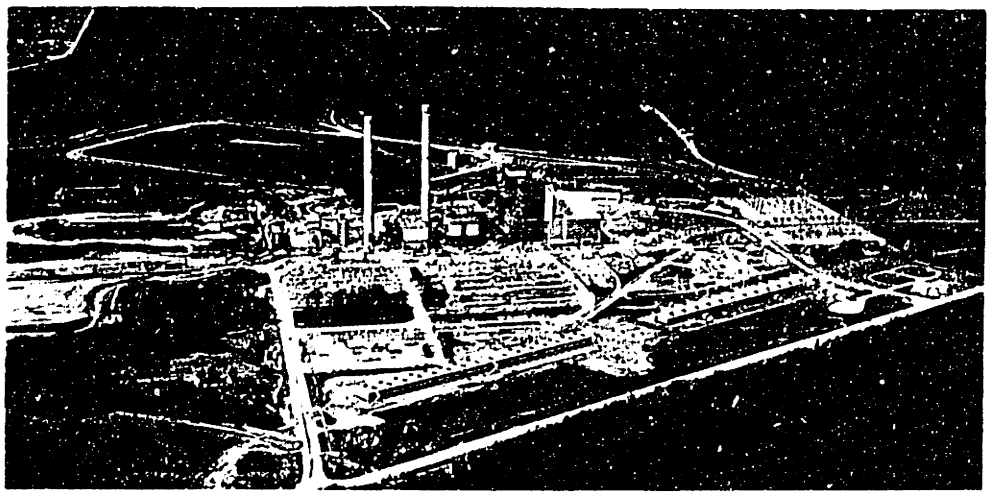

Figure 2.1 Power plant in Chouteau.

In this case, FRP turned out to be the best candidate for the wet and corrosive environment. A 17.4x3.0x0.7 m^3 platform was fabricated and implemented within a chlorine production area for Dow in Freeport, Texas. It was constructed of 6", 8", 10" and 12" wide flange beams and it was completely assembled at the site using a cherry picker in less than a day (Figure 2.2). Here, the ease of handling and erection played an important role.

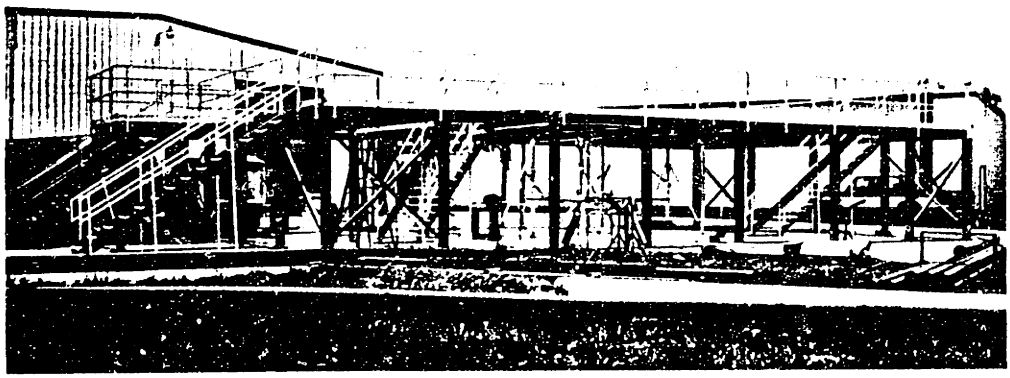

Figure 2.2 GFRP platform in Freeport.

A full spectrum of structural fiberglass products was installed in a new sodium chlorate plant in North Vancouver, British Columbia (Figure 2.3). Because of the high voltage and corrosive materials used in the process, fiberglass was the preferred material.

Figure 2.3 Sodium chlorate plant in Vancouver.

A major case for the superiority of pultruded FRP products is demonstrated through adoption of these materials in some of the facilities of the steel industries. Bethlehem Steel in Johnstown selected fiberglass-resin structural supports for a substructure in its zinc plating line because of lightweight, easy installation and high resistance to sulfuric acid (Figure 2.4).

Figure 2.4 Zinc plating line substructure, Johnstown.

Four volatile organic compound scrubbing towers located in the City of Delray Beach, at Florida's Waste Water Treatment Plant were constructed entirely of FRP products. Pultruded structural shapes were designed for interconnecting walkways, perimeter work platforms and substructure supports (Figure 2.5).

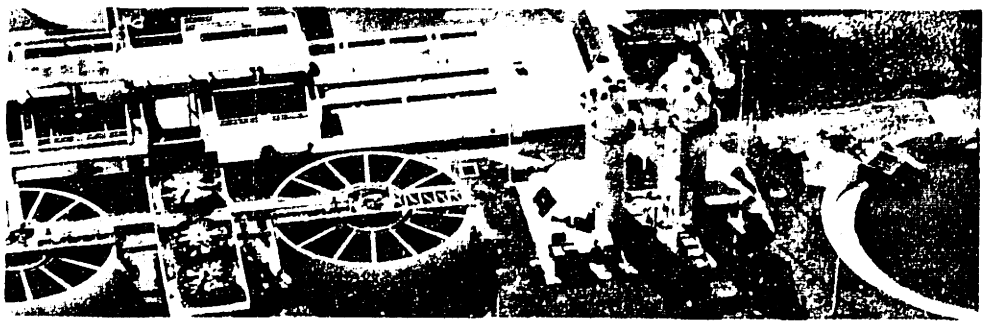

Figure 2.5 Waste water treatment plant in Florida.

Other applications are found in structures where electromagnetic conductivity is a problem, such as frames and/or superstructures of buildings for electromagnetic test operations, communication equipment or sensitive computer circuitry plating rooms. The first all GFRP building was the electromagnetic interference (EMI) test laboratory for Apple Computer installed in 1985. Such an EMI test laboratory enclosure building requires that all the building components above the ground level must be nonmetallic, be radio frequency transparent, and not reflect EMI emissions. The Sun Bank building in Orlando was, for instance, supplemented on its top with four three-story turrets (one of which is shown in Figure 2.6) to house communications equipment. The structure is fully built out of FRP composites to exclude any radio magnetic interference.

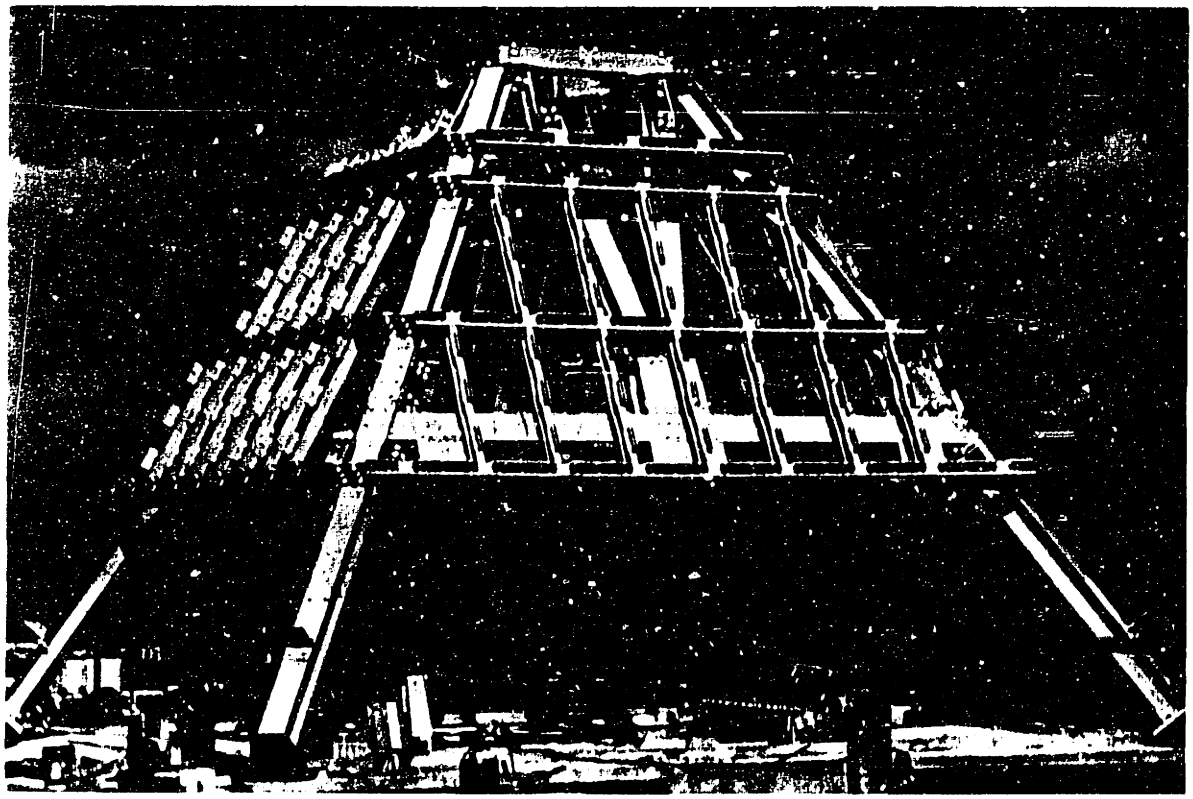

Figure 2.6 Three story turret on top of the Sun Bank building in Orlando.

Another structure of this type was built by the Department of Defense to support equipment used in a magnetic fusion experiment (Figure 2.7). Again, it was entirely constructed of pultruded GFRP shapes. A third example represents the five-story superstructure used for

an IBM computer circuitry plating room (Figure 2.8). Here, the electromagnetic transparency was of highest importance.

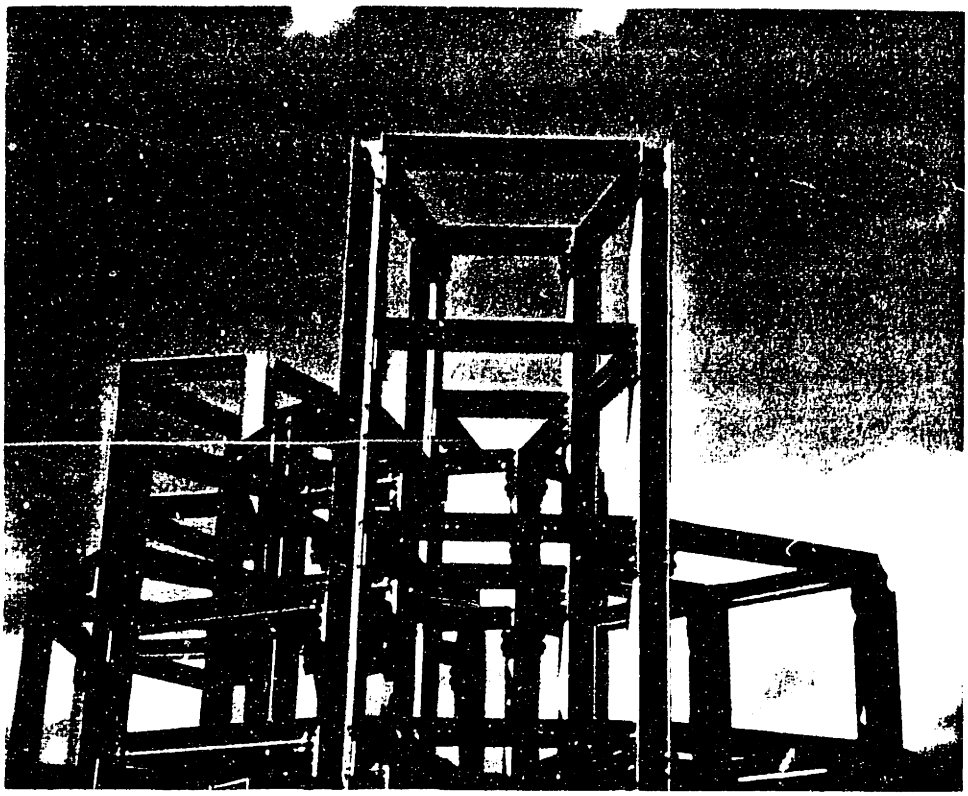

Figure 2.7 Non-electromagnetic interference building.

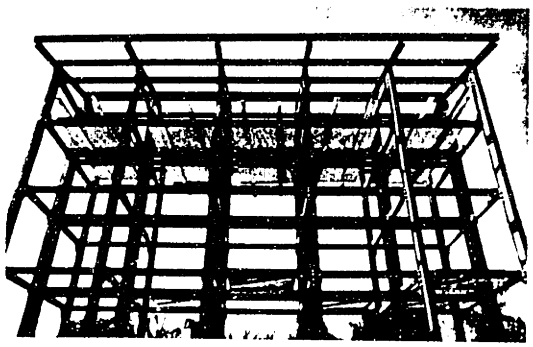

Figure 2.8 IBM computer circuitry plating room.

The newest incentives for the use of pultruded sections are directed to applications in bridge decks and supporting bridge girders. The longest (in the U.S) fiberglass pedestrian bridge spans over Devil's Pool in Fairmount Park, Philadelphia, Pennsylvania. It is manufactured out of four 15 m span beams and was additionally prestressed with Kevlar cables. The main features include low weight (only 1100 kg), corrosion resistance, aesthetic appearance (Figure 2.9) and low cost. The estimated $100k for an equivalent

conventional steel bridge were decreased by four times. A detailed description of other GFRP bridges is given by Meier (1991).

Figure 2.9 Pedestrian bridge over Devil's Pool in Philadelphia.

A listing of bridges presented in his paper reads as follows: (a) Tel Aviv pedestrian bridge, built early seventies, 30m span, "U" shaped cross section: (b) Virginia pedestrian bridge (see also McCormick 1978), built 1976, 4.9m long, triangular cross section; (c) Westminster Cathedral footbridge, London, 25 m long, "U" shaped; (d) Chongquing pedestrian cable-stayed bridge, built 1986 in China, 27.4m long main span, box girder; (e) Guinanyinqiao pedestrian bridge, built 1988 in China, span 70m, concrete/GFRP space frame with 19m long GFRP girders; and (f) Miyun GFRP highway bridge, built in 1982 northeast of Beijing, 21m long, five prismatic box girders filled with honeycomb-like structures. From here it can be concluded that the initiative for GFRP bridge design already gives valuable results and that in the future many other structures may be encountered.

In many of the current applications the proposed hybrid beam concept can provide important improvements and significant savings. Horizontal members in frames of pultruded sections made of hybrid beams could increase both span lengths and ductility and lower cost without loosing their corrosion resistance and EMI transparentness, and hence, would represent a competitive solution. A much larger field in construction where the hybrid beam concept could be appreciated is related to bridges. It can be anticipated that box girders made of large pultruded sections with layers of concrete on top can find their place in future designs.

2.3 Composite Construction

The term "composite construction", in general, refers to structural systems in which there is interaction between different materials such as steel and concrete in reinforced concrete, steel and timber in flitched beams, glass fibers in resin matrix, or brick infill panels in a steel frame. In this thesis composite construction will be used to refer to interaction between concrete and an other structural material in such combinations as a steel or FRP beam interacting compositely with a concrete slab or layer. Moreover, the case of composite action between a GFRP/CFRP beam and a concrete layer will be referred to as a hybrid beam. The most common form of composite construction, used for many years for highway bridges, results from the combined action of conventional steel beams with a cast-in-place concrete deck slab. The same type of composite construction is also used with increasing frequency in buildings. In both cases the concrete deck and floor slabs represent the load distributing medium, transferring load superimposed on them to a supporting structure of steel beams. Composite structural systems are therefore important, accounting for a considerable proportion of the annual construction output. Attempts to improve the efficiency of these systems have clear economic advantages, which can easily be demonstrated.

The history of composite construction is intimately connected with that of reinforced concrete. The first experimental investigation and extended design theory to deal with the problem of a concrete slab resting on the top flange of a steel beam was conducted by Caughey and Scott in 1929. A distinction was made between the loading case when the slab was propped until it had hardened and the unpropped case. Elastic design methods based on conventional beam theory had been developed and the composite system was beginning to attract the attention of designers and inventors. Unfortunately, the construction industry is always very slow in adopting a new method, even if it is shown to be economical. A major improvement on this plan was made after the World War II, when the steel shortage in Europe forced engineers to adopt the most economical design methods available to reconstruct the bridges and buildings destroyed.

Although the most commonly used form of composite systems is that employing solid web steel beams supporting concrete slabs, other types were implemented, as well. Examples can be found with box, truss and castellated beams or open web joists and are given in Figure 2.10. The concrete slab may partially or wholly enclose the beam or, where a steel box beam is used, form the top flange of the box. The requirement is that

composite action must be ensured by means of suitable shear connection or a reliable natural or adhesive bond between steel and concrete. The supporting beams in composite construction are capable of carrying their own dead weight and that of the associated concrete, thus leading to considerable simplification of the construction process. The same idea is applicable to the hybrid beam concept.

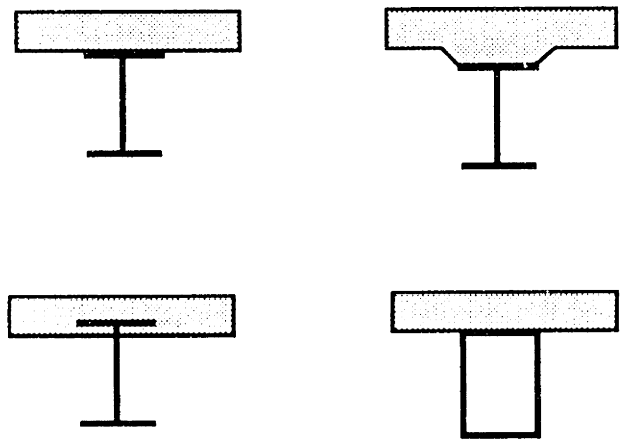

Figure 2.10 Composite construction examples.

The design of structures for buildings and bridges is mainly concerned with the provision and support of load-bearing horizontal surfaces. Except in long-span bridges, these floors or decks are usually made of reinforced concrete, since no other material has a better combination of low cost, high strength, and resistance to corrosion, abrasion and fire. The economical span for a reinforced concrete slab is little more than that at which its thickness becomes just sufficient to resist the point loads to which it may be subjected or, in buildings, to provide the sound insulation required. At larger spans it is cheaper to support the slab on beams or walls than to thicken it. Here the composite construction finds its market, since it becomes cheaper. The concrete-steel composites, due to the susceptibility of steel to damage by fire, were restricted to applications where this was not a problem, such as bridges and multi-story car garages. With the introduction of hybrid GFRP-concrete beams not only this limitation can be extinct, but also the problem of corrosion eliminated.

Another perspective giving advantage to the composite construction is related to the construction process and time. No profit is achieved from invested equity in the construction of a multi-story building until the building is occupied. At the time of rapid inflation and high interest rates, no comparison of the relative costs of different types of structures is meaningful unless account is taken of construction times. Therefore, the

proposed hybrid beam concept can represent additional savings in construction time, if considering the easy handling of the GFRP sections and their scaffolding role for the concrete layer. It can be concluded that composite construction is particularly competitive in large span structures, where a concrete slab is needed as a supporting layer and where there is a premium on rapid construction. In addition, the fire and corrosion resistance of FRP-concrete hybrid elements enhance the range of applicability.

2.4 Summary

From the background overview presented in this chapter it can be concluded that the use of fiber reinforced plastics for the construction of composite structures has the potential to become a technological "must" in future structural applications. Combining the advantages provided by FRP and concrete from the aspect of material properties and composite construction from the structural aspect, it appears that hybrid FRP-concrete members may present a promising way to create new, durable and cost effective structures. This concept is explored in this thesis.

Chapter 3

SHORT TERM MONOTONIC ANALYSIS

3.1 Introduction

In this chapter a model for the analysis of the short term behavior of the hybrid FRP-concrete members as well as an appropriate design methodology are developed. The hybrid member is made by combining three different materials, namely concrete, GFRP and CFRP, and for each of them an appropriate material model is obtained. The general assumptions are presented together with the possible failure modes associated with the corresponding nonlinear material behavior. Both classical and Timoshenko beam theory are implemented and a computerized procedure is developed in order to numerically simulate the bending behavior of the hybrid element. The concept of pseudo-ductile failure behavior is introduced and taken into consideration for the design procedure. Finally, a simplified approach for preliminary design is given along with a more sophisticated numerical analysis for exact calculations at final design stages. The follow up, a long term analysis, is given in the next chapter.

3.2 Mechanical Behavior of Hybrid FRP-Concrete Elements

3.2.1 Assumptions Made in Analysis

In the analysis performed the classic beam theory approach was implemented, using Timoshenko's shear flow for the calculation of deformations. The main assumptions are:

- Plane sections remain plane in the bending analysis,
- The adhesive contribution in the analysis is neglected,
- Failure prediction is defined by the maximum strain criterion,
- Concrete and GFRP are represented with nonlinear material behavior,
- Properties of webs and flanges of GFRP box beams are defined separately,

- Shear stresses are constant along the width of the GFRP webs and concrete,
- Concrete has not cracked due to shrinkage.

3.2.2 Concrete Model

The uniaxial stress-strain relationship for concrete has been derived assuming a in part linear-elastic and in part nonlinear response, using the most commonly reported and easily available test values. These values usually are the 5% fractile strength, $f_c^{'}$, of concrete cylinders with a height to diameter ratio of approximately 2, and the elastic modulus, E_c, measured in the elastic region at approximately 20% of the concrete strength. Given these values and defining the strain at ultimate stress to 0.2% and at failure to ε_c^{u} = 0.35%, an analytical expression was derived. In addition, it was assumed that the response for strains less than 0.05% is linear elastic and defined with the elastic modulus. The stress at failure is defined at 75% of the ultimate stress.

Based on these assumptions, the uniaxial stress-strain relationship for concrete can be obtained as a fourth order polynomial for strains larger than 0.05% and as a straight line for smaller strains. This is shown in Figure 3.1. Applying the boundary conditions:

$$\sigma_c = 0.05\% E_c; \quad \frac{d\sigma_c}{d\varepsilon_c} = E_c; \quad (@\varepsilon_c = 0.05\%) \tag{3.1}$$

$$\sigma_c = f_c^{'}; \quad \frac{d\sigma_c}{d\varepsilon_c} = 0; \quad (@\varepsilon_c = 0.2\%) \tag{3.2}$$

$$\sigma_c = 0.75 f_c^{'}; \quad (@\varepsilon_c = 0.35\%) \tag{3.3}$$

The fourth order polynomial is obtained as follows:

$$\begin{aligned} \sigma_c = \quad & (0.642 f_c^{'} - 0.000864 E_c) + \\ & (4.91 E_c - 2950 f_c^{'}) \varepsilon_c + \\ & (4.16e6 f_c^{'} - 5350 E_c) \varepsilon_c^{\,2} + \\ & (2.10 E_c - 1.77e9 f_c^{'}) \varepsilon_c^{\,3} + \\ & (2.35e11 f_c^{'} - 2.71e8 E_c) \varepsilon_c^{\,4} \end{aligned} \tag{3.4}$$

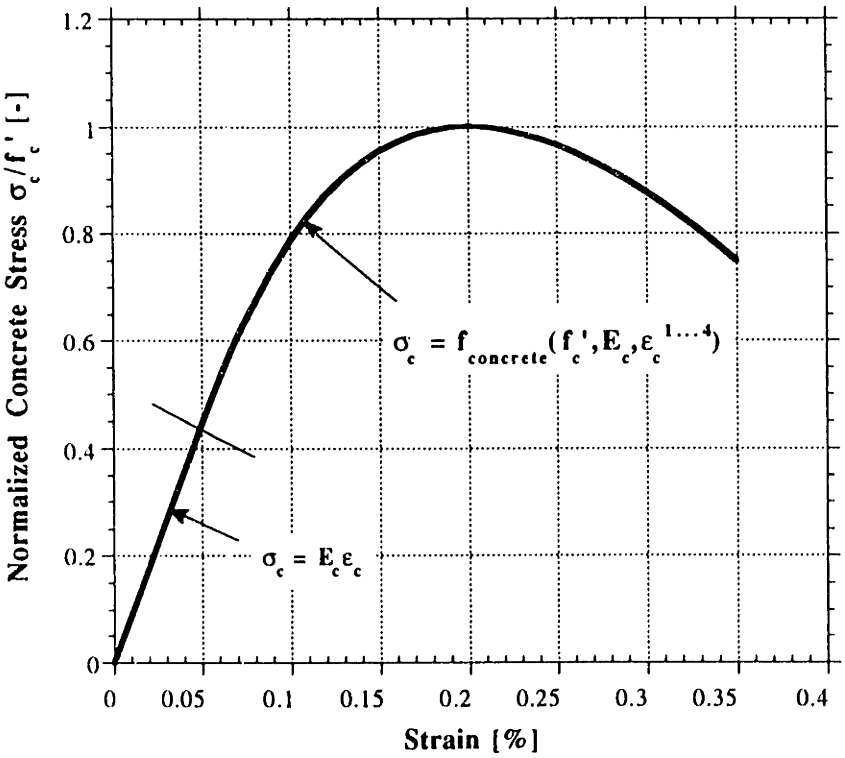

Figure 3.1 Concrete stress-strain relationship in compression.

The behavior of concrete in uniaxial tension is assumed to be linear elastic to failure, defined as (ACI 1989):

$$f_t = 0.664\sqrt{f_c'} \tag{3.5}$$

Furthermore, the modulus of elasticity in tension is the same as that in compression, E_c. Poisson's ratio for concrete, ν_c, is assumed to be 0.2, which is a most commonly reported value for normal concrete, and thus the shear modulus, G_c, can be calculated from elasticity theory as:

$$G_c = \frac{E_c}{2(1+\nu_c)} \tag{3.6}$$

The shear strength of concrete was not used directly in the analysis of the hybrid beam, but was rather taken into account through the maximum principal tensile stress in the concrete

layer, which was set equal to the tensile strength of concrete and as such defined a shear failure mechanism.

3.2.3 GFRP Model

There are several models that were developed in order to represent the behavior of GFR plastics. The laminate theory (Jones 1975, Holmes and Just 1982), relying on continuum theory (the latter name being more general will be used throughout this thesis) is able to predict analytically the material behavior to a satisfactory level, but mainly in its elastic region. The assumptions here are: (a) the matrix contributes to the behavior of the composite; (b) the multilayer composite is made of single homogeneous orthotropic or isotropic layers, and the fiber/matrix element is regarded as a continuum; (c) compatibility between the layers is maintained; and (d) Hook's law is valid. Still, the results of the continuum theory approach are often empirical, and depend heavily on experimental values such as the fiber volume fraction and matrix and fiber material properties, which again involve substantial experimental scatter, so it is questionable how effective this theory can be. When, in addition, the highly non-homogeneous GFRP is subjected to load levels beyond its elastic region, effects of fiber-matrix interface, and the appropriateness of the imposed failure criterion can cause substantial deviations of the theoretical from the real data. Another approach is given by the net theory of the membrane (Agarwal and Broutman 1980) which accounts for stresses generated in the fibers only, but neglects the matrix and shear transfer between fibers. This theory describes the behavior of composites at stress levels causing substantial cracking, delamination and fiber rupture quite well, but relies again on experimental data such as fiber properties and volume fraction. A third method, covering load ranges between matrix cracking initiation and fiber rupture is the layered fracture analysis (Meier 1990). This method was particularly developed after the introduction of computers and assumes that when failure of fibers in one layer is reached, this one disintegrates and its contribution to the behavior of the composite is set to zero.

In order to simulate the full behavior of a composite from its elastic response to the failure load, a combination of the three theories would be an ideal solution. But apart from the fact that it would be questionable how to separate the overlapping ranges of the three methods, the computational effort required would be enormous. Therefore the model for the GFRP used in this thesis describes the material using empirical data from experiments and casts them into easy to manipulate mathematical relations. Figure 3.2 shows a typical example where an experimental curve describing the stress-strain relationship of GFRP

obtained from coupon tests in uniaxial tension is modeled with a fourth order polynomial. This approach was used to model the uniaxial properties of the GFRP box beam; different relationships were implemented for the web and the flange, because in general the material properties might vary due to manufacturing constraints (such as thickness associated with size effects and voids inclusions, position during curing and the similar), or due to the design requirements.

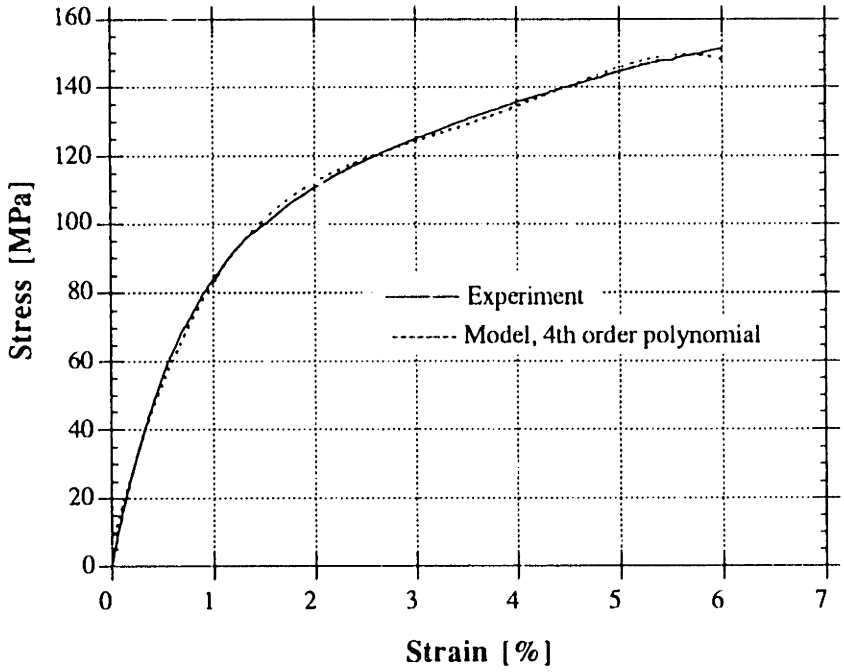

Figure 3.2 GFRP stress-strain relationship in tension.

The curve fit was achieved using the least squares method with the condition that the error be less than 1%. In order to obtain better agreement between data and the model, a straight line passing through the origin was assumed in the elastic region. The transition between the linear elastic and nonlinear region was taken at a strain of 0.15 %. The nonlinearity of the stress-strain curve is increasingly pronounced as the fiber orientation in the layers of the GFRP coupon deviates from unidirectional (0° fibers). This is a result of the effect of shearing of the matrix between the fibers. In the flanges the stresses are mainly normal and unidirectional, and thus a higher percentage of 0° fibers is preferred implying that the stress-strain diagram is closer to that of a linear elastic material. On the other hand, the webs, being mainly loaded with shearing stresses, are preferably composed of ± 45° fibers and hence a nonlinear stress-strain curve is appropriate. This justifies the assumption of different material laws for the flanges and the web due to design requirements.

The elastic modulus of GFRP, E_g, is defined directly from the stress-strain diagram by taking the slope in the elastic region:

$$\frac{d\sigma}{d\varepsilon}(@\varepsilon = 0) = E_g \tag{3.7}$$

This value is only used for initial equilibrium calculations of the hybrid member to obtain good initial estimates for the iteration procedure describing the nonlinear response. The shear modulus of GFRP, G_g , can be obtained through continuum theory, as described later in Chapter 4. If the normal stress levels generated in the webs are in the elastic region and assuming the fiber direction in the webs to be $\pm 45°$, the principal stresses generated by the shear force will be mainly in the fiber direction. This implies that the resulting shear stress-strain curve will be close to linear. An empirical value for the shear modulus can be obtained by measuring the shear strains, γ, at points where the shear stress, τ, is known or can be calculated with sufficient precision. Applying Hook's law for shear the value of G_g can be calculated as follows:

$$\frac{d\tau}{d\gamma}(@\gamma = 0) = G_g \tag{3.8}$$

The Poisson's ratio of GFRP sections, ν_g, can be obtained from continuum theory as described in Chapter 4.

3.2.4 CFRP Model

The third constituent of the hybrid element is a unidirectional composite of high strength and high modulus fibers embedded in a resin matrix. If in addition the fiber content is assumed to be above 65%, it is apparent that the fibers are dominant for the uniaxial tension response of the material. On the other hand, the high performance fibers show a substantially brittle behavior and thus the adopted CFRP model constitutes a stress-strain relationship corresponding to that of a perfectly linear elastic material. The slope of the stress-strain curve is constant and represents the elastic modulus of CFRP, E_2. This is shown in Figure 3.3. At ultimate strain the material ruptures in a highly destructive manner, and for small thickness CFRP laminates failure is associated with complete fracture of the cross section. This is a very important feature for the pseudo-ductile failure behavior of the hybrid member, described later in this chapter.

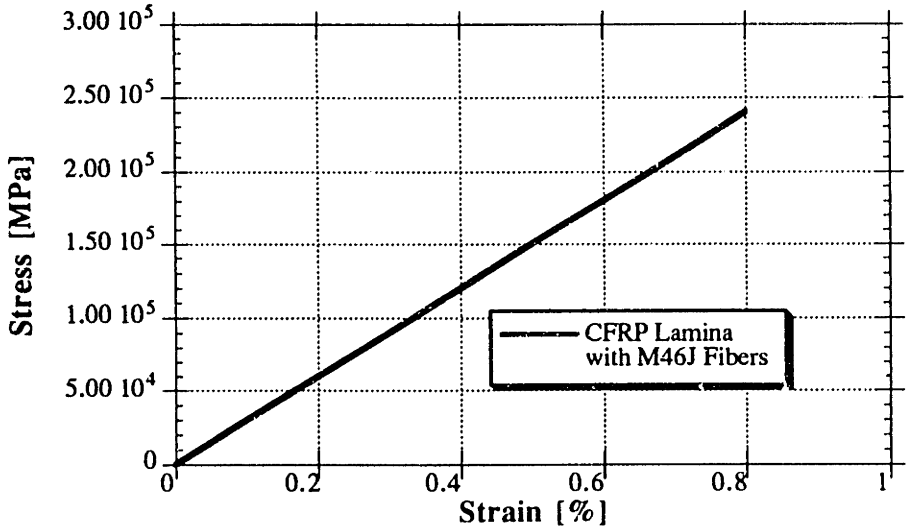

Figure 3.3 CFRP stress-strain relationship in tension.

3.2.5 Failure Analysis

An idealization of the proposed cross section for hybrid FRP-concrete beam elements is shown in Figure 3.4. The webs have a depth d and a thickness t_w; the bottom and top GFRP flanges have thicknesses t_1 and t_3 , respectively, and the concrete layer has a thickness c; the CFRP laminate has a thickness t_2 (if the width of CFRP is $b_2<b$, then an equivalent thickness $t_2 b_2/b$ can be considered); and the section has a width b. The properties of the different materials constituting the cross section are as follows: E_c = Young's modulus of concrete; $f_c^{'}$ = compressive strength of concrete; ε_c^u = ultimate compressive strain of concrete; E_w = longitudinal Young's modulus of webs; E_{wT} = transverse Young's modulus of webs; G_w = shear modulus of webs; ν_L = longitudinal Poisson's ratio of webs; ν_T = transverse Poisson's ratio of webs; τ_{fw}^* = web shear fracture strength; E_1 = Young's modulus of GFRP bottom flange; ε_1^* = tensile failure strain of GFRP bottom flange; E_2 = Young's modulus of CFRP laminate; and ε_2^* = tensile failure strain of CFRP.

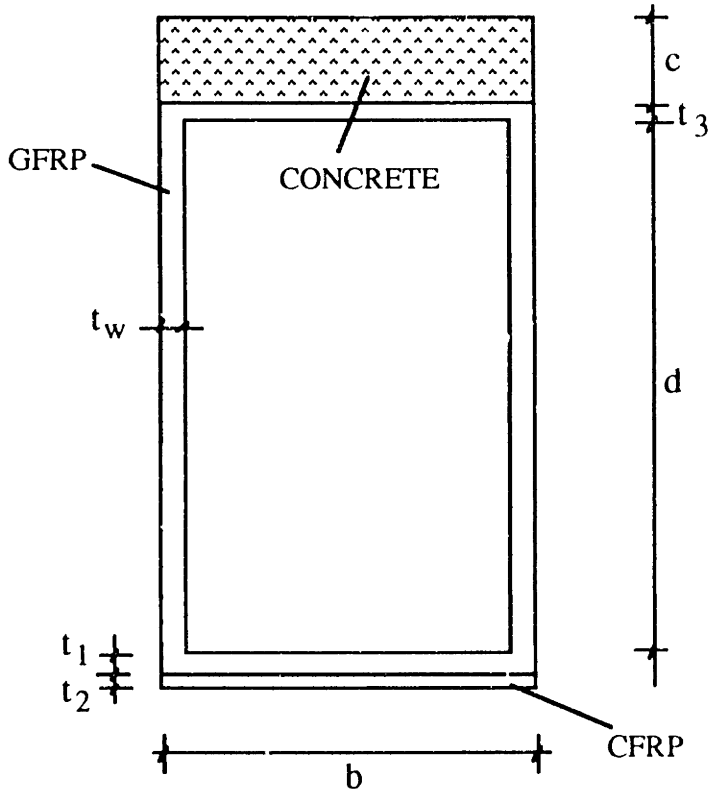

Figure 3.4 Idealized hybrid FRP-concrete section.

The hybrid section loaded in bending can fail in a number of possible ways. The webs may fracture or buckle due to shear stresses, resulting in shear failure; one or more of the beam's elements may fail due to normal stresses, resulting in flexural failure; the beam may buckle laterally (lateral torsional buckling); if the cross section is not properly dimensioned the principal tensile stresses in the concrete may exceed the cracking strength; and the bond at the GFRP-concrete or the GFRP-CFRP interface may fail causing debonding. The failure mechanisms are discussed next.

3.2.5.1 Concrete Crushing

In this section the failure mode causing the hybrid section to fail when the concrete layer has reached its compressive capacity is described. A perfect bond between the GFRP and the concrete is assumed and the influence of the adhesive is neglected. Figure 3.5 shows the stress and strain distributions in a typical cross section at failure. The stress-strain relationships for concrete, GFRP and CFRP were adopted according to the material models described earlier in this chapter.

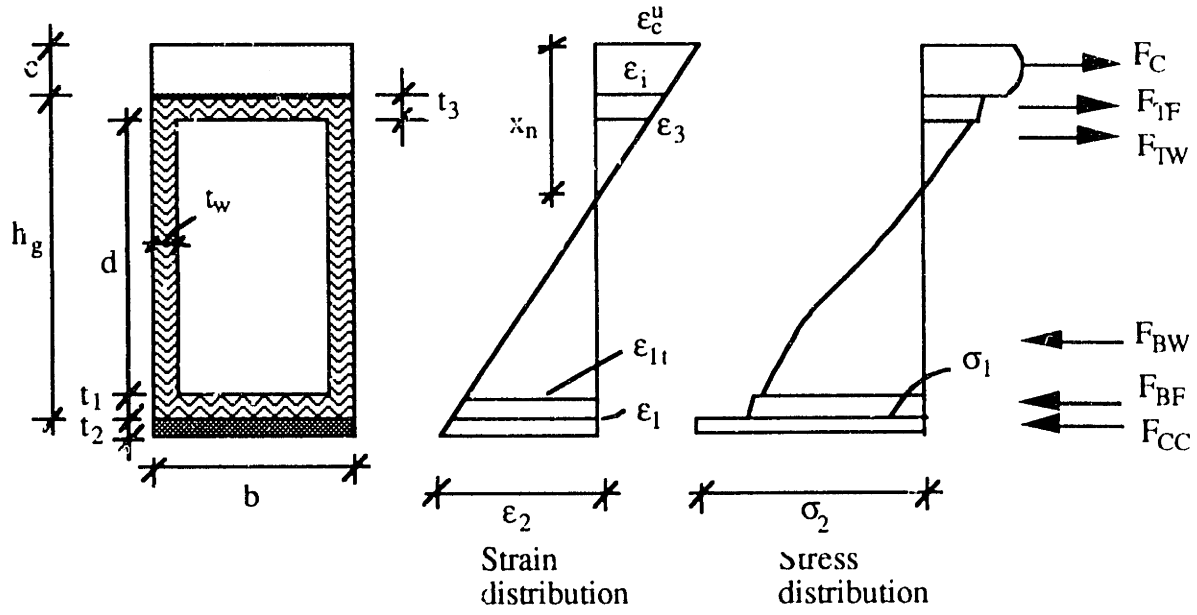

Figure 3.5 Stress and strain distributions at concrete crushing.

Strain compatibility in Figure 3.5 gives:

$$\frac{\varepsilon_c^u}{\varepsilon_2} = \frac{x_n}{h_g + c - x_n + t_2} \tag{3.9}$$

and the depth of the neutral axis is derived as

$$x_n = \frac{\varepsilon_c^u (h_g + c + t_2)}{\varepsilon_c^u + \varepsilon_2} \tag{3.10}$$

giving the following expressions for the various strains:

$$\begin{aligned}
\varepsilon_i &= \varepsilon_c^u \frac{(x_n - c)}{x_n} \\
\varepsilon_3 &= \varepsilon_c^u \frac{(x_n - c - t_3)}{x_n} \\
\varepsilon_{1t} &= \varepsilon_c^u \frac{(h_g + c - x_n - t_1)}{x_n} \\
\varepsilon_1 &= \varepsilon_c^u \frac{(h_g + c - x_n)}{x_n}
\end{aligned} \tag{3.11}$$

Equilibrium of normal forces gives the following equation:

$$F_C + F_{TF} + F_{TW} = F_{BW} + F_{BF} + F_{CC} \tag{3.12}$$

where:

$$F_C = b\int_0^c f_{concrete}(E_c, f_c', \varepsilon_c(x))dx \tag{3.13}$$

$$F_{TF} = t_3 b\frac{(\varepsilon_i + \varepsilon_3)}{2}E_3 \tag{3.14}$$

$$F_{TW} = 2t_w \varepsilon_3 \frac{(x_n - c - t_3)}{2}E_w \tag{3.15}$$

$$F_{BW} = 2t_w \int_0^{h_g + c - x_n - t_1} f_{GFRP-web}(\varepsilon_g(x))dx \tag{3.16}$$

$$F_{BF} = bt_1 f_{GFRP-flange}(\frac{\varepsilon_{1t} + \varepsilon_1}{2}) \tag{3.17}$$

$$F_{CC} = t_2 b \varepsilon_2 E_2 \tag{3.18}$$

It should be pointed out that the functions $f_{concrete}$, $f_{GFRP\text{-}web}$ and $f_{GFRP\text{-}flange}$ are the analytical models presented earlier for the material stress-strain relationships. Yet, the integrations are preferably performed numerically within a computer routine. The values $\varepsilon_c(x)$ and $\varepsilon_g(x)$ are the concrete and GFRP strains, respectively, in segment dx, given as a function of the distance x from the neutral axis. It is further assumed that the neutral axis of the cross section lies relatively close to the GFRP-concrete interface, implying a small strain ε_3. Thus, the linear-elastic portion of the GFRP stress-strain are adopted in equations (3.14) and (3.15).

The flexural capacity of the cross section can now be calculated by taking moments with respect to the neutral axis. Note that the unknown ε_2 is obtained from (3.12) numerically. This can be carried out with a computer program incrementing this value until equilibrium is obtained. Moment equilibrium gives:

$$\begin{aligned} M_u = {} & F_C x_{con} + \\ & F_{TF}\left(x_n - c - \frac{t_3}{2}\right) + F_{TW}\frac{2}{3}(x_n - c - t_3) + \\ & F_{BW}x_{web} + F_{BF}\left(h_g + c - x_n - \frac{t_1}{2}\right) + \\ & F_{CC}(h_g + c - x_n + \frac{t_2}{2}) \end{aligned} \tag{3.19}$$

where x_{con} and x_{web} are the lever arms of F_C and F_{BW}, respectively, obtained by numerical integration as follows:

$$x_{con} = \left[\int_0^c x\, f_{concrete}(E_c, f_c', \varepsilon_c(x))dx\right] / (F_C b) \tag{3.20}$$

$$x_{web} = \left[\int_0^{h_g+c-x_n-t_1} x\, f_{GFRP-web}(\varepsilon_g(x))dx\right] / (2F_{BW}t_w) \tag{3.21}$$

To get a warning of imminent failure, it is desirable to have the CFRP laminate rupture prior to concrete crushing. This will be the case if ε_2 exceeds ε_2^*. If this occurs, the analysis for the ultimate moment M_u applies by setting $t_2 = 0$. Then, equations (3.12) to (3.19) change slightly since the terms involving F_{CC} vanish.

3.2.5.2 Concrete Crushing - Neutral Axis in Concrete

The above analysis holds only if x_n from equation (3.10) is less than c, implying that the neutral axis is below the GFRP-concrete interface and that the concrete layer is all in compression. For an optimum design this should always be the case, but in order to apply the analysis generally, this assumption can be relaxed. In fact it is feasible that the neutral axis goes into the concrete layer and introduces tension in it. The tensile stresses sum up to the shear stresses generated in this region and develop principal stresses that might exceed the concrete tensile strength, causing failure of the concrete and eventually collapse of the member. Therefore, this failure mode has to be treated separately and at the same time for the calculation of M_u it can be checked to what extent the neutral axis can enter the concrete layer without the concrete to crack. This will be presented next.

Since the ratio of shear force to bending moment applied to one cross section of the hybrid member depends on the loading configuration, and in addition the normal and shear stresses vary nonlinearly across the height of the beam at the same cross section, there is a number of combinations that could potentially produce the maximum principal stress at different locations, and one single analytical expression for the ultimate load could not be derived. Therefore, for the analysis presented here some simplifications have to be adopted. It is assumed that, as far as concrete cracking is concerned, there are only two critical locations: (a) one at the concrete-GFRP interface with maximum normal tensile stresses and the corresponding shear, and (b) one at the neutral axis with maximum shear stresses. The latter case (concrete shear failure) will be discussed in Section 3.2.5.5,

while for the first case it can be assumed for simplicity that the shear stresses are much lower than the tensile stresses. Using these assumptions, a set of equations can be derived giving either the ultimate bending moment of the beam, M_u , caused by concrete crushing, similar to the one described earlier, or indicating a premature failure due to concrete cracking at the interface. The strain and stress distributions for the case when the neutral axis lies within the concrete layer are given in Figure 3.6.

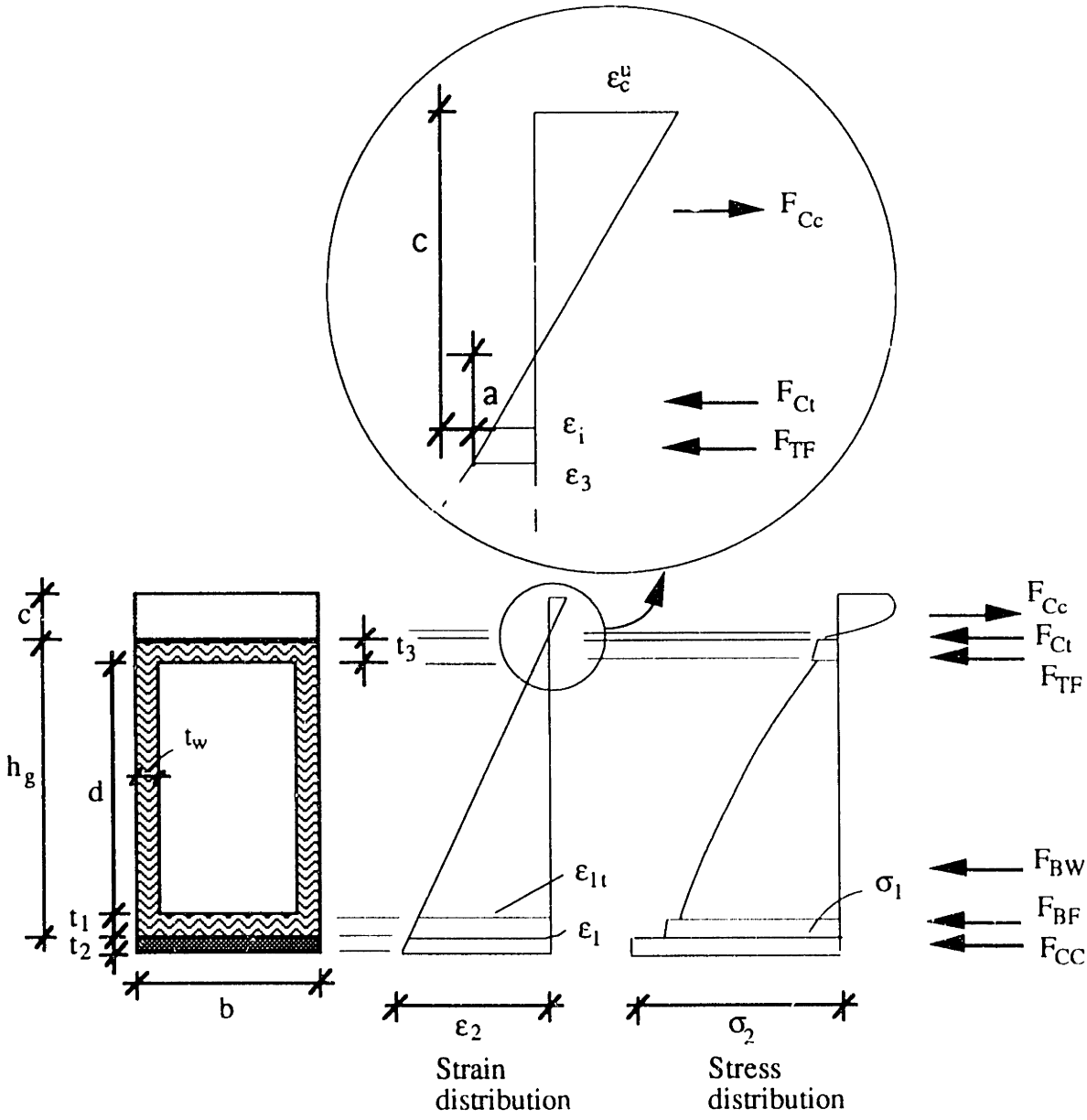

Figure 3.6 Stress and strain distributions when concrete is in tension.

From strain compatibility, the distance of the neutral axis from the GFRP top flange can be derived as:

$$a = c - \frac{(h_g + c + t_2)}{(\varepsilon_c^u + \varepsilon_2)} \varepsilon_c^u \tag{3.22}$$

giving the various strains as follows:

$$\begin{aligned}
\varepsilon_3 &= \varepsilon_c^u \frac{(a + t_3)}{(c - a)} \\
\varepsilon_i &= \varepsilon_c^u \frac{a}{(c - a)} \\
\varepsilon_{1t} &= \varepsilon_c^u \frac{(d + t_3 + a)}{(c - a)} \\
\varepsilon_1 &= \varepsilon_c^u \frac{(d + t_3 + a + t_1)}{(c - a)}
\end{aligned} \tag{3.23}$$

Equilibrium of normal forces gives the following equation:

$$F_{Cc} = F_{TF} + F_{Ct} + F_{BW} + F_{BF} + F_{CC} \tag{3.24}$$

where

$$F_{Cc} = b \int_0^{c-a} f_{concrete}(E_c, f_c', \varepsilon_c(x)) dx \tag{3.25}$$

$$F_{Ct} = b \frac{a E_c \varepsilon_i}{2} \tag{3.26}$$

$$F_{TF} = t_3 b \frac{(\varepsilon_i + \varepsilon_3)}{2} E_3 \tag{3.27}$$

$$F_{BW} = 2 t_w \int_0^d f_{GFRP-web}(\varepsilon_g(x)) dx \tag{3.28}$$

while F_{BF} and F_{CC} were defined earlier in equations (3.17) and (3.18), respectively. Thus, the only unknown in equation (3.24) is ε_2 which can be found numerically. Finally, the ultimate moment capacity M_u can be calculated from the following relation:

$$M_u = F_{Cc} x_{con} + F_{TF}\left(a + \frac{t_3}{2}\right) + F_{Cf}\frac{2}{3}a + F_{BW} x_{web} + F_{BF}\left(a + t_3 + d + \frac{t_1}{2}\right) + F_{CC}\left(a + t_3 + d + t_1 + \frac{t_2}{2}\right) \quad (3.29)$$

where:

$$x_{con} = \left[\int_0^{c-a} x\, t_{concrete}(E_c, f_c', \varepsilon_c(x))\, dx\right] / (F_{Cc} b) \quad (3.30)$$

$$x_{web} = \left[\int_0^{d} x\, f_{GFRP-web}(\varepsilon_g(x))\, dx\right] / (2F_{BW} t_w) \quad (3.31)$$

It has to be pointed out that, as mentioned before in this section, if the bottom face strain ε_2 exceeds the ultimate strain of CFRP the latter will rupture and its contribution to the calculation of M_u has to be disregarded by setting its thickness t_2 equal to zero. Also the above formulas apply only if $\varepsilon_i < f_t / E_c$.

3.2.5.3 CFRP Fracture

The most desirable failure mode to occur first is CFRP rupture. This is explained by the fact that after this mode materializes, the remaining constituents, concrete layer and GFRP box beam, remain intact and they, if properly designed, are able to carry the same or a higher load until another failure mode is reached causing total collapse of the element, but with substantial deformations and energy dissipation. In other words the CFRP laminate acts as a sensor on one hand and as a stiffening component on the other. The analysis for this failure mode is analogous to the one for concrete crushing. The concrete and GFRP stress-strain relationship employed here were described in Sections 3.2.2 and 3.2.3. The stress and strain distributions at failure of the CFRP laminate are shown in Figure 3.7, where the only unknown parameter is the maximum strain ε_c in the concrete.

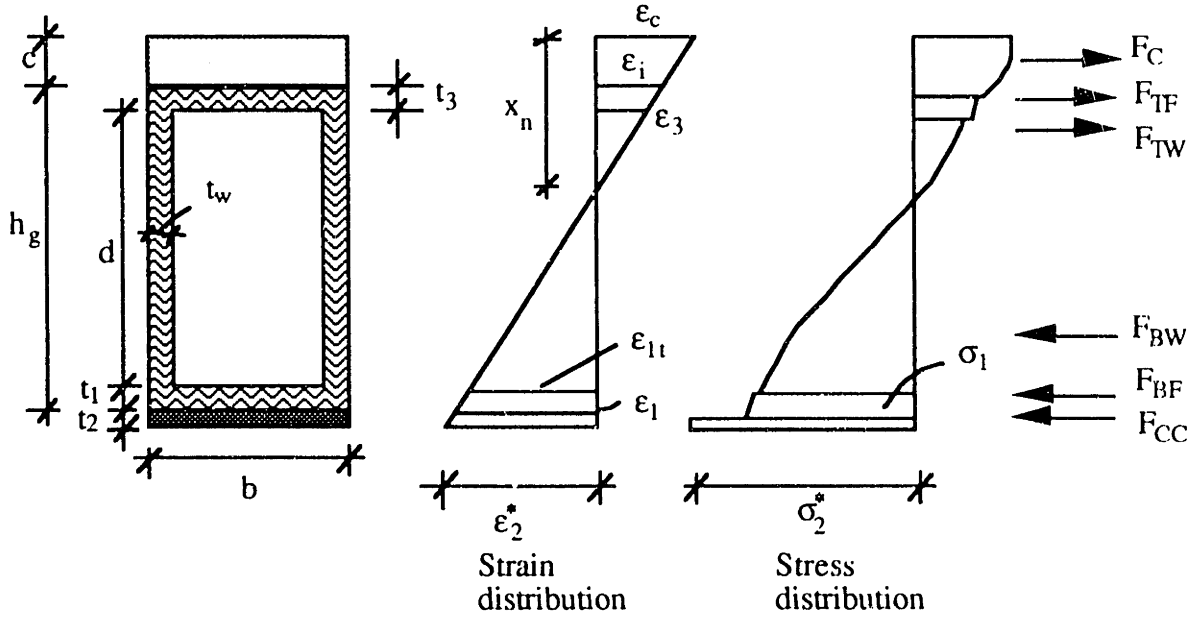

Figure 3.7 Stress and strain distributions at CFRP fracture.

The neutral axis is obtained from strain compatibility as follows:

$$x_n = \frac{\varepsilon_c (h_g + c + t_2)}{\varepsilon_c + \varepsilon_2^*} \tag{3.32}$$

The strain distribution is consistent with the one given for concrete crushing in equation (3.11) substituting ε_c^u and ε_2 by ε_c and ε_2^*, respectively. Equilibrium of normal forces is given by equations (3.12) to (3.17). Note that the force generated in the CFRP laminate is calculated with:

$$F_{CC} = t_2 b \varepsilon_2^* E_2 \tag{3.33}$$

A computer program was developed to find incrementally the concrete top strain using numerical integration for the force calculation. Once the appropriate ε_c is found, the ultimate moment capacity at CFRP failure can be calculated using equation (3.19). Finally, for the case when the neutral axis lies in the concrete layer, equations (3.22) to (3.31) apply with ε_c^u and ε_2 substituted by ε_c and ε_2^*, respectively.

3.2.5.4 GFRP Tensile Failure

Once the CFRP laminate has ruptured, one of the possible failure modes to occur next can be tensile failure of the GFRP bottom flange. The analysis for this failure mode is quite similar to that for CFRP failure; here it is assumed that the CFRP laminate does not exist, and the bottom fiber strain is set to the ultimate tensile strain of GFRP, ε_1^*. The stress and strain distributions for this mode are shown in Figure 3.8.

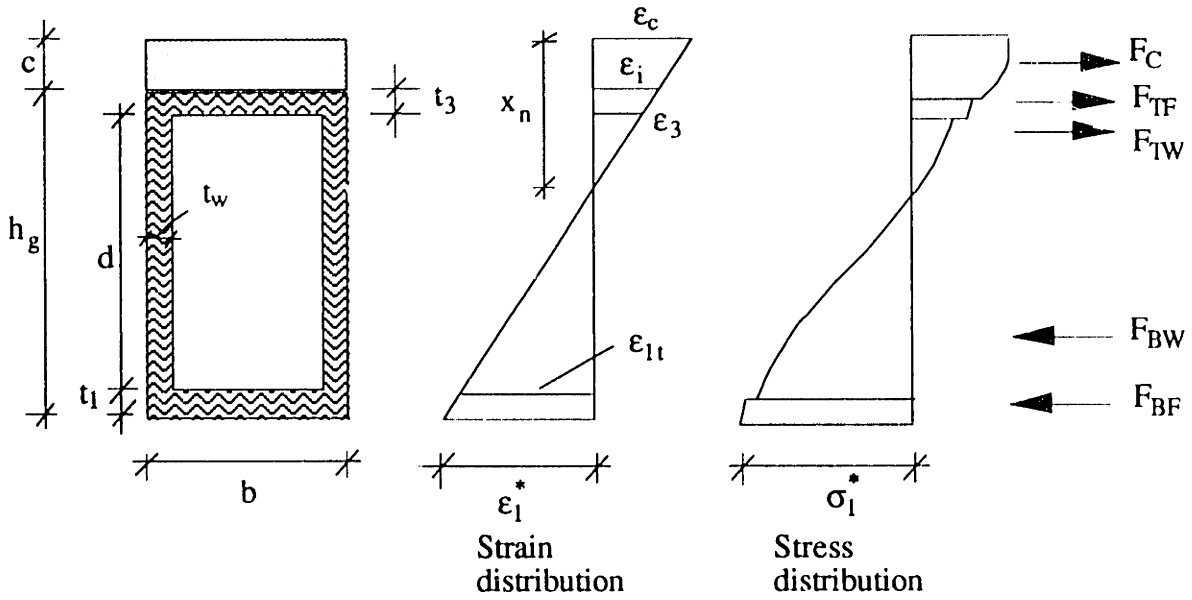

Figure 3.8 Stress and strain distributions at GFRP tensile failure.

The neutral axis is calculated as:

$$x_n = \frac{\varepsilon_c (h_g + c)}{\varepsilon_c + \varepsilon_1^*} \tag{3.34}$$

Next, the strains can be expressed as a function of the only unknown ε_c as follows:

$$\begin{aligned} \varepsilon_i &= \varepsilon_c \frac{(x_n - c)}{x_n} \\ \varepsilon_3 &= \varepsilon_c \frac{(x_n - c - t_3)}{x_n} \\ \varepsilon_{1t} &= \varepsilon_c \frac{(h_g + c - x_n - t_1)}{x_n} \end{aligned} \tag{3.35}$$

Taking equilibrium of normal forces in Figure 3.8 the following equation was obtained:

$$F_C + F_{TF} + F_{TW} = F_{BW} + F_{BF} \tag{3.36}$$

where the forces are as defined earlier by equations (3.13) to (3.17). A numerical iterative procedure is required to solve for ε_c, and this was carried out with a computer program. The ultimate moment capacity of the section just before GFRP tensile failure is then obtained as:

$$\begin{aligned} M_u = {} & F_C x_{con} + \\ & F_{TF}\left(x_n - c - \frac{t_3}{2}\right) + F_{TW}\frac{2}{3}(x_n - c - t_3) + \\ & F_{BW} x_{web} + F_{BF}\left(h_g + c - x_n - \frac{t_1}{2}\right) \end{aligned} \tag{3.37}$$

where the expressions for x_{con} and x_{web} were given in equations (3.20) and (3.21). For the case of the neutral axis in the concrete layer, equations (3.22) to (3.31) apply substituting ε_c^u and ε_1 with ε_c and ε_1^*, respectively, and setting F_{CC} and t_2 equal to zero. As a last note, it may be desirable for this failure mode to occur almost simultaneously with concrete crushing, so that all materials in the cross section are used optimally.

3.2.5.5 Shear Failure

After having analyzed all the flexural failure modes, it is the next subject to evaluate failure modes associated with mechanisms caused by shear forces acting on the hybrid member. Figure 3.9 shows a schematic view of the shear stress distribution along the height of the cross section for two different positions of the neutral axis. It is assumed that the stresses are constant across the width of the member and that the bond between different materials provides full compatibility. This can be justified when the thickness of the adhesive layers is very small. In the analysis presented here, the contribution of the concrete layer to the shear resistance of the member is taken into account.

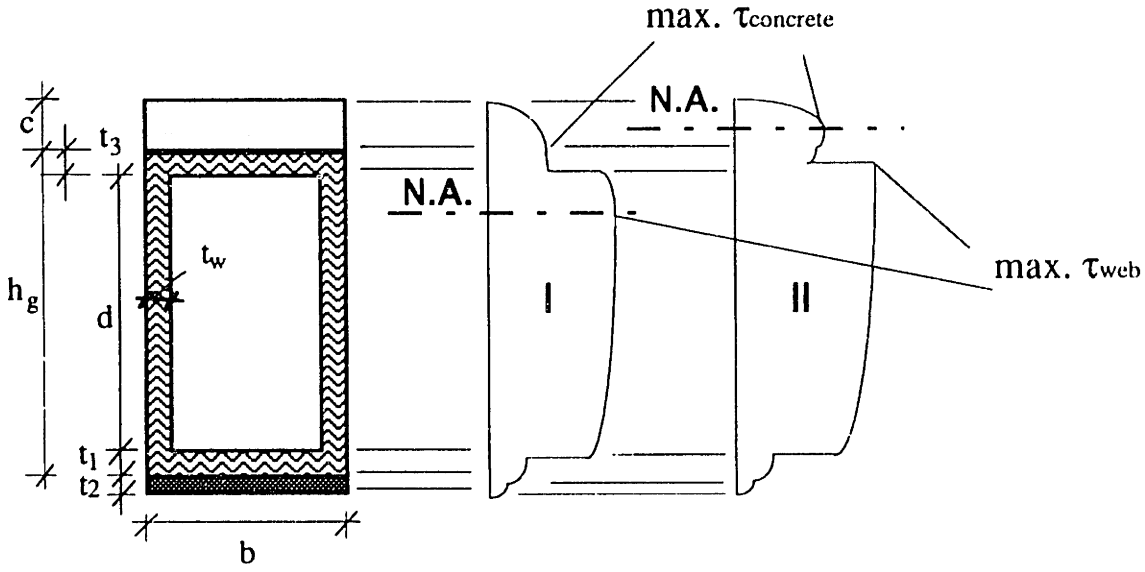

Figure 3.9 Shear stress distribution for two positions of the neutral axis.

Two possible critical failure modes are considered. The first deals with the maximum shear stress in the GFRP box beam webs either at the level of the neutral axis (if the neutral axis lies within the web, diagram I) or at the web top fiber (if the neutral axis lies above the web, diagram II). The second failure mode involves the maximum shear stress generated in the concrete layer, either at the concrete-GFRP interface (diagram I) or at the neutral axis (diagram II). If the materials involved in the calculation of shear stresses have linear elastic behavior and the location of the neutral axis is defined just from the geometric layout (independent of the level of normal stresses), the shear formula from classic beam theory can be used:

$$\tau = \frac{VQ}{Ib} \tag{3.38}$$

where V is the shear force, Q is the shear rigidity, I is the moment of inertia and b is the width of the member. On the other hand, if the materials constituting the cross section are loaded into their nonlinear range and the location of the neutral axis is dependent on the load magnitude, a more basic approach has to be implemented. We obtain shear stresses from normal stresses by means of stress equilibrium, hence the distribution of the normal stresses also determines the distribution of the shear stresses. Given the normal stress distribution in two adjacent cross sections the shear force can be obtained directly. This is shown in Figure 3.10. Of course, this approach can be implemented only numerically in a computer program.

In the previous sections of this chapter we derived the normal stress distribution along the cross section for the different flexural failure modes at their corresponding ultimate moment capacities. A similar procedure can be followed to obtain the normal stress distributions corresponding to any value of the external loads.

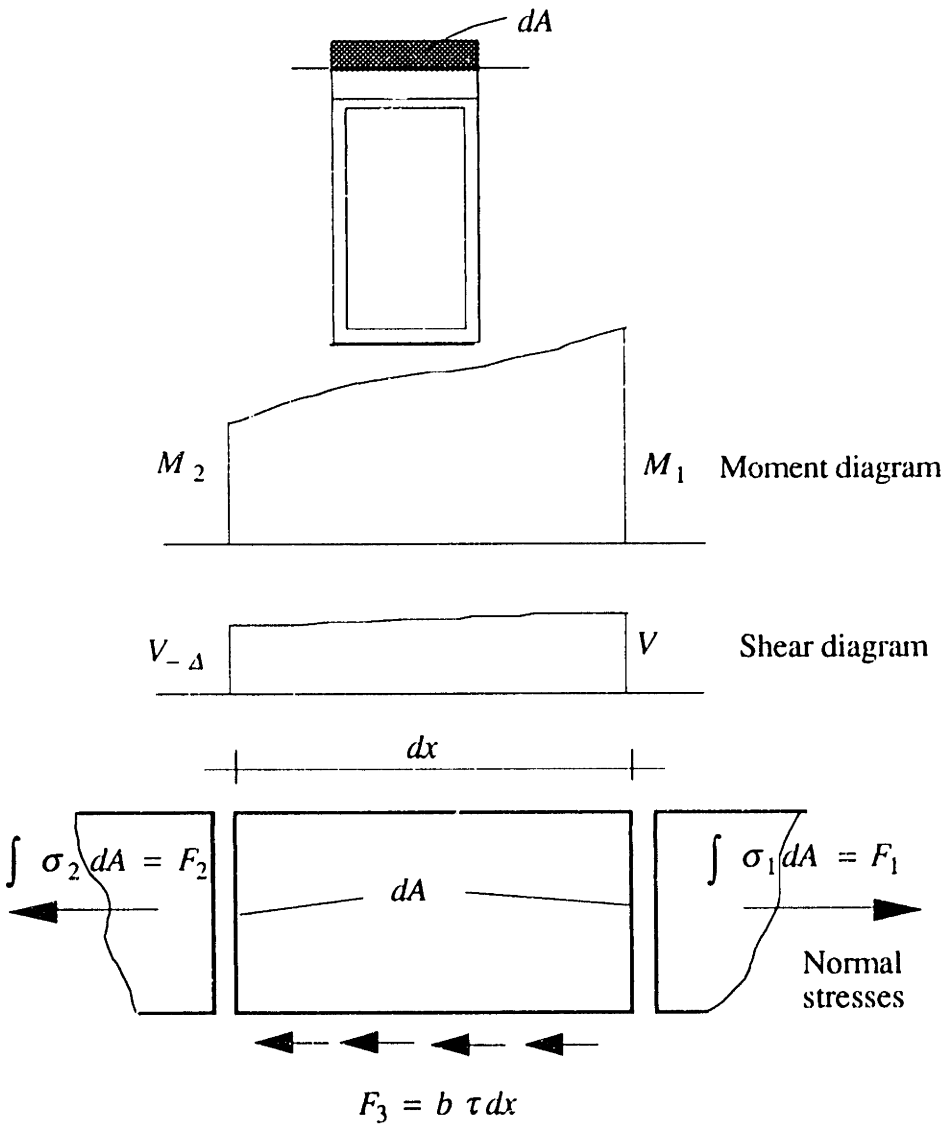

Figure 3.10 Normal and shear force equilibrium.

Next, from stress equilibrium in Figure 3.10 we can write:

$$F_3 = b\,\tau\,dx = F_1 - F_2 \tag{3.39}$$

Note, that in a numerical approach the infinitesimal value dx can be substituted with a finite value. Given the moments M_1 and M_2 and the shear force, V, at two adjacent cross sections, the distance, l, between them can be found with:

$$dx = l = \frac{M_u - M_{u-\Delta}}{V} \tag{3.40}$$

Further, if the normal forces F_1 and F_2 at these two sections are known, the shear stresses can be calculated. When the neutral axis is within the GFRP web the maximum shear stress generated in the concrete is at the concrete-GFRP interface, while the maximum shear stress in the web is at the neural axis:

$$\tau^{I}_{concrete} = \frac{(F'_C - F'_{C-\Delta})V}{b\,(M_1 - M_2)} \tag{3.41}$$

$$\tau^{I}_{web} = \frac{(F'_C + F'_{TF} + F'_{TW} - F'_{C-\Delta} - F'_{TF-\Delta} - F'_{TW-\Delta})V}{2t_w\,(M_1 - M_2)} \tag{3.42}$$

where F'_C, F'_{TF} and F'_{TW} are the integrals of the normal stresses corresponding to M_1 in the concrete, the top GFRP flange and the GFRP web, respectively. $F'_{C-\Delta}$, $F'_{TF-\Delta}$ and $F'_{TW-\Delta}$ are the same normal forces at a somewhat smaller moment, $M_{u-\Delta}$. If the neutral axis lies within the concrete layer, the shear stresses are critical either at the neutral axis or at the top of the GFRP web. They are obtained as follows:

$$\tau^{II}_{concrete} = \frac{(F'_{Cc} - F'_{Cc-\Delta})V}{b\,(M_1 - M_2)} \tag{3.43}$$

$$\tau^{II}_{web} = \frac{(F'_{Cc} - F'_{Ct} - F'_{TF} - (F'_{Cc-\Delta} - F'_{Ct-\Delta} - F'_{TF-\Delta}))V}{2t_w\,(M_1 - M_2)} \tag{3.44}$$

where the forces F'_{Cc} and F'_{Ct} are the integrals of the compressive and tensile normal stresses in the concrete layer, respectively.

Setting the shear stress τ in equations (3.42) and (3.44) equal to the ultimate shear strength of the GFRP web, τ^{*}_{fw}, the maximum shear force V_{max} that the section can resist can be obtained. Similarly, for concrete shear failure the maximum principal tensile

stress, f_1, equals the tensile strength of concrete, f_t'. f_1 is expressed in terms of the normal and shear stresses from Mohr's circle theory as follows:

$$f_1 = -\frac{\sigma}{2} + \sqrt{\left(\frac{\sigma}{2}\right)^2 + \tau^2} \tag{3.45}$$

where τ is the shear stress given by equations (3.41) and (3.43) and σ is the corresponding normal stress (which is zero for Case I). It should be noted that the maximum value of f_1 is obtained when the compressive stresses are minimum and the shear stresses are maximum. Finally, the maximum shear force is found by substituting equations (3.41) or (3.43) into equation (3.45) and solving for V.

3.2.5.6 Interface Debonding

Closely related to the shear failure modes discussed in the previous section, interface debonding is a further source of failure associated with the hybrid beam design. The bond between the concrete layer and the GFRP, as well as between CFRP and GFRP, is achieved using a structural adhesive of certain thickness and known mechanical properties. This bond is typically characterized by given shear strength. Yet, the load acting on the hybrid beam may induce high shear stresses at the interfaces between dissimilar materials, which may eventually lead to debonding.

In general, the shear strength of most adhesives is several times higher than that of concrete. For instance, epoxies may have a shear strength of the order of 25 MPa (Ciba-Geigy 1992) compared to 4-8 for concrete (Kaiser 1989). Hence, it can be assumed that concrete shear failure will always precede concrete-GFRP debonding, unless the top GFRP surface is poorly prepared. Moreover, debonding at the CFRP-GFRP interface is rather unlikely to occur because the shear stresses there are quite low.

On the other hand, quality control is an important issue in respect to the performance of the bond and if not appropriately applied, the adhesion quality at the interface might be governing for the collapse mechanism. Here a fracture mechanics approach gives a possible alternative for the analysis. A bond line may fail in a sudden manner as a result of the propagation of a crack along the interface of two different materials. Possible reasons for the existence of such a crack are imperfections in the spreading of the adhesive or shear microcracking in the concrete. Debonding through horizontal interfaces in beams loaded in bending is typically characterized by mode II

fracture. The problem of the propagation of an interface crack is treated by considering the relationship between the strain energy release rate required for crack propagation and the compliance of a member. The compliance method described by Knott (1973) has been used by Anandarajah and Vardy (1985) to analyze the interfacial shear fracture of open sandwich beams in conjunction with a finite element procedure. In the compliance method, the strain energy release rate, G_{II}, for in-plane shear delamination satisfies the condition (Triantafillou and Plevris 1992):

$$G_{II} = \frac{kP^2}{b}\left(\frac{\partial C}{\partial a}\right) \tag{3.46}$$

where b is the width of the member, P is the applied load, a is the crack length, k is a constant and C is the inverse of the stiffness, that is:

$$C = \frac{v}{P} \tag{3.47}$$

where v is the displacement under the load P. The constant k relates the load and the displacement to the strain energy U as follows:

$$U = k\,v\,P \tag{3.48}$$

In equation (3.46) the term $\partial C/\partial a$ depends on the applied load P. For a particular value of P the relationship between the compliance , C, and the crack length, a, can be established by analyzing the beam using a finite element procedure. The gradient $\partial C/\partial a$ corresponding to any particular crack length is then obtained and the strain energy release rate G_{II} calculated. Fracture occurs when the strain energy release rate equals the critical strain energy release rate for the interface, G_{IIC} . The load causing debonding is then calculated from the relation, $G_{II} = C_{IIC}$. Finally, the critical strain energy release rate for the interface, G_{IIC} , can be measured experimentally using double-shear specimens pulled in tension, as described by Triantafillou and Gibson (1989).

3.2.5.7 Other Failure Modes

Two additional failure modes, web shear buckling and overall instability are discussed in Section 3.3.

3.2.6 Deformation and Stiffness Calculation

In the analysis presented above, relationships for the ultimate loading capacity of the hybrid FRP/concrete beam were derived. It is of further interest to describe the stiffness of the hybrid member and calculate its deformations for a given loading configuration and support system. The stiffness and deflections for a linear elastic beam are given in a closed form solution by classical beam theory and can be found in any structures or strength of materials textbook. On the other hand, for mixed material systems where the constituent materials are characterized by nonlinear stress-strain relationships, these formulas can not be used any more. A more fundamental approach has to be employed. From classical beam theory, the most general form for defining the deflection v of a beam is given through the basic differential equation of the deflection curve:

$$\kappa = \frac{1}{\rho} = \frac{d\theta}{dx} = \frac{d^2v}{dx^2} \tag{3.49}$$

where κ is the curvature, ρ is the radius of curvature, θ is the angle of rotation of the axis of the beam and x is the distance along the beam axis. Here small slopes are assumed, neglecting the difference between curved and straight infinitesimal lengths. Also the effects of shear are disregarded in this part.

An appropriate method for deflection calculations is that of virtual forces, here specifically modified to a suitable form which comprises the curvature. This is shown in the following expression:

$$v = \int_0^L \frac{M_0 m_1}{D} dx = \int_0^L \kappa m_1 dx \tag{3.50}$$

where M_0 is the moment due to the applied loads , m_1 is the moment from the virtual unit force applied at the point where the deflection v is calculated, D is the flexural rigidity and L is the member length. For concentrated loading, m_1 is a linear function along the length of the beam while κ for inelastic material behavior varies nonlinearly. To calculate the integral in equation (3.50) the moment-curvature relationship, (M_0 -κ), has to be established. This is achieved on the basis of the flexural analysis described in Section 3.2.5. Through an incremental procedure the strain profile is increased up to the one giving the ultimate moment of the cross section, and at each increment the associated curvature and moment are recorded. Note that the integration is carried out numerically

along the length of the beam. Figure 3.11 shows schematically the procedure described above for the three point loading case. Other loading patterns follow along the same lines. Since this involves substantial computational effort, a computer program performing this operation numerically was developed.

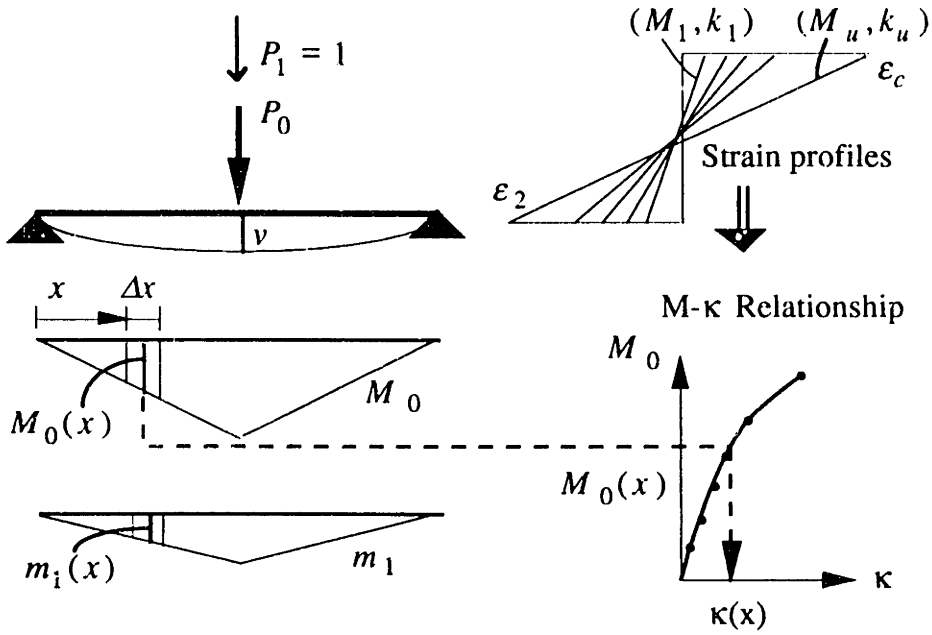

Figure 3.11 Deflection calculation scheme.

Although the effects of shear deformations on the deflection of isotropic beams are usually relatively small compared to the effects of flexural deformations, they can not be neglected in the case of composite materials. In order to obtain the shear deformations the method of virtual work can be employed. The method requires that expressions for both the external and internal work be obtained. The external work is equal to the virtual force acting on the structure times the unknown shear deformation w:

$$W_{ext} = 1 \bullet w \tag{3.51}$$

The internal virtual work is the work performed by the real stresses on the virtual deformations or vice-versa. The real shear stresses generated in the beam undergoing inelastic material behavior can be found from equation (3.39) at any position along the height of the beam for given external moments and shear forces acting on it. The virtual shear deformations can be found by first obtaining the virtual shear stresses in the same way as the real (substituting the real shear force with the resulting virtual one), and then

dividing these virtual shear stresses by the corresponding shear modulus of the material at each point along the cross section. Now integrating the product of these stresses and shear strains throughout the volume of the beam the internal work is obtained, which when set equal to the external work gives the shear deformation, w as follows:

$$w = \int \tau_0 \, \gamma_1 dxdydz = \int \frac{\tau_0 \tau_1}{G} dxdydz \tag{3.52}$$

where the index 0 and 1 denote the real and the virtual components, respectively.

In a more simplified approach the assumption that only the webs carry shear can be made implying that the integration should be made only over its area. Another simplification can be made by assuming that the shear stress distribution along the webs is equal to the average one, defined as:

$$\bar{\tau} = \frac{V}{2t_w d} \tag{3.53}$$

Then, assuming linear elastic material behavior of the webs, the resulting shear deformation is given by:

$$w = \frac{V L}{K_s \, k_l \, 2t_w d \, G_w} \tag{3.54}$$

where G_w is the shear modulus of the webs, k_l is a factor depending on the loading pattern (k_l = 2 for 3-point bending and 3 for 4-point bending), K_s is the shear coefficient depending on the beam geometry and material properties. Bank (1987) gives the dependence of K_s for thin walled composite beams as a function of geometry and material properties as follows:

$$\begin{aligned} K_s = \frac{E_1}{G_w} 20(\alpha + 3n)^2 \, / [& \frac{E_1}{G_1}(60m^2n^2 + 6\alpha mn^2) + \\ & \frac{E_1}{G_w}(180m^3 + 300\alpha m^2 + 144\alpha^2 m + 24\alpha^3) + \\ & \nu_1(60m^2n^2 + 4\alpha mn^2) + \nu_w(30m^2 + 6\alpha m - 4\alpha^2)] \end{aligned} \tag{3.55}$$

where $n = b/h_g$, $m = 2b\,ht_w$ and $\alpha = E_w/E_1$ (equal thickness and elastic moduli of top and bottom flange are assumed). The Poisson's ratios ν_1 and ν_w of the flange and web,

respectively, are obtained from continuum theory as described in Chapter 4. Typical values of K_s for rectangular thin walled composite beams are found between 0.6 and 0.71.

3.3 Hybrid FRP-Concrete Beam Design

The analysis of the mechanical behavior of the hybrid FRP-concrete elements presented in the previous section was quite detailed. Even though all the calculations involved were performed by means of computer programs, a more simplified approach is desirable for preliminary design purposes. In order to get an estimate on the geometry and material properties required to satisfy given constraints, such as span length, load magnitude and stiffness restrictions, some of the assumptions in Section 3.2 have to be relaxed. This mainly refers to the nonlinear material models and some of the failure modes. Further, the variations in material properties throughout the cross section (web-flange in GFRP) can be neglected for preliminary designs. This is also in agreement with the idea of having only concrete in the compressive zone, wherein the GFRP top flange is used only to support the concrete layer and to provide for the shear transfer to the GFRP webs. This implies that very thin GFRP flanges would suffice, and hence their ommitance in the analysis for bending can be justified. Taking all this into account, a simplified analysis is presented next which can be used in order to obtain rough estimates of the design variables, which can then be refined with the more exact analysis presented in Section 3.2. The preliminary design procedure is given in the following.

3.3.1 Simplified Failure Analysis of FRP-Concrete Members

In Figure 3.4 the assumed layout of the proposed hybrid cross section was given along with a description of the parameters involved in Section 3.2.5. In this part it is assumed that the flange supporting the concrete layer is very thin and does not affect the behavior of the section. The material behavior for both FRPs is assumed to be linear elastic, while for concrete the nonlinearity is considered only at failure. The failure modes considered (based on the design methodology proposed by Triantafillou and Meier, 1992) are presented next.

3.3.1.1 Web Shear Fracture

As an approximation, the maximum shear stress τ_{max} in the web may be taken to be equal to 1.5 times the average shear stress in the web, thus:

$$\tau_{max} = \frac{3}{2}\frac{V_u}{2t_w d} \tag{3.56}$$

where V_u is the section's ultimate shear strength. Shear fracture occurs when the maximum shear stress equals the in-plane fracture shear strength of the webs τ^*_{fw}, giving

$$V_u = \frac{4}{3} t_w d \tau^*_{fw} \tag{3.57}$$

3.3.1.2 Web Shear Buckling

The average web shear buckling stress τ^*_{bw} can be determined theoretically as follows (Timoshenko and Gere 1961, Holmes and Just 1983):

$$\tau^*_{bw} = \frac{4K\sqrt[4]{D_L D_T^3}}{t_w d^2} \qquad \text{for} \quad \theta > 1 \tag{3.58}$$

or

$$\tau^*_{bw} = \frac{4K\sqrt{D_T H}}{t_w d^2} \qquad \text{for} \quad \theta < 1 \tag{3.59}$$

where

$$D_L = \frac{E_w t_w^3}{12(1-\nu_L \nu_T)} \tag{3.60}$$

$$D_T = \frac{E_{wT} t_w^3}{12(1-\nu_L \nu_T)} \tag{3.61}$$

$$H = \frac{1}{2}(\nu_L D_T + \nu_T D_L) + \frac{G_w t_w^3}{6(1-\nu_L \nu_T)} \tag{3.62}$$

$$\theta = \frac{\sqrt{D_L D_T}}{H} \tag{3.63}$$

and the value of K depends on θ as shown in Table 3.1. Shear buckling occurs when the average shear stress equals the shear buckling stress:

$$V_u=2t_w d t^*_{bw} \tag{3.64}$$

Table 3.1 Values of θ against K in web.

θ	0	0.2	0.5	1.0	2.0	3.0	5.0	10.0	20.0	40.0
K	18.6	18.9	19.9	22.2	18.8	17.6	16.6	15.9	15.5	15.3

3.3.1.3 Flexural Failure

In a well designed hybrid FRP-concrete section the CFRP laminate fails first (thus giving a warning of collapse) at a moment M_2. The stresses are then redistributed and the section has a moment carrying capacity until the concrete crushes in compression when the maximum compressive strain equals the ultimate failure strain of concrete ε_c^u. Crushing of concrete defines flexural collapse of the cross section at a moment M_u which is higher than M_2. This feature of the hybrid beam is referred to as pseudo-ductility, since the CFRP laminate is used as a sensor and once it fails reaching its strength, the loading capacity of the element is not yet exhausted, but the beam undergoes substantial deformations allowing for additional load to be applied prior to total collapse. This is also shown schematically in Figure 3.12.

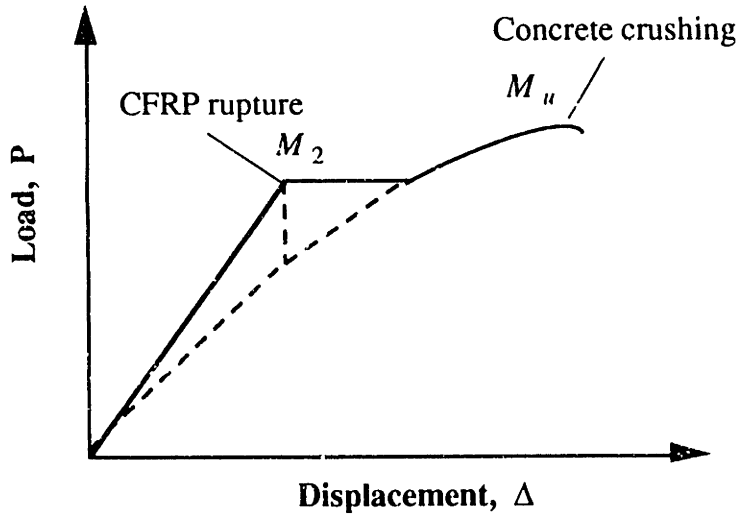

Figure 3.12 Pseudo-ductile failure.

The normal strain and stress distributions corresponding to M_2 are given in Figure 3.13. Assuming that when the CFRP laminate fails the concrete is still linear elastic, the depth of the neutral axis is given by:

$$y=\frac{-\frac{1}{2}n_c bc^2+n_1 bdt_1+n_2 bdt_2+t_w d^2}{n_c bc+n_1 bt_1+n_2 bt_2+2t_w d} \tag{3.65}$$

where $n_c=E_c/E_w$, $n_1=E_1/E_w$, $n_2=E_2b_2/E_w b$ and y is the depth of the neutral axis from the concrete bottom fiber. M_2 is now calculated as:

$$M_2=n_c\varepsilon_2^* E_w bcy\frac{\left(d+\frac{c}{2}\right)}{(d-y)}+n_c\varepsilon_2^* E_w bc^2\frac{\left(d+\frac{2}{3}c\right)}{2(d-y)}+\varepsilon_2^* E_w t_w y^2\frac{\left(d-\frac{y}{3}\right)}{(d-y)}-\frac{1}{3}\varepsilon_2^* E_w t_w (d-y)^2 \tag{3.66}$$

under the condition that the strain at the concrete top fiber is less than ε_c^u, that is

$$y<\frac{d\varepsilon_c^u-c\varepsilon_2^*}{\varepsilon_c^u+\varepsilon_2^*} \tag{3.67}$$

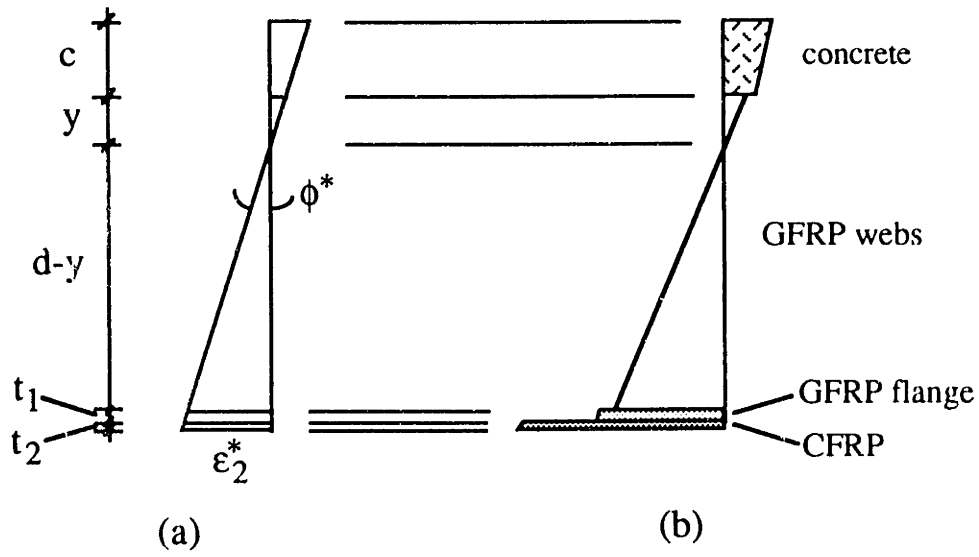

Figure 3.13 (a) Strain and (b) stress distributions at CFRP fracture.

The normal strain and stress distributions corresponding to the ultimate flexural capacity of the cross section are illustrated in Figure 3.14. The stresses in the concrete

layer are calculated here based on the equivalent rectangular stress block approach (e.g., Park and Paulay 1975). The depth of the neutral axis y_u is established from internal force equilibrium

$$y_u=\frac{-\beta_1 f_c' bc^2+n_1 bdt_1+t_w d^2}{\frac{\beta_1 f_c' bc}{\varepsilon_c^u E_w}+n_1 bt_1+2t_w d} \tag{3.68}$$

and, finally, moment equilibrium gives the flexural capacity of the cross section

$$M_u=\beta_1 f_c' bc\left(d+\frac{c}{2}\right)+\varepsilon_c^u E_w t_w y_u^2\frac{\left(d-\frac{y_u}{3}\right)}{(c+y_u)}-\varepsilon_c^u E_w t_w\frac{(d-y_u)^3}{3(c+y_u)} \tag{3.69}$$

under the constraint that the GFRP flange has not fractured ($\varepsilon_1<\varepsilon_1^*$), that is

$$y_u>\frac{d\varepsilon_c^u-c\varepsilon_1^*}{\varepsilon_c^u+\varepsilon_1^*} \tag{3.70}$$

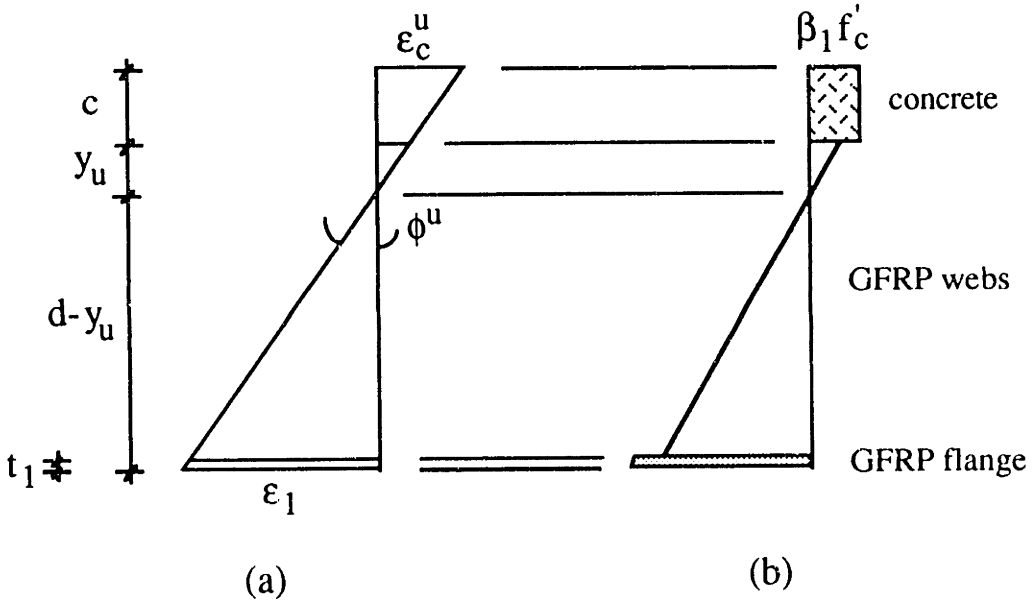

Figure 3.14 (a) Strain and (b) stress distributions at concrete crushing.

3.3.1.4 Lateral Instability

Although box sections have a high resistance to lateral torsional buckling in general, limits to a section's height to width ratio are often imposed to prevent lateral instability and satisfy other practical design requirements. Hence, a constraint inequality of the form

$$\frac{c+d}{b} < k_1 \tag{3.71}$$

is adopted in this study, where k_1 is a constant to be chosen by the designer. Practical experience with composite material sections and with thin-walled hybrid sections made of other materials indicates that a number around 3 is a reasonable conservative estimate for k_1.

3.3.2 Ductility Considerations

At the cross section level, ductility can be defined as the ratio of the curvature at failure (ϕ^u) to that at the deviation from the linear elastic response, that is when the CFRP laminate fractures (ϕ^*). From Figures 3.13 and 3.14 the curvature ductility is calculated as

$$\frac{\phi^u}{\phi^*} = \frac{\varepsilon_c^u}{\varepsilon_2^*} \frac{(d-y)}{(c+y_u)} \tag{3.72}$$

3.3.3 Simplified Stiffness Calculation

The flexural rigidity D of the hybrid FRP-concrete section, assuming all materials linear elastic is given by

$$D=E_w\left[\frac{n_c b c^3}{12} + n_c bc\left(y+\frac{c}{2}\right)^2 + n_1 b t_1 (d-y)^2 + n_2 b t_2 (d-y)^2 + \frac{t_w d^3}{6} + 2t_w d\left(\frac{d}{2}-y\right)^2\right] \tag{3.73}$$

where y is the depth of the neutral axis from the concrete bottom fiber given by equation (3.65). In thin walled box sections under a vertical shear force most of the shear load is carried by the webs. Hence, a simple approximate formula for the shear rigidity Q gives

$$Q=2G_w t_w d \tag{3.74}$$

3.3.4 Design Methodology for FRP-Concrete Elements

The problem under consideration here is the selection of the cross section's geometric variables (d, t_w, c, b, t_1 and t_2) in terms of the given material properties, so that a given set of design requirements is satisfied at the minimum cost. A typical set of design constraints could consist of a bending moment and a shear force to be carried safely by the cross section (strength constraints), as well as a maximum displacement limit (stiffness constraint). Some essential concepts towards the development of an appropriate design procedure are discussed next: (a) the proposed hybrid section does not offer a shear strength considerably higher than that of a geometrically similar GFRP section without the concrete and the CFRP layers; (b) the webs are designed optimally when they fail simultaneously according to all their associated failure modes; (c) CFRP is an expensive material and the primary purpose of its application should be to provide a pseudo-ductile response in bending; (d) the ductility increases when the thickness of the CFRP laminate decreases; (e) if the area fraction of CFRP used is extremely low, the CFRP laminate will fail prematurely at a low load; (f) if the load at failure of the CFRP is a high fraction of the ultimate load and given that the jump of either the load or the displacement at CFRP failure should not be too high, warning of an imminent collapse comes too late; and (g) concrete is a very cheap material and its use in the cross section should be maximized.

Item (b) above suggests that (3.62)-(3.64) should all be satisfied, indicating that d and t_w can be obtained in terms of the material properties and the ultimate shear force

$$d=\sqrt{\frac{3V_u}{4\tau_{fw}^*}\sqrt{\frac{K\sqrt[4]{E_wE_{wT}^3}}{2(1-\nu_L\nu_T)\tau_{fw}^*}}} \qquad \text{for} \quad \theta>1 \qquad (3.75)$$

$$d=\sqrt{\frac{3V_u}{4\tau_{fw}^*}\sqrt{\frac{K\sqrt{E_{wT}\left[\frac{1}{2}(\nu_LE_{wT}+\nu_TE_w)+2G_w\right]}}{2(1-\nu_L\nu_T)\tau_{fw}^*}}} \qquad \text{for} \quad \theta<1 \qquad (3.76)$$

$$t_w=\frac{3V_u}{4t_{fw}^*d} \qquad (3.77)$$

In addition, items (e) and (f) suggest that the designer should specify a certain ratio of the moment at CFRP fracture to the ultimate moment, say

$$M_2=k_2M_u \qquad (3.78)$$

Finally, from (g) we may conclude that inequality (3.71) should be used in the form of an equation:

$$\frac{c+d}{b}=k_1 \tag{3.79}$$

Given the above considerations, the proposed design methodology (omitting here for simplicity the application of load and resistance uncertainty factors) for hybrid FRP-concrete sections is summarized as follows:

1. Design the cross section for shear by solving (3.75)-(3.77) for d and t_w.
2. Select a very low CFRP thickness t_2.
3. Solve the nonlinear system of (3.69), (3.78) and (3.79) for c, b and t_1.
4. Calculate the flexural and shear rigidities and hence the deflection at a given load.
5. If the stiffness requirement is not met, increase d and possibly t_2 and repeat steps 3-4 until the stiffness constraint is satisfied.

It must be noted that box-type sections are inherently stiff. Furthermore, separation of the stiff concrete and CFRP layers is expected to increase the rigidity of the cross section considerably, and it is believed that the stiffness constraint will rarely be activated. The design methodology presented above is better illustrated in the following example.

3.3.5 Design Example

A simply supported hybrid FRP-concrete beam is to carry a heavy load P_u=80 kN over a span L=3 m. The material properties adopted here are listed in Table 3.2; they are representative of pultruded GFRP, unidirectional CFRP and normal strength concrete. The design requirements for three-point bending are given as follows: $M_u=P_uL/4$=60 kNm; $V_u=P_u/2$=40 kN; and the allowable displacement at a load $P_s=0.5P_u$ is $\Delta_{max}=L/200$. From (3.75)-(3.77) we calculate d=294 mm and t_w=3.51 mm and select d=300 mm and t_w=3.5 mm. Furthermore, assuming a thin CFRP laminate of t_2=0.1 mm, (3.69), (3.78) and (3.79) give c=53.64 mm, b=117.88 mm and t_1=1.05 mm (for k_1=3 and k_2=0.75), which are rounded off to c=54 mm, b=120 mm and t_1=1.1 mm. A check of the stiffness requirement shows that it is satisfied. Furthermore, none of inequalities (3.67) and (3.70) is violated. The selected design variables indicate that CFRP fracture occurs at a load of

60.9 kN which (for a displacement control test) suddenly drops to 56 kN, and then the load increases until the concrete crushes at 82.1 kN.

For the sake of comparison, we assume next that the same member (subjected to the same stiffness and strength design requirements) is made of a box GFRP pultruded profile with material properties as given in Table 3.2. The top and bottom flanges are assumed here to be identical. Note that the design of GFRP beams is usually controlled by stiffness, and the best use of material in the flanges of a box section for a given stiffness is made when they are the same. To carry the shear force of 40 kN, the webs of the GFRP section are designed identical to those of the hybrid section (d=300 mm and t_w=3.5 mm). Furthermore, the width is taken as above (b=120 mm). The remaining unknown design variable, the flange thickness t_1, is then calculated to satisfy the stiffness requirement and the following strength constraints: top flange crushing; top flange local buckling; and bottom flange fracture. The compressive crushing strength of GFRP is taken as 60% of its tensile strength and the buckling stress of the top flange is calculated by the following formula (Timoshenko and Gere 1961, Holmes and Just 1983)

$$\sigma_{bf}^{*}=\frac{4\pi^2}{b^2 t_1}(\sqrt{D_L D_T}+H) \tag{3.80}$$

where D_L, D_T and H are calculated by (3.60)-(3.62) with ν_L=0.3, ν_L=0.1, and E_w, E_{wT}, G_w and t_w substituted by E_1, E_{1T}=10 GPa, G_1=8 GPa and t_1, correspondingly. Based on this approach, the flange thickness is calculated as t_1=10 mm, which just satisfies the stiffness requirement (and corresponds to over-designing the section for bending by about 30%).

Finally, based on the relative material densities and costs given in Table 3.3, we conclude that the hybrid FRP-concrete section is 2.6 times heavier than the GFRP section (but still quite light compared to a traditional concrete or steel section) at an approximately 50% materials cost reduction. At the same time, the hybrid section possesses ductility characteristics which are not offered by the GFRP section.

Table 3.2 Material properties used in design example.

Concrete

E_c [GPa]	β_1	f_c' [MPa]	ε_c^u
30	0.8	40	0.003

CFRP

E_2 [GPa]	ε_2^*
120	0.008

GFRP webs

E_w [GPa]	E_{wT} [GPa]	G_w [GPa]	ν_L	ν_T	τ_{fw}^* [MPa]
17	15	9	0.3	0.2	29

GFRP flange

E_1 [GPa]	ε_1^*
25	0.012

Table 3.3 Relative material densities and costs.

	Concrete	GFRP	CFRP
Rel. Density	24	16	13
Rel. Cost/Weight	0.1	18	160

3.4 Computer Program for Analysis of Hybrid Beam

On several occasions earlier in this chapter is was mentioned that the various calculations were performed numerically and/or iteratively by means of computer routines, especially in the detailed analysis sections. This subject will be described in this section.

The program's main objectives are to find the relationship between deformations and applied loads as well as the associated displacements for given load distributions. The resulting strains and stresses are compared to ultimate values and if these are exceeded the corresponding failure modes are flagged. In order to achieve these goals an incremental procedure was developed which sweeps through a discrete number of strain profiles and finds the associated internal forces at the cross sectional level, checks for the occurrence of

failure modes and accounts for their consequences, and finally calculates the corresponding displacements. Several routines were needed to accomplish this:

- main routine, connects the different routines and organizes the flow of the calculations, finds equilibrium of normal forces iteratively, calculates the associated internal forces and finally gives the total displacements of the system,
- routines describing the nonlinear stress-strain relationships of the materials involved,
- routine for numerical integration of stress diagrams corresponding to a given strain distribution,
- routine that calculates the sum of normal forces at cross sectional level,
- routine that calculates the curvatures for a given bending moment (needed for the displacement calculations),
- routine that calculates the shear stresses at cross sectional level,
- routine that calculates the shear displacements integrating numerically over the volume of the beam,
- routines for input and output.

The flow of the program is given in Figure 3.15 and described next. For every incremental procedure the boundary conditions have to be defined first. The incrementation is carried out on the strain profile and for this purpose the top fiber strain, ε_c, was initialized at a small value (e.g., 0.03 %, eventually can even be zero) while the bottom fiber strain, ε_2, was obtained by incrementing it from zero until equilibrium of normal forces at cross sectional level was reached. The ε_2 strain increment should, due to accuracy considerations, not exceed 0.02%, while the ε_c strain increment should be less then 0.01%. These are the initial boundary conditions. Since the incrementation starts with low strain values, the materials are still in their elastic range and an elastic analysis can be used to increase the programs speed using closed form solutions. The area, A, and the first and second moments of area, B and I, are calculated as (see Figure 3.4):

$$A = b(E_c c + E_3 t_3 + 2E_w t_w d / b + E_1 t_1 + E_2 t_2) \tag{3.81}$$

$$\begin{aligned} B = {} & bE_c c^2 / 2 + bE_3 t_3 (c + t_3 / 2) + 2E_w t_w d(c + t_3 + d / 2) + \\ & bE_1 t_1 (c + t_3 + d + t_1 / 2) + bE_2 t_2 (c + t_3 + d + t_1 + t_3 / 2) \end{aligned} \tag{3.82}$$

$$\begin{aligned} I = {} & bE_c c^3 / 3 + bE_3 t_3 (c + t_3 / 2)^2 + 2E_w t_w d(c + t_3 + d / 2)^2 + \\ & bE_1 t_1 (c + t_3 + d + t_1 / 2)^2 + bE_2 t_2 (c + t_3 + d + t_1 + t_3 / 2)^2 + 2E_w t_w d^3 / 12 \end{aligned} \tag{3.83}$$

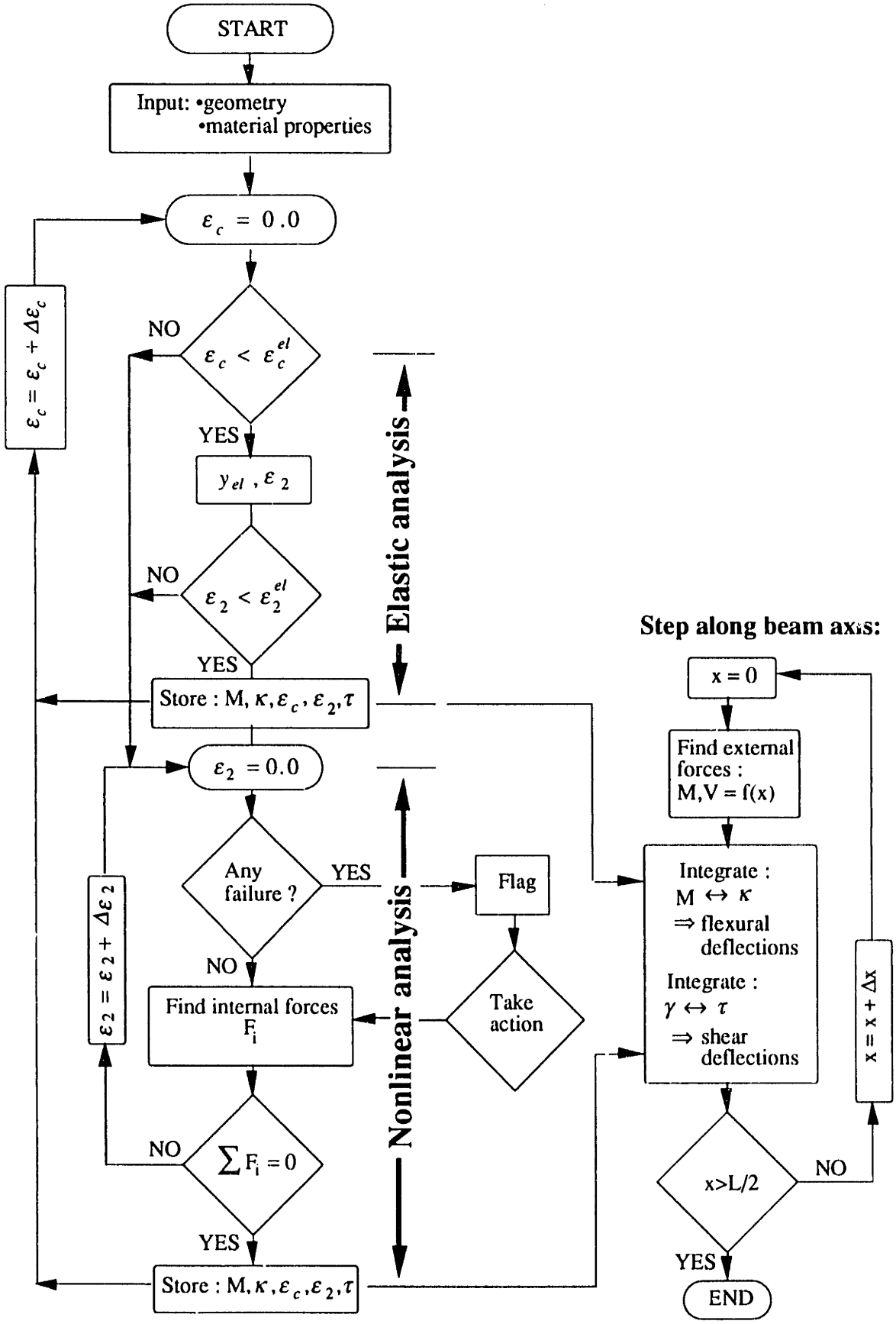

Figure 3.15 Flow chart of short term computational procedure.

The elastic neutral axis measured from the top of the GFRP web can now be found as:

$$y = B / A - c - t_3 \tag{3.84}$$

and the corresponding bending moment as a function of the top fiber strain, ε_c:

$$M_{el} = \varepsilon_c(-B + \frac{I A}{B}) \tag{3.85}$$

This analysis is valid only as long as all strains are below the corresponding cut-off values defining the nonlinear region (see Sections 3.2.2 and 3.2.3). Once this region is reached, the nonlinear analysis has to be used as described in Section 3.3. Here, for every new increment of the top fiber strain the equilibrating bottom strain is found and with it the corresponding stresses and internal forces such as bending moment and shear force. For each new increment, the initial boundary conditions are those satisfying equilibrium of normal forces in the previous one. Each time an equilibrium position is found throughout the incremental analysis, all the possible failure modes are checked, and a modification to the cross section properties is carried out if necessary (e.g., $t_2 = 0$ if CFRP fails). The boundary conditions imposed here are either strain (e.g., concrete crushing, concrete cracking, GFRP rupture, CFRP rupture) or stress (concrete or GFRP shear failure) controlled. If any of the failure modes is reached, a flag describing it is set and sent back to the user. At each increment the shear stress at discrete points of the cross section and the curvature are calculated and stored, in order to be retrieved later for deflection calculations. As a result of the incremental analysis, the moment versus normal strain, curvature versus moment and shear stress versus shear force distributions at discrete points are known. This is shown in Figure 3.16.

What remains is the calculation of deflections, which is easily performed using the virtual force method described in Section 3.2.10. The integration for the virtual force method is carried out numerically, but at probably different discrete points, than those used so far. In this case, a linear interpolation can be used with sufficient accuracy, particularly if the increments used for ε_c were small.

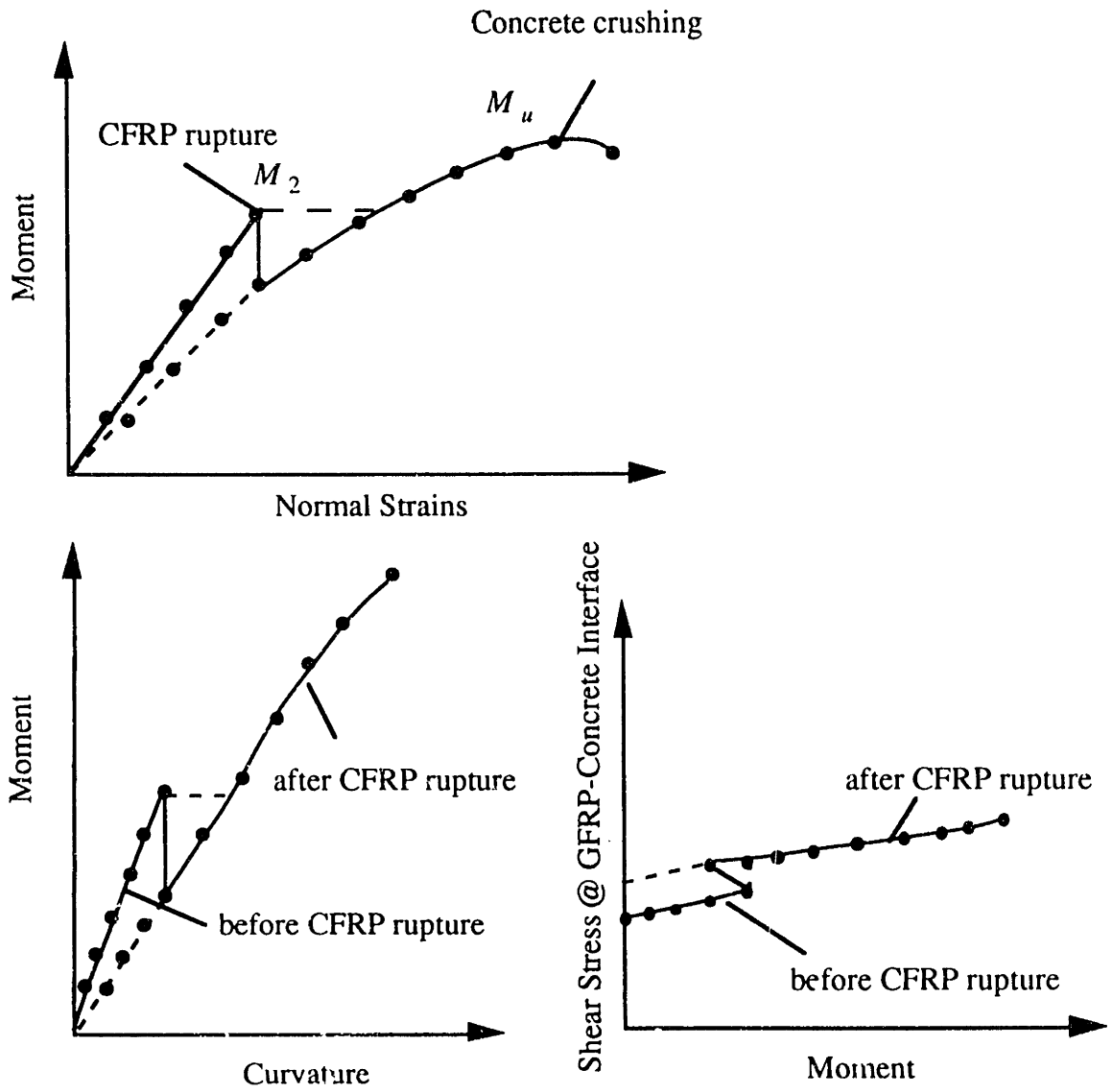

Figure 3.16 Curvature, shear stress and normal strain versus moment diagrams.

3.5 Synopsis

This chapter has focused on the analysis and design of hybrid FRP-concrete sections in short term loading conditions. On the other hand, the practical applications of these members are usually associated with loads that are constantly acting on the structure or repeating themselves throughout time. Therefore, the next step in studying the mechanical behavior characteristics of the combined material system is focused on the long term response. The effects of shrinkage, creep, fatigue and temperature are studied in the next chapter.

Chapter 4

LONG TERM ANALYSIS

4.1 Introduction

The subject of this chapter is to describe and quantify the long term behavior of the hybrid FRP-concrete members. Models for the analysis of these innovative composite elements are developed. The response of the element due to shrinkage, creep and fatigue is studied. The residual short term strength remaining after a certain long term load history is determined using appropriate models.

In this study shrinkage was assumed to be associated with concrete only, and hence a model to simulate this behavior was adopted and implemented in the analysis. The viscoelastic properties of both concrete and GFRP were considered. Two models describing this time dependent behavior of GFRP were developed. One was developed directly from experimental results giving an empirical approach, while the other was obtained from continuum theory using experimental data for creep of the matrix only. A standard model for concrete creep was adopted from ACI (1971). The analysis presented in Chapter 3 was expanded in order to account for creep effects. Apart from the viscoelastic response, the analysis for residual strength calculation was developed, too.

The effects of cyclic loading were also analyzed. Appropriate models for concrete and GFRP were developed and implemented in order to predict the response of the hybrid member under fatigue loads. Special emphasis was put on the stiffness reduction and its effect on the fatigue life of the beam. The residual strength of a fatigued member was derived analytically and implemented in a computerized procedure. The bending behavior of the hybrid element was numerically simulated taking the influence of fatigue into account. The derivations and the software developed in Chapter 3 were used again and modified accordingly to include the effects of fatigue. Finally, the effect of temperature on the hybrid beam was discussed and local effects at the GFRP-CFRP interface were analyzed.

4.2 Shrinkage

Shrinkage represents a process where the volume of a body is decreased due to reactions within the material as a function of time. Shrinkage at the macroscopic level will induce stresses into a structure only if a volumetric deformation is restrained in any direction or along any boundary. There are two types of shrinkage involved with the hybrid beam concept. One is caused by concrete shrinkage while the other is generated during the curing process of the matrix within the two composites, CFRP and GFRP. The manufacturing process of the hybrid FRP-concrete beam is described in Chapter 5. From there it is apparent that any shrinkage effects of the matrix of either GFRP or CFRP will cause a deformation of the two constituent materials but, since the materials can be stored for enough time until used for the hybrid element, this will not affect the stress distribution over the hybrid beam. All stresses at the microscopic level (between fibers and matrix) are assumed to be negligible due to the low shrinkage characteristics of commonly used matrices, and are disregarded in this work. Hence, the GFRP box beam as well as the CFRP sheets are assumed to be shrinkage free at and after the time they have been built into the final member. Effects of moisture are assumed not to affect the FRP matrix since appropriate coatings are available to prevent this from happening. The only material remaining to introduce shrinkage stresses into the hybrid member is therefore concrete. The basic assumptions and guidelines for the analysis and a material model for shrinkage (adopted for the analysis) will be presented next.

4.2.1 Concrete Shrinkage Analysis

During the curing process of concrete at the microscopic level water is present within its volume either as free or absorbed or it is bonded in the form of hydrates. This concrete has to be in equilibrium, and the moisture filling the existing voids and crystalline structure is maintaining it. When concrete loses moisture by evaporation, inter- and intracrystalline forces tend to cause internal tensile stresses trying to maintain internal equilibrium and as a result the concrete shrinks. Shrinkage strains are independent of the stress conditions caused by external forces in the concrete. If restrained, they can cause cracking of concrete due to tension and will induce compressive forces to the confinement In the case of the hybrid beam, this results in a strain and stress profile as shown in Figure 4.1.

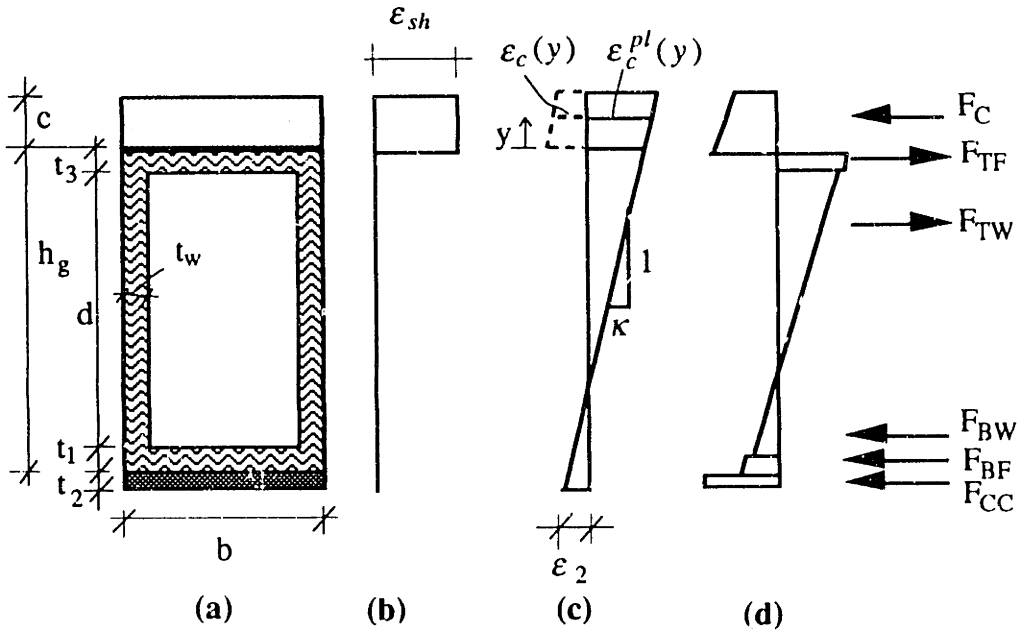

Figure 4.1 Stress and strain profile for concrete shrinkage: (a) geometry of section, (b) shrinkage strain distribution, (c) equilibrating strain profile, (d) final stress distribution.

Shrinkage in the concrete is represented through a tensile strain, ε_{sh}, inducing a equilibrating compressive force into the FRP box section. The curvature, κ, and the bottom strain, ε_2, of the hybrid (the top strain can be calculated from compatibility considerations) in Figure 4.1(c) can be found from equilibrium of internal forces by solving a two dimensional system of equations.

$$\left.\begin{aligned} &\sum F = 0 \\ &\sum M = 0 \end{aligned}\right\} \Rightarrow \kappa, \varepsilon_2 \qquad (4.1)$$

Here the assumption of all materials being in their linear elastic range is admissible since ε_{sh} and therefore all the other strains are small. The derivation of the forces and stresses for this case is omitted since the dead loads of the hybrid beam are already sufficient to change the strain and stress profile. It has to be pointed out that the compressive force applied to the top of the FRP box section is acting outside of its core and hence will produce tensile stresses in the bottom of the box section as shown in Figure 4.1(d). It is seen that the concrete is in tension although the actual strains in it are

compressive. Figure 4.2 shows the stress and strain distribution when external loads are acting on the section in conjunction to shrinkage.

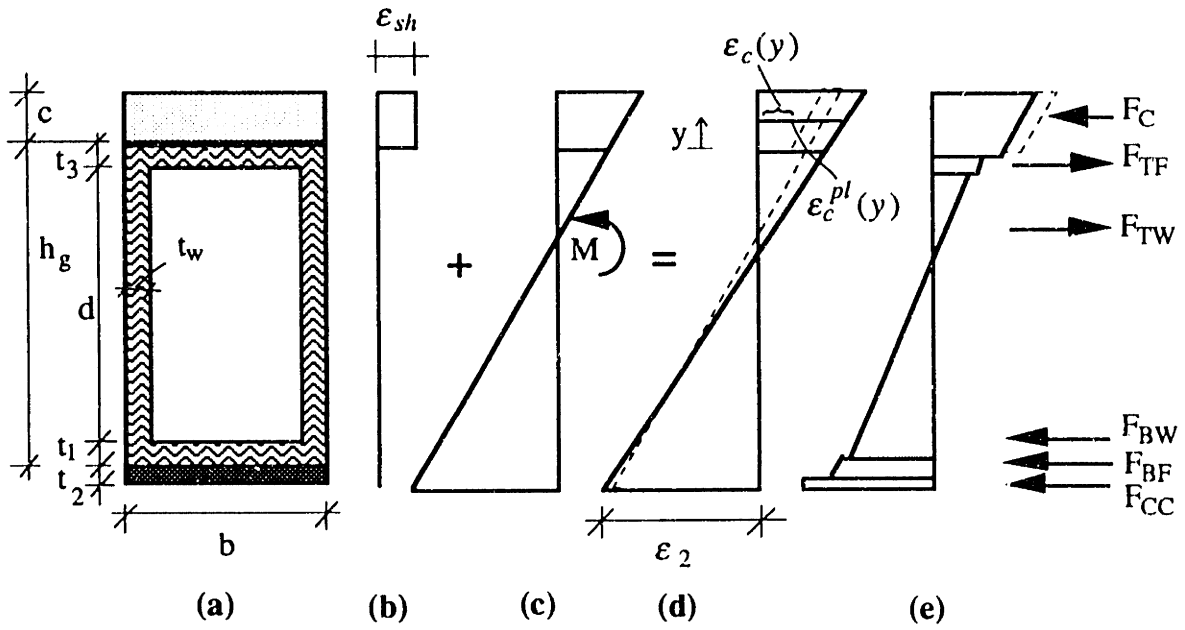

Figure 4.2 Combined effect of shrinkage with external loading: (a) geometry of section, (b) shrinkage strain distribution, (c) external load strain distribution, (d) equilibrating strain profile, (e) final stress distribution.

The shrinkage effect is accounted for during the calculation of the strain profile equilibrating the internal forces. For the computation of the concrete force, F_C, the concrete stresses were obtained from the stress-strain material law by using an effective strain, ε_c^{eff}. This strain is found by subtracting the shrinkage strain, ε_{sh}, from the real strain, ε_c^{st}, which satisfies the assumption that plane sections remain plane, or expressed analytically, at any point along the concrete layer:

$$\varepsilon_c^{eff}(y) = \varepsilon_c^{st}(y) - \varepsilon_{sh} \tag{4.2}$$

where y defines the distance from the concrete-GFRP interface. From here the stresses in the concrete can be derived according to the analysis described in Chapter 3. Hence, this is the only required change affecting the analysis through which shrinkage of concrete will be taken into account. All the other assumptions mentioned earlier and equations derived still hold and can be used directly. It is important to note that once the beams are produced, the

best storage position is the one inducing compressive stresses in the concrete (e.g., simply supported with dead weight), since any occurrence of shrinkage cracks will be canceled.

4.2.2 Concrete Shrinkage Model

Shrinkage of normal strength concrete occurs at a decreasing rate with time. The final shrinkage strains vary greatly, and are generally in the range from 0.02 to 0.1 %. Shrinkage is mainly a reversible phenomenon, meaning that after concrete has shrunk to a certain extent due to drying, and then is saturated with water again, it will expand back to its original volume. It is important to keep this in mind when designing the hybrid beam since it implies that the concrete crushing failure might be more likely when the concrete is wet than when dry. Other factors that affect the magnitude of shrinkage strain depend on the environment and the composition of concrete. Both ACI Committee 209 (1971) and the CEB-FIB (1970) have proposed empirical methods for the estimation of shrinkage strains. The former approach is adopted in this work for the shrinkage model of concrete. According to this method the unrestrained shrinkage strain at any time t after the age of 7 days for a normal weight concrete is given by:

$$\varepsilon_{sh} = \varepsilon_{shu} \frac{t^{\alpha}}{f + t^{\alpha}} \tag{4.3}$$

where ε_{shu} is the ultimate shrinkage strain, t is the time in days, and α and f are empirical values that have normal ranges of 0.9 to 1.1 and 20 to 130 days, respectively. The value for ε_{shu} depends on several correction factors and can be calculated as their product by:

$$\varepsilon_{shu} = 780\,\gamma_{cp}\gamma_{\lambda}\gamma_{h}\gamma_{v/s}\gamma_{s}\gamma_{\psi}\gamma_{c}\gamma_{\alpha}\,10^{-6} \tag{4.4}$$

where $\gamma_{cp}, \gamma_{\lambda}, \gamma_{h}, \gamma_{v/s}, \gamma_{s}, \gamma_{\psi}, \gamma_{c}$ and γ_{α} are the correction factors for initial moist curing, relative humidity, average thickness of the member, volume-surface ratio, slump, fine aggregate percentage, concrete content and air content, respectively. These factors can be obtained from empirical tables given in ACI Committee 209 (1971), but in general better results are obtained if experimental data are used directly and a curve fit of equation (4.3) is performed with all three variables, α, f and ε_{shu}.

4.3 Creep

4.3.1 Introduction

The stress and strain state of deformable bodies is according to the theory of elasticity of classical mechanics uniquely defined for a given loading configuration. A time dependent change of either stress or strain state is therefore theoretically not possible. Controversially, in reality some materials do experience a certain change. The time dependent increase of strain in materials subjected to sustained stress is defined as creep. Materials with creep characteristics are often referred to as viscoelastic, since their response is a combination of viscous and elastic components, or in other words they behave as both fluids and solids. Going back to the hybrid beam at least two of its components are sensitive to creep: the concrete and the FRP matrix. It can be argued that the fibers may show creep deformations as well, but these values are relatively small compared to those of concrete and FRP matrix, and therefore they will be neglected throughout the derivations presented here. The matrix, being a polymer, shows viscoelastic behavior, and similarly the cement in the concrete can be considered to behave viscoelastically. The general relationships describing the generation and development of deformations of any material originated by an acting force or temperature change taking into account the factor of time are summarized in the field of rheology. Rheological models for both FRP and concrete exist but an exact solution for the stress and strain state from these relationships is only possible for some special cases and even then they involve tedious differential equations and Laplace transformations and are not suitable for the analysis presented here.

Instead, for the analysis of the hybrid beam simple models representing the time dependent behavior of concrete and FRP were developed. For FRP two models were considered, one being empirical and using data from uniaxial coupon tests, the other applying continuum theory and using experimental data for the creep of the matrix only. The model for concrete was adopted from ACI (1971). Using these models, an analytical procedure was created in order to predict the response of the hybrid member when subjected to sustained load. The residual loading capacity of the beam after a certain loading history was analyzed. All the calculations were performed by means of computer programs developed in this study.

4.3.2 Creep Model for Concrete

It is known that the stress-strain relationship of concrete is a function of time. Concrete under stress undergoes a gradual increase of strain and the final value might be several times as large as the initial elastic value. This is shown in Figure 4.3.

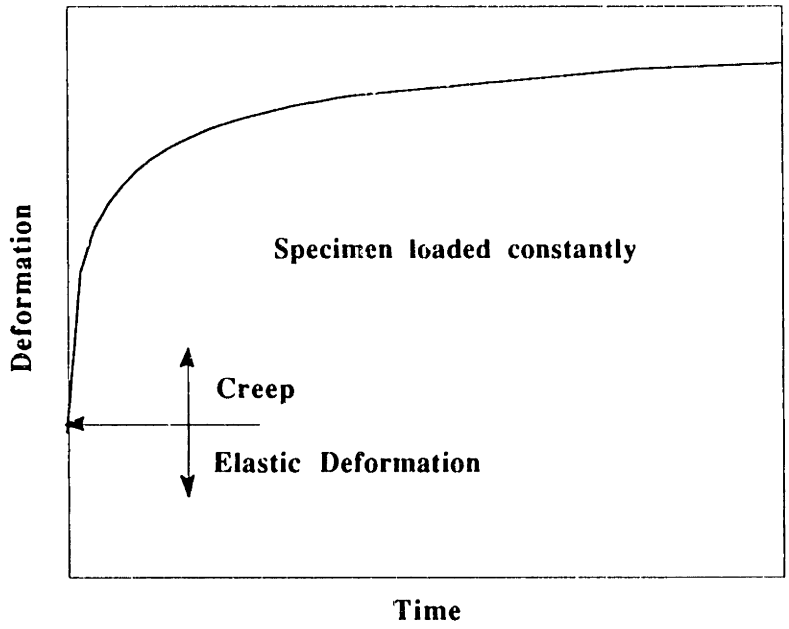

Figure 4.3 Typical creep curve for concrete under constant stress.

The creep strain is obtained by subtracting from the total measured strain in a loaded specimen the sum of the initial instantaneous elastic strain due to the sustained stress, the shrinkage, and the eventual thermal strain. It is believed that the cause of creep in concrete is the cement paste and creep is related to internal movement of absorbed or intracrystalline water, that is internal seepage. On the other hand, the creep-time curve shows a definite decrease in its slope which indicates a change in the mechanism of creep. According to Neville (1971) the behavior here is attributed to viscous flow or sliding between the gel particles. Nevertheless, it has to be concluded that the exact mechanism of creep is still unknown, but it is apparent that creep, mainly as a property of the cement paste, depends to a large extent on a grosser structure of colloidal dimensions and only indirectly on the chemical composition. The creep behavior of concrete is partially reversible which suggests that the deformation may consist of partially reversible viscoelastic movements and possibly also a non-reversible plastic deformation. Consideration of these types of deformation has led to the development of rheological models, that is fictitious devices

combining ideal springs, dashpots and sometimes friction and non-return valves. One of these models was suggested by Hansen (1958) and is shown in Figure 4.4.

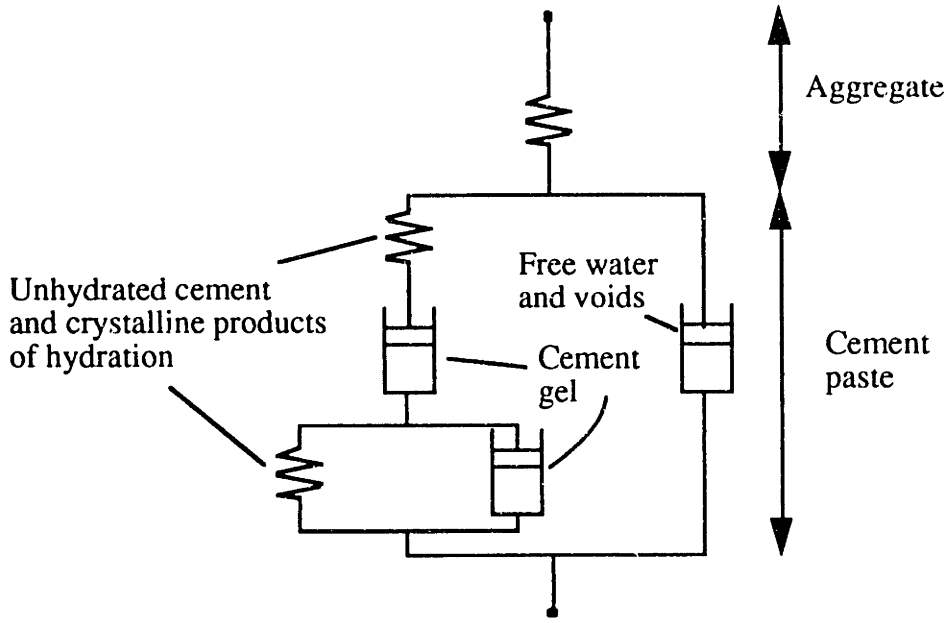

Figure 4.4 A rheological model of creep of concrete.

Experimental evidence indicates that the creep strain occurring over a given period is proportional to the applied stress provided the stress level is not high. Uncertainty is associated with respect to the stress level at which the linearity between creep and applied stress ceases. Values from as low as 20% and as high as 50% of f_c' for the loss of linearity have been suggested. Nevertheless, the assumption of a linear relationship between creep strain and applied stress for the usual range of service load stresses results in acceptable accuracy and will be adopted in the analysis presented here.

The magnitude of the creep strain depends, very much like shrinkage, on the composition of the concrete, the environment and the loading history. Composition factors affecting the creep may be given through aggregate type and proportions, cement type and content, water/cement ratio and additives. The type of aggregate has an influence because of different absorption and elastic properties of the aggregates. An increase in aggregate content generally decreases the creep strains in concrete since aggregates are volumetrically more stable than the cement paste. W/C ratio, cement content and air content are all proportional to the creep magnitude. Environmental factors affecting creep are humidity and member shape and size. It was mentioned earlier that creep is associated with movement of absorbed or intracrystalline water and therefore a low relative ambient

humidity is beneficial to creep strains. Loss of water from a member depends on its shape and size and enables development of creep. Hence, the creep of large members is reduced. The influence of size and shape of concrete is represented by the ratio of volume to surface area or by an effective thickness. The stress-time history influences creep of concrete depending on the age at the stage of first loading. Loading at early age causes higher creep strains.

The model adopted for the analysis of the creep response of the hybrid beam is the one proposed by ACI Committee 209 (1971). The model is similar to the one given for shrinkage in Section 4.2.2. Creep of concrete is represented as a multiplier of the initial elastic strain and is referred to as the creep coefficient. It is a function of the ultimate creep coefficient and the time, t, since when the load was applied. This is given with the following relation:

$$\varphi_c(t) = \varphi_{ul} \frac{t^{\psi}}{d + t^{\psi}} \tag{4.5}$$

where t is the time in days, and ψ and d are empirical values that have normal ranges of 0.4 to 0.8 and 6 to 30 days, respectively. The value for φ_{ul} depends on many variables taking into account all of the above mentioned creep factors and can be calculated as their product by:

$$\varphi_{ul} = 2.35 \gamma_{la} \gamma_{cp} \gamma_{\lambda} \gamma_h \gamma_{v/s} \gamma_s \gamma_{\psi} \gamma_c \gamma_{\alpha} \tag{4.6}$$

where $\gamma_{la}, \gamma_{cp}, \gamma_{\lambda}, \gamma_h, \gamma_{v/s}, \gamma_s, \gamma_{\psi}, \gamma_c$ and γ_{α} are the correction factors for loading age, initial moist curing, ambient relative humidity, average thickness of the member, volume-surface ratio, slump, fine aggregate percentage, concrete content and air content, respectively. These factors can be obtained from empirical tables given in ACI Committee 209 (1971), but in general better results are obtained if experimental data are used directly and a curve fit is performed. The resulting concrete strain taking into account the creep effects is now obtained as a function of time by:

$$\varepsilon_c(t) = \varepsilon_o^c (1 + \varphi_c(t)) \tag{4.7}$$

where ε_o^c represents the initial strain of concrete and the creep coefficient $\varphi_c(t)$ is given by equation (4.5). Since the stress state in a specimen under sustained load does not change with time, in the analysis of the hybrid beam it can be assumed that for a given strain at

time t the corresponding initial strain can be found from equation (4.7) and then the associated stress level from the short term stress-strain relationship. This will be described in detail in Section 4.3.4. The time dependence of the elastic modulus can be found from the creep strain:

$$E_c(t) = E_o^c \frac{\varepsilon_o^c}{\varepsilon_c(t)} \tag{4.8}$$

where E_o^c represents the elastic modulus at time $t = 0$. Assuming that the shear stress magnitudes for the sustained loads applied are not high and lie within the elastic range and that the Poisson's ratio of concrete does not change with time, classical theory of elasticity can be applied for the definition of the time dependence of the shear modulus :

$$G_c(t) = \frac{E_c(t)}{2(1+\nu_c)} \tag{4.9}$$

4.3.3 Creep Models for FRP

Fiber reinforced plastics consist of two materials: fibers and a polymer matrix. The magnitude of the creep of a material is mainly dependent on the bond energy. Since the atomic bonds define the elastic modulus it is apparent that materials with a higher elastic modulus will show smaller creep strains. The elastic modulus of glass fibers is approximately 20 times larger than that of the matrix. For engineering applications it is then justified to neglect creep of the fibers. If the fibers are made of carbon this ratio lies in the range of 100 to 160 times and therefore, even for a scientific approach their creep effect can be neglected. Polymers, on the other hand, can not be analyzed with elastic theory if the loads applied have a sustained character. The time dependent characteristics of the material have to be included. The response of a polymer is that of a viscoelastic material representing a combination of a viscous and an elastic component. The viscous component in polymers is caused by chains moving past one another in the crystalline zones and depends on time. The elastic component arises from the elastomeric behavior of the amorphous chains plus the more nearly Hookean elastic response of the crystalline zones.

In respect to the creep behavior of the hybrid beam, the fiber orientation in the CFRP laminate is unidirectional and their volume fraction is assumed to be quite high. This implies that the contribution of the matrix to the response of the CFRP sheet is very

small (usually less than 1%), while the main behavior is attributed to the carbon fibers which are considered to be creep free. This has led to the assumption made throughout the creep analysis that the CFRP laminate shows no time dependent strain increase. Controversially, the response of the GFRP box beam, consisting of lower modulus glass fibers oriented in various directions, is influenced by the matrix behavior to a larger extent and hence the creep has to be modeled accordingly. Two models were considered for the representation of the creep behavior of the GFRP box beam. One was developed directly by fitting experimental data to an adopted functional dependence, while the other was obtained using a continuum theory model where only experimental data for the creep of the matrix were considered.

4.3.3.1 Empirical Approach

The best way to use an empirical relationship is to calibrate the parameters with experimental data obtained from the same material for which the behavior is to be described and under the same conditions. For the definition of the time dependence of the GFRP box beam creep strain the results from coupons cut out of its webs and flanges were used. The influence of the stress magnitude has been neglected here since it is assumed that the load levels are in the range where linear viscoelasticity gives reasonably good estimate.

For the description of the creep strains, Findley's (1951) power law model was adopted. Here, it is assumed that the stress level applied is accounted for through the initial strain and that the creep strains at any time t are linearly proportional to it, which is consistent with linear viscoelasticity. The model is defined by:

$$\varepsilon_g(t) = \varepsilon_o^g(1 + mt^n) \tag{4.10}$$

where ε_o^g represents the instantaneous strain at $t = 0$, and m and n are empirical values that have to be obtained from a least squares curve fit to experimental data. Figure 4.5 shows a typical example where an experimental curve describing the creep behavior of GFRP obtained on a coupon test in uniaxial tension is modeled with equation (4.10). The least squares method was used with the requirement for the error to be less than 1%. The webs and the flanges were modeled with different curve fits, similar to the short term stress-strain relationship (see Section 3.2.3). For epoxy GFRPs the range of values for the exponent n is between 0.2 and 0.5.

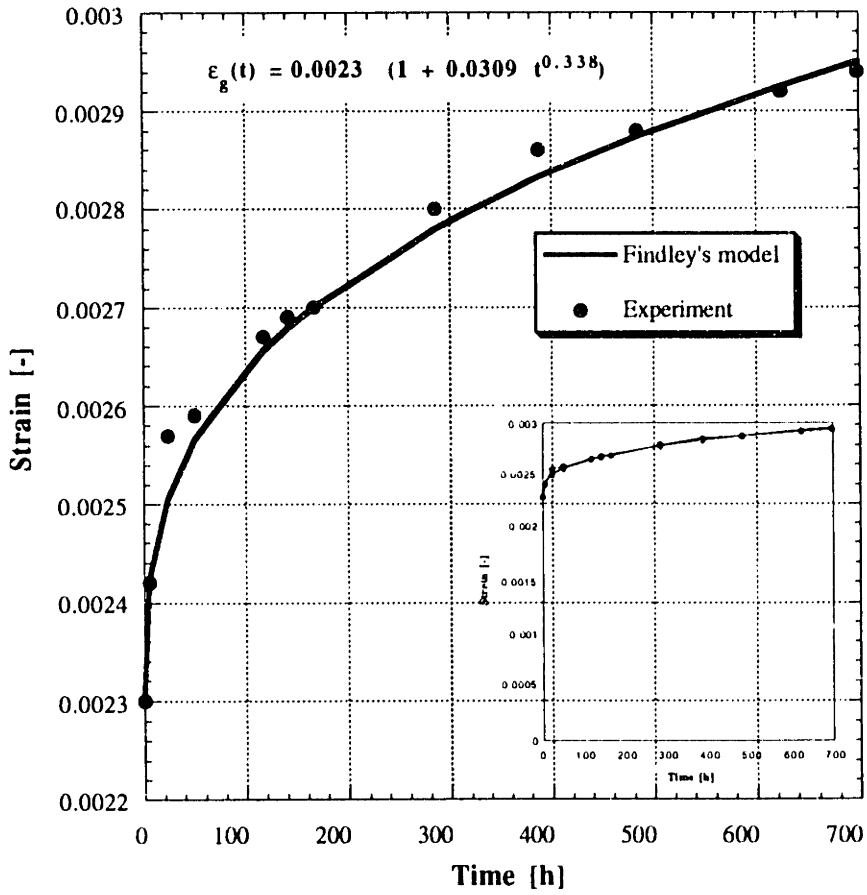

Figure 4.5 Experimental calibration of Findley's creep model.

It has to be pointed out that, in general, linear viscoelasticity has a limited application potential. Many practical problems involve constitutive relations which are a function of the applied stress level. Even though the stresses at the macro level might appear small, in composites the stress concentrations around the fibers may induce localized regions of high stresses resulting in a nonlinear viscoelastic response. In addition to this, experience with FRP confirms that the elastic response is much more linear than the time dependent behavior. Hence caution is needed to avoid errors of assumed linearity on application of composite FRPs. A number of models have been developed for describing nonlinear viscoelastic behavior. An expansion of the linear model was given by Findley and Peterson (1958) who added nonlinear coefficients to the power law:

$$\varepsilon_g(t,\sigma) = \varepsilon_o^{''} \sinh(\sigma / \sigma_\varepsilon) + m^{''} \sinh(\sigma / \sigma_m) t^n \qquad (4.11)$$

where the various parameters $\varepsilon_o^{"}, \sigma_\varepsilon, m^{"}, \sigma_m$ and n are all material properties which may be functions of temperature, absorbed moisture content, etc., but are assumed not to be functions of the applied stress level. The models presented here were used directly in the calculation of equilibrium of stresses at the cross sectional level for the analysis of the hybrid member. This is given in more detail in Section 4.3.4.

4.3.3.2 Continuum Theory Approach

In order to obtain the long term characteristics of laminates usually creep tests on coupons are performed. If this is not possible, but creep data for the constituents of the composites (fibers and matrix) are available instead, a model describing the GFRP time dependence can be created. It was mentioned earlier that the creep behavior of glass is much less than that of the epoxy matrix and therefore, the former will be disregarded in the analysis presented here. The assumption is made that only the elastic modulus of the matrix E_M is a function of time and Findley's power law is used to model the viscoelastic behavior of it. This is given in the next relationship assuming linear viscoelasticity:

$$E_M(t) = \frac{\sigma}{a + bt^n} \tag{4.12}$$

where a, b and n are obtained from curve fits to experimental data of the matrix and σ is the applied stress. Using the rule of mixture and given the expression for E_M the properties of a unidirectional lamina can be calculated as a function of time. Here, it will be assumed that the Poisson's ratio of the matrix, ν_M, is constant. The unidirectional elastic constants are then transformed using continuum theory (Jones 1975) into a global coordinate system in order to obtain the material properties from an arbitrary fiber orientation. This procedure will be described next. Given the volume fraction of the fibers, V_F, for a unidirectional lamina and the elastic material properties of both the fibers and the matrix, the following relation for the calculation of the properties of the lamina can be derived:

$$G_M(t) = \frac{E_M(t)}{2(1+\nu_M)} \tag{4.13}$$

$$E_{\|}(t) = V_F E_F + (1 - V_F) E_M(t) \tag{4.14}$$

$$\nu_{\perp\|} = V_F \nu_F + (1 - V_F)\nu_M \tag{4.15}$$

where G_M, $E_\|$ and $\nu_{\perp\|}$ are the shear modulus of the matrix, the elastic modulus of the lamina in the direction of the fibers and the Poisson's ratio for stress applied parallel to the fiber orientation.

For the calculation of the elastic modulus of the lamina perpendicular to the fiber direction and the lamina's shear modulus a semi-empirical formula was proposed by Puck (1967):

$$E_\perp(t) = E_M^o(t)\frac{1 + 0.85{V_F}^2}{V_F \dfrac{E_M^o(t)}{E_F} + (1 - V_F)^{1.25}}, \text{ where } E_M^o(t) = \frac{E_M(t)}{1 - {\nu_F}^2} \tag{4.16}$$

$$G_\#(t) = G_M(t)\frac{1 + 0.60{V_F}^{0.5}}{V_F \dfrac{G_M(t)}{G_F} + (1 - V_F)^{1.25}} \tag{4.17}$$

Now the Poisson's ratio of the lamina, for a stress applied perpendicular to the fiber orientation, is given by:

$$\nu_{\|\perp} = \frac{E_\perp}{E_\|}\nu_{\perp\|} \tag{4.18}$$

Laminates are compounds of several layers of laminae with different fiber orientations. The properties of the single layers are transformed into a global coordinate system using continuum theory and are summed up across the thickness of the laminate, in order to obtain the full stiffness matrix of the multilayer composite. The angle between the fiber orientation in the single lamina and the global axis, α_k, as well as the lamina properties derived with equations (4.14) to (4.18) are sufficient to obtain the global elastic constants of the laminate, or, for the case of the GFRP box beam, the macromechanical values for $\overline{E}_x, \overline{E}_y, \overline{G}_{xy}$ and $\overline{\nu}_{xy}$. From continuum theory, Hook's law for a transversely isotropic unidirectional layer in the state of plane stress is given by (Jones 1975):

$$\begin{bmatrix} \sigma_\| \\ \sigma_\perp \\ \tau_\# \end{bmatrix} = \begin{bmatrix} d_\| & d_{\|\perp} & \\ d_{\perp\|} & d_\perp & \\ & & d_\# \end{bmatrix} \begin{bmatrix} \varepsilon_\| \\ \varepsilon_\perp \\ \gamma_\# \end{bmatrix} \tag{4.19}$$

where the components of the stiffness matrix read as follows:

$$d_{\parallel} = \frac{E_{\parallel}}{1 - \nu_{\perp\parallel}\nu_{\parallel\perp}} \tag{4.20}$$

$$d_{\parallel\perp} = \frac{\nu_{\parallel\perp}E_{\perp}}{1 - \nu_{\perp\parallel}\nu_{\parallel\perp}} \tag{4.21}$$

$$d_{\perp} = \frac{E_{\perp}}{1 - \nu_{\perp\parallel}\nu_{\parallel\perp}} \tag{4.22}$$

$$d_{\perp\parallel} = \frac{\nu_{\perp\parallel}E_{\parallel}}{1 - \nu_{\perp\parallel}\nu_{\parallel\perp}} \tag{4.23}$$

and

$$d_{\#} = G_{\#} \tag{4.24}$$

The transformation of the stiffness matrix to the global coordinate system is obtained through the following formulas:

$$d'_{11k} = d_{\parallel k}\cos^4\alpha_k + d_{\perp k}\sin^4\alpha_k + \frac{1}{2}D'_{1k}\sin^2 2\alpha_k \tag{4.25}$$

$$d'_{22k} = d_{\perp k}\cos^4\alpha_k + d_{\parallel k}\sin^4\alpha_k + \frac{1}{2}D'_{1k}\sin^2 2\alpha_k \tag{4.26}$$

$$d'_{12k} = d'_{21k} = d_{\perp\parallel} + \frac{1}{4}D'_{2k}\sin^2 2\alpha_k \tag{4.27}$$

$$d'_{33k} = d_{\#k} + \frac{1}{4}D'_{2k}\sin^2 2\alpha_k \tag{4.28}$$

$$d'_{13} = d'_{31} = \frac{1}{2}\left[D'_{2k}\sin^2 2\alpha_k - (d_{\parallel k} - D'_{1k})\right]\sin 2\alpha_k \tag{4.29}$$

$$d'_{23} = d'_{32} = \frac{1}{2}\left[(d_{\perp k} - D'_{1k}) - D'_{2k}\sin^2 2\alpha_k\right]\sin 2\alpha_k \tag{4.30}$$

where:

$$D'_{1k} \equiv d_{\parallel\perp k} + 2d_{\#k} \tag{4.31}$$

and $$D'_{2k} \equiv d_{\parallel\perp k} + d_{\perp\parallel} - 2D'_{1k} \tag{4.32}$$

The resulting stiffness matrix for the lamina in the global coordinate system yields:

$$\underline{\underline{d}}'_k = \begin{bmatrix} d'_{11k} & d'_{12k} & d'_{13k} \\ d'_{21k} & d'_{22k} & d'_{23k} \\ d'_{31k} & d'_{32k} & d'_{33k} \end{bmatrix} \tag{4.33}$$

The thickness t_k of the single lamina k is considered in the composition of the stiffness matrix, $\underline{\underline{d}}_k$:

$$d^*_{ijk} = \left[d'_{ijk}\right] t_k \tag{4.34}$$

giving the final stiffness matrix of the lamina in the global system with:

$$\underline{\underline{d}}^*_k = \begin{bmatrix} d^*_{11k} & d^*_{12k} & d^*_{13k} \\ d^*_{21k} & d^*_{22k} & d^*_{23k} \\ d^*_{31k} & d^*_{32k} & d^*_{33k} \end{bmatrix} \tag{4.35}$$

The summation of the stiffnesses of all the layers in a laminate results in its synthesized stiffness matrix, $\underline{\underline{D}}$:

$$\underline{\underline{D}} = \begin{bmatrix} d_{11} & d_{12} & d_{13} \\ d_{21} & d_{22} & d_{23} \\ d_{31} & d_{32} & d_{33} \end{bmatrix} \tag{4.36}$$

where:

$$d_{ij} = \sum_{k=1}^{n} d^*_{ijk} \tag{4.37}$$

The assumption required for this superposition to be valid is that the compatibility between the layers is met, that is neighboring layers are subjected to the same strains at the interface. From here the average engineering elastic constants across the laminate thickness, t_l , in the global coordinates can be determined with:

$$\overline{E}_x = \frac{1}{t_l}(d_{11} - \frac{{d_{12}}^2}{d_{22}}) \tag{4.38}$$

$$\overline{E}_y = \frac{1}{t_l}(d_{22} - \frac{{d_{12}}^2}{d_{11}}) \tag{4.39}$$

$$\overline{G}_{xy} = \frac{1}{t_l} d_{33} \tag{4.40}$$

and $$\overline{\nu}_{xy} = \overline{\nu}_{yx} = \frac{d_{12}}{d_{11}} \tag{4.41}$$

These constants are functions of the matrix elastic modulus, which is a function of time and hence, they all are time dependent. The total creep strain of a GFRP laminate, $\varepsilon_g(t)$, can be derived from here as a function of time after which a sustained stress has been applied:

$$\varepsilon_g(t) = \varepsilon_o^g \frac{E_o^g}{\overline{E}_x(t)} \tag{4.42}$$

where $\overline{E}_x(t)$ was defined by equation (4.38). A typical curve showing the creep strain of a $\pm 45^\circ$ GFRP laminate using this procedure implementing given data for the matrix creep, volume fraction of fibers and layer buildup is depicted in Figure 4.6 and compared to the same coupon test results as in Figure 4.5. It is seen that this semi-empirical model describing the creep behavior of GFRP by means of continuum theory can achieve satisfactory results similar to the fully empirical model developed in Section 4.3.3.1.

4.3.4 Creep Analysis of Hybrid Beam

The time dependent analysis of the innovative hybrid element is largely based on the assumptions and derivations developed in Chapter 3. Using the models for the characterization of creep behavior of concrete and GFRP the factor time was introduced in the analysis. The stress-strain relationships of both materials were modified dependent on the time elapsed from the sustained load application by changing the corresponding tangent modulus. In most practical applications, the usual range of sustained load magnitudes lie in the range from 20 to 40% of the ultimate capacity. Accounting for this fact in the analysis

for creep, it was assumed that a failure of the hybrid system is less likely and that most of the stress levels of the member's components can be expected in the elastic range justifying the use of linear viscoelasticity for the description of the behavior.

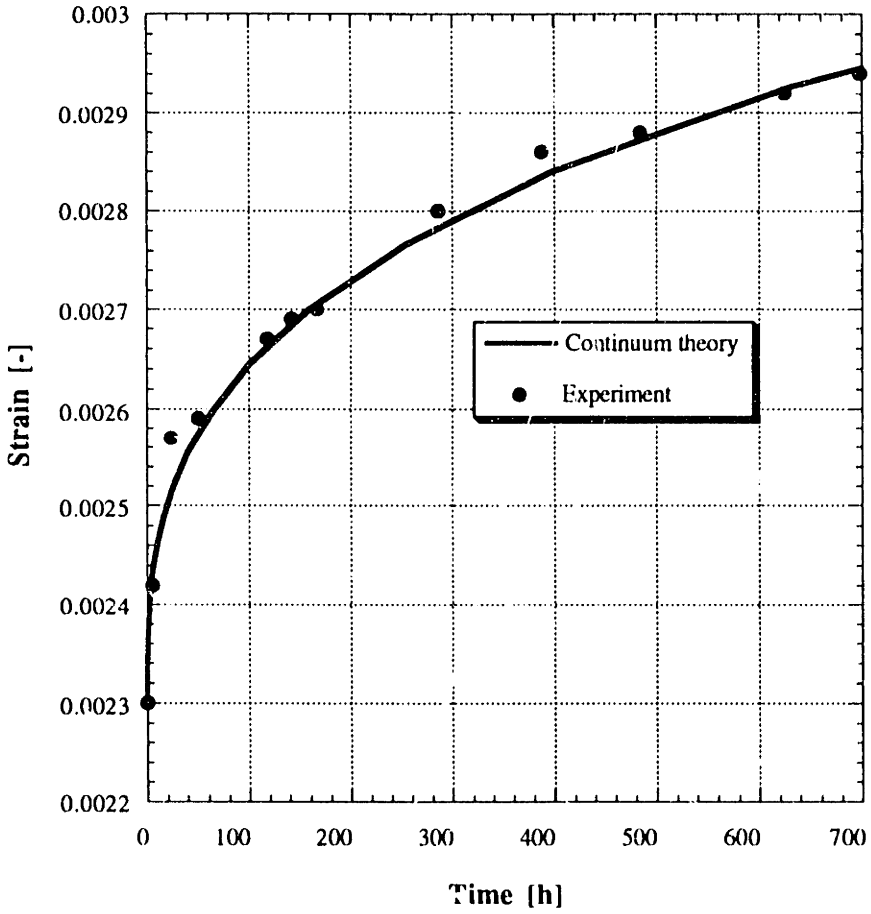

Figure 4.6 Typical result from continuum theory creep response of laminates.

The computer routines described in Section 3.4 were expanded in order to account for creep effects and the whole creep analysis was performed using the resulting software.

Considering the computer program from Section 3.4, changes were carried out in the main routine introducing a loop for the time accounting for creep. A routine calculating the creep coefficients of the different constituents was created. These coefficients are obtained from equations (4.7), (4.10) and (4.42) as follows:

$$\varphi_x(t) = \frac{\varepsilon_x(t)}{\varepsilon_o^x} \tag{4.43}$$

where the index x stands for the appropriate material creep model (concrete, GFRP empirical or GFRP continuum theory). The most important assumption in this analysis deals with a virtual generation of isochronic stress-strain diagrams. Isochronic stress-strain diagrams are obtained by plotting curves through corresponding pairs of points of associated strain and stress at equal times. A schematic isochronic diagram is shown in Figure 4.7.

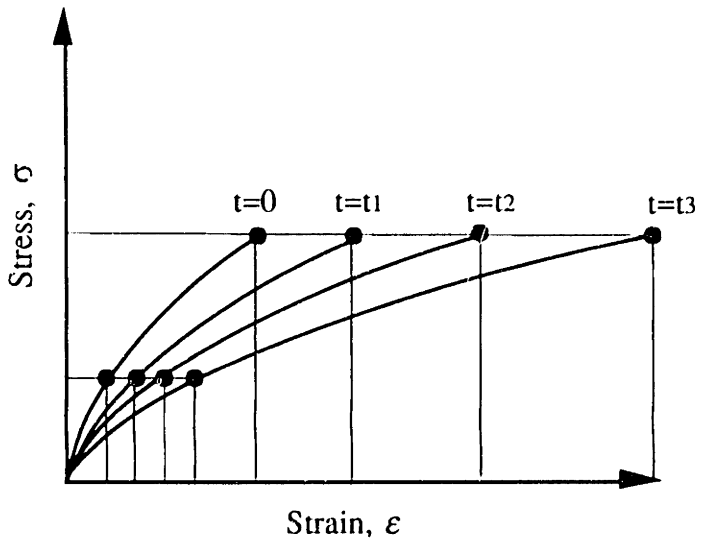

Figure 4.7 Isochronic stress-strain relationship.

Usually these diagrams are obtained experimentally by loading several specimens at different load levels and varying load duration. On the other hand, from the short term stress-strain relationship and the time dependence of creep strains these diagrams can be obtained analytically. Rearranging equation (4.43) the initial strains can be obtained from creep strains:

$$\varepsilon_o^x = \frac{\varepsilon_x(t)}{\varphi_x(t)} \tag{4.44}$$

For these initial strains the corresponding stress is obtained from the short term ($t=0$) stress-strain law. Since in creep the stress levels are maintained constant throughout time this value equals to the one at time t_o. The procedure is shown schematically in Figure 4.8.

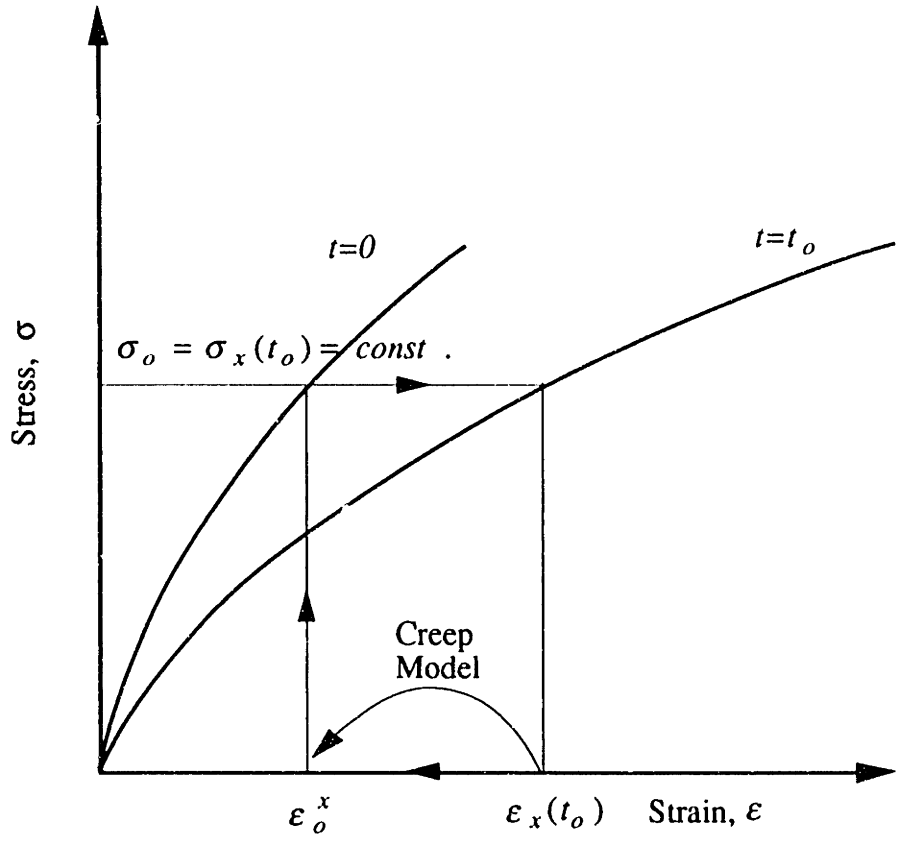

Figure 4.8 Stress equality at initial and creep strain.

This principle was implemented in the main routine of the program. A description of the program's flow is given in Table 4.1. All the variables were described in Chapter 3. Note that in step 13 the applied load, here given through M_o, is approached with this incremental procedure from lower values, and as soon as a strain profile is found that gives a higher external moment $M_i(t)$, the iteration is terminated. This can be further optimized by iterating between $M_i(t)$ and $M_{i-1}(t)$ using any iterative method, but assuming that the increments in step 14 for the strain profiles are small this can be omitted. Throughout the analysis it has to be constantly checked whether any of the failure modes were encountered during the incrementation procedure, and if this was the case the appropriate action has to be taken. This will be automatically carried out in the computer program since all the checks were defined and implemented already for the short term analysis. The design of the hybrid beam should be such that for usual service load magnitudes a failure should not occur due to a sustained load, but in the case this is inevitable the CFRP rupture should precede any other mode and give a warning while the remaining member is still safe.

Table 4.1 Creep analysis program flow.

Step #	Description of computation or action performed	Variables involved
1	Data input.	Material and geometric properties
2	Start loop over time, initial value $t = 0$.	t
3	Call routines to define creep coefficients.	$\varphi_c, \varphi_{web}, \varphi_{flange}$
4	Assume an initial top fiber strain. 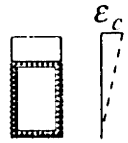	ε_c
5	Start loop incrementing bottom fiber strain. 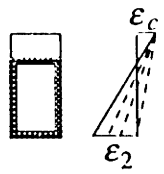	ε_2
6	Calculate the strains across the strain profile.	ε_x
7	Find the corresponding initial strains.	ε_o^x
8	Call the routines describing the stress-strain relationship and get the stress magnitudes.	σ_x
9	Call the routine for stress integration and normal forces in cross section.	F_{XX}
10	Call routine for the calculation of the sum of normal forces and check whether cross section is in equilibrium at this strain profile.	
11	If yes continue, otherwise go back to step 5 and find new strain profile.	
12	Calculate the external moment equilibrating the section and store the curvature. Index i defines this strain profile. 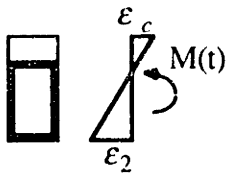	$M_i(t)$, $\kappa_i(t)$
13	Compare the applied sustained moment, M_o, to $M_i(t)$. If larger continue, otherwise go to step 15.	
14	Increment the top fiber strain and go back to step 4.	$\varepsilon_c + \Delta\varepsilon_c$
15	Call the function to calculate the deflections and call the printout routine.	v
16	Increment t to next value and go back to step 3.	$t + \Delta t$

4.3.5 Residual Strength of Hybrid Beam

The previous section discussed the behavior of the hybrid member subjected to sustained loads. The analysis was obtained to predict the strain profiles and deformations of the beam. Due to the viscoelastic effects the member changes its stress and strain state over time. These changes affect the strain magnitudes directly and influence the remaining load capacity to collapse of the member, since all the failure modes defined earlier occur when the ultimate strain of any of the components is reached. This remaining capacity is defined as the residual strength of the member. The residual strength is characterized as the short term strength of a member that has been subjected to some loading history, in this case creep deformations due to a sustained load.

The analysis of the residual strength is a combination of the short term analysis given in Chapter 3 and the analysis for creep described in Section 4.3.4. As a basic guideline, two stages of the analysis have to be differentiated. The first includes the creep analysis which has to be carried out giving a new deformed state of the member. The second involves a short term analysis, for which the results from the previous stage represent an initial state and which has to be performed until a failure mode is reached. The material models and assumptions developed in Section 4.3.3 are valid for the creep portion of the analysis while for the second stage additional assumptions have to be made.

The first assumption deals with the residual strength of the materials involved. In general it is seen that the strength of some materials which were subjected to some loading history is decreased in respect to their short term strength, but the magnitude of the ultimate strain at failure is unchanged and remains constant. This is associated with the maximum strain failure criterion. In other words, a material that is in a certain strain state will be able to carry more stress only until the resulting strain does not exceed the ultimate value, regardless of what the cause of the initial strain was. In the analysis performed here, it will be assumed that both concrete and GFRP comply with this residual strength definition. Figure 4.9 shows typical stress-strain relationships for concrete and GFRP, which may be used for the residual strength calculation. The curves are plotted for different time spans of sustained stress applied and the resulting strain. The curve for time $t = 0$ is the short term uniaxial stress-strain diagram and is described with a function $\sigma = f(\varepsilon)$. The curve for time $t = t_o$ is obtained as a series of points defined by $[\varepsilon, f(\varepsilon / \varphi(t_o))]$, where $\varphi(t_o)$ represents the creep coefficient given in equation (4.43). It can be seen that the ultimate stress decreases as the time t_o increases. Simultaneously, the ultimate strain is maintained.

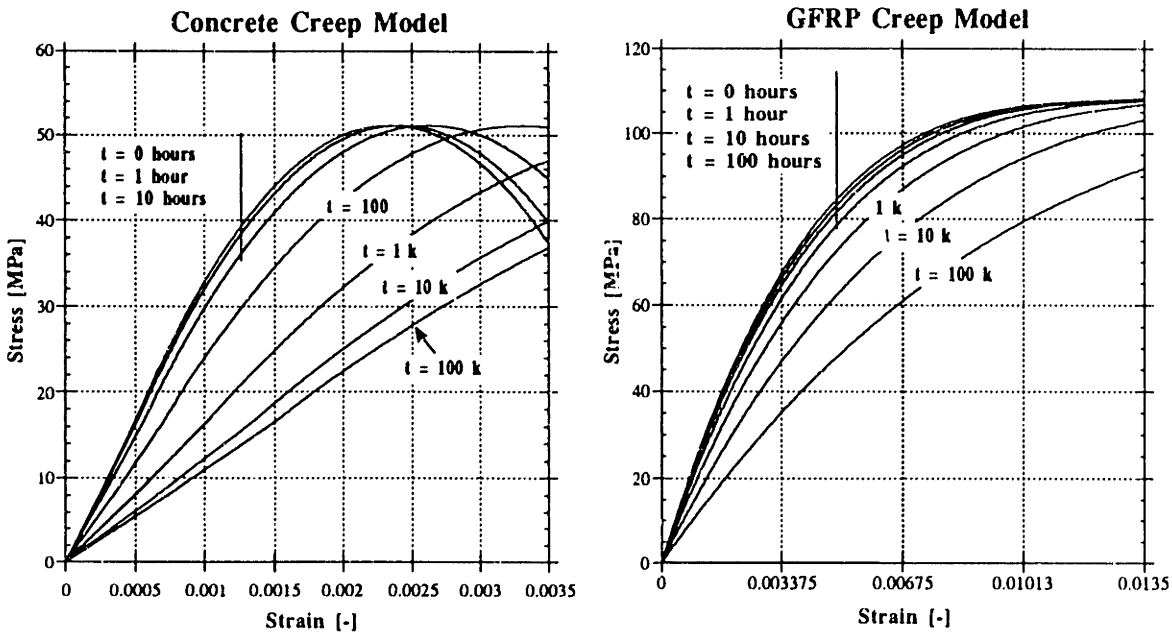

Figure 4.9 Isochronic stress-strain relationships.

The second assumption is related to the definition of the short term response after the material has deformed already due to creep. A schematic representation of the associated stress-strain relationship is shown in Figure 4.10. The curve for $t=t_o$ will be referred to as the residual stress-strain diagram.

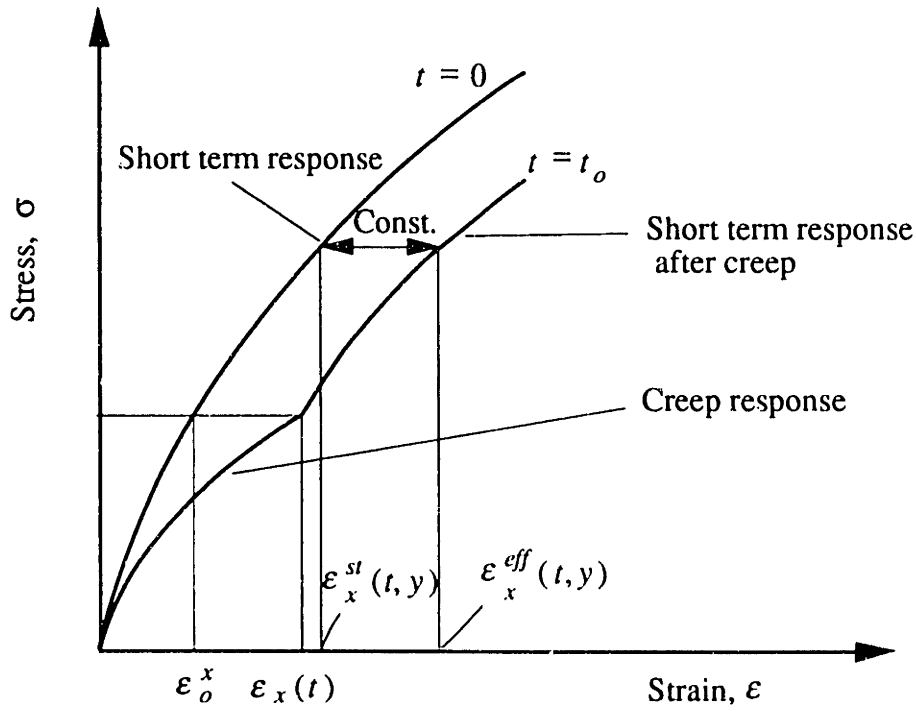

Figure 4.10 Stress-strain relationship for residual strength calculation.

The residual curve complies with the creep curve until additional stress is applied, after which the curve is parallel to the short term one shifted by the amount of the creep curve. This is justified with the reasoning that the residual curve is related to the short term one but the strains are increased due to viscoelastic effects. Hence, for the computation of the stresses from a given strain profile the strains generated during long term loading have to be known first. It has to be pointed out that the ultimate strain for the residual curve equals the one for short term. The computational procedure required for the determination of residual stresses at any point along the hybrid beam's cross section is described next.

Using the same procedure as given in Table 4.1, the strain profile of the hybrid beam giving equilibrium of normal forces at an internal moment $M_i(t) = M_o$ can be calculated. The top and bottom strains are $\varepsilon_c(t)$ and $\varepsilon_2(t)$, respectively. They define the strain profile which represents the initial state at time t for a short term response to a load, M_{st}, larger than M_o. If the member is actually loaded with a moment M_{st}, the equilibrating strain profile is defined through new top and bottom strains, denoted as $\varepsilon_c^{st}(t)$ and $\varepsilon_2^{st}(t)$, respectively. The strain profiles at time t before and after the additional moment $M_{st} - M_o$ was applied are shown in Figure 4.11.

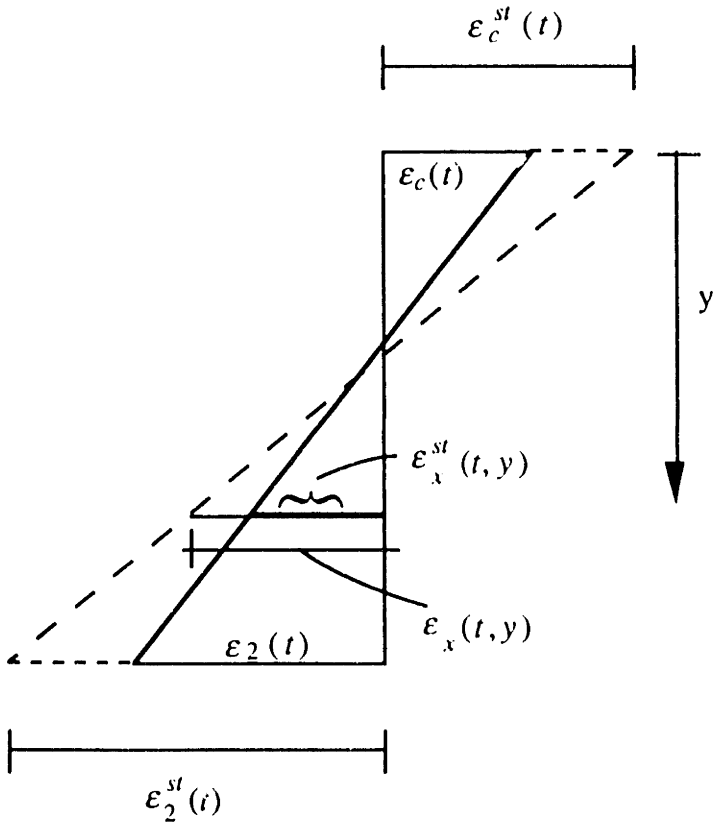

Figure 4.11 Strain profile for post-creep response.

The corresponding stresses are obtained from the known short term stress strain relationship through an effective strain which takes creep effects into account and transforms actual strains from the residual curve into matching ones on the short term curve. This strain, $\varepsilon_x^{eff}(t,y)$, at any point, y, along the member's cross section can be determined as follows:

$$\varepsilon_x^{eff}(t,y) = \varepsilon_x^{st}(t,y) - \varepsilon_x(t,y)(\varphi_x(t)-1) \tag{4.45}$$

where $\varepsilon_x^{st}(t,y)$ is the actual strain for M_{st} at point y and $\varepsilon_x(t,y)(\varphi_x(t)-1)$ represents the difference between the strain at $t=t$ including creep effects and the instantaneous strain at $t_o=0$ (see Figure 4.10, $\varepsilon_x(t)-\varepsilon_o^x$) which was generated at the same point due to the sustained moment M_o. In other words, it is the additional strain that occurred during viscoelastic response. $\varphi_x(t)$ is the creep coefficient of the material at point y and time t. From Figure 4.11 the creep strain $\varepsilon_x(t,y)$ can be found from the strain profile with:

$$\varepsilon_x(t,y) = \frac{\varepsilon_c(t)+\varepsilon_2(t)}{\varepsilon_c^{st}(t)+\varepsilon_2^{st}(t)}\left[\varepsilon_c^{st}(t)+\varepsilon_x^{st}(t,y)\right] - \varepsilon_c(t) \tag{4.46}$$

Close to the neutral axis, due to a shift of the strain profile, the creep strain can become negative, indicating compressive creep strain. This would result (from equation (4.45)) in an effective $\varepsilon_x^{eff}(t,y)$ larger than the actual one, which, physically, is impossible. Since in this case, these strains are small and their contribution to the equilibrium of the cross section is insignificant, for the case equation (4.46) yields a negative $\varepsilon_x(t,y)$, the latter can be neglected in the calculations and set equal to zero. This implies that the effect of some creep history for an element at point y close to the neutral axis will not be considered and was as such adopted in the analysis. Now the resulting stress at point y is obtained from the short term stress-strain curve of material x with:

$$\sigma_x(t,y) = f_x\left(\varepsilon_x^{eff}(t,y)\right) \tag{4.47}$$

where the functions f_x depend on the material model and were defined in Sections 3.2.2 and 3.2.3. In the derivations given above it is seen that the effective strain, $\varepsilon_x^{eff}(t,y)$, and hence the corresponding stress, $\sigma_x(t,y)$, are not only functions of the time of creep t but also of the applied load, M_o, since they depend on the strain profile (defined by $\varepsilon_c(t)$ and

$\varepsilon_2(t)$) generated by it. This means that in the case of the hybrid beam loaded in three (or four) point bending tests where every (most) cross section has a different moment applied on it, a different calculation is needed for each. The significance of this is found in the calculation of the beam deflections and will be discussed next.

The response of a member which was initially subjected to a long term loading configuration and then is loaded up to its residual strength with short term loads can be referred to as the post-creep response. The analysis of the post-creep behavior of the hybrid beam was implemented in a computer program. The main objective of the program is to compute the response of an element to a short term load up to its residual strength, after it has been loaded in creep for a certain period of time, t_o. The expected load pattern is given in Figure 4.12.

The first part of the program determines the creep response at the cross sectional level for several sustained moments, M_{oi}. This is achieved in much the same way as described in Table 4.2, step 1 to 14. The only difference is that the loop in step 2 is substituted with one repeating the procedure for different values of M_{oi}. This is needed to obtain a number of discrete initial states for the calculation of the post-creep part.

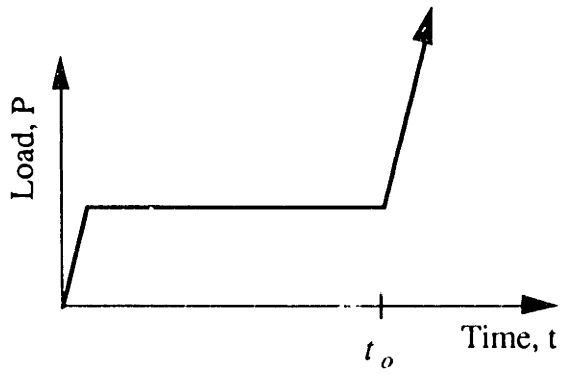

Figure 4.12 Load configuration for residual response.

Then, in the second part, starting from the final strain profile of part one and using the short term procedure described in Section 3.4, the strain profile is further incremented giving new positions and the associated internal moments. In this part the stresses generated by the strain profile are calculated with the derivation given in equation (4.47). Typical results from the analysis are shown schematically in Figure 4.13.

Failure checks are performed for every new equilibrium position found and the appropriate flags triggered. For a good design the CFRP rupture mode should be reached first, and another flexural mode giving the residual strength, thereafter. Throughout the routines described, data on the curvature as a function of the applied load (moment) were

stored to be used for the deflection calculations. Figure 4.14 shows the data stored in a graphical form. It should be pointed out that only discrete points are obtained but if small increments of strain profile were used sufficient density can be achieved. The different branches of the curves result form different sustained loads M_{oi}.

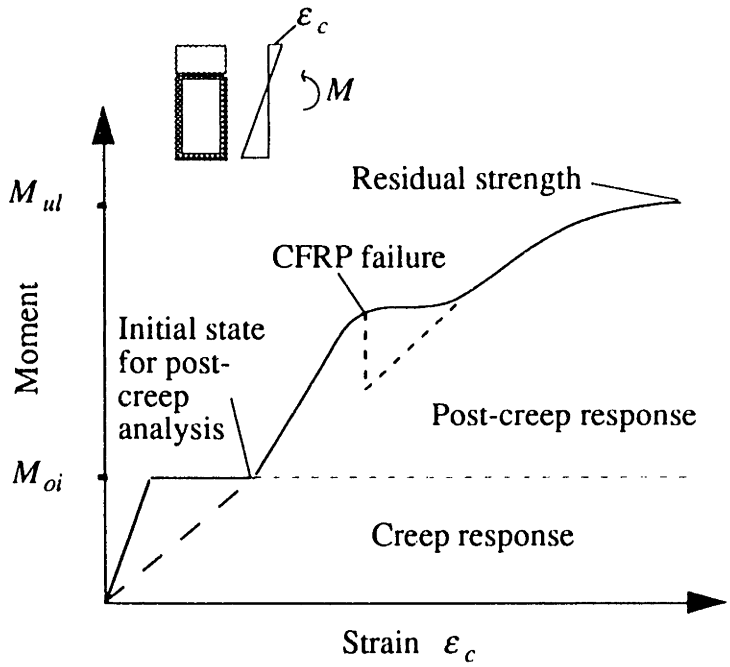

Figure 4.13 Typical moment versus top fiber strain diagram.

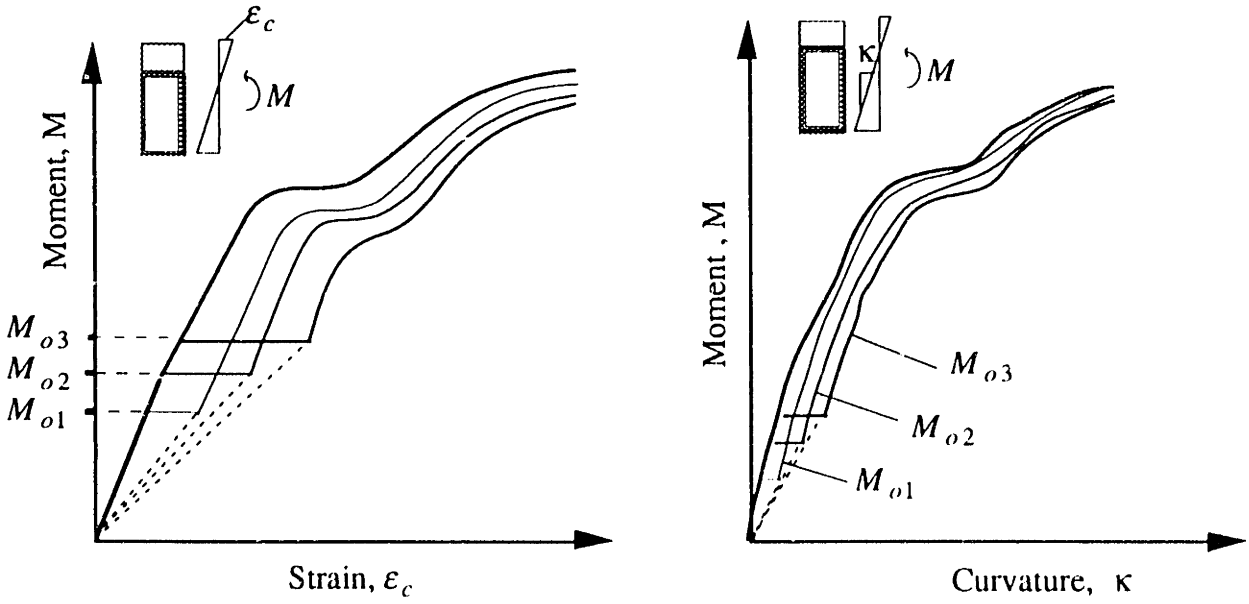

Figure 4.14 Moment-top strain and moment-curvature diagrams.

The deflections of the element for a given load can now be computed. The approach presented in Section 3.2.6 was implemented with an appropriate modification. During the integration of the internal work of virtual forces along the element's length, L, κ has to be picked from a different curve in the moment-curvature diagram for every cross section. First the moment M_{oi}^{x}, which the current cross section was subjected to during creep from sustained load, has to be found. From here the corresponding branch of the M-κ diagram is defined. Now given the current moment $M(x)$, the corresponding curvature $\kappa(x)$ can be determined. Since the M-κ data have only been computed for discrete values of M_{oi}, an interpolation has to be performed in order to get better accuracy. A weighted average was used to obtain the required curvature as follows:

$$\kappa(x) = \alpha\kappa_{oi}(M(x)) + (1-\alpha)\kappa_{oi-1}(M(x)) \tag{4.48}$$

where:

$$\alpha = \frac{M_{oi}^{x} - M_{oi-1}}{M_{oi} - M_{oi-1}} \tag{4.49}$$

is the weight factor. In Figure 4.15 the interpolation method is given graphically.

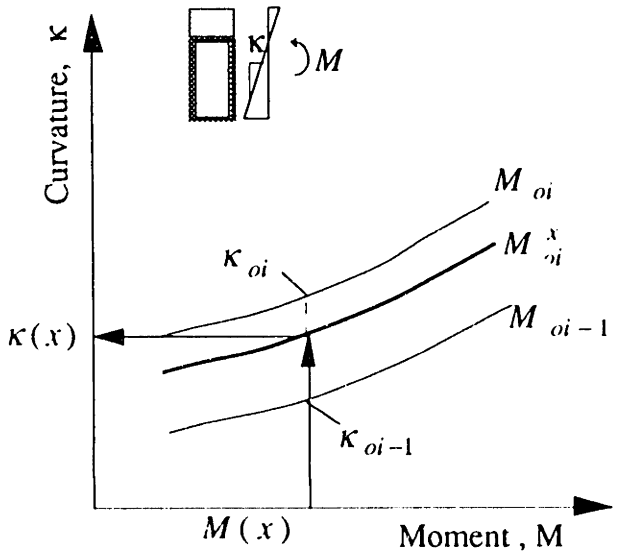

Figure 4.15 Determination of curvature using interpolation.

It should be noted that the curves for M_{oi} are also composed of discrete points and a second interpolation should be used to get the corresponding κ_{oi} values and achieve higher

precision. Both interpolations were implemented in the routine for the calculation of the curvature for a given moment.

Shear deformations can be computed using the same method as described in Section 3.2.6, where it is recommended to use the simplified approach since the computational effort becomes significantly large if the method of virtual forces is used. Shear creep has been accounted for in the GFRP-continuum theory model. Here, under the assumption of a constant Poisson's ratio, the matrix creep model affects the shear modulus of GFRP and therefore induces shear creep. On the other hand, shear creep in concrete was neglected in the analysis. The shear creep effect can be omitted for the calculation of deflections of long (aspect ratio > 5) beams subjected to bending, since the shear deflections are already an order of magnitude smaller than flexural ones (Sims et al. 1987). Also, any additional shear creep, represented as a fraction of the shear deflection, would result in very small values which can therefore be neglected. In general, if shear creep effects were to be considered, an analogous approach to the one for axial creep described earlier in this chapter can be implemented. The appropriate creep coefficients would have to be modeled from experimental data of shear strains and be used for the shear deflection calculation.

4.4 Fatigue

4.4.1 Introduction

Fatigue is a process of progressive permanent internal structural damage in a material subjected to repetitive stresses. Most engineering components are subjected to load histories that vary in time over their period of service and thus the subject of fatigue is an important topic to be considered when developing new structural elements. The reduction of stiffness and the subsequent failure of the hybrid member subjected to repeated loading is addressed and described in this section.

The short term behavior can be analyzed using classical mechanics to represent a fixed geometry and the consequences of applied loads or displacements. Controversially, in long term loading conditions the applied loads and other effects may vary with time, resulting in property changes due to fatigue processes occurring at the microscale. For many nonhomogeneous materials these micro-events control the degradation of properties and performance and have to be studied. However, the mechanisms causing these changes are fundamentally different for different materials and are extremely involving so that the application of an approach based on models at the micro-level for the analysis of the hybrid

beam described here, would not be appropriate. Other factors affecting the long term response are chemical changes occurring within the material mainly due to environmental exposure such as corrosion, oxidation and corrosion assisted cracking. The analysis associated with these effects goes beyond the subject of this work and will be omitted. Models which can be implemented are associated with the physics of the global material and while material properties are thought to be constant for short term behavior, they can be considered as variables and modeled appropriately for long term performance. This approach was used for the stiffness reduction calculation in this work. Another reason why analysis at the microscale is not necessary for the models required here deals with the fact that the failure of the hybrid system, if appropriately designed according to the procedure described in Chapter 3, should not be governed by fatigue failure of the constituents, but rather by stress redistribution due to stiffness loss and by exceeding the ultimate strains. The main interest is hence oriented towards the description of the response influenced by the stiffness reduction due to long term effects of the constituents and the residual strength remaining after a given loading history.

The fatigue behavior of the hybrid element was studied as a function of cyclic loading applied to the beam. The influence of the number of cycles to the member's response was evaluated and fatigue models for the constituent materials were described. The models for fatigue of concrete and GFRP were adopted from the literature, while it was assumed that the CFRP unidirectional CFRP lamina loaded uniaxially in the fiber direction is not affected by long term loading conditions. This was explained in detail in Section 4.3.3 under the assumption that carbon fibers are virtually fatigue neutral (Phillips 1989, Budelman et al. 1990).

4.4.2 Concrete Fatigue Model

A number of research studies have been conducted in the past to evaluate the fatigue characteristics of concrete (e.g., ACI 1974). The influence of applied stress level, number of cycles, loading frequency, environmental conditions, wave form of loading cycle, mix proportions and age range of concrete were investigated. All the models developed were basically empirical and lack of more fundamental knowledge of concrete behavior in fatigue is reflected in the few but often different codes and regulations which are available for design purposes. A common conclusion from several studies was that loading frequencies between 1 and 15 Hz has little effect on fatigue strength and stiffness degradation, provided that the maximum stress is less than 75 per cent of the static strength (ACI 1974). In this

work only the effects of stress level and cycle number have been considered since the investigation of other factors is beyond the scope of the subject discussed here.

In the analysis of the global fatigue response of concrete both creep and pure fatigue (endurance) induced effects have to be included. Unlike linear viscoelastic analysis where the stress level does not play an important role for the determination of the creep strains, in fatigue, where higher stresses can be expected, nonlinear viscoelasticity has to be implemented. This implies that an appropriate model for concrete fatigue needs to comprise a creep and an endurance part, both of which are dependent on the applied stress level; and while the former is a function of time, the latter is a function of the number of cycles.

The model adopted here was developed by Holmen (1982) who proposed a bifunctional relationship between the total strain and the number of cycles, where the long term strain, ε_{tot}, consists of two components, as given in the following equation:

$$\varepsilon_{tot} = \varepsilon_e + \varepsilon_{cr} \tag{4.50}$$

where ε_e is related to the endurance of the specimen and ε_{cr} is the time dependent strain and can be referred to as the creep deformation. Regarding the mechanism of creep under cyclic stress, a distinction should be made between behavior under small and under large ranges of stress. In the latter case, microcracking is probably involved to a large extent, at least in early stages. However, at low ranges of stress, the mechanism under cyclic stress is probably the same as that under a static stress, the effect of cycling being to accelerate creep. Holmen (1982) found that the total strain depends on the cycle ratio, which is defined as the quotient between the number of cycles, N, and the fatigue life, N_F. The analytical evaluation of experimental data showed that the distribution of fatigue lives at each stress level can be approximated with a log-normal one. Data for 5 Hz tests with a maximum stress level equal to 60 per cent of concrete strength resulted in the following relationship:

$$\log N_F = 2S_{\max}{}^{-3}(-\log L)^{0.06} \tag{4.51}$$

where L is the complement probability of failure (usually taken as 5%), $S_{\max}$ is the ratio between maximum stress applied during cycling and the concrete strength, f_c', and N_F is the required number of cycles to failure. The model further distinguishes three stages of strain development: (a) a rapid increase from 0 to 10% of total life; (b) a uniform increase from 10 to 80%; and (c) a rapid increase until failure, if failure takes place at all. Based on

test data for a 45 MPa concrete, the following expressions for the fatigue strain, ε_e, and the creep strain, ε_{cr}, per thousands were derived:

Stage one: $0 < (\frac{N}{N_F}) \leq 0.1$

$$\varepsilon_e = \varepsilon_o |1 + \frac{3.180}{S_{\max}}(1.183 - S_{\max})(\frac{N}{N_F})^{0.5}| \quad ; \quad \varepsilon_{cr} = 0.413 S_C{}^{1.184} \ln(t+1) \tag{4.52}$$

Stage two: $0.1 < (\frac{N}{N_F}) \leq 0.8$

$$\varepsilon_e = \frac{1.11\varepsilon_o}{S_{\max}}|1 + 0.677(\frac{N}{N_F})| \quad ; \quad \varepsilon_{cr} = 0.413 S_C{}^{1.184} \ln(t+1) \tag{4.53}$$

where ε_o represents the total strain (per thousands) in the first load cycle and S_C is the characteristic stress level, given as the sum of the mean stress, $S_m = (S_{\min} + S_{\max})/2$, and the root mean square value, *RMS*, defined as:

$$RMS = \sqrt{\frac{1}{T_o}\int_0^T \sigma^2(t)dt} \tag{4.54}$$

where $\sigma(t)$ is the stress as a function of time, t, and T_o is the total time, that is the duration of the cyclic loading. For sinusoidal loading with amplitude $S_{\max} - S_{\min}$ the *RMS* value is given by:

$$RMS = \frac{1}{2\sqrt{2}}(S_{\max} - S_{\min}) \tag{4.55}$$

The secant modulus of elasticity, E_c, is reduced during fatigue life. Applying the previous approach for the determination of the total strain and Hook's law the modulus of elasticity can be derived from:

$$E_c = \frac{\sigma_{\max}}{\varepsilon_{tot}} \tag{4.56}$$

where $\sigma_{\max}$ represents the maximum stress applied during cyclic loading.

The implementation of the fatigue model to the hybrid beam analysis is described next with some relevant issues. The whole iteration procedure is summarized in Figure 4.16, where part (a) gives the flow chart of the iteration algorithm and part (b) shows a schematic representation of the iteration process.

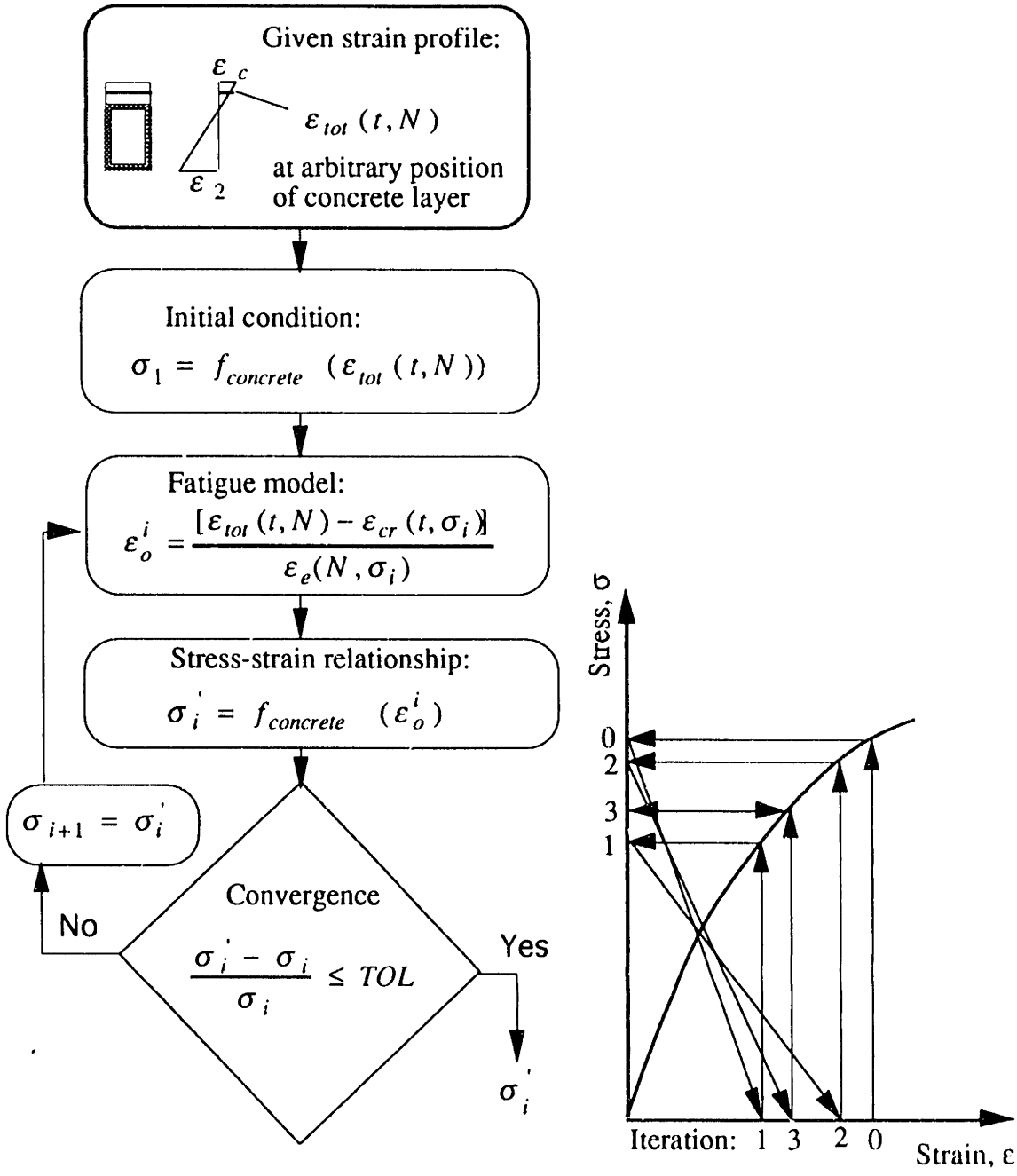

(a) (b)

Figure 4.16 Stress calculation with fatigue model: (a) iteration flow chart; (b) schematic representation of the iteration process.

The adopted fatigue models give the relationship between the total strain, ε_{tot}, and the initial strain, ε_o, the time in fatigue, t, the number of cycles, N, and the applied stress level, σ. Going back to the hybrid beam analysis and referring to Figure 3.7, in the computation of equilibrium of normal forces at the cross sectional level the associated normal stresses are obtained from a known strain profile. On the other hand, the strain profile itself, as a function of long term effects, is also dependent on the stress level applied. The model for the short term stress-strain relationship, as well as the model describing the fatigue response are both nonlinear and, in addition, they are coupled with each other. Therefore, an associated pair of stress and strain can be obtained only through iteration. This is carried out successfully in a computer routine. The basic guidelines are presented next.

The goal is to determine the stress level from a given strain magnitude if the long term parameters (t, N) are known. First, for a given fatigue strain, $\varepsilon_{tot}(t,N)$, an initial stress level has to be assumed. A good initial estimate is obtained by using the short term stress-strain relationship, which was defined earlier in Chapter 3:

$$\sigma_1 = f_{concrete}(\varepsilon_{tot}(t,N)) \tag{4.57}$$

The initial strain, ε_o^i (the superscript i indicates the iteration step), that is the one that would have occurred in the first cycle, for a given fatigue strain, $\varepsilon_{tot}(t,N)$, can be found from the fatigue model adopted for a given material:

$$\varepsilon_o^i = \frac{\left[\varepsilon_{tot}(t,N) - \varepsilon_{cr}(t,\sigma_i)\right]}{\varepsilon_e(N,\sigma_i)} \tag{4.58}$$

where ε_{cr} and ε_e were defined earlier with equations (4.52) and (4.53) representing creep and fatigue, respectively, and σ_i is the assumed stress level. Substituting this stress with the value from equation (4.57) the initial strain, ε_o^1, in the first iteration step is obtained:

$$\varepsilon_o^1 = \frac{\left[\varepsilon_{tot}(t,N) - \varepsilon_{cr}(t,\sigma_1)\right]}{\varepsilon_e(N,\sigma_1)} \tag{4.59}$$

This strain is used in the short term static stress-strain relationship for the material considered to compute the associated stress:

$$\sigma_1^{'} = f_{concrete}(\varepsilon_o^1) \tag{4.60}$$

In order for the analysis to hold, this value has to be equal to the initially assumed σ_1. If this is the case, a valid stress level corresponding to the fatigue strain $\varepsilon_{tot}(t,N)$ is obtained, otherwise another iteration step is required. For the next iteration step, $\sigma_{i+1} = \sigma_i^{'}$ is used until convergence is reached. The convergence criterion adopted here is of the standard form:

$$\frac{\sigma_i^{'} - \sigma_i}{\sigma_i} \leq TOL \tag{4.61}$$

where the tolerance, TOL, is set to a small value.

4.4.3 GFRP Fatigue Model

Damage events which occur in progressively localized regions of a composite laminate cause changes in load paths through the material and in the load carrying ability of the material around the damaged zone. The result is an increase in the global engineering compliance of the laminate. Changes in the cyclic stress and strain behavior of the composites are related to various damage mechanisms. These can be divided into three groups including: (a) fracture of reinforcing fibers; (b) failure at the interface between fibers and matrix; and (c) failure modes associated with matrix damage. The first two mechanisms are activated close to the fatigue failure of the composite, while the third one is greatly affecting the stiffness reduction at earlier stages of fatigue life. The proposed FRP/concrete member concept can be classified into deformation limited, or stiffness critical structures, since for large strains the time-independent component (CFRP laminate) is likely to fail before fatigue strength limits are reached. Therefore, the fatigue model for GFRP of interest for the analysis presented here should focus on the stiffness reduction occurring before the fatigue life of any component is exhausted. This implies that models evaluating the damage mechanisms of the matrix are to be considered. The effects of delamination, fiber breakage or splitting of layers are disregarded since they appear to have much less influence at earlier fatigue life stages.

In this section two methods for the stiffness reduction of GFRP are discussed. The first is purely empirical, adopting a model proposed by Ogin et al.(1985) for which the required parameters were calibrated with results obtained from coupon tests in fatigue. The

second deals with the description of the fatigue response through continuum theory and known fatigue behavior of the unidirectional composite layers. Both models incorporate a functional dependence of the response to the applied stress level and the number of cycles as well as nonlinear viscoelasticity for creep effects. The two models will be presented next.

4.4.3.1 Empirical GFRP Fatigue Model

In this model it is assumed that matrix cracking is a principal cause of stiffness reduction in laminated composites loaded either in fatigue or quasi-statically. In fatigue, the stiffness falls gradually as the density of matrix cracks increases during cycling. Poursartip et al. (1982) analyzed curves of the stiffness reduction with cycles for a (0/90) GFRP laminate at different load levels and showed that the slope of these curves was proportional to a power law of the peak stress. Ogin et al. (1985) used an approach assuming a linear relationship between elastic modulus and crack density as well as the total crack length as a power function of the stored elastic energy. They created a model where the change in stiffness of GFRP due to cycling is proportional to the maximum stress level applied, σ_{max}, as follows:

$$-\frac{1}{E_o}\frac{dE}{dN} = A\left[\frac{{\sigma_{max}}^2}{{E_o}^2(1-E/E_o)}\right]^n \tag{4.62}$$

where A and n are constants which have to be obtained from least square fits to experimental data and E_o is the uncracked elastic modulus of the composite. A schematic stiffness reduction curve obtained from experimental readings is given in Figure 4.17.

The curve can be divided into three regimes: an initial rapid reduction in modulus followed by a much slower reduction, until a final rapid fall-off just prior to failure. The modulus reduction rate, $-\frac{1}{E_o}\frac{dE}{dN}$, at a given value of E/E_o is simply the tangent to the curve at that value of E/E_o. A convenient approach to calibrate the parameters A and n is to use a log-log diagram of stiffness reduction data for different stress levels and fit a straight line as shown in Figure 4.18.

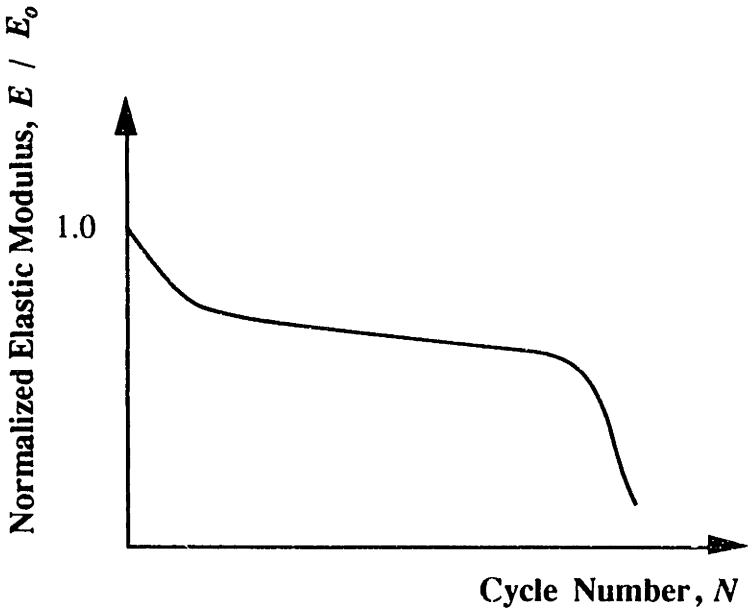

Figure 4.17 Stiffness reduction curve of GFRP laminates.

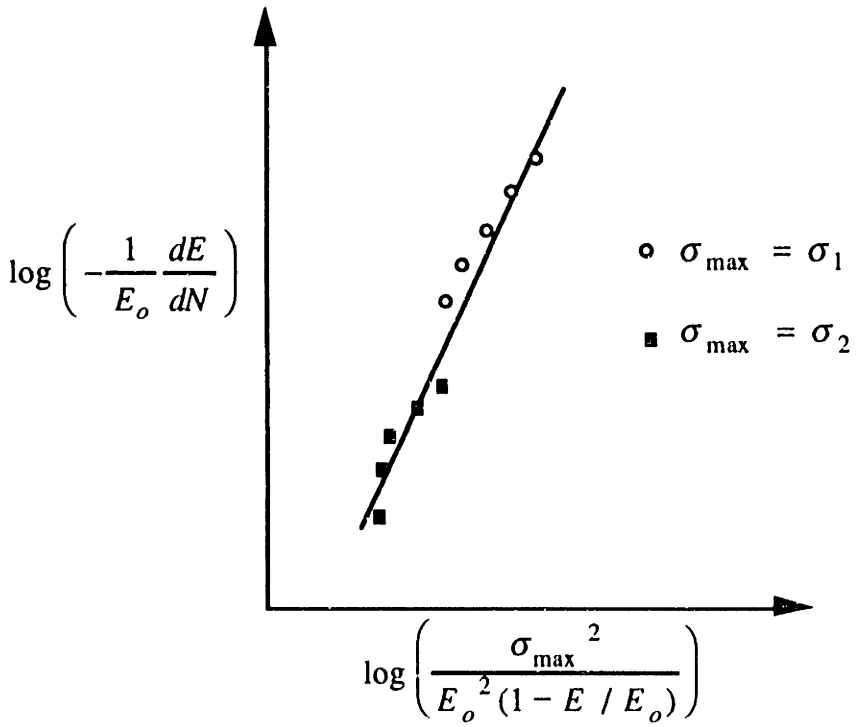

Figure 4.18 Modulus reduction rate in log-log scale.

Integrating equation (4.62) the relationship between the ratio of the current value of the modulus, E, and the initial one, E_o, the cycle number, N, and the maximum stress, σ_{max}, is given with:

$$\phi(N,\sigma) = \frac{E}{E_o} = 1 - [(n+1)A]^{\frac{1}{n+1}} \left[\frac{\sigma_{max}}{E_o}\right]^{\frac{2n}{n+1}} N^{\frac{1}{n+1}} \tag{4.63}$$

where $\phi(N,\sigma)$ represents a stiffness reduction factor taking the effect of stress level and cycle number into account. The strain resulting from the stiffness reduction is increased and can be expressed with:

$$\varepsilon_g(\sigma,N) = \frac{1}{\phi(N,\sigma)}\varepsilon_o \tag{4.64}$$

where ε_o is the initial strain generated by the stress σ_{max} in the first load cycle, obtained from the static (short term) stress-strain relationship defined in Chapter 3.

Expanding the model's application to the hybrid beam analysis, the reversed process of finding stresses from known strains has to be solved for. Similarly to the concrete fatigue model described in the previous section, in order to find the associated stress to a given strain value, ε_g, for a known cycle number, N, an iterative procedure has to be implemented. The iteration is required to find the stress level σ_{max} satisfying equilibrium of the following equation:

$$\varepsilon_g = \frac{1}{\phi(N, f_{GFRP}(\varepsilon_o))}\varepsilon_o \tag{4.65}$$

where f_{GFRP} is a function defining the static stress-strain relationship for the element considered. This functional dependence was described in Section 3.2.3. The scheme for the solution of equation (4.65) was already given in Figure 4.16 if the fatigue model given there is substituted with $\varepsilon_o^i = \varepsilon_g \phi(N,\sigma_i)$ and the stress-strain relationship with f_{GFRP}. In the analysis for the fatigue behavior of the hybrid beam this procedure was performed within a computer routine. Convergence of the iterative procedure does not need to be demonstrated mathematically since in the case of a convex short term stress-strain relationship the solution is warranted. The convergence was shown schematically in Figure 4.16(b). Problems might occur with convergence when the solution of equation (4.65) lies within the failure region of the GFRP. In this case the iteration step should be

chosen as $\sigma_{i+1} = (\sigma_i + \sigma_i^{'})/2$. On the other hand, it is not likely for the stress levels to be in this region for real-life applications.

In the previous analysis and calibration of the fatigue parameters A and n, the effect of viscoelastic behavior was not considered, because it was assumed that the stiffness reduction versus number of cycles curves were obtained from measurements which excluded creep. This can be accomplished by setting the displacement gauge reading back to zero every time before taking data for a particular number of cycles. In practice, creep can not be avoided and therefore viscoelastic strains have to be included in the calculations. Then, equation (4.64) becomes:

$$\varepsilon_g(t,\sigma,N) = \frac{1}{\phi(N,\sigma)}\varepsilon_o + \varepsilon_{creep}(t,\sigma) - \varepsilon_o \tag{4.66}$$

where $\varepsilon_{creep}(t,\sigma)$ is the creep strain which was given by equation (4.10) and (4.11) for linear and nonlinear viscoelasticity, respectively. In the latter case the stress level has to be used for the creep model, and is obtained as the sum of the mean stress during cycling and the root mean square value *RMS* defined by equations (4.54) and (4.55).

4.4.3.2 Continuum Theory Approach

The fatigue model developed here is based on the theory established for the analysis of composites in static loading configurations, expanded to predict the stiffness and deformation pattern of GFRP during cyclic loading. The assumptions required for the continuum theory to hold are: (a) perfect compatibility between fibers and matrix as well as between single layers is satisfied; (b) the matrix contributes to the carrying capacity; and (c) the composite is made of single homogenous orthotropic or isotropic layers. In Section 4.3.3.2 the continuum theory has already been described and used to evaluate the creep response of GFRP. The main objective there was to derive a simple model for the behavior of the constituent elements (basic unit) and then use this result to predict the overall response of the composite element. In this context, a creep model for the matrix was implemented to analyze the creep of a multilayered composite. In the fatigue model presented here, though, the unidirectional layer was used instead, as the basic unit, and the resulting model was incorporated for the fatigue analysis of GFRP.

It was mentioned earlier that the model has to focus on the description of the stiffness reduction of the composite material, since this is the crucial aspect of fatigue

damage in case of the hybrid beam design. Bitterli (1987) investigated the influence of cyclic loading on the response of unidirectional GFRP laminates. From a large series of experimental data he found that all of the elastic material properties, including the elastic moduli in both directions, $E_{\parallel}$ and $E_{\perp}$, and the Poisson's ratios, $\nu_{\parallel\perp}$ and $\nu_{\perp\parallel}$, do not change significantly when loaded with cyclic loading, except for the shear modulus, $G_{\#}$, which was found to be dependent on both cycle number and stress level. It is believed that the shear stiffness reduction is due to damage of the matrix. A two variable least squares surface fit to this experimental data was attempted with the following simple relationship:

$$G_{\#} = G_{\#}^{o}\left[f_1(\tau) - f_2(\tau)\log(N)\right] \tag{4.67}$$

where $G_{\#}^{o}$ is the static initial shear modulus, $f_1(\tau)$ is a function describing the nonlinear character of the $\tau - \gamma$ diagram for unidirectional GFRP composites, with τ being the maximum stress amplitude applied during cycling, and $f_2(\tau)$ is a function describing the stiffness reduction caused by the cycle number, N. A typical configuration of the surface described here is given in Figure 4.19.

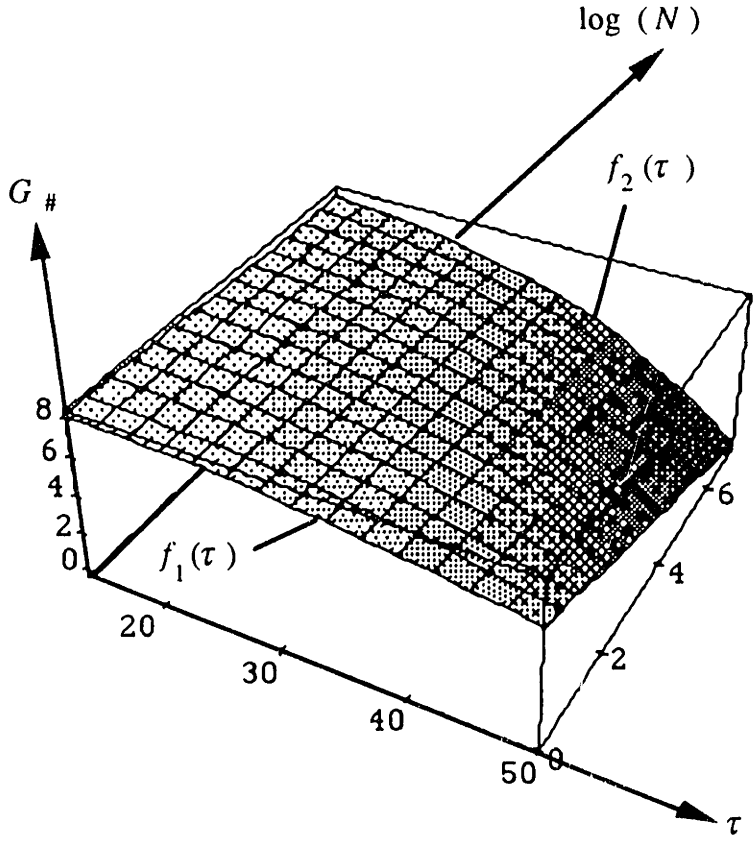

Figure 4.19 Shear modulus as a function of cycle number and stress level.

It is seen that the shear modulus reduction due to cycle number follows a linear pattern in logarithmic scale and that the stress amplitude amplifies this effect exponentially. At higher stress levels and/or cycle numbers, that is close to fatigue failure, significant nonlinearity is observed, which is not of concern for the response of the hybrid beam because the prime effect of fatigue is stiffness reduction.

The experiments performed by Bitterli (1987) were carried out using specimens with the same volume fraction, matrix and fiber properties as the ones used for the GFRP box beams tested in this work. Therefore, the application of his results can be justified. The variation analysis fitting experimental data to equation (4.67) gave the following result:

$$f_1(\tau) = 1 + 0.00015\ \tau - 0.00012\ \tau^2 + 1.37e-7\ \tau^3 \tag{4.68}$$

and

$$f_2(\tau) = 0.002\ e^{0.08\,\tau} \tag{4.69}$$

The error was about 2%, which gives reasonable approximations to test results. The derivations given earlier in Section 4.3.3.2 describing the continuum theory approach can be used for the fatigue analysis too. In fact, all the equations (4.13) to (4.41) are valid, and the fatigue effect is accounted for by modifying only equation (4.17) in agreement with the fatigue model defined in equation (4.67). The equation for the shear modulus of the unidirectional laminate is then given by:

$$G_{\#}(t, N, \tau) = G_M(t)\frac{1 + 0.60{V_F}^{0.5}}{V_F\dfrac{G_M(t)}{G_F} + (1 - V_F)^{1.25}}\left[f_1(\tau) - f_2(\tau)\log(N)\right] \tag{4.70}$$

It should be pointed out that the above analysis is quite general, and includes both the model for creep and the one for fatigue at the same time. Moreover, the resulting average engineering elastic constants across the multilayered laminate are a function of three parameters: time, t, number of cycles, N, and maximum stress level, τ. Here, the stress amplitude τ has to be derived from the global stress acting on the composite. For a composite with $\pm 45°$ fiber orientation and symmetrical layer buildup this relation can be obtained directly using Mohr's theory. In the general case Mohr's theory gives the transformation equations for plane stress as follows:

$$\tau_\theta = -\frac{\sigma_{xy}}{2}\sin 2\theta + \tau_{xy}\cos 2\theta \tag{4.71}$$

where σ_{xy} and τ_{xy} are the normal and shear stresses resulting from the external loads, respectively. In the case of the hybrid beams this implies that the shear stress, τ_θ, for the GFRP layers oriented at $\theta = \pm 45°$ is obtained directly from the normal stress with $\tau = \sigma / 2$, which is also shown in Figure 4.20. For other fiber directions continuum theory has to be used to transform the stress state. Considering the continuum theory result, it is also interesting to note that while the global elastic constants $\overline{E}_x, \overline{E}_y$ and $\overline{\nu}_{xy}$ are functions of t, N, and τ, the shear modulus, $\overline{G}_{xy}$, of the $\pm 45°$ composite is not affected by a change of the unidirectional laminate shear modulus, $G_\#$, and hence is only a function of time and the creep model. This can be observed in equation (4.28) where the stiffness component $d_\#$ cancels out.

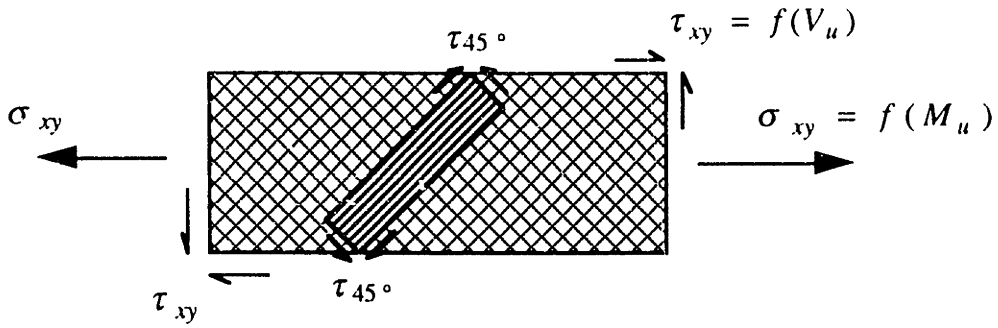

Figure 4.20 Shear stresses in GFRP layer.

The total strain of a GFRP laminate, $\varepsilon_g(t,N,\tau)$, can be derived from the global elastic modulus, $\overline{E}_x$, and the initial strain generated during the first load cycle, ε_o^g, with:

$$\varepsilon_g(t,N,\tau) = \varepsilon_o^g \frac{E_o^g}{\overline{E}_x(t,N,\tau)} \tag{4.72}$$

Referring to the analysis of the hybrid beam, the stress associated with a particular total strain, ε_g, can be found from the initial strain, through the static short term stress-strain relationship for the material. But since the stress has to be known apriori in order to obtain the proper elastic modulus, $\overline{E}_x$, an iterative procedure, similar to the one described earlier in the empirical GFRP fatigue model, has to be implemented. The iteration is required to find the stress level, σ_{max}, satisfying equilibrium of the following equation:

$$\varepsilon_o^g = \varepsilon_g \frac{\overline{E}_x(t,N,f_{GFRP}(\varepsilon_o^g)/2)}{E_o^g} \tag{4.73}$$

where f_{GFRP} defines the static stress-strain relationship as described in Section 3.2.3. The scheme for the solution of the iteration procedure was given in Figure 4.16, where the fatigue model should be substituted with equation (4.73), and the stress-strain relationship with f_{GFRP}. In the analysis for the fatigue behavior of the hybrid beam this procedure was performed within a computer routine.

4.4.4 Fatigue Analysis of Hybrid Beam

The analysis of the hybrid element is analogous to the time dependent analysis described in Section 4.3.4. Using the models for the characterization of fatigue behavior of concrete and GFRP the effect of cycle number was investigated. Since in practical applications the viscoelastic deformations can not be excluded during fatigue loading, the material models adopted include creep strains. Unlike in sustained (creep) loading configurations where it is assumed that the material properties were linearly dependent on the stress level applied and linear viscoelasticity was adopted, during fatigue the nonlinear dependence of the response to stress amplitudes has to be considered.

The design of the hybrid beam is conceptualized in such a manner that the stiffness reduction due to fatigue effects is governing for the failure of the member. In fact, due to the softening of the two constituents, concrete and GFRP, the third one, CFRP, which is idealized as fatigue neutral, is increasingly stressed with the number of cycles. At a certain point of cyclic loading the CFRP ruptures, reaching its ultimate strain, and sensors a warning. The deformations increase producing further energy dissipation but collapse of the member is still not imminent. The remaining GFRP box and concrete layer give a sufficient safety margin for repair or other measures. Hence, the analysis of the fatigue response only up to CFRP failure is crucial for the designer and fatigue induced damage beyond this stage is not of concern in this work. What is of interest is the remaining strength of the partially damaged element.

The calculations were performed within a computer program based on the procedure described for the analysis of the viscoelastic behavior in Section 4.3.4. The main routine contains a loop over both number of cycles and elapsed time. If the frequency is constant these two values are related by:

$$N = 3600\, f\, t \tag{4.74}$$

where t is time in hours and f is the frequency in Hz.

First, the equilibrium at the cross sectional level was analyzed. Starting at a low top fiber strain a routine incremented the bottom fiber strain until equilibrium of normal forces was obtained. For each incremental strain profile the strains at discrete points of the cross section were calculated. Five and ten discrete points were used across the concrete layer and the GFRP web, respectively, while one value was sufficient for the GFRP top and bottom flange. For each of these strains the associated initial strain was computed from the corresponding fatigue and creep model. An iterative procedure was required here since the fatigue creep is nonlinearly dependent on the applied stress level. This was shown in Figure 4.16(b). Once the initial strain was found, the associated stress was calculated directly from the corresponding static stress-strain relationship. After the stresses at all points were defined, the normal forces were calculated and equilibrium of the cross section checked. If it was not satisfied the strain profile was incremented to the next position until the equilibrating state was reached. Knowing the normal force distribution, the moment capacity of the section was calculated and stored with the obtained curvature. The top fiber strain was then incremented and a new equilibrating strain profile was found, until a moment capacity exceeding the actual (imposed by external cyclic forces) was obtained. If small top fiber strain increments are used, good approximations can be obtained. In this work, a top fiber strain increment of 0.01‰ was used and showed good results. If higher precision is needed, iteration of the top fiber strain can be performed.

The second part analyzes the deflections from moment and curvature data obtained in the first. The procedure was described in Chapter 3 and is fully applicable. Finally, the analysis was repeated for the next time and/or cycle number until a failure mode is reached. At this point it should be mentioned that throughout the analysis it needs to be constantly checked whether any of the failure modes were encountered during the incrementation procedure, and if this was the case the appropriate action has to be taken. For proper design, CFRP failure should take place first, but the member should still be able to carry the same load, after which remedies can be carried out. This will be automatically carried out in the computer program since all the checks were defined already for the short term analysis and are still implemented for this part of the fatigue analysis. Table 4.2 shows the flow of the computational procedure implemented for the analysis of fatigue behavior.

Table 4.2 Procedure for fatigue analysis of the composite beam.

Step #	Description of computation or action performed	Variables involved
1	Data input.	Material and geometric properties
2	Start loop over time and number of cycles, initial values: $t=0$ $N=1$	t,N
3	Assume an initial top fiber strain. 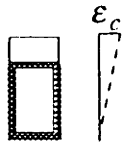	ε_c
4	Start loop incrementing bottom fiber strain. 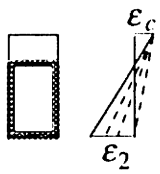	ε_2
5	Calculate the strains across the strain profile.	ε_x
6	Start iteration loop over stress level applied, find the corresponding initial strains from corresponding fatigue models. Index i defines iteration.	σ_i , ε_o^x
7	Call the routines describing the stress-strain relationship and get the stress associated with ε_o^x. Compare with σ_i. Go back to step 6 until convergence reached.	σ_i'
8	Call the routine for stress integration and normal forces in cross section.	F_{XX}
9	Call routine for the calculation of the sum of normal forces and check if cross section is in equilibrium at this strain profile.	$\sum F_{XX} = 0$
10	If yes continue, otherwise go back to step 4 and find new strain profile.	
11	Calculate the external moment equilibrating the section and store the curvature. Index i defines this strain profile. 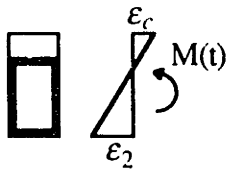	$M_i(t)$, $\kappa_i(t)$
12	Compare the applied sustained moment, M_o, to $M_i(t)$. If larger continue, otherwise go to step 15.	
13	Increment the top fiber strain and go back to step 3.	$\varepsilon_c + \Delta\varepsilon_c$
14	Call the function to calculate the deflections and call the printout routine.	v
15	Increment t and N to next value and go back to step 3.	$t + \Delta t$ $N + \Delta N$

4.4.5 Residual Strength after Fatigue

The short term strength of a hybrid member which was subjected to a cyclic loading history represents its residual strength. The analysis to be performed here is a expansion of the residual creep analysis which was described in detail in Section 4.3.5. Apart from the creep deformations, the member is here additionally deformed due to the fatigue stiffness reduction. The changes of the stress state and the strain increase in the element are even more significant and the likelihood of failure is even greater.

The procedure for the analysis consists of two parts. The first includes the fatigue analysis for known cycle number, time and externally applied loads, giving a new deformed state of the member. The strain profile is defined from here and the portions of it produced by creep, stiffness reduction and elastic deformations are distinguished. The second part involves a short term analysis, for which the results from the previous stage represent an initial state and which has to be carried out in order to determine the ultimate loading capacity until a failure mode is reached. The analysis in the first part complies with the one presented in the previous section and all the material models, short and long term, are still valid. The assumption on the ultimate strains being constant regardless of the loading history, made in Section 4.3.5, is also adopted here.

The only new feature of the analysis developed here, is related to the short-term response after the material has already been subjected to a known loading state which is referred to as the residual response. In order to predict the residual response it is necessary to go back to the derivation of the total strain of a material which was subjected to cyclic stresses. In general it can be concluded that the total strain is comprised of three components: (a) the short term strain, ε_{st}; (b) the strain due to creep, ε_{cr}; and (c) the fatigue strain, ε_{fat}. Schematically, this is represented in Figure 4.21.

The model adopted for the residual response assumes that the short term strain moves along the short term response curve, the creep strain remains constant at the value generated during the loading history, ε_{cr}, and the fatigue strain increases linearly as a function of the short term strain. This last consideration is based upon the fact that due to cycling a stiffness reduction of the material has occurred defining a new secant modulus whose ratio to the short term modulus remains constant during residual response. This assumption can be represented numerically with the following equation for the total strain in residual response (see Figure 4.22):

$$\varepsilon_x(t,N) = \varepsilon_o^x + \varepsilon_{cr}(t) + \frac{\varepsilon_{fat}(N)}{\varepsilon_{st}}\varepsilon_o^x \tag{4.75}$$

where ε_o^x represents the short term response, ε_{st} is the short term strain during cycling depending on the applied stress level, $\varepsilon_{cr}(t)$ is the final creep strain due to the sustained characteristic stress level (see Section 4.4.2) depending on the creep model used, and $\varepsilon_{fat}(N)$ is the fatigue strain due to cyclic loading, defined with the fatigue model. It should be noted that the values for ε_{st}, $\varepsilon_{cr}(t)$ and $\varepsilon_{fat}(N)$ were obtained in the first part of the analysis and had to be stored for each integration point (5 points for concrete and 10 for the GFRP webs) along the beam's cross section in order to be used for the residual strength analysis. They are considered to be constants for the residual response, independent of stress. The computational procedure required for the determination of residual stresses at any point along the hybrid beam's cross section is analogous to the one described in detail in Section 4.3.5 and can be adopted almost identically.

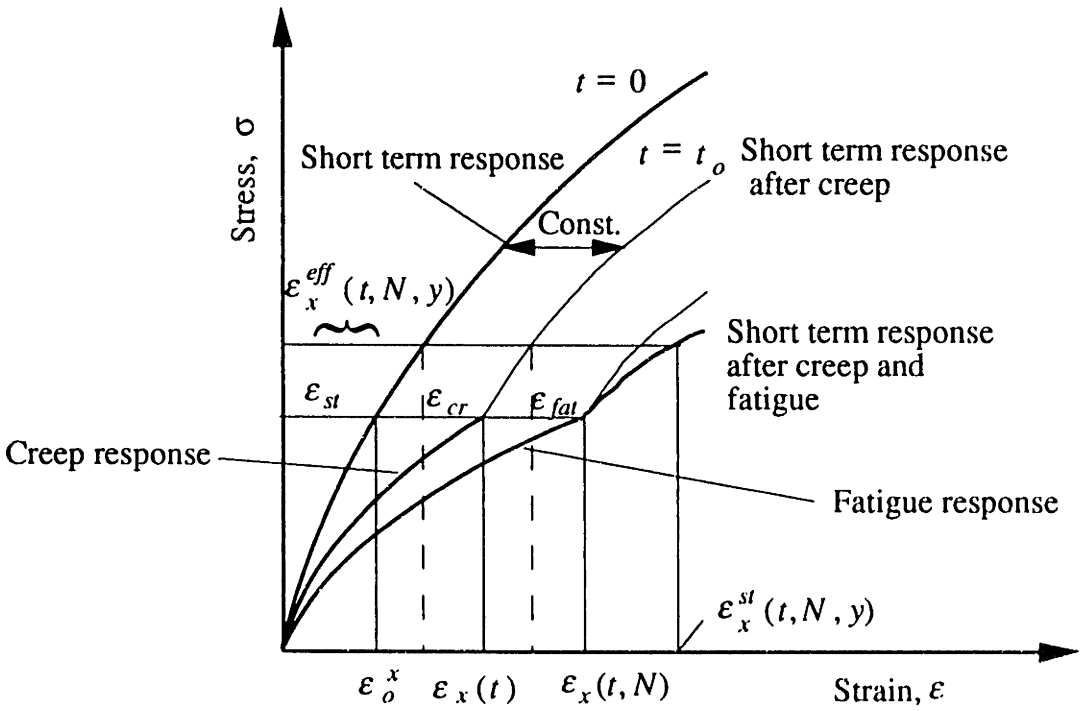

Figure 4.21 Stress-strain relationship for residual response.

The only modification is required when the effective strain is calculated from the actual strain since there is an additional term involving fatigue strains and all the variables

are functions of both time and number of cycles. Therefore equation (4.45) has to be transformed to:

$$\varepsilon_x^{eff}(t,N,y) = \frac{1}{\left[1+\frac{\varepsilon_{fat}(N)}{\varepsilon_{st}}\right]}\left[\varepsilon_x^{st}(t,N,y) - (\varepsilon_{cr}(t)\right] \tag{4.76}$$

where $\varepsilon_x^{st}(t,N,y)$ is the actual residual strain and $\varepsilon_x^{eff}(t,N,y)$ is the effective strain used for the stress calculation as defined with equation (4.47). For a more precise analysis, where the number of discrete integration points could be arbitrarily increased, the effective strain, $\varepsilon_x^{eff}(t,N,y)$, can be calculated from the known strain profile after N cycles and time t with the following relation:

$$\varepsilon_x^{eff}(t,N,y) = \phi\left[\varepsilon_x^{st}(t,N,y) - \varepsilon_x(t,N,y)\frac{\phi(\varphi-1)}{1+\phi\varphi-\phi}\right] \tag{4.77}$$

where $\varepsilon_x(t,N,y)$ represents the total strain at time t and after N cycles at location y and is calculated from equation (4.46) (see also Figure 4.10), $\varepsilon_x^{st}(t,N,y)$ is the actual residual strain, and ϕ <1 and φ >1, are the stiffness reduction and creep coefficients, respectively. They depend on the model adopted for the long term analysis, the material involved and the stress level which was acting during long term loading at the location y. The stiffness reduction coefficient was defined for GFRP by equation (4.64) and (4.72) for the empirical and the continuum theory, respectively. For concrete this coefficient is defined as the ratio of the initial strain and the endurance strain, $\varepsilon_o / \varepsilon_e$ which can be derived from equations (4.52) or (4.53). The creep coefficient for concrete is defined with $\varepsilon_o / \varepsilon_{cr}$ from the same equations. For GFRP the creep coefficient was defined as the ratio of the total strain to the initial strain, $\varepsilon_g / \varepsilon_o$, using equations (4.10) and (4.42) for the empirical and the continuum theory model, respectively.

4.5 Temperature

Whenever different materials are combined into structural elements temperature oscillations introduce changes in the stress and strain distributions. Since each material has a different thermal expansion coefficient the deformations resulting from a temperature change also vary. This is of particular interest for the analysis of the hybrid beam

presented in this study. Several aspects of temperature induced effects have to be considered. First, in order to equilibrate the internal forces and satisfy compatibility , the analysis of the hybrid member has to be adjusted to account for temperature changes. Second, temperature introduces shear stresses at the interface between different constituents (such as the concrete-GFRP and the GFRP-CFRP interface), and the magnitude of these stresses needs to be evaluated.

Further, temperature generates residual interlaminar stresses between the differently oriented fibers across the thickness of the GFRP box beam. During temperature increase the resulting stresses in the matrix are compressive and inversely, they are tensile during temperature drop. For instance, for typical fiber volume fractions of 0.5 to 0.7 and a temperature drop of 50°C, the stresses are in the range of 5 MPa (Meier 1990). Since these values lie well below the ordinary stress levels introduced with external forces and the temperature changes expected in practice are relatively small ($\approx$ 50°C), the residual stresses within and between the GFRP layers can be neglected in the analysis of the hybrid beams.

Controversially, the influence of temperature on the overall response of the hybrid member is important and is discussed here. The analysis developed earlier for short term and creep response is modified and the temperature effect is incorporated. Also, the interface stresses at the GFRP-CFRP bond are investigated since significant differences in the thermal expansion coefficients between the two materials are anticipated. On the other hand, since the thermal expansion coefficients of concrete and GFRP are relatively close, small shear stresses are expected in the concrete-GFRP interface, and, therefore, the latter are not considered.

Temperature also affects the long term response of materials (and especially plastics). In practice, accelerated creep tests on FRPs are performed by introducing high temperatures. This effect is not significant with low temperature ranges, which are expected to be encountered in the application of hybrid beams, and were thus, also neglected in the analysis implemented here.

4.5.1 Thermal Expansion Coefficients of Constituting Materials

The thermal expansion coefficients of three different materials were used for the analysis of hybrid beams under thermal loading. First, the thermal characteristics of concrete are described. The main factors affecting the value of the thermal expansion coefficient of concrete are the type and amount of aggregate, as well as the moisture content. Other factors, such as mix proportions, cement type and age influence its

magnitude to a lesser extent. Since the total aggregate content in hardened concrete varies from 65 - 80 % and the elastic modulus of aggregate is generally five times that of the hardened cement component, the rock expansion coefficient dominates in determining the expansion of the composite concrete. Assuming the distribution of aggregates to be uniform, it can be assumed that the thermal expansion coefficient of concrete is isotropic. Standard lower and upper bound values for concrete are in the range between 0.85 and 1.2×10^{-5} 1/°C (ACI 1971). The latter value was adopted for the analysis presented here.

From the composition of FRPs it is evident that substantial anisotropy in mechanical behavior is to be expected. A method to quantify the mechanical anisotropy of FRPs was presented in Section 4.3.3.2 where the properties of unidirectional FRP layers were derived from known properties of the fibers and the matrix. Such anisotropy, although to a smaller extent, characterizes thermal behavior, too.

Given the elastic moduli, Poisson's ratios and thermal expansion coefficients of the fibers and the matrix, the thermal expansion coefficient of the unidirectional layer parallel, $\alpha_{\|}$, and perpendicular, $\alpha_{\perp}$, to the fiber orientation can be obtained through the following relations (Schneider 1971):

$$\alpha_{\|} = \alpha_{F\|} + \frac{\alpha_M - \alpha_{F\|}}{\frac{V_F E_{F\|}}{(1-V_F)E_M} + 1} \tag{4.78}$$

$$\alpha_{\perp} = \alpha_M - (\alpha_M - \alpha_{F\perp}) \left[\frac{2(\nu_M^3 + \nu_M^2 - \nu_M - 1)1.1V_F}{1.1V_F(2\nu_M^2 + \nu_M - 1) - (1+\nu_M)} - \frac{\nu_M E_{F\perp}/E_M}{E_{F\perp}/E_M + (1-1.1V_F)1.1V_F} \right] \tag{4.79}$$

where $\alpha_{F\|}$ and $\alpha_{F\perp}$ are the thermal expansion coefficients of the fibers in the fiber direction and perpendicular to it, respectively; $E_{F\|}$ and $E_{F\perp}$ are defined in an analogous mannerr for the elastic modulus of the fibers. All other parameters were defined earlier in Section 4.3.3.2. Unlike glass fibers, carbon fibers show large anisotropy in both the elastic and the thermal properties. Typically, the elastic modulus in the fiber direction is 1000 - 3000 times larger than the one in the perpendicular direction.

When unidirectional layers of FRP are compounded into a multilayered composite, the thermal expansion coefficients need to be transformed into global coordinates. The following equation gives this transformation:

$$\alpha_{x\theta} = \alpha_{\|} \cos^2\theta + \alpha_{\perp} \sin^2\theta \tag{4.80}$$

where θ is the angle between the fiber direction of the unidirectional layer and the global axis. Given the material properties of the fibers and the matrix, the thermal expansion coefficients can be determined as a function of the fiber volume fraction. For instance, using the material properties given in Table 4.3, Figure 4.22 was obtained. Here, the thermal expansion coefficients of a ±45° GFRP and a unidirectional CFRP are plotted as a function of the fiber volume fraction.

Table 4.3 Material properties for the calculation of thermal expansion coefficients.

	Elastic modulus, parallel [MPa]	Elastic modulus, perpendicular [MPa]	Poisson's ratio [-]	Coefficient of thermal expansion, parallel [10^{-5}/°C]	Coefficient of thermal expansion, perpendicular [10^{-5}/°C]
Matrix	4000		0.35	6.8 - 7.0	
Glass fiber	72000		0.22	0.5	
Carbon fiber	440000	≈ 500	0.28	-0.26	4.3

It is seen that the thermal expansion coefficient of GFRP is very close to that of concrete for high fiber volume fractions, and hence the assumption of small shear stresses at the concrete-GFRP interface is verified in this particular case. It should be pointed out that in the general case, for other fiber orientations, material properties or volume fractions, the shear stresses at the interface might be more significant and need to be checked. At the same time (assuming from Figure 4.22 the CFRP volume fraction to be ≈70%), the largest difference in the thermal expansion coefficient is found between GFRP and CFRP in the perpendicular direction. It is also noted that the thermal expansion coefficient of CFRP in the fiber direction is very insensitive to fiber volume fraction variations. This is generally true for unidirectional composite laminates. Although usually larger differences between the thermal expansion coefficient of GFRP and CFRP in the longitudinal direction are to be expected, for the case of ±45° GFRPs and high fiber volume fractions these differences are relatively small. Therefore, only the interface stresses in the lateral direction were considered here, but at the same time the analysis given is applicable to the general case.

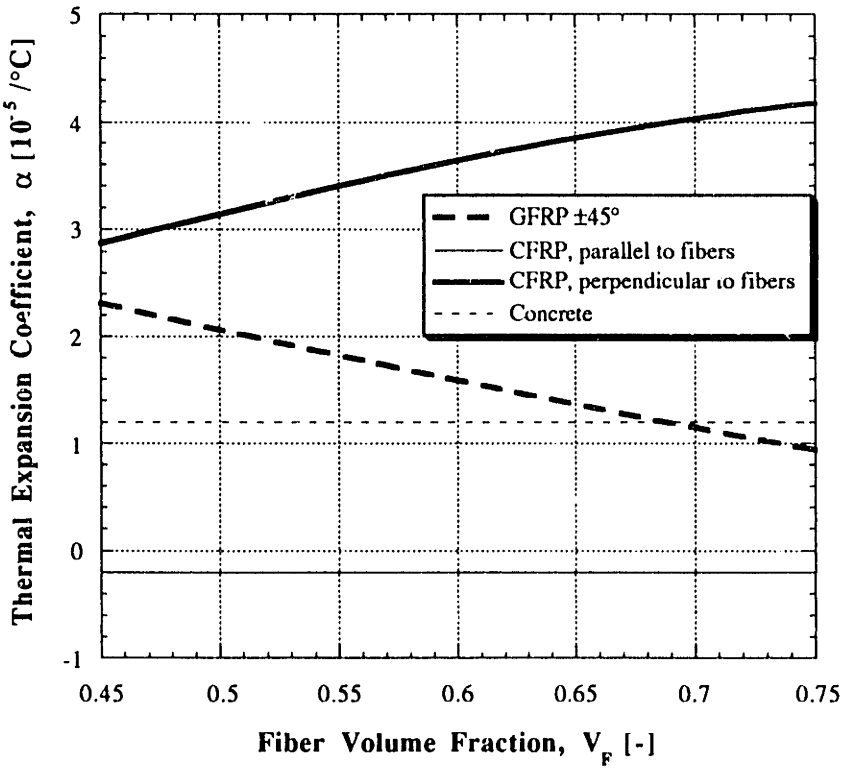

Figure 4.22 Thermal expansion coefficients of different laminates.

4.5.2 Interface Stresses Induced by Temperature Change

The problem imposed here is to solve for the distribution of normal and shear stresses at the interface between the GFRP and CFRP composites. Assuming a given temperature change and known geometric and material characteristics the resulting stress magnitudes can be determined from simple mechanics. The analysis follows the concepts found in Triantafillou and Deskovic (1991). Consider the structural member (in the future text referred to as "beam") shown in Figure 4.23. It has a length L, a height h and a width b. Since the analysis applies to the general case, the "beam" can be either the bottom flange of the GFRP box beam (when considering temperature effects in the lateral direction), or the whole hybrid beam (when considering the longitudinal direction). The thicknesses of the composite sheet and the adhesive layer are t_2 and d_a, respectively. The material properties are as follows: E_1 = Young's modulus of beam material, E_2 = Young's modulus of fiber-composite sheet in beam direction; and G_a = shear modulus of adhesive.

It is assumed that an increase in temperature takes place and that the thermal expansion coefficient of the FRP is less than that of the beam. The same analysis applies

also if a temperature drop occurs. Due to different deformations of each material, a temperature increase produces a normal tensile stress in the CFRP, $\sigma_2(x)$ and a compressive stress $\sigma_1(x)$ at the bottom fiber of the beam; the stress transfer from the FRP sheet to the beam is achieved through shearing of the adhesive layer, the shear stress at a distance x from the origin (beam mid-point) being $\tau(x)$.

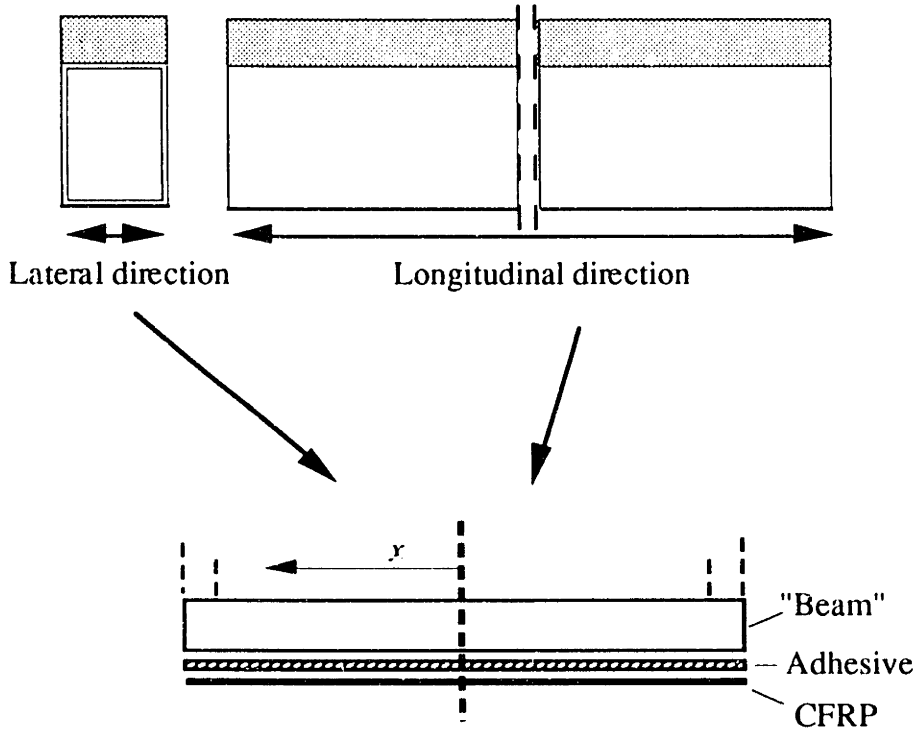

Figure 4.23 Geometric layout considered in the analysis for temperature.

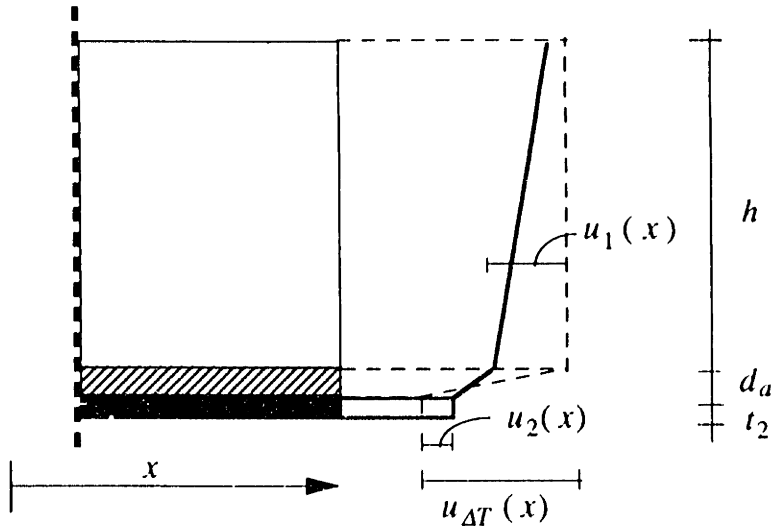

Figure 4.24 The deformation pattern of the FRP-adhesive system under temperature.

Figure 4.24 illustrates the displacements at x of the three different components (CFRP, adhesive, beam) before and after the temperature is increased. The following notation is used: $u_{\Delta T}(x)$= relative temperature deformation of CFRP and beam; $u_2(x)$= extension of the CFRP equilibrating internal forces; and $u_1(x)$=shortening of the beam at the bottom fiber equilibrating internal forces. The analysis presented next is based on the following assumptions: a) the materials are linear elastic; b) the governing deformation mode in the adhesive layer is shear; and c) the CFRP sheet and the beam have only axial deformations, which are uniform along their height.

The shear strain in the interface at a distance x from the origin can be written as:

$$\gamma = \frac{u_{\Delta T} - u_2 + u_1}{d_a} \tag{4.81}$$

and the interface shear is:

$$\tau = \frac{G_a}{d_a}\left(u_{\Delta T} - u_2 + u_1\right) \tag{4.82}$$

Differentiation of the shear stress with respect to x gives:

$$\frac{d\tau}{dx} = \frac{G_a}{d_a}\left(\frac{du_{\Delta T}}{dx} - \frac{du_2}{dx} + \frac{du_1}{dx}\right) = \frac{G_a}{d_a}\left(\frac{\sigma_{\Delta T}}{E_2} - \frac{\sigma_2}{E_2} + \frac{\sigma_1}{E_1}\right) \tag{4.83}$$

From beam theory the stress at the bottom fiber of the beam, $\sigma_1(x)$, can be expressed in terms of the normal stress in the composite, $\sigma_2(x)$, as follows:

$$\sigma_1(x) = -\xi\sigma_2(x) \tag{4.84}$$

where for a rectangular cross section (lateral direction case) ξ can be calculated as (Deskovic 1991):

$$\xi = \frac{bt_2}{bh} + \frac{bt_2}{bh^3}\frac{12}{4}\frac{h^2}{} = \frac{4t_2}{h} \tag{4.85}$$

while for the longitudinal direction case ξ can be expressed as:

$$\xi = bt_2\left[\frac{E_1}{\sum A_i E_i} + \frac{E_1}{D}\left(d + t_3 + \frac{t_1}{2} - y\right)^2\right] \tag{4.86}$$

Here, y and D were defined earlier with equations (3.65) and (3.73), respectively. Furthermore, the shear and normal stresses at the interface give:

$$t_2 \frac{d\sigma_2}{dx} = -\tau \tag{4.87}$$

By combining equations (4.83), (4.84) and (4.87) and differentiating the result we obtain:

$$\frac{d^2\tau}{dx^2} = \omega^2 \tau \quad , \quad \omega^2 = \frac{G_a}{d_a t_2}\left(\frac{1}{E_2} + \frac{\xi}{E_1}\right) \tag{4.88}$$

The solution of the last differential equation is of the form:

$$\tau = Ae^{\omega x} + Be^{-\omega x} \tag{4.89}$$

which represents the shear stress distribution in the interface. From the boundary conditions

$$\begin{aligned} \tau(x = 0) &= 0 \\ \tau(x = L/2) &= \tau_{max} \end{aligned} \tag{4.90}$$

the elastic shear stress distribution is obtained as follows:

$$\tau(x) = \frac{\tau_{max}}{\sinh\frac{\omega L}{2}} \sinh\omega x \tag{4.91}$$

where τ_{max} represents the maximum interface shear occurring at $x=L/2$. Differentiating equation (4.91) and combining the result with equation (4.83) we obtain:

$$\sigma_2(x) = \frac{\sigma_{\Delta T} - \dfrac{E_2 d_a \omega \tau_{max}}{G_a \sinh\dfrac{\omega L}{2}} \cosh\omega x}{1 + \xi\dfrac{E_2}{E_1}} \tag{4.92}$$

Now, considering equilibrium at any cross section we get:

$$\sigma_2(x)t_2 = \int_{L/2}^{L/2-x} \tau(x)dx \tag{4.93}$$

After applying the boundary condition $\sigma_2(x=0)=0$ onto the result from the above integral, combining it with equation (4.92) and evaluating it at midspan ($x=0$), along with the definition of ω (see equation (4.88)) we obtain:

$$\tau_{max} = \frac{\sigma_{\Delta T} G_a}{d_a \omega E_2 \coth\frac{\omega L}{2}} \tag{4.94}$$

Substituting the last result back into equations (4.91) and (4.92) we obtain the expressions for the interface shear stress and CFRP normal stress distributions, respectively, as follows:

$$\tau(x) = \frac{\sigma_{\Delta T} G_a}{d_a \omega E_2 \coth\frac{\omega L}{2}} \sinh\frac{\omega L}{2} \sinh\omega x \tag{4.95}$$

$$\sigma_2(x) = \frac{\sigma_{\Delta T}\left(1 - \frac{1}{\sinh\frac{\omega L}{2}\coth\frac{\omega L}{2}}\cosh\omega x\right)}{1+\xi\frac{E_2}{E_1}} \tag{4.96}$$

What remains is to determine the stress resulting from the thermal expansion differential of CFRP and the beam:

$$\sigma_{\Delta T} = (\alpha_2 - \alpha_1)\Delta T E_2 \tag{4.97}$$

where α_1 and α_2 are the thermal expansion coefficients of the beam and the CFRP, respectively, determined from equations (4.78) through (4.80) and ΔT is the temperature increment. It is important to note that the magnitudes of α_2 and E_2 will change depending on whether the lateral or the longitudinal case of interface stresses is considered.

Since the former case is more critical, a calculation example for it will be given next. The material properties and geometry used in the example are given in Table 4.4. It

is shown later in Chapters 5 and 6 that this example complies with the features of the specimens used in the experimental program.

Table 4.4 Parameters used for the analysis of temperature effects at the CFRP-GFRP interface.

E_2 [MPa]	E_1 [MPa]	G_a [MPa]	h [mm]	L [mm]	ΔT [°C]	α_1 [1/°C]	α_2 [1/°C]
21950	20000	900	5	180	50	$4\ 10^{-5}$	$1.2\ 10^{-5}$

Figures 4.25 and 4.26 depict the solution of equations (4.95) and (4.96) for the interface shear and CFRP normal stress, respectively, for various adhesive and CFRP thicknesses. The stress magnitudes are given along the lateral axis of the GFRP flange, and since they are almost constant in the central part (x = 0 - 80 mm), only the segment close to the edge (x = 80-90 mm) is shown. It is seen that maximum values of normal stresses are not affected by the adhesive thickness but are inversely proportional to the thickness of the CFRP sheet. At the same time the maximum interface shear stresses are inversly proportional to the adhesive thickness, but are proportional to the CFRP thickness.

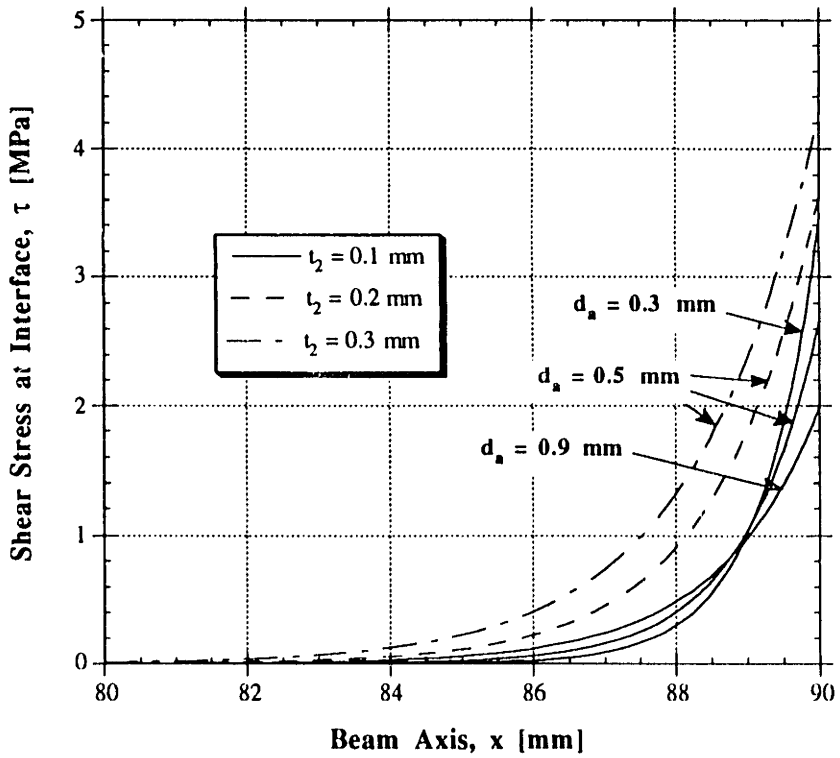

Figure 4.25 Interface shear stress distribution in lateral direction due to temperature change.

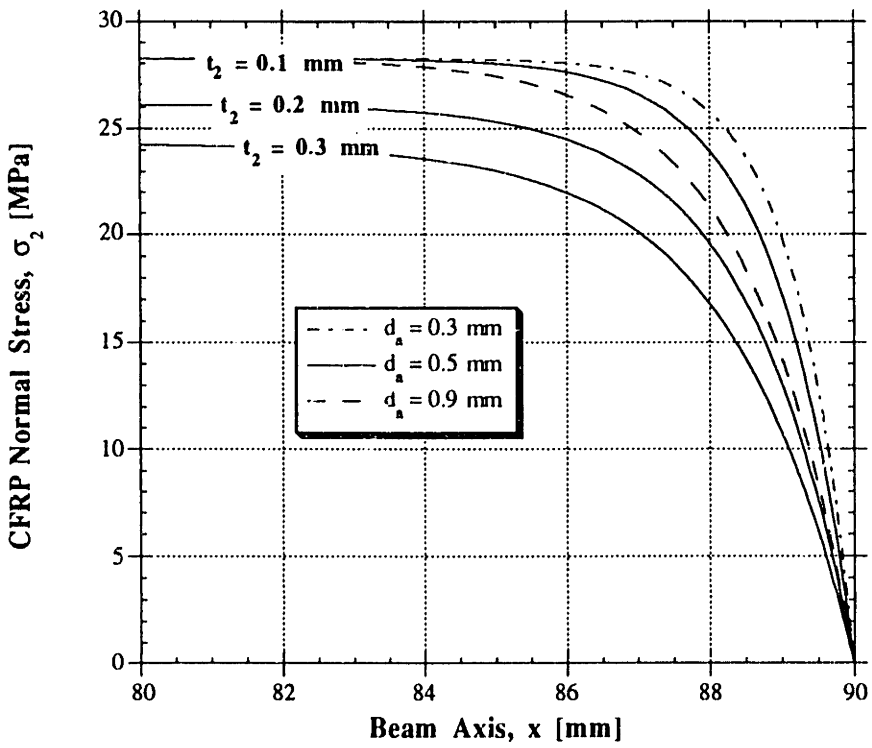

Figure 4.26 Normal stress distribution in CFRP due to temperature change.

Although extreme conditions (high ΔT) were imposed, it can be noted that the interface shear stress values are small when compared to the shear strength of the materials involved (the shear strength of the structural adhesives or epoxy resins is around 20 MPa). On the other hand, the normal stresses in the CFRP are of the same order as its strength (usually the transverse strength of unidirectional CFRP is less than the tensile strength of the matrix = 70-90 MPa) and hence, this might cause longitudinal cracking of the CFRP sheet. It should be pointed out that longitudinal cracking of the CFRP sheet has no effect on the stability of the hybrid beam, because the CFRP's properties in the longitudinal direction are maintained, but it enables environmental impact and deterioration of the matrix. It is therefore recommended to use some transverse fiber reinforcement to increase its strength or to use thicker sheets and decrease the stresses generated. Figure 4.27 shows the normal strain ($\varepsilon_2 = \sigma_2 / E_2$) in the CFRP sheet induced by the temperature change. The normal stresses generated in the GFRP flange bottom fiber (at the interface) are depicted in Figure 4.28. Also here, the resulting values are relatively small. Therefore, it can be concluded that for the layout of the hybrid beam examined in this example temperature oscillations will have a minor effect, assuming that some transverse fiber reinforcement is included in the CFRP sheet.

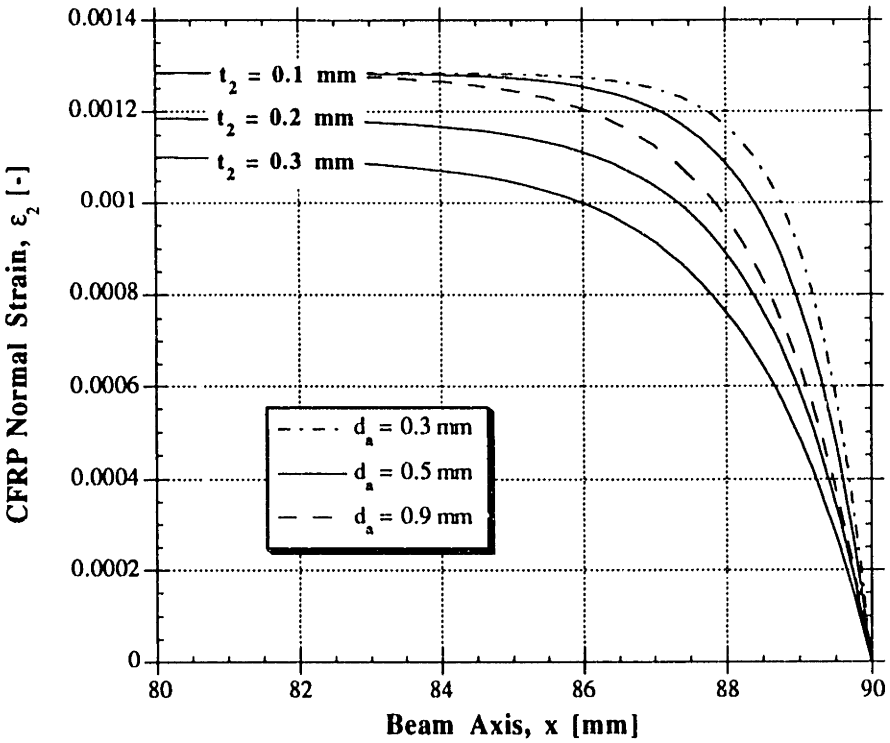

Figure 4.27 Normal strain distribution in CFRP due to temperature change.

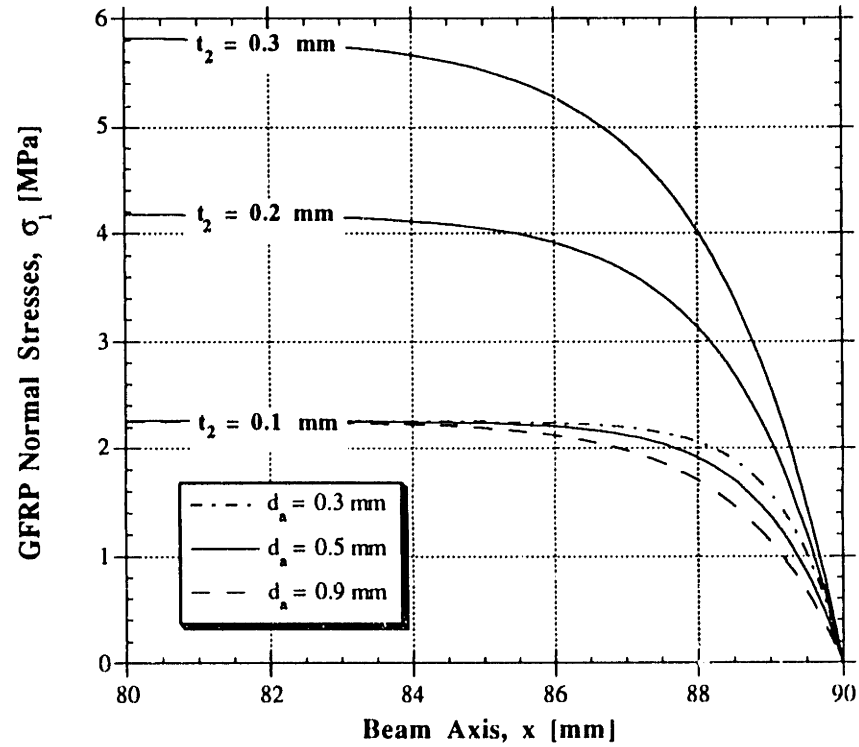

Figure 4.28 Normal stress distribution in GFRP due to temperature change.

4.5.3 Analysis of Hybrid Beam with Temperature Effect

The effect of temperature on the response of the hybrid beam is taken into account in the analytical procedures described earlier in Sections 3.4 and 4.3.4. During the calculation of the equilibrating internal forces at cross sectional level the actual strain, $\varepsilon_x^{st}(y)$, at any location y is modified taking the temperature deformations into account. This is accomplished by introducing an effective strain, $\varepsilon_x^{eff}(y)$, which can be expressed with the following equation:

$$\varepsilon_x^{eff}(y) = \varepsilon_x^{st}(y) - \alpha_x(T - T_o) \tag{4.98}$$

where the index x denotes different materials (e.g., concrete, GFRP or CFRP), T is the actual temperature and T_o is the reference temperature (during beam construction). From here the associated stresses are calculated from the short term stress-strain relationship. All the other assumptions and models mentioned earlier still hold and can be used directly.

4.6 Synopsis

The analysis for the characterization of the long term response of the hybrid beam was developed and described in this chapter. Models for concrete and GFRP were adopted and implemented in computer programs to simulate the behavior numerically. Shrinkage, creep and fatigue properties were considered and incorporated within the computational effort. Further, the temperature impact onto the hybrid beam was investigated. The verification and comparison of the assumptions and calculations performed will be given in the following chapters.

Chapter 5

EXPERIMENTAL PROCEDURE FOR TESTING OF HYBRID BEAMS

5.1 Introduction

The models and analytical procedures developed in Chapters 3 and 4 for the short and long term response of hybrid concrete/GFRP/CFRP beams were verified experimentally through an extensive testing program. The content of this chapter describes the design and manufacturing procedure of the specimens needed for the experimental program, as well as the test setup for static, creep and fatigue behavior investigations. The assumptions and analysis of the short term behavior presented in Chapter 3 were tested with two types of specimens. The first comprises small scale specimens produced with standard "off-the-shelf" pultruded GFRP box members with dimensions 60x80 mm and varying spans from 0.45 to 1.4 m. The second type includes full size beams manufactured with custom made filament wound GFRP box beams with dimensions 180x300 mm and a span length of 3.0 m. The latter beams were also used for long term tests in creep and fatigue, and hence gave experimental results for comparison with the derivations of Chapter 4.

5.2 Specimen Manufacturing

The experimental program was conducted employing two considerably different cross section designs. The first, which will be referred to as small scale specimens, was produced from a pultruded glass fiber reinforced polyester box section with different mixes and dimensions of the concrete layer in the compression flange and different CFRP laminates in the tension flange. In some beams the CFRP laminate was additionally pretensioned. The design parameters described in Chapter 3 were restricted here, because the material properties and dimensions of the GFRP profile were predefined through the manufacturers availability list. The second section, defined as the full size section, was

designed according to the design procedure described in Section 3.3.4. The resulting section was manufactured specially for this research work since no similar sections were available from the pultrusion market. The construction method included the filament winding technique for the GFRP box beam, casting of adhesive bonded concrete in the compression zone and epoxy bonding of the CFRP laminate in the tension zone. Only one characteristic cross section was produced for all full size tests.

5.2.1 Small Scale Specimens

Construction of the small scale hybrid beams involved three different material types: pultruded GFRP box beams obtained off-the-self (and hence not necessarily optimized), concrete and unidirectional CFRP sheets. Two different concrete mixes were employed, a normal strength and a high strength carbon fiber reinforced concrete (HS-FRC) containing silica fume. Moreover, two different types of CFRP were used, namely, a carbon/epoxy and a hybrid carbon/glass/epoxy (G/CFRP). A schematic layout of the members constructed is shown in Figure 5.1.

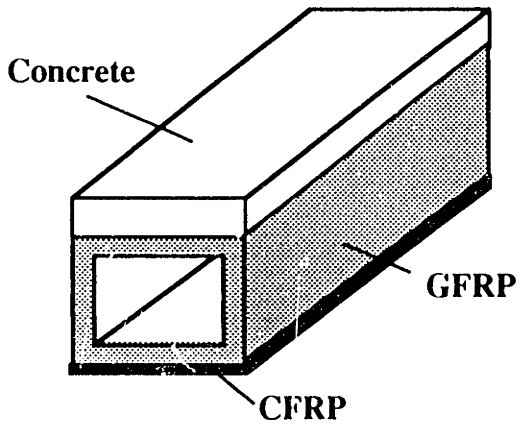

Figure 5.1 Layout of hybrid beam.

The GFRP box sections had dimensions 60x80 mm with wall thicknesses of 3 and 4 mm for the webs and flanges, respectively. For the test program a total of 16 hybrid beams was produced with the concrete layer cast on top of a GFRP box beam and a CFRP sheet bonded on the bottom. The analysis in Chapter 3 shows that it is very likely that a section would require a very thin CFRP sheet to ensure that CFRP failure precedes

concrete crushing. Moreover, it is also possible that a GFRP box section with given dimensions can not be combined with any CFRP composite, since the strain required to fail the latter results in quite high stresses in the tension zone, which can not be balanced in the compression zone because the concrete may crush. Due to this fact it was concluded that by using CFRP of relatively high strain at failure one may expect concrete crushing to occur first. The implication is that the CFRP sheet is not fully utilized and the desired pseudo-ductile behavior is lost. One solution to this problem is the use of low failure strain CFRP or the use of CFRP with the main direction of the fibers oriented at an angle with respect to the member's axis. At the time this specimen series was manufactured only high failure strain unidirectional CFRPs were available and thus, an alternative was found by pretensioning the CFRP prior to bonding it on the GFRP beam, thus inducing an initial strain and reducing the additional strain (due to the external loads) required to fail the element in tension. This approach was followed in some of the experiments conducted in this study.

5.2.1.1 Concrete Casting

Figure 5.2 is a schematic illustration of all the beams cast in normal strength concrete, with the dimensions and the casting layout. Beams 3 to 10 were cast in two continuous forms, where the beam cut-offs were obtained by inserting steel plates in the fresh concrete mix at given locations. Beams 13 to 17 were cast with high strength carbon fiber reinforced concrete (containing silica fume). The mixing procedure was performed according to the following steps: (a) silica fume and concrete were mixed for 2 minutes; (b) water and superplastisizer were added and mixed for 2 minutes; and (c) carbon fibers were added and mixed for another 2 minutes. The mix was reasonably workable and the fibers appeared well distributed. The casting layout for HS-FRC is given in Figure 5.3.

As a first step in the beam construction sequence, the concrete layer was cast on top of the GFRP beam which was roughened with sand paper. Plywood planks and silicone filler were employed to provide for a watertight form. The interface connection between the concrete and the GFRP was obtained with a two-component epoxy-based structural adhesive (density=0.0014 g/mm^3 and thickness about 0.5 mm). This adhesive has been used in construction for the construction joints and casting interruptions where fresh concrete has to be bonded onto already hardened one. In addition to the bonding effect, the adhesive also creates a shield between the concrete and the pultruded section,

thus protecting the GFRP from the alkalinity of the concrete environment. Shortly before the adhesive was applied the GFRP surface was cleaned with acetone. The adhesive was left to cure for approximately 20 minutes prior to pouring the fresh concrete over it.

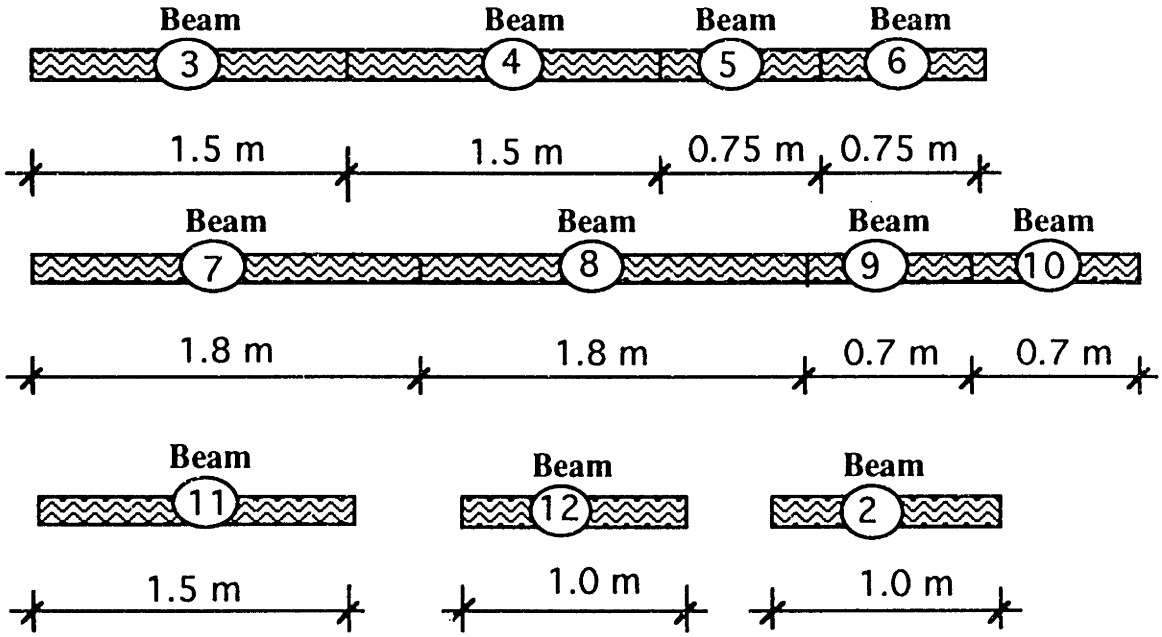

Figure 5.2 Normal strength concrete beam casting.

The beams were cured for 7 days in water (a layer of water was poured above the fresh concrete in the forms) to prevent shrinkage cracking until some tensile strength of concrete was obtained, and then left at 20 °C and 70% relative humidity. After 28 days the concrete layer was cut to the appropriate thickness using a diamond-blade horizontal smoother with water cooling system.

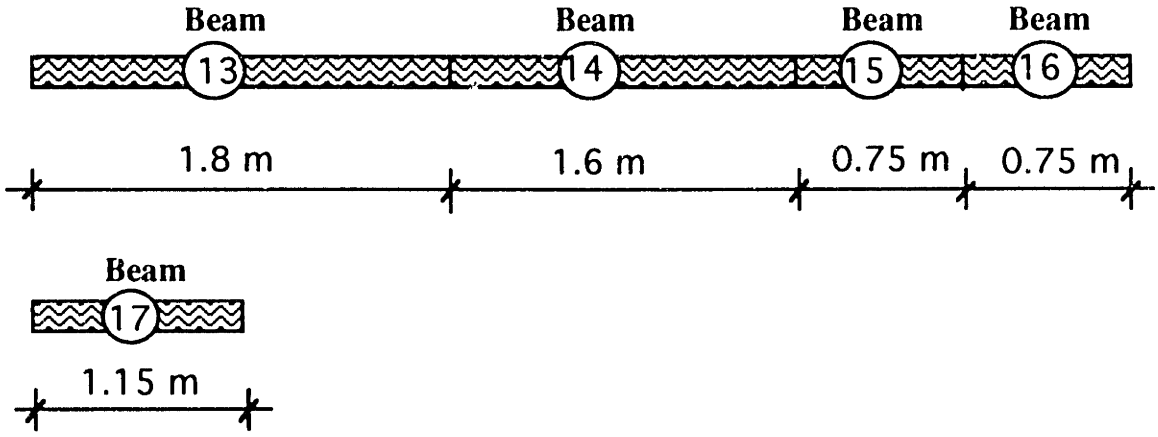

Figure 5.3 HS-FRC silica fume concrete beam casting.

5.2.1.2 CFRP Bonding

A thin laminate of CFRP was bonded on the tensile face of the hybrid beams using a high performance epoxy adhesive. Careful surface preparation was employed by removing the resin-rich surfaces of both the CFRP and the GFRP with sand paper and subsequently cleaning them with acetone. The adhesive was then applied on the CFRP and beam surfaces and the beam was placed on top of the CFRP sheet. The pressure at the epoxy line was increased to about 0.05 MPa by placing lead weights directly on the beam. A continuous support for the CFRP sheet was provided with a soft wood plank. Finally, the adhesive was left for 18 hours at room temperature to harden.

In beams 4, 8 and 14 the CFRP sheet was pretensioned before bonding on the GFRP beam. Prestressing was introduced by attaching (using adhesion) each end of the CFRP sheet to a pair of steel plates. The prestressed composite sheet spanned over a steel frame and was pin-connected to a hydraulic jack on one end and a load cell on the other. The pretension force was introduced in the sheet through the hydraulic jack up to the desired value and the adhesive was then applied to the CFRP and beam surfaces. The beam was next placed on top of the pretensioned sheet. Lead weights were used again to provide for a surface pressure, and after the adhesive was cured the pretension force was gradually released from one end with the hydraulic jack and transmitted to the beam. All beam designs produced are summarized in Table 5.1. Note that beams 1 and 18 were used as control specimens and consisted of plain GFRP. A photograph of the cross section of a typical hybrid FRP-concrete beam is shown in Figure 5.4.

The geometry of the specimens used was predefined to a large extent by the GFRP box beam. The design parameters included the material properties and thickness of the concrete layer, the CFRP lamina properties, its level of prestress (if any at all) and the span length. The design was based on the analysis described in Section 3.4.3, and the test results are described in Chapter 7. The scope of these tests was to verify the assumptions in the analysis and establish an effective procedure of manufacturing of hybrid beams. Different failure modes were encountered by changing the span length, thus switching from shear to flexure governed modes. Figure 5.5 shows a typical functional dependence of the ultimate carrying capacity to the span length and concrete dimensions for given lamina and concrete material properties. The stiffness requirement used in this plot was L/360.

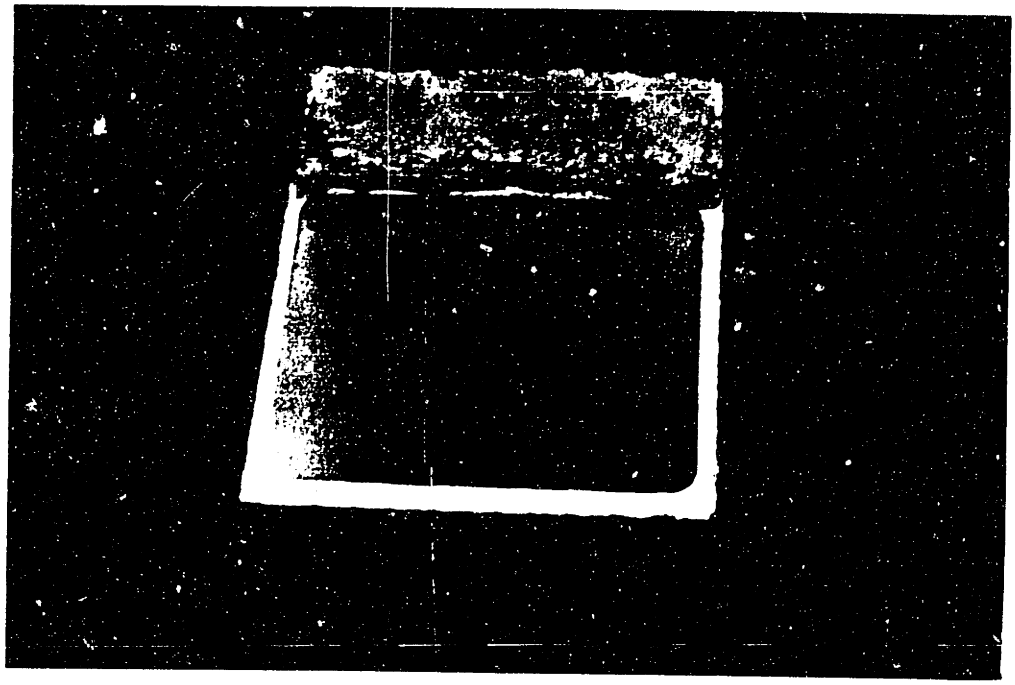

Figure 5.4 Cross section of hybrid FRP-concrete beam.

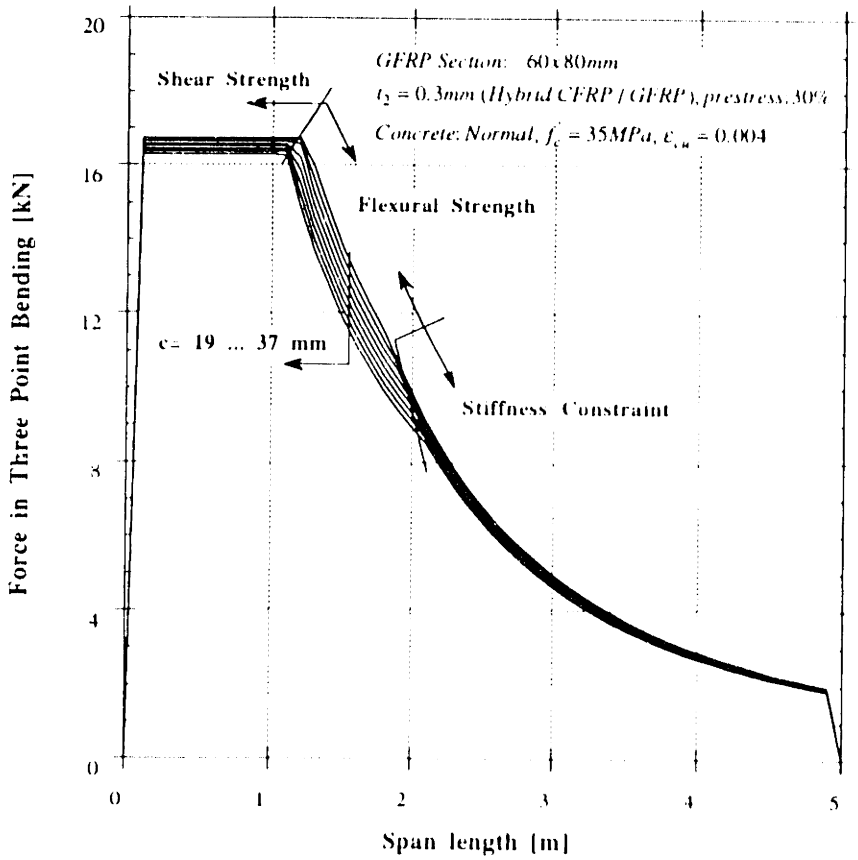

Figure 5.5 Ultimate load capacity as function of span length.

Table 5.1 Hybrid beam designs.

Beam	Concrete Type	Concrete Thickness [mm]	CFRP Type	CFRP Thickness [mm]	Pretension Strain [%]	Span Length [m]
1	-	-	-	-	-	0.50
2	normal	25	-	-	-	0.90
3	normal	25	G/CFRP	0.30	-	1.40
4	normal	25	G/CFRP	0.30	0.58	1.40
5	normal	15	G/CFRP	0.30	-	0.65
6	normal	25	G/CFRP	0.30	-	0.50
7	normal	31	G/CFRP	0.30	-	1.40
8	normal	31	G/CFRP	0.26	0.63	1.40
9	normal	15	G/CFRP	0.30	-	0.50
10	normal	31	CFRP	0.45	-	0.40
11	normal	25	-	-	-	1.40
12	normal	25	G/CFRP	0.30	-	0.90
13	HS-FRC	28	G/CFRP	0.30	-	1.40
14	HS-FRC	28	G/CFRP	0.30	0.34	1.40
15	HS-FRC	28	G/CFRP	0.30	-	0.65
16	HS-FRC	15	G/CFRP	0.30	-	0.50
17	HS-FRC	28	-	-	-	1.05
18	-	-	-	-	-	1.40

5.2.2 Full Size Beams

5.2.2.1 Design of Full Size Beam

In this section the reasoning behind the material selection and geometrical layout of the full size hybrid beam will be given. It was assumed that the resulting member has to be able to carry a load of 100 kN over a span of 3.0 m. These values appear realistic in order to simulate a common, or at least close to a common, beam element found in the construction industry, be it a floor beam of a residential building or a secondary girder of

a small bridge. The stiffness constraint was set to L/200 limiting the mid-span deflections to 15 mm at service loads. The worst scenario for the beam element is certainly when the whole load is concentrated at mid-span giving a three point bending configuration.

First, the materials to be used have to be selected. The discussion in Chapter 4 showed that a matrix with higher elastic modulus results in less creep, and since the matrix is the main parameter for controlling both creep and fatigue of the GFRP, to reduce the long term deformation of the beam, epoxy-based resins are to be used. In addition, the volume fraction of the fibers has to be kept as high as possible and thus a value of 65% or more was enforced. As mentioned earlier, the GFRP box beam is mainly used for the shear transfer between the compression concrete zone and the tension carrying CFRP laminate on one side, and for stiffness on the other. Since loaded in shear, an optimal fiber orientation for the webs of the GFRP box beam would be ± 45°. The corresponding equivalent material properties can be calculated using the principles of continuum theory for laminates, which was described in Chapter 4. For standard values of epoxy and glass material properties, Figure 5.6 illustrates the dependence of the elastic material properties of a ±45° GFRP as a function of the fiber volume fraction.

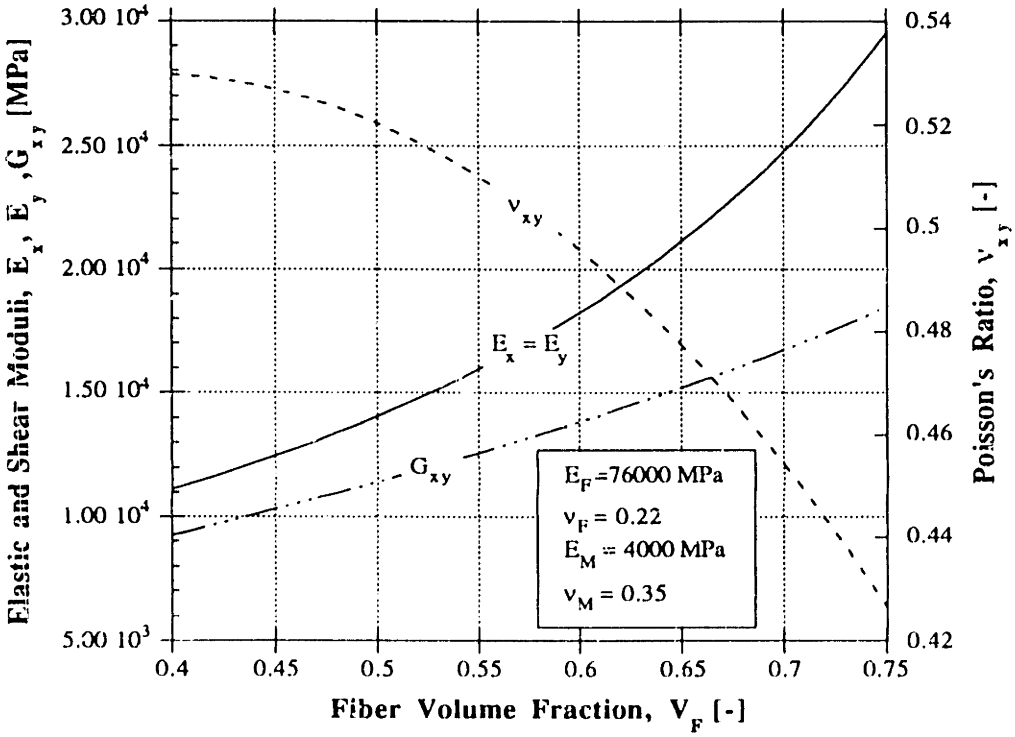

Figure 5.6 Elastic properties of ±45° GFRP.

The concrete strength is taken to be 50 MPa with the corresponding elastic modulus given by Paulay et al. (1990):

$$E_c = 6000\sqrt{f_c'} \qquad \text{(in MPa)} \qquad (5.1)$$

This value was anticipated for easily workable and still strong concrete, for which mix and aggregate were already available. Of course, a higher strength concrete would be even more desirable since it would reduce the dimension of the concrete layer and thus its weight for the same compressive carrying capacity, but this was not specially considered in this part. The constraints imposed on the CFRP laminate focused on low strain at failure but high modulus in order to carry most of the force in the tension zone. The lamina with M46J carbon fibers represented a good candidate. A summary of the material properties of all beam constituents resulting from previous prelminary design is given in Table 5.2. Using these values and a series of combinations of design parameters a parametric study was carried out on the design of the hybrid beams, given in Table 5.3. The design procedure will be described only for the case of BM-14.

Table 5.2 Preliminary material properties.

Material	Elastic Modulus	Ultimate Strain	Poisson's ratio	Shear Strength	Shear Modulus
Concrete	42 GPa	3.5 ‰	0.2	5.9 MPa	17.5 MPa
CFRP	300 GPa	0.8 %	-	-	-
GFRP	21 GPa	1.35 %	0.44	100 MPa	15.3 MPa

Once the material properties are defined, the dimensions of the GFRP section height and web thickness have to be designed using equations (3.75) to (3.77). Figure 5.7 shows the two constraints imposed by shear failure and shear buckling, where the dependence of the ultimate load in three point bending, P_u, to the height of the web, d, for different web thicknesses, t_w, is given. For a desired load capacity, P_u, the minimum value d is selected such that it satisfies both the shear buckling and the shear fracture failure criterion. The corresponding load capacity was purposely set higher than the required one at 200 kN, in order to eliminate the GFRP shear failure mode in the experimental program and have a safety factor of approximately 2.0. Figure 5.7 shows that the dimensions were chosen at d =295 mm and t_w =5.0 mm such that the two conditions are satisfied simultaneously.

Table 5.3 Parametric study for design parameters.

Beam	Lateral instab. coefficient, k_1 [-]	Web height, d [mm]	Top flange thickness, t_3 [mm]	Web thickness, t_w [mm]	CFRP's E-Modulus, E_2 [GPa]
BM-1	2.0	260	2.0	4.0	300
BM-2	2.0	260	2.0	5.0	300
BM-3	2.0	260	2.0	4.0	175
BM-4	2.0	260	2.0	5.0	175
BM-5	2.0	260	3.0	4.0	300
BM-6	2.0	260	3.0	5.0	300
BM-7	2.0	260	3.0	4.0	175
BM-8	2.0	260	3.0	5.0	175
BM-9	2.0	240	2.0	4.0	300
BM-10	2.0	240	3.0	4.0	300
BM-11	2.0	280	2.0	5.0	300
BM-12	2.0	280	3.0	5.0	300
BM-13	2.0	300	2.0	5.0	300
BM-14	2.0	295	3.0	5.0	300
BM-15	2.0	320	3.0	5.0	300
BM-16	2.0	320	3.0	5.5	300
BM-17	2.2	320	3.0	5.0	300

The next step is to define the section width b, which is coupled to the concrete thickness c (see equation (3.79)), the flange thickness t_1 and the CFRP thickness t_2. The nonlinear system of equations coupling these parameters can be solved approximately using a numerical approach. Here, the three variables are varied parametrically in order to assign the desired value for k_2 as defined with equation (3.78) and obtain a pseudo-ductile design. The results can be presented graphically and are given in Figure 5.8. If the desired value for k_2 is 0.8, then it is seen that a good combination is given by taking t_1 = 3.0 mm, t_2 = 0.1 mm and b = 180 mm. This choice provides a low CFRP content for pseudo-ductility and low cost and gives a load capacity of about 115 kN which complies well with the required one.

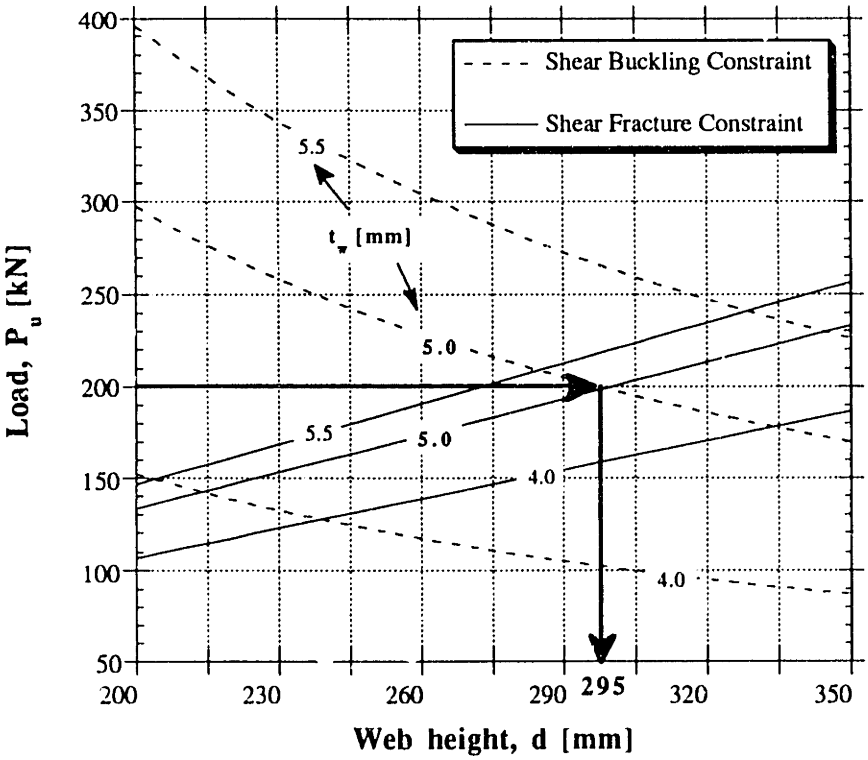

Figure 5.7 GFRP web selection of dimensions.

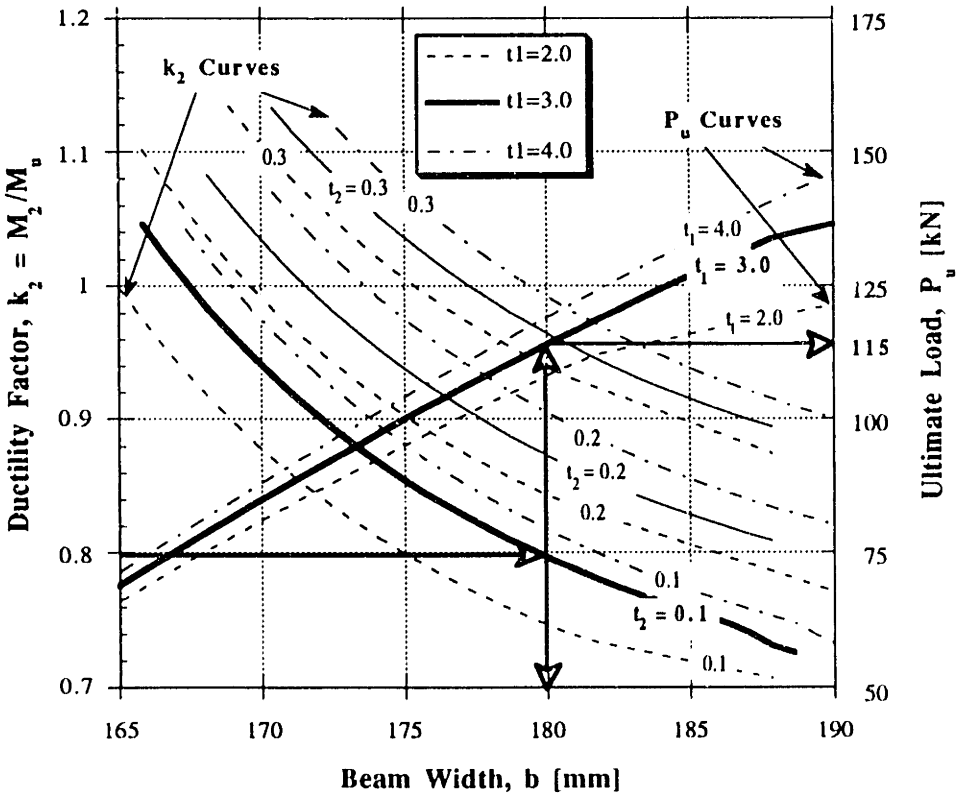

Figure 5.8 Selection of geometry of flanges.

At the end the stiffness requirement has to be checked. For simplicity, linear elastic behavior of all materials is assumed and the stiffness is obtained from the deflection at mid-span due to a load of 10 kN. From here, assuming the service loads to be at about 50% of the required ultimate, the stiffness can be found in terms of deflection versus span length. The variation of stiffness in respect to geometric parameters is given in Figure 5.9. The contribution of the shear deformation is given separately in the figure.

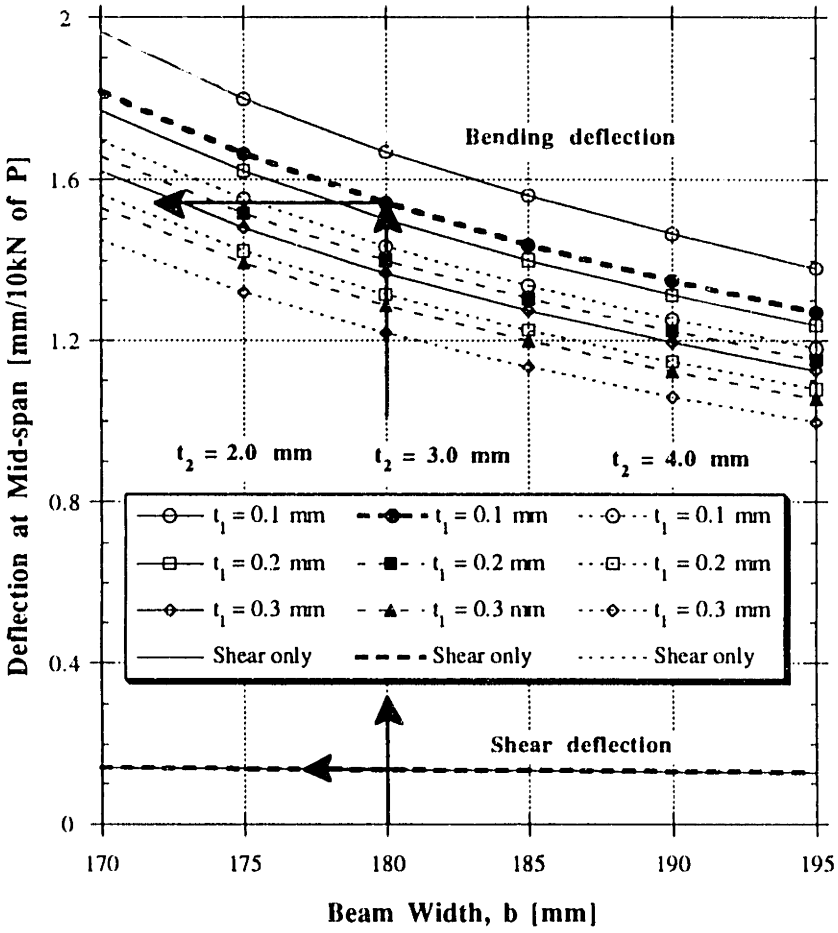

Figure 5.9 Stiffness variation with design parameters.

It is seen that the stiffness for the above design of BM-14 is $\Delta(50\%\ P_u/10.0) = 1.7(10.0/2)$ = 8.5 mm = L/350 which again complies with the design requirement for stiffness. The final results obtained for the design of BM-14 together with the results for some other beams are given in Table 5.4. From here it is evident that the design BM-14 gives the best solution to the imposed constraints and will therefore be used as the sample design for the manufacturing of the full size test specimens.

Table 5.4 Resulting designs.

Design	t_1 [mm]	t_2 [mm]	b [mm]	P_u Shear	P_u Flexure	$k_2 = M_2/M_u$	Δ [L/x]	Comment
BM1	2.0	0.2	155	117	69	0.88	L/210	Low Shear
BM2	2.0	0.2	160	230	82	0.89	L/240	Low capacity
BM3				117		> 1.0		Not p-ductile
BM4				230		> 1.0		Not p-ductile
BM5	3.0	0.1	155	117	73	0.80	L/220	Low Shear
BM6	2.0	0.2	160	230	82	0.91	L/270	Low Capacity
BM7				117		> 1.0		Not p-ductile
BM8				230		> 1.0		Not p-ductile
BM9	2.0	0.2	145	125	55	0.90	L/180	Low Capacity
BM10	2.0	0.2	145	125	57.5	0.92	L/190	Low Capacity
BM11	3.0	0.2	170	210	98	0.88	L/330	Low Capacity
BM12	3.0	0.2	170	210	100	0.90	L/350	High k_2
BM12'	2.0	0.2	170	210	95	0.86	L/330	Low Capacity
BM13	3.0	0.2	180	200	115	0.88	L/370	Good
BM14	3.0	0.1	180	200	115	0.80	L/350	Good
BM15	3.0	0.2	190	185	130	0.86	L/500	Too strong
BM16	3.0	0.2	195	245	150	0.84	L/580	Too strong
BM16'	3.0	0.2	200	245	161	0.80	L/600	Too strong
BM16"	3.0	0.3	200	245	161	0.88	L/660	Too strong
BM17	3.0	0.2	180	185	142	0.81	L/500	Low Shear
BM17'	3.0	0.3	180	185	142	0.90	L/550	Low Shear

5.2.2.2 GFRP Box Beam Manufacturing

In this section the description of the manufacturing process of the GFRP box beam is given. The choice of the appropriate manufacturing process is dependent on many parameters. Basically, there are two groups of systems used from the fabrication of glass fiber reinforced plastic products, namely open mold processes and closed mold processes. The open, or single mold processes are those that are generally used for the production of large components for structural engineering applications, while the closed

mold systems are predominately used for smaller components, usually with more precise geometry, for applications in other branches of technology. The various processes comprising both these groups are depicted in Figure 5.10.

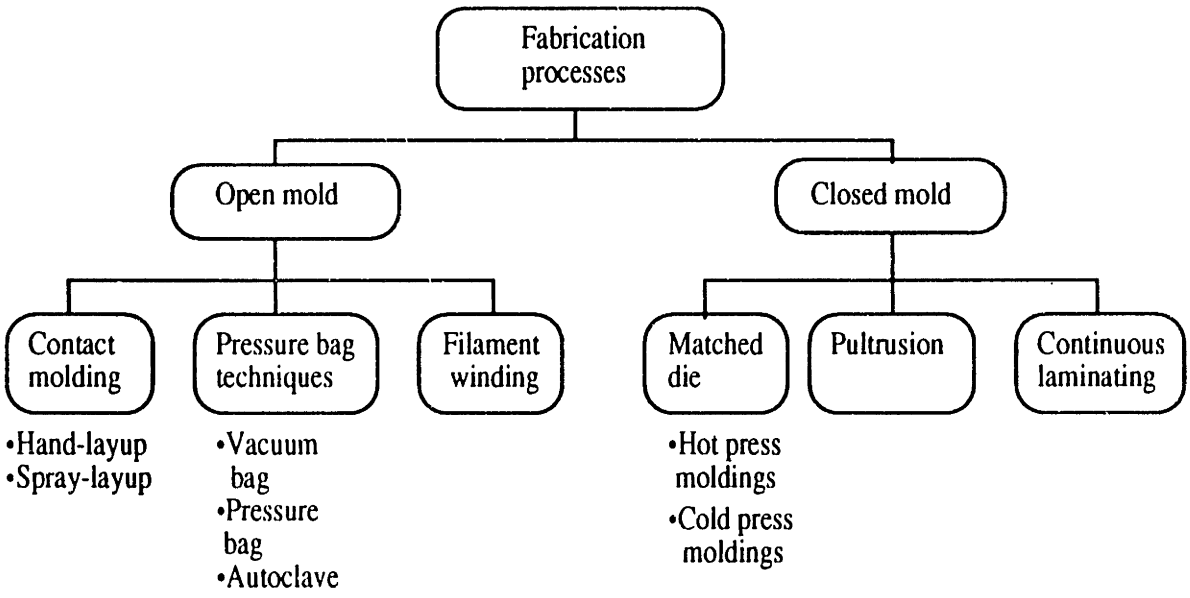

Figure 5.10 Processes used for the manufacture of GFRPs.

It should be pointed out that any of the closed mold methods were disregarded as alternatives since they all require extensive tooling and equipment investment up front, which can be justified only for large production series. For the experimental program planned here where only few beams are to be used, such an approach would be associated with too high a cost. On the other hand, for future practical applications and serial production lines the pultrusion method seems the most appropriate of all since the high initial cost is easily overruled by production speed, quality and low labor requirement. This process consists of impregnating continuous glass strands, usually in the form of roving, in a resin bath before drawing them through a die to obtain the desired shape of the section. Rapid curing is carried out in an oven or alternatively, by externally heating the die.

The hand-layup method, being one of the feasible alternatives for the box beam required here, was rejected since quality requirements such as predefined fiber orientation and high fiber volume fraction could not be met (according to this method, maximumV_F= 0.45). Other characteristics of this method are the requirement of low initial investment but high labor and time intensity. The method is based on filling a precast mold with subsequent layers of resin and glass fiber reinforcement. A release

agent is used to impede bonding of product and mold. The first layer, called "gel coat", is made of an even, thick resin film, usually impregnated with pigments and a tissue mat, and is specially designed to protect the following layers from environmental effects and to create a smooth external face of the product.

The filament winding method, although cost involving, was the only remaining solution, which in combination with the vacuum bag and autoclave technique led to the production of the desired beam specimens. Filament winding uses continuous reinforcement, usually roving, thus utilizing the inherent strength of glass fibers most effectively. This continuous reinforcement is fed through a resin bath, passed over a hot roller until tacky, and then wound on to a rotating mandrel via a transversing mechanism. The reinforcement may be led at any helix angle by suitably adjusting the movement of the transversing mechanism relative to the mandrel. The wall of the finished product may consist of several fiber layers in various orientations to satisfy the strength requirements of the particular design. After the composite has cured on the mandrel, either at ambient temperature or in an oven, the mandrel is removed from the product. For better curing the vacuum bag technique can be implemented. Before curing has advanced, a rubber or PVC membrane is placed over the component, all joints are sealed, and a vacuum is created under the bag, thus forcing out air and excess resin. Additional improvement of the curing process and product quality can be achieved with an autoclave where external pressure and increased temperature are applied.

The necessary steps for the production are: (a) preparation of all accessories and constituent materials; (b) prefabrication of components; (c) filament winding and curing; and (d) final finishing. Figure 5.11 shows the resulting cross section from the design procedure described earlier in this section. It was mentioned earlier in Chapter 3 that an optimum design is achieved by minimizing the GFRP's top flange thickness (ideally it should vanish). On the other hand, the filament winding method and technical reasons related to supporting the concrete layer, require the top flange to exist and in addition the same thickness of top and bottom flange has to be warranted. Therefore, it must be emphasized that the GFRP box beam design adopted for the experimental program is not necessarily an optimum one, but one that, given the manufacturing method, will make it possible to validate the analysis.

Due to the fact that the manufacturing of the beam is based on the filament winding method, a problem related to varying wall thicknesses arises. Although the design produced equal thicknesses of the compression and tension flange, the webs of the beam need to be thicker in order to avoid early shear failure. On the other hand, the thickness of the flanges could not be increased because the desired pseudo-ductile

behavior could not be obtained. The solution to the problem is found by inserting GFRP plates in the web walls between two layers of wound fibers. This is shown in Figure 5.12. The plates are produced with glass fiber prepregs. The required length of the beam is 3.2 meters but a mandrel of 3.6 meters was used in order to account for the warping and bulling of roving close to the ends of the core.

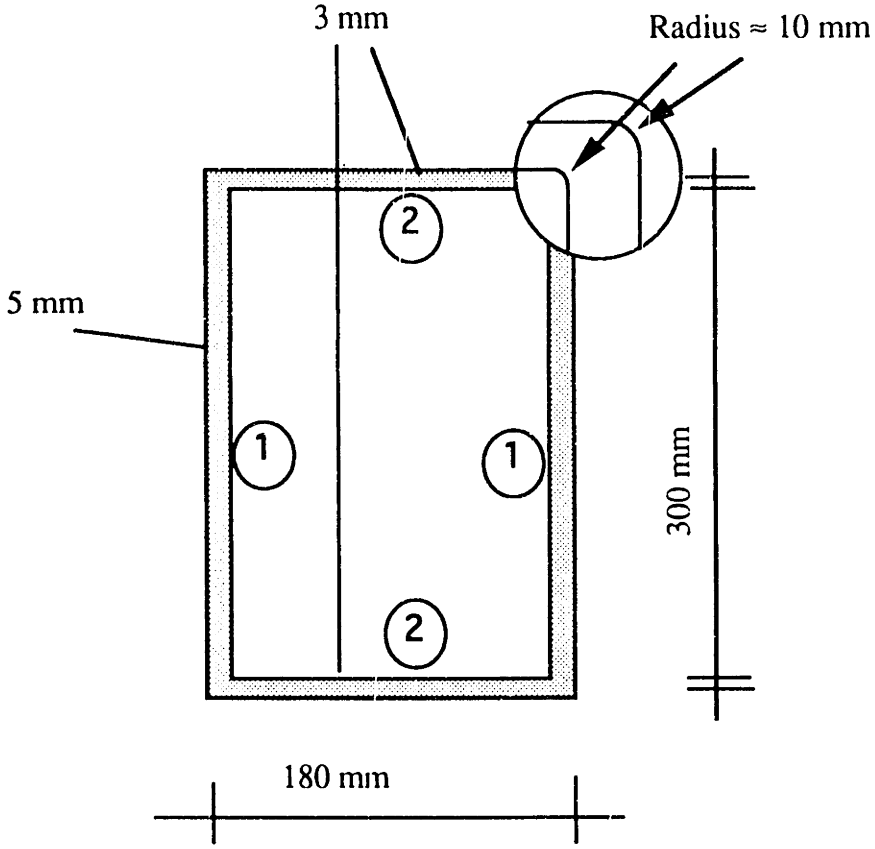

Figure 5.11 GFRP design geometry.

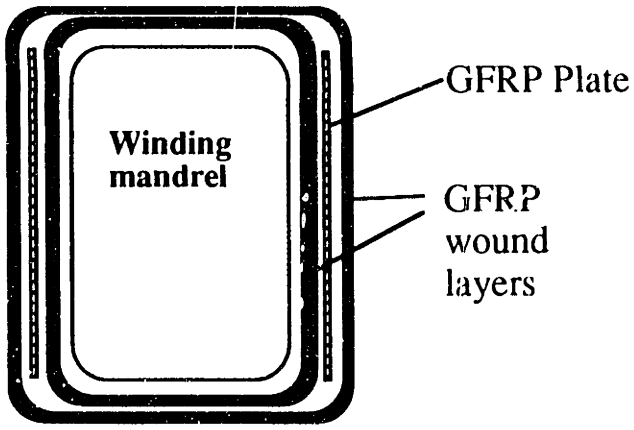

Figure 5.12 Filament winding layout.

5.2.2.2.1 GFRP Plates Manufacturing

The sheets required for the web walls of the GFRP box beam have to be compatible with the remaining wall material, otherwise stress concentrations at the interfaces are to be expected. This was achieved by producing plates out of glass fiber reinforced prepregs which were bonded and cured such that the volume fraction of fibers of the plate matches the one of the remaining beam. Prepregs are resin impregnated fibers where the curing of the matrix has been interrupted, and which can be bonded to other materials or to each other only under the influence of high temperature or pressure. Prepregs are usually delivered in rolls of 1 m diameter and the single layers are covered with a non-adhesive sheet protecting the surface to be used in the bond. They are stored at low temperatures (usually -18°C) to prevent curing of the epoxy resin.

Two plates with dimensions 3600x280 mm and a thickness of 2 mm were required for each GFRP beam, which was achieved by bonding 8 layers of Tex 1200 glass fiber prepregs. The prepregs were delivered with fiber orientation 0/90°, while the filament wound fibers were oriented with ± 45°. Therefore, stripes had to be cut and placed at ±45°(4 layers in each direction), such that overlapping never occurred at the same location. This is shown in Figure 5.13 (a).

For the curing of the plates the vacuum bag and autoclave techniques were used in order to achieve good properties and high fiber volume fractions matching those from filament winding. The prepregs were first covered on both sides with a Teflon impregnated nylon grid which was used as the releasing barrier. Then on one side a perforated PVC sheet was put to create a smooth surface and was further covered with an Aerowave® saturation tissue which absorbed the excessive epoxy. Two aluminum plates were put on both sides to create even surfaces and then vacuum was applied. This is also shown in Figure 5.13 (b). The whole package was then cured in the autoclave for 4 hours under a pressure of 2 bars and a temperature of 120°C.

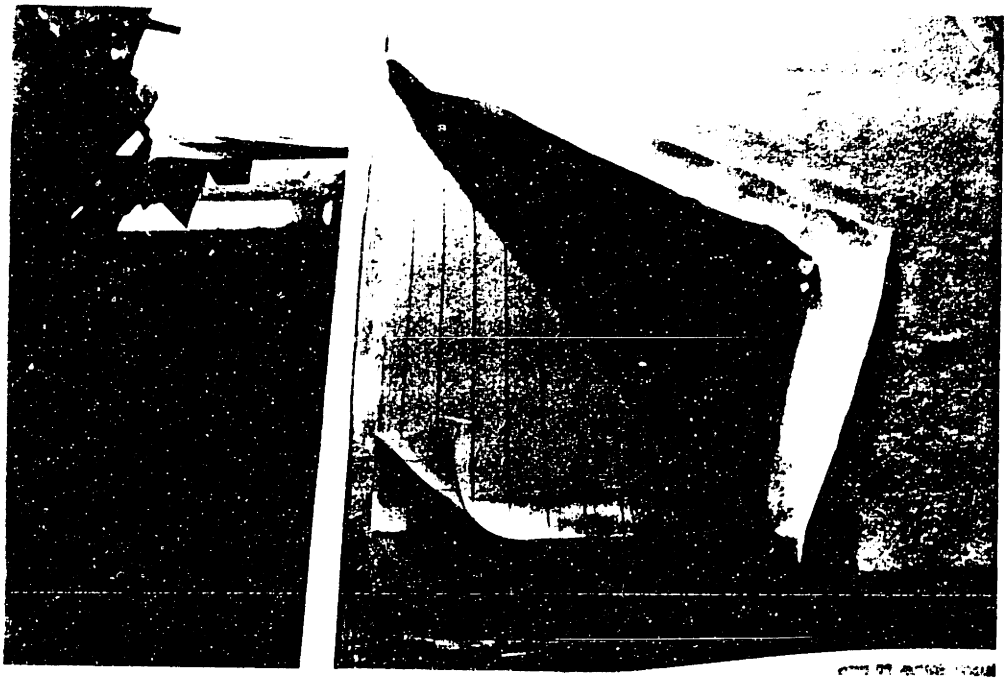

(a)

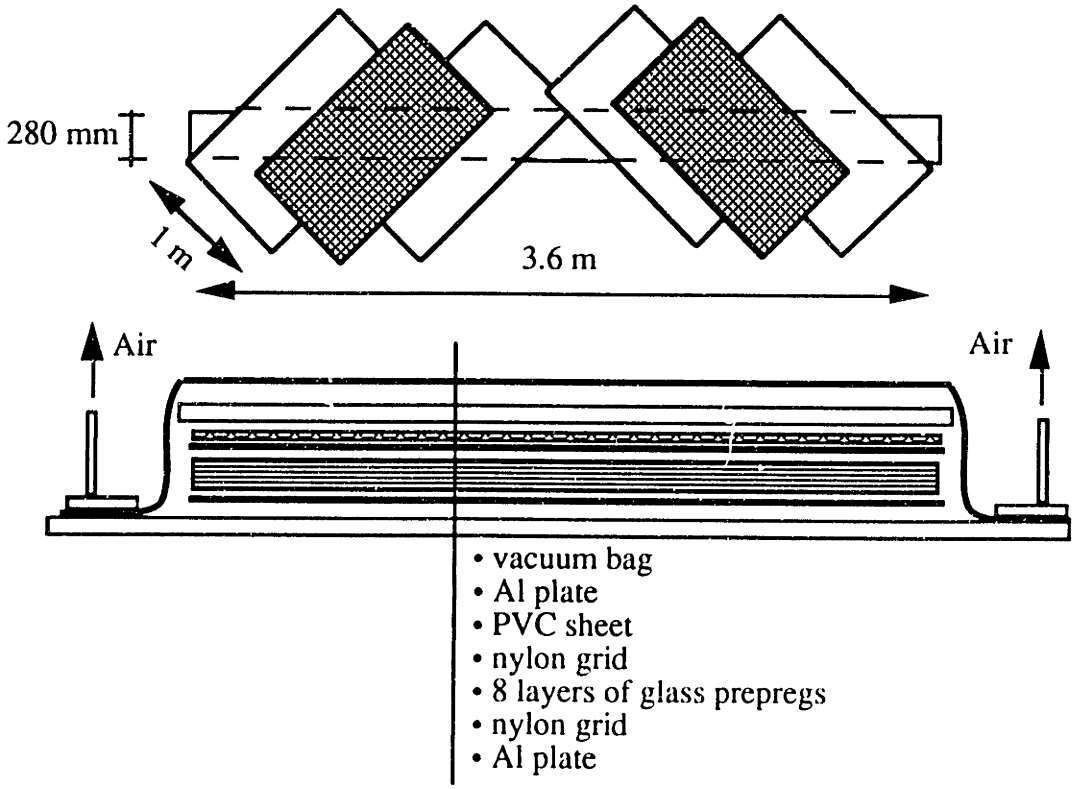

(b)

Figure 5.13 (a) GFRP prepreg packaging for autoclave; (b) GFRP plate production.

5.2.2.2.2 Filament Winding

The filament winding machine resembles a somewhat extended torque machine in the turn mouth of which a mandrel is affixed. Along the side, in the longitudinal direction, an electrically powered car is moving back and forth. Two roving spools are affixed on it, two roller systems with roving speed control, two resin baths with incorporated heating plates and a spooling die guiding the united roving to the mandrel circumference, are also attached as shown in Figure 5.14. The mandrel around which the beam is been wound had cross sectional dimensions of 295x170 mm and was made of welded steel plates with a corner radius of 10 mm. At the ends and at quarter span points inside the mandrel steel stiffeners are welded to enhance the lateral torsional and flexural stability. These plates function also as torque transfer elements from the torque machine to the mandrel.

The winding of the beams was conducted with glass rovings of type Tex 1200 (g/1000m). The matrix was Ciba-Geigy's LY 556 resin with the hardener HY 917 and the accelerator DY 070. The mix proportions were 100:115:0.2 by weight. The winding procedure was as follows: (a) winding two layers with ±45° angle, achieving a thickness of 1.5 mm; (b) inserting the prefabricated GFRP plates on the web sides and positioning them by running one winding with a steeper angle; and (c) winding of two more layers with ±45° angle and a thickness of 1.5 mm. A layer was constructed with many roving strands laid next to each other until the whole beam surface was covered (see Figure 5.15). This was calculated to occur after the car moved back and forth 54 times and created a thickness of 0.75 mm. The movement of the car carrying the winding supply was computer guided in order to achieve precise laying of the rovings at ±45°. To have sufficient impregnation of the rovings, the pullout speed is not to exceed 4 m/min. The pullout force was set to 20 N, which enables a smooth laying of the rovings and air bubble free structural elements to be produced. After the plates were inserted, short carbon fibers saturated with epoxy resin were used to fill the triangular gap which was created along the beam at the locations where the inserted plates join together with the surrounding wound layers. To make this gap smaller the edges of the GFRP plates were ground down to trapezoidal form. Each layer required approximately 1 hour to be constructed, and with further time needed for the plate insertion, an average of 5-6 hours was needed for the winding of each beam.

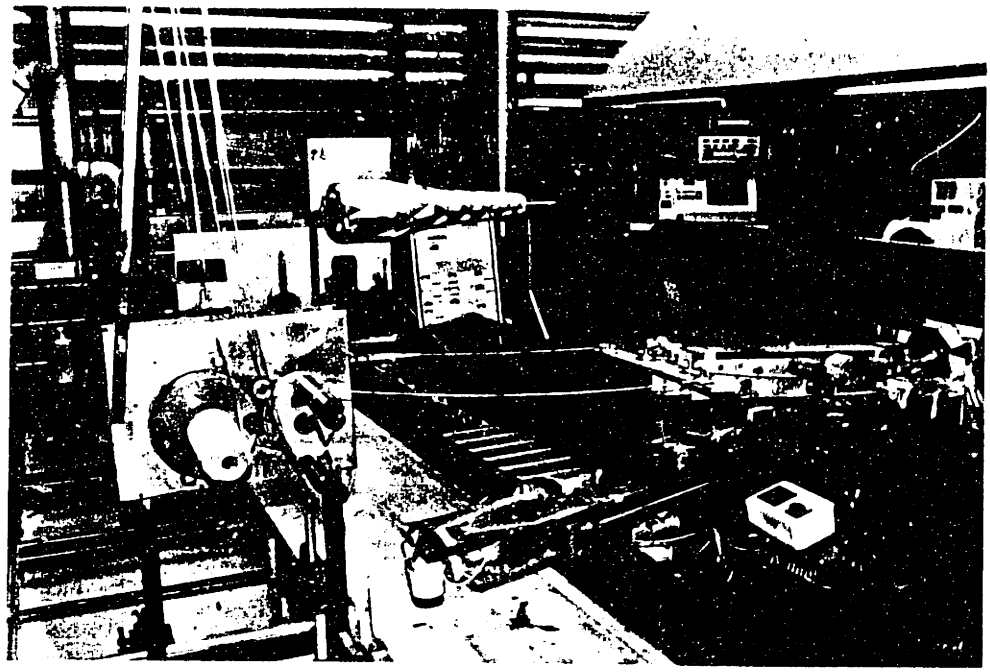

Figure 5.14 Winding car with roving spools and resin bath.

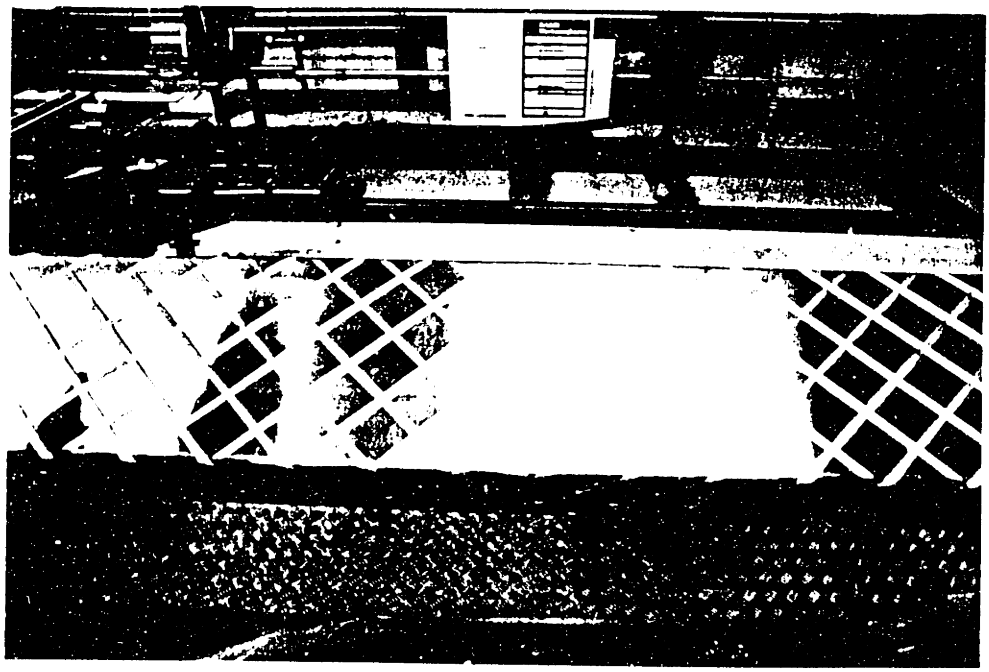

Figure 5.15 ±45 rovings laid over mandrel.

5.2.2.2.3 GFRP Beam Curing

The next step includes packaging of the beam. The wound beam was immediately wrapped with a silicone impregnated nylon mesh, which absorbed some of the excess resin. The beam, being drop-free, was wrapped with two layers of 3M Scotch tape, which was used to produce a smooth surface. The tape had to be additionally perforated with a sharp object to allow for resin leakage. Four aluminum plates were pressed onto the beam's walls in order to achieve a smooth contact between the rovings and the steel core. Everything was then wrapped with the Aerowave® tissue for the absorption of excessive resin, and at the end, the vacuum bag made of heat resistant nylon foil bonded with a special gasket spackle completed the equipment for curing in the autoclave. The packed beam was removed together with the mandrel from the winding machine, and placed in the autoclave which is shown in Figure 5.16.

The autoclave (see Figure 5.17), a 4 m long and 2.2 m in diameter cylindrical vessel which can at the same time produce external pressure, applied suction to the vacuum bag and worked as an oven, according to the diagram shown in Figure 5.18.

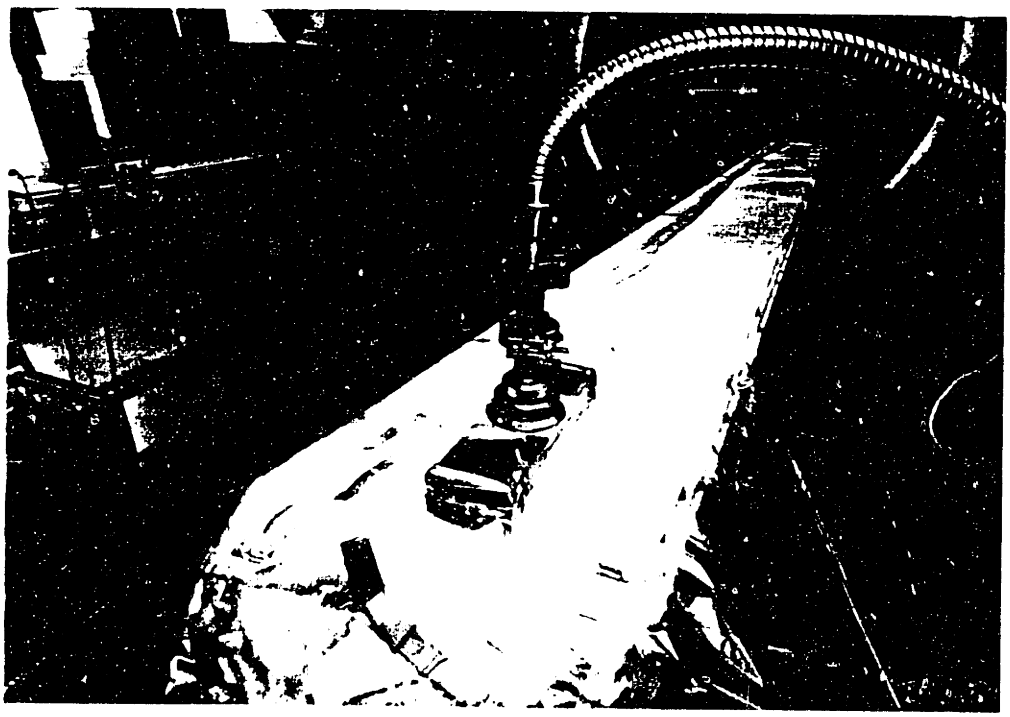

Figure 5.16 Ready packed beam for curing in autoclave.

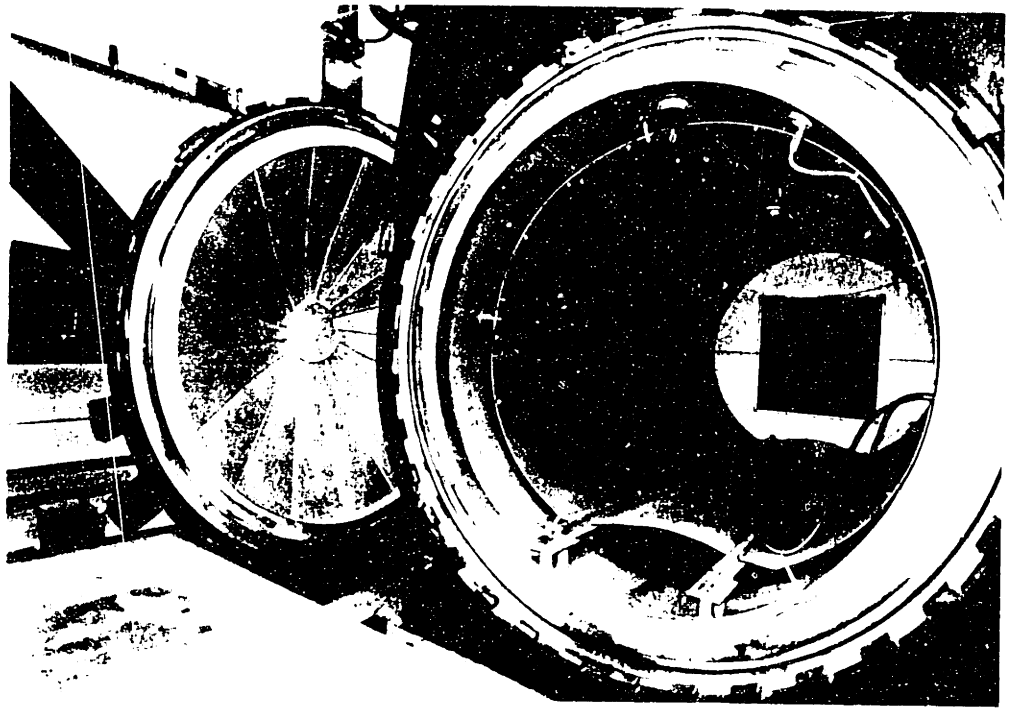

Figure 5.17 Autoclave used for curing.

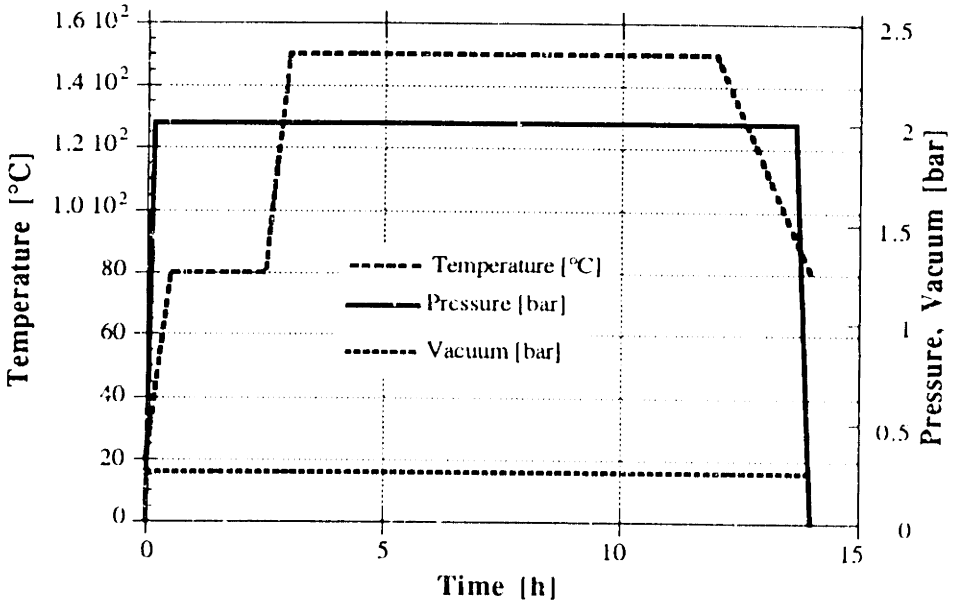

Figure 5.18 Autoclave cycle.

During the temperature increase to 80°C the viscosity of the resin increased. The suction inside the vacuum bag enabled an even more thorough impregnation of the rovings, as well as extraction of the remaining air bubbles. The external pressure

impeded extraction of the resin from the element. After the gel state of the resin was reached, the temperature was raised to 150°C and held for 9 hours to accommodate proper curing.

After curing, the packaging was removed form the beam, except for the peel-off nylon mesh which was kept in order to provide a protection for the surfaces which would be used for adhesion with concrete and CFRP. The next task was to remove the mandrel core from the hardened GFRP box beam. The half spheres at the ends were first cut out with an electric saw. A specially designed beam with a mouth on one side and a hydraulic jack on the other was used to extrude the core from the GFRP encasing, as shown in Figure 5.19.

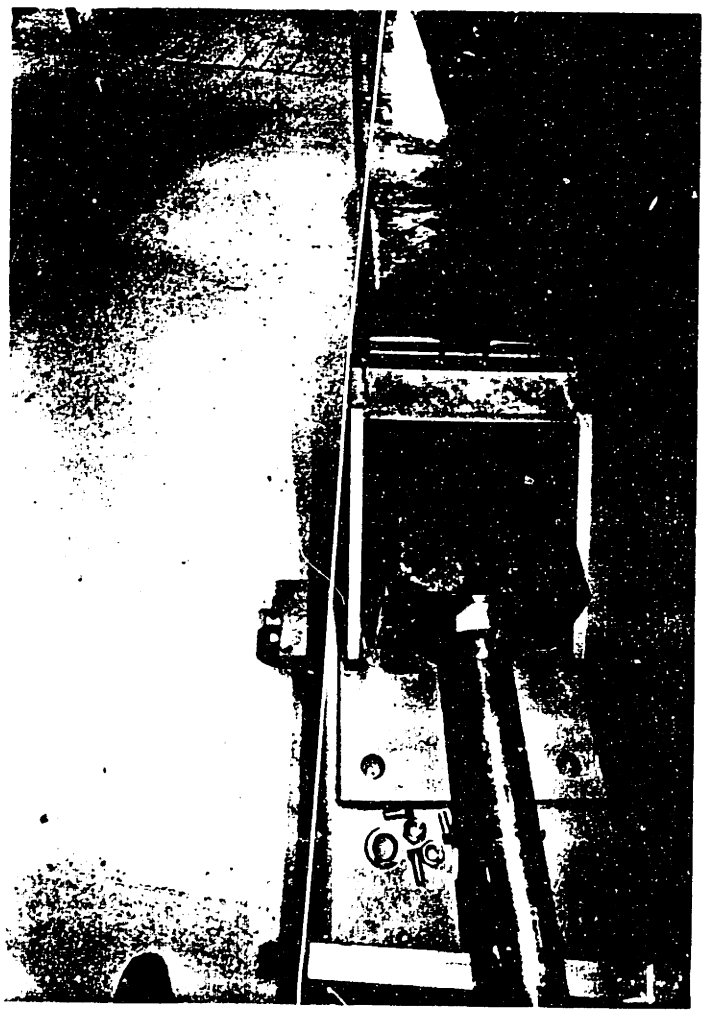

Figure 5.19 Pullout apparatus for the extraction of the winding mandrel.

The thermal expansion coefficient of the GFRP used here was almost equal to the one of steel and therefore no interface stresses were generated after cooling down to room

temperature. In some cases it is necessary to freeze the steel core in order to be able to pull the mandrel out. Wooden plates were bonded onto the GFRP to have enough surface to transfer the force from the pullout beam to the box element. A force of 15 kN was required to detach the GFRP box from the core. Finally, the GFRP box beam was cut to proper dimensions and prepared for casting of concrete and bonding of CFRP.

5.2.2.3 Hybrid Beam Construction

Construction of the hybrid beam can be divided into three stages: (a) casting and curing of concrete on the top flange of the GFRP box beam; (b) CFRP bonding onto the tensile flange; and (c) application of shear connectors. All three stages will be discussed in detail in this section. A total of seven beams with dimensions as specified by the design procedure described earlier in Section 5.2.2.1 were produced.

5.2.2.3.1 Concrete Casting

The first step in the preparation for concrete casting included preparation of the GFRP surface. The nylon grid was peeled-off from the top flange providing a clean and rough surface, which, in the general case, is ideally suited for adhesion with epoxy based adhesives. A mold was made of plywood planks and fastened with clamps around the beam as shown in Figure 5.20. Next, the mold was sealed with silicone filler in order to create a watertight form. The whole structure was then placed in a horizontal position. The same adhesive as described in Section 5.2.1 for the small scale specimens was employed at the interface between concrete and GFRP. The GFRP surface was cleaned with acetone and then the two-component structural adhesive was applied in a thin film ($\approx$ 0.5 mm) on top. The adhesive was left to cure for approximately 20 minutes before fresh concrete was poured over it. Simultaneously, the concrete mix was prepared by mixing the aggregate, cement, water and a superplastisizer (with the proportions described in Chapter 6) for 90 seconds in a 50 liter horizontal mixer. The fresh concrete was finally placed into the mold and then vibrated. The final surface look was given by leveling up with a wooden plank.

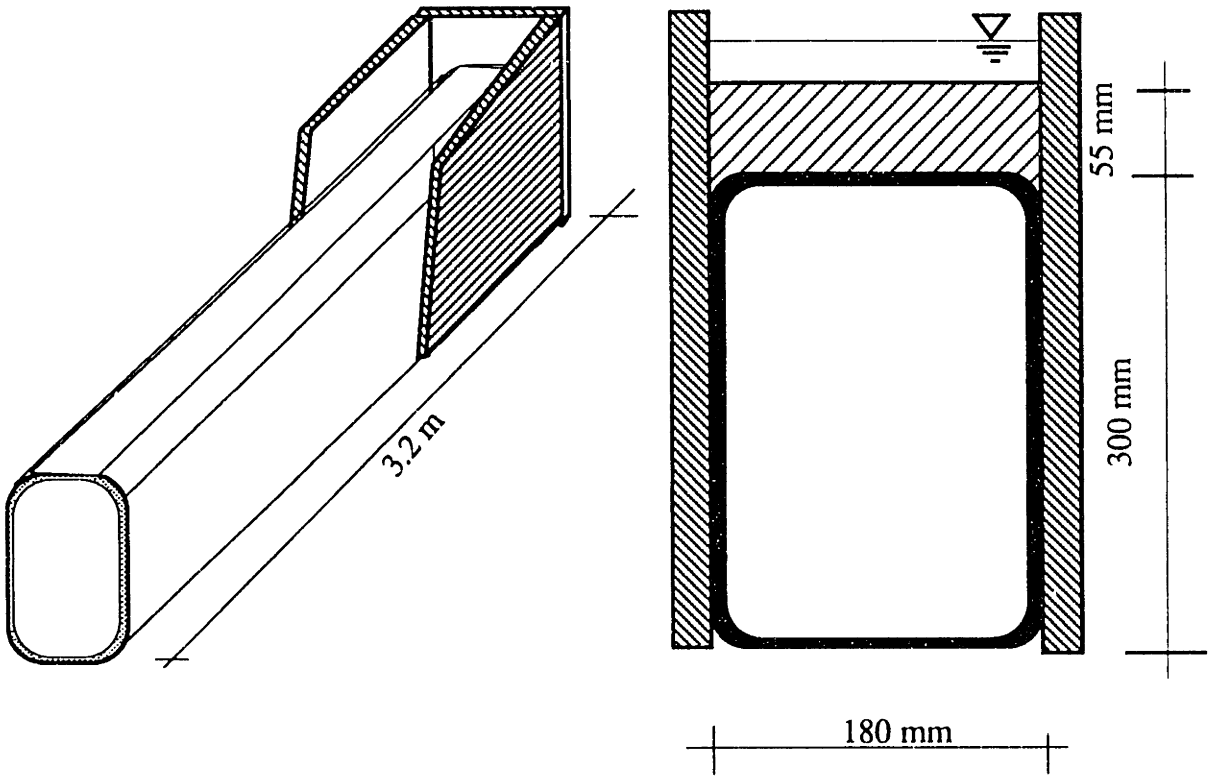

Figure 5.20 Molds used for casting of the concrete layer.

It should be pointed out that although the water to cement ratio of the concrete was low, good workability was obtained through the use of additives; in addition, the shape of the concrete layer was favorable in relation to compacting and accessibility. At the end, a layer of water was poured above the fresh concrete to prevent shrinkage cracking until some tensile strength of concrete was reached. After 7 days the molds were removed and the beams were cured at 20°C and 70% relative humidity for 28 days to reduce the shrinkage effect. The beams were produced in sequences of two beams in a row, and the molds were reused for each sequence. Storage of the beams was best managed by suspending the beams as simply supported ones, since this way the concrete was subjected to compression equilibrating the tensile stresses generated by shrinkage.

During preliminary tests on Beams 1 and 2 in static three point bending, the interface bond between concrete and GFRP failed in shear. Since it was shown that the poor bond was due to penetration of silicone into a thin surface layer of GFRP, the top flange surfaces of Beams 1, 2 and 7 were sand smeared with a rotating grinder and thoroughly cleaned with acetone before the adhesive was applied. In this manner most of the silicone was removed and a substantially better bond was achieved. Nevertheless, this is a warning to the reliability of a manufacturing process and it can be anticipated that

similar problems might occur in practice. Therefore, it is strongly suggested not to rely on adhesion only, but rather provide adequate mechanical connectors to enhance the safety of these hybrid members.

5.2.2.3.2 CFRP Bonding

The design performed in Section 5.2.2.1 suggested that a CFRP thickness of 0.1 mm be used for the hybrid beam construction, providing the required safety and at the same time allowing for a pseudo-ductile failure pattern in bending. On the other hand, it is hard to manufacture and handle laminates that are so thin, and an alternative solution was found by reducing the width and increasing the thickness of the CFRP laminate such that the total cross sectional area was maintained the same. It was anyway assumed throughout the analysis that the strain distribution across the width of the beam was constant, and hence no modification of the analysis would be necessary. The fact that the centroid was slightly shifted due to a locally thicker CFRP sheet can be neglected and the analysis developed earlier is still valid. Thus, the thin CFRP sheets which resulted from the analysis were substituted with two straps of CFRP 1.0 mm thick, but only 10 mm wide, located close to the boundaries of the bottom flange. The CFRP application procedure was very much alike the one described for the small scale beams. The nylon mesh was first peeled-off from the GFRP flange as shown in Figure 5.21. It can be seen that the beam was placed upside down and supported in such a manner to impose only compression in the concrete (ideally when the supports are within quarter points of the total beam length). The rough surface obtained was cleaned with acetone and prepared for the adhesion. The shear stresses to be induced at the CFRP/GFRP interface are an order of magnitude less than those at the concrete/GFRP interface, and therefore the problem with the poor bond mentioned earlier was not an issue here.

The CFRP was produced according to the pultrusion process by a local manufacturer using M46J carbon fibers at a fiber volume fraction of more than 70% and an epoxy matrix. The supplied sheets had cross sectional dimensions of 1x100 mm. These sheets were cut into straps of 10 mm. The surface of the CFRP sheet was first sand-papered and then wiped with an acetone saturated tissue until no signs of resin could be found on it. This was very important, in order to remove the resin rich cover of pultruded CFRP laminates which represents a weak point in adhesion. The adhesive used was a two-component epoxy based structural adhesive from Ciba-Geigy (Araldit). It was applied to both the CFRP and GFRP surfaces. After the CFRP straps were placed into

their final position, two steel profiles were laid on top and fastened with clamps providing an evenly distributed pressure on the bond. This is shown in Figure 5.22. The adhesive was cured for 18 hours after which the clamps were removed and the adhesive reached its full strength.

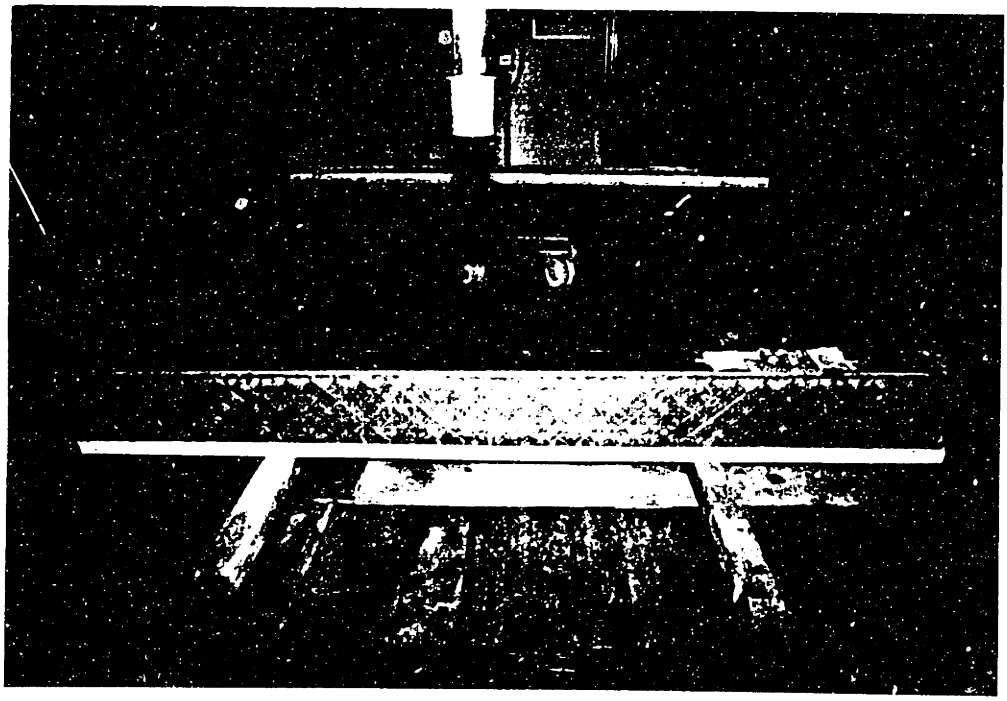

Figure 5.21 Surface preparation for CFRP bonding.

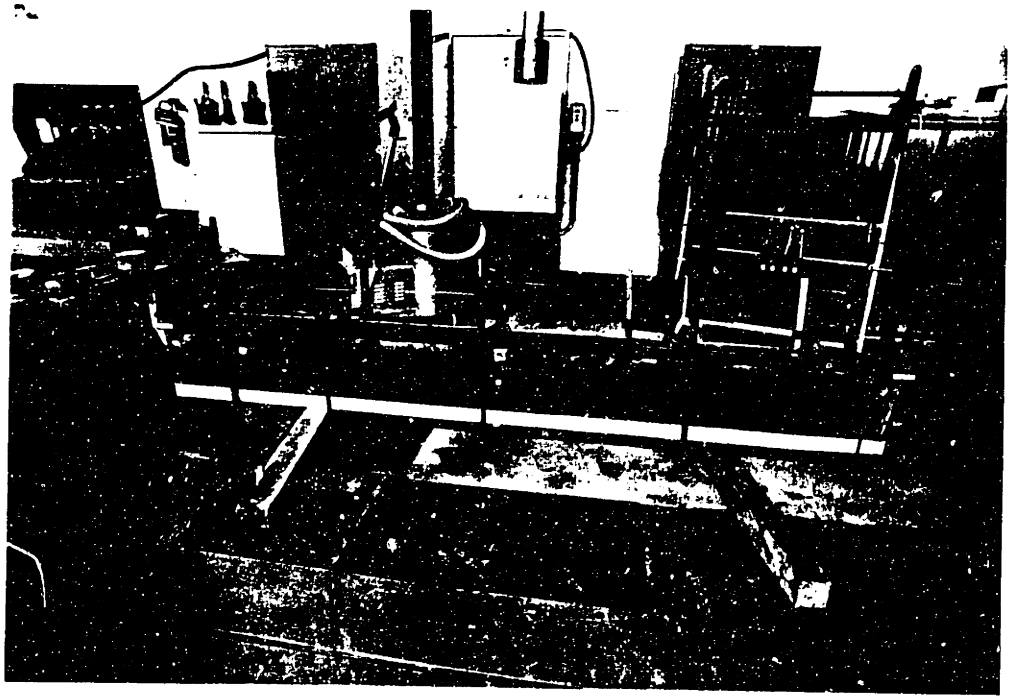

Figure 5.22 CFRP bonding.

5.2.2.3.3 Shear Connectors

It was mentioned earlier that the bond at the interface between the concrete and the GFRP was not satisfactory to transfer the shear force across it. Findings from an investigation using infrared spectroscopy indicated that at the surfaces of the failed bond remainders of the silicone impregnation of the nylon peel-off mesh and the adhesive from the Scotch band used were identified. These apparently contributed to the weakening of the bond between the box beam and the concrete layer. It was found that due to the rough surface cleaning with acetone was not sufficiently effective, and parts of the silicone impregnation were left behind in microscopic grooves. The recommendation for future GFRP box beam construction includes (a) the substitution of the silicon impregnation with a Teflon based one for the peel-off nylon mesh and (b) the discharge of the Scotch tape. In addition, after the impregnated mesh was peeled-off, the surface should be cleaned repeatedly with a clean tissue, and then rasped until some fibers become visible. Finally, the whole surface should be blasted by compressed air.

The weakness in the bond was overcome by applying mechanical shear connectors on beams 3 to 6. The connectors were made of standard M8 steel bolts, using 50 mm wide plates to transfer the bolt force into the concrete and GFRP, avoiding stress concentrations. Holes were drilled through the concrete and GFRP flange with a diamond drill based on water cooling; after placing the bolts, the gap in the holes was grouted with a penetrating viscous epoxy resin which when hardened provided perfect support for the bolts. The bolts were prestressed with a torque key to 9 Nm producing a tensile force of 14 kN in each of them. An alternative to the steel bolts was obtained by prestressing Kevlar bars and anchoring them with epoxy resin. The procedure includes: (a) drilling holes through concrete and GFRP; (b) anchoring one side of the Aramid bar by splicing and bending single fiber bundles of the bar and embedding them in epoxy resin; (c) inserting the stud in the hole from the inside of the beam and prestressing it with an ARAPREE® conical socket anchor (see Figure 5.23) and an expansion cell; (d) slicing the prestressed end and inserting a conical insert (which can be made of CFRP); and (e) grouting and anchoring with epoxy resin. This procedure was tested and showed satisfactory results, but the method has to be modified and automated in order to represent a viable alternative from the economic viewpoint. In general, the issue of mechanical fasteners has to be adjusted to the availability of adequate models which can be implemented easily in the construction practice, as well as the decision made on

inserting and fixing them onto the GFRP box beam before the concrete is poured on top of them.

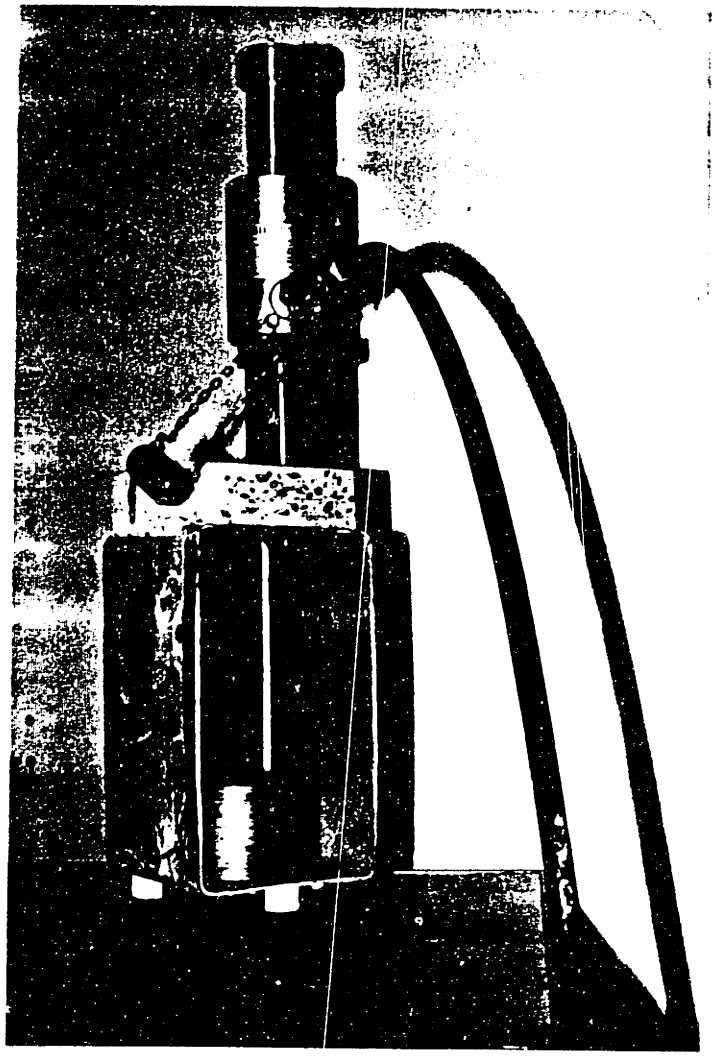

Figure 5.23 Prestressing of Kevlar shear connectors .

Beams 3 and 4 were loaded in three point bending and needed shear connectors throughout the whole length, while Beams 5 and 6, loaded in four point bending, needed fasteners only in the outer span regions. A total of 32 shear bolts was used for beams 3 and 4, as shown in Figure 5.24, and only 20 for Beams 5 and 6. The connectors were evenly distributed along the beam in two parallel rows. The number of studs was calculated from the condition that they should be able to carry the same amount of shear required to fail the concrete, which is assumed to be the weakest material in shear.

Figure 5.24 Shear bolt layout.

5.3 Static test setup

All the small scale beams were subjected to three point bending tests up to failure, the plain GFRP beams were all loaded in three point bending in their elastic region to obtain their equivalent stiffness and from there the GFRP material elastic moduli, and the full size hybrid Beams 1, 3 and 4 were loaded in three point bending to failure, too. Beams 1 and 2 were also loaded in three point bending but failed prematurely by debonding of the concrete due to poor bond. The GFRP box profiles of these beams were reused, and after a better surface preparation new concrete was cast providing the compressive zone.

5.3.1 Small Scale Tests

In order to study the behavior of the small scale hybrid beams experimentally, a series of three point bending tests was carried out using an INSTRON 1521 machine with a load capacity of 200 kN. A linear voltage differential transducer (LVDT) was installed to measure the mid-span displacement, so that the complete load-displacement curve was

recorded using an X-Y plotter. All tests were carried out by controlling the cross head displacement rate at 10 mm/min. The 18 beams were tested at an age between approximately 30 and 45 days to failure and failed according to various mechanisms, which will be discussed in Chapter 7. The test setup is given in Figure 5.25. The deformation of the supporting frame was measured separately and used to correct the deflection measured with the LVDT.

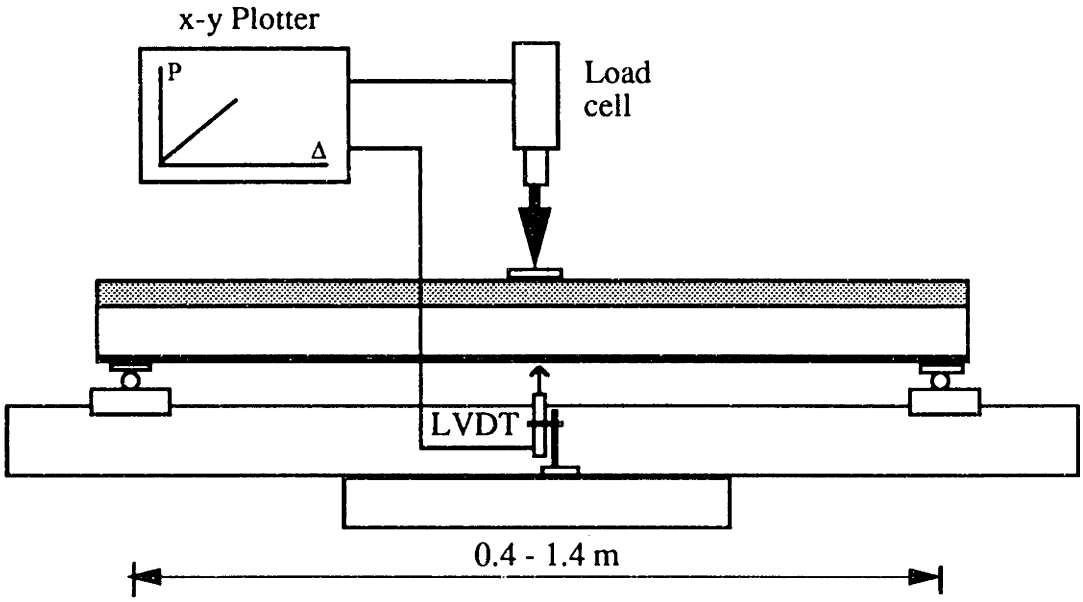

Figure 5.25 Small scale tests setup.

5.3.2 Full Size Test

Two types of tests were carried out in three point bending. One was implemented in order to obtain approximate stiffness properties of the plain GFRP box beam, while the other was used to evaluate the response of hybrid beams to failure. All tests were performed over a span of 3.0 m on the same loading frame. The load was applied through a 150 kN capacity hydraulic jack which was powered by a compressor unit. The supports consisted of 110 mm long and 20 mm thick steel plates on which the beams were grouted using a fast curing mortar mix. The length of the plates was computed from the condition that the compressive stress on the GFRP webs, localized at the load application points, was not to exceed the material's compressive strength. Additionally, at the support and at mid-span plywood diaphragms were inserted and fastened with adhesive and clamps to prevent localized sidesway buckling of the webs. The

diaphragms were also necessary to distribute the reactions from the support into the GFRP box beam webs.

The load was measured using a linear voltage pressure cell which was calibrated prior to testing with a high accuracy load cell. Strains were measured by strain gauges and at some locations with a 200 mm digital deformmeter, which had a displayed accuracy of 0.001 mm. The latter method was used to verify the strain gauge readings and to obtain an average measurement of deformations over a larger area. The displacements were recorded with two LVDTs of ± 50 mm deformation range, which were fixed to the loading frame and measured the deformation at mid-span of the beam, and at mid-height of the web.

The data resulting from the experiments were recorded using a static data acquisition system (DAS) obtaining readings from strain gauges, LVDTs and the pressure cell. The data acquisition system had the capability of recording up to 60 channels, with a maximum reading interval frequency of 1 Hz. The deformmeter readings, used especially in the plain box beam stiffness tests, were recorded by hand at specific load level increments.

5.3.2.1 Static Three Point Bending on Plain GFRP Beams

Figure 5.26 shows the test layout used for the measurement of the stiffness of plain GFRP beams. The intent was to obtain an equivalent shear modulus by using a nondestructive procedure and implementing simple beam theory. At the same time the assumption on the web and flange material properties could be verified by comparing experimental and analytical results. The test was carried out on all 7 box girders applying the loads within the elastic response range (the maximum load was 10 kN). Two data types were extracted: (a) mid-span deflection; and (b) strains at 500 mm (beams 3, 4, 5, 6 and 7) and 1000 mm (beams 1 and 2) from the support, where bending moments and shear forces could be calculated. The data were then manipulated properly to obtain the average material properties.

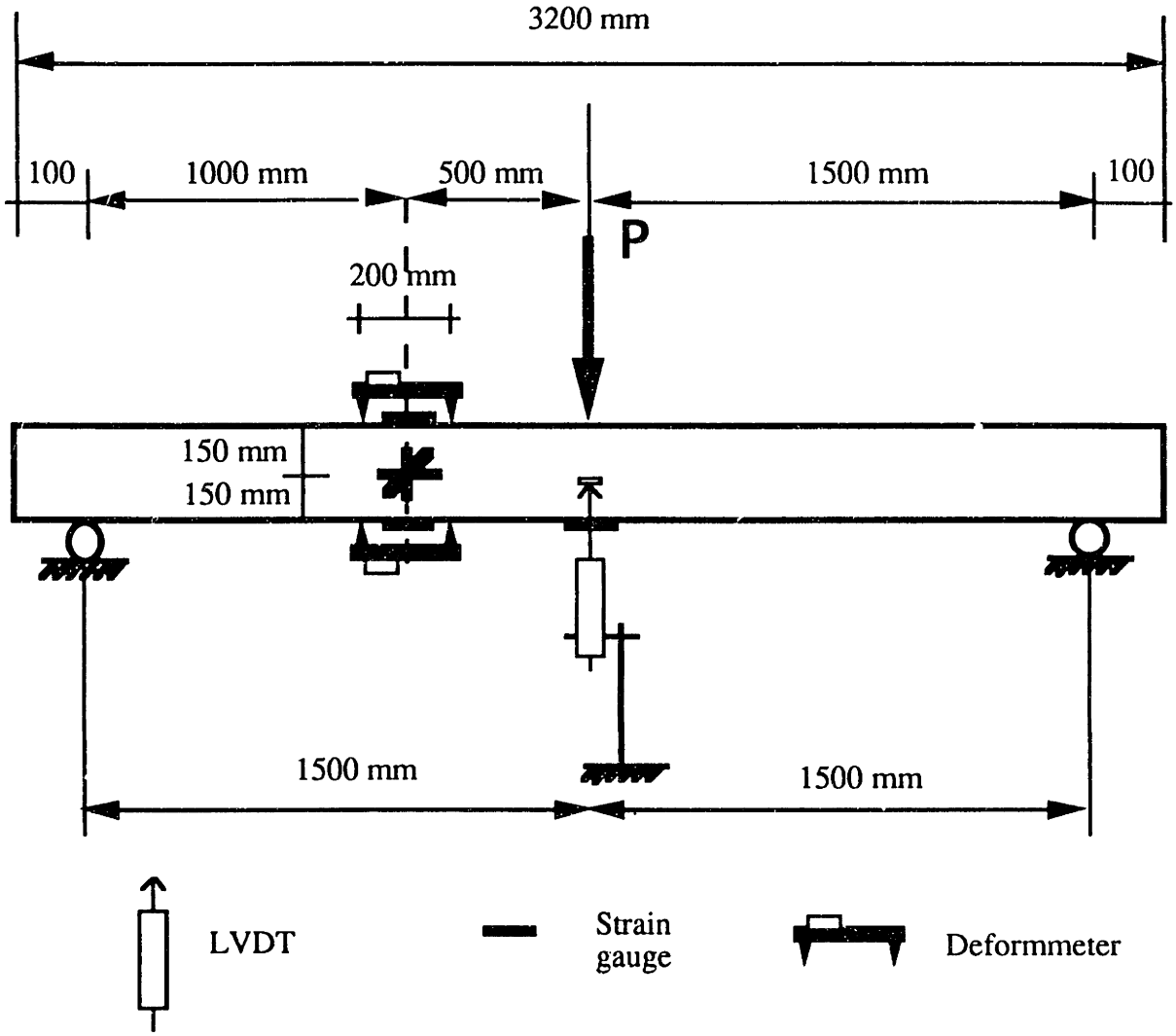

Figure 5.26 GFRP box beam stiffness test setup.

The strain was measured at the top and bottom flange with a 10 mm strain gauge bonded onto the GFRP surface, and with a set of deformmeter bolts. At the mid-height of the web a 0/45/90° rosette (Figure 5.27) with 10 mm gauge region was used to obtain data for the calculation of shear strains. A total of 6 channels were required for the DAS and the readings were recorded continuously at 1s intervals. The measurements with the deformmeter were carried out at 2.5 kN load increments. The loading speed was 4 kN/min which would probably result in some creep of the beam during testing, but since very low load values were applied the effect of creep was neglected in the calculations.

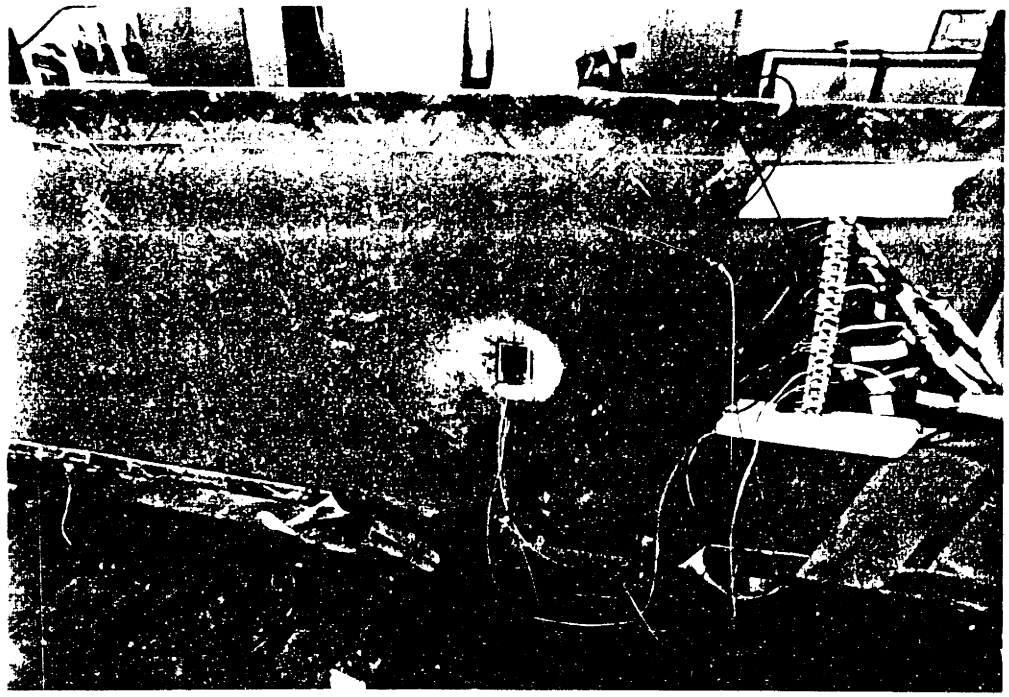

Figure 5.27 Application of rosette on GFRP web.

5.3.2.2 Static Three Point Tests on Hybrid Beams

Beams 1, 3 and 4 were tested in three point bending up to failure. Beams 3 and 4 were constructed with shear connectors, while a good bond between concrete and GFRP of Beam 1 relied only on the improved surface preparation and on the use of strong adhesion. Two locations were used for the measurement of cross sectional strains. Section 1 was defined 200 m from mid-span and was used to monitor strains at a section as close as possible to the maximum bending moment position. Strain gauges were bonded at the GFRP bottom flange and CFRP laminates as shown in Figure 5.28, in-between deformmeter bolts. A 50 mm long strain gauge provided the concrete strains in the concrete surface. The application of strain gauges to concrete deserves special attention. The surface had to be smooth, which was achieved by grinding down the concrete surface with a diamond blade grinder and using a two component primer. For accurate results the strain gauge length should be at least 2 to 3 times larger than the maximum aggregate size. Section 2 was defined at the same location where strains for the stiffness tests were measured and was equipped with the same layout of strain gauges as section 1. An additional feature of section 2 was the rosette at the GFRP web wall and a strain gauge attached to the top GFRP flange and embedded within the concrete layer.

This strain gauge was covered with a special silicone layer to protect it from moisture in concrete and eliminate any bond with concrete ingredients.

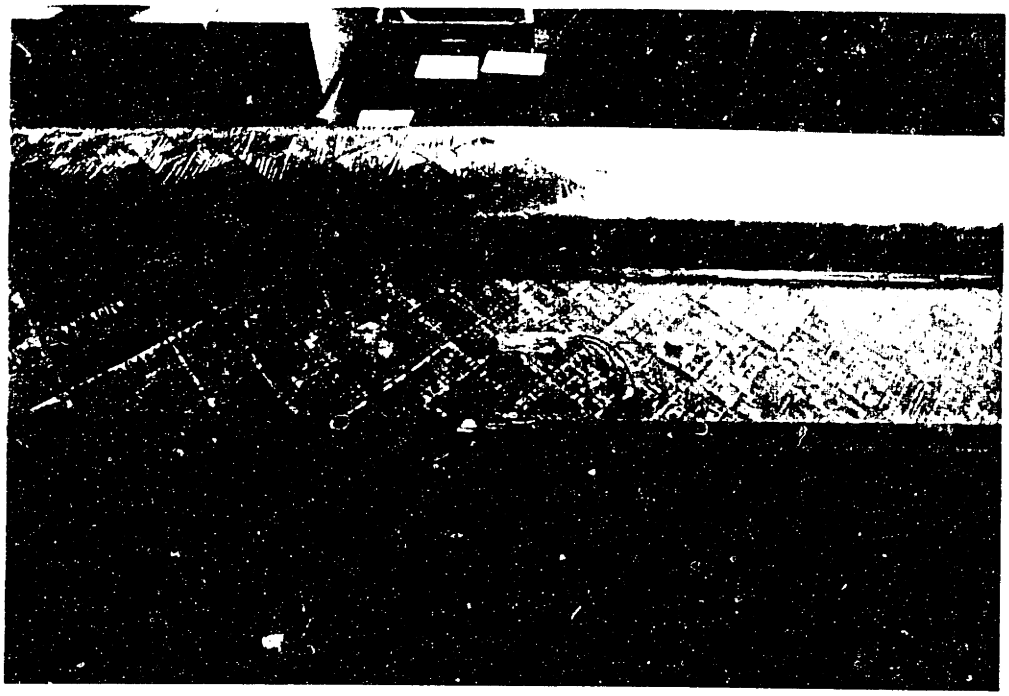

Figure 5.28 Bottom flange strain gauge layout.

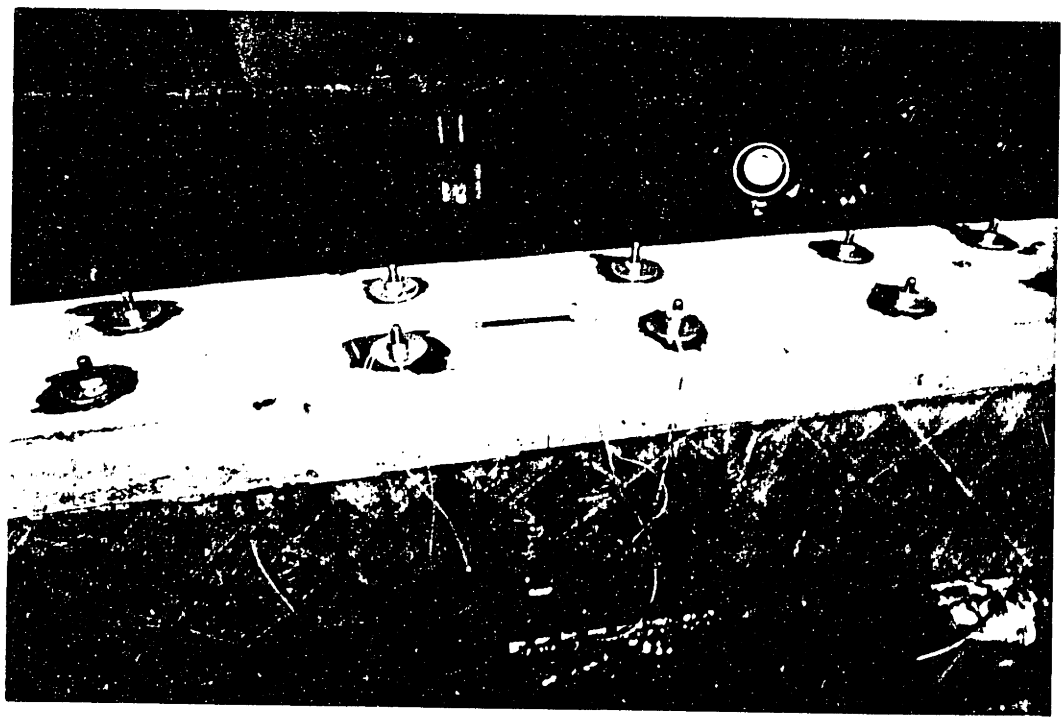

Figure 5.29 Concrete strain gauge and web rosette.

Figure 5.29 shows the concrete strain gauge and the rosette on the GFRP web. Two LVDTs (one at each side) were used at mid-span to record the mid-span displacements, which if averaged eliminated any torsional effects. It was shown that the two readings were identical and hence the beam deflection was maintained in a vertical plane. To measure the strain causing CFRP rupture, a strain gauge was attached to it at mid-span and strains were recorded with the DAS. This increased the number of channels required for data acquisition to 11. The load incrementation speed was set to 20 kN/min, which did not require the creep effects to be considered in the calculations but since the loading was driven up to failure, nonlinear material behavior had to be introduced. Figure 5.30 shows the test geometry while Figure 5.31 gives the setup.

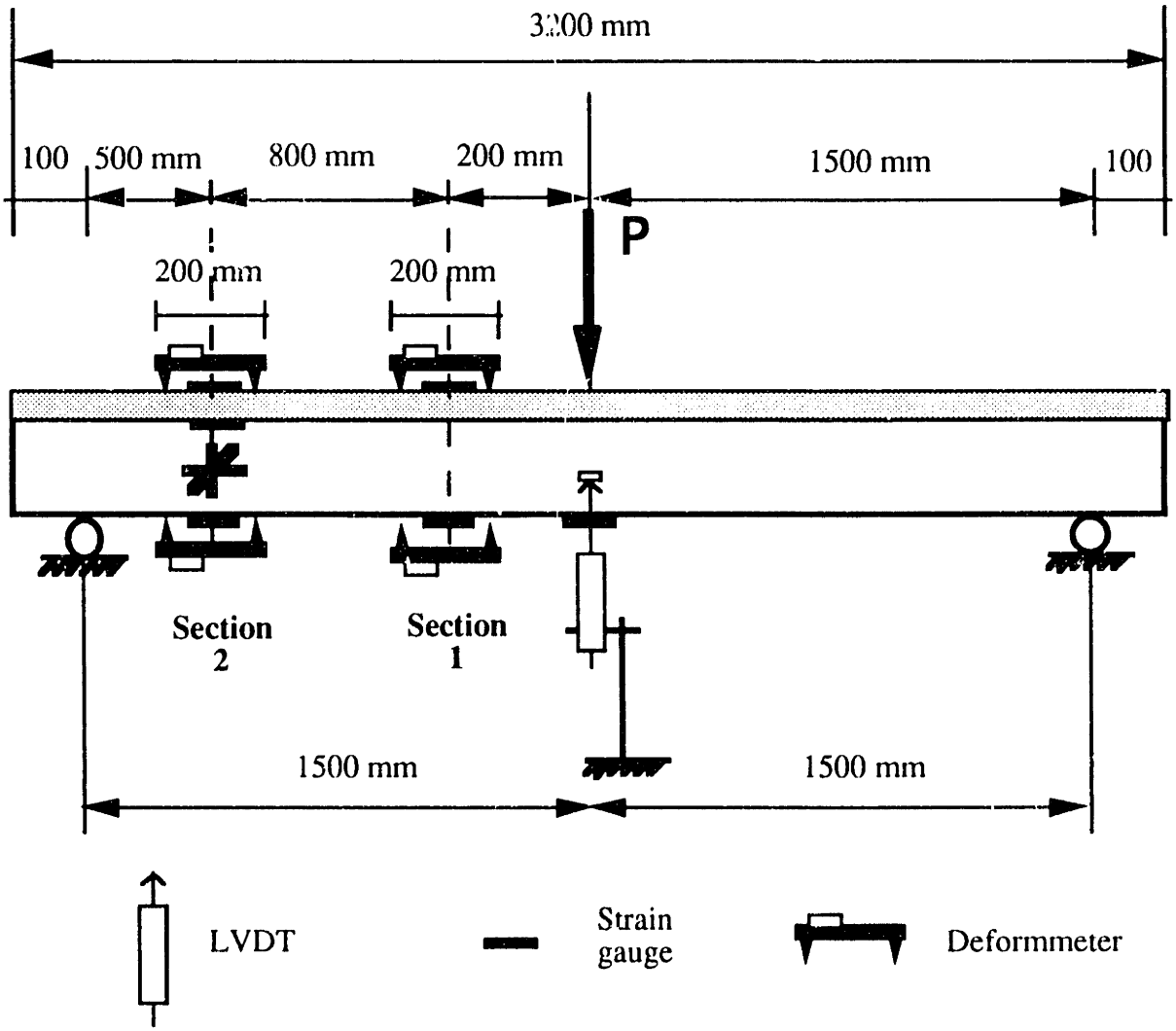

Figure 5.30 Hybrid beam static three point bending test geometry.

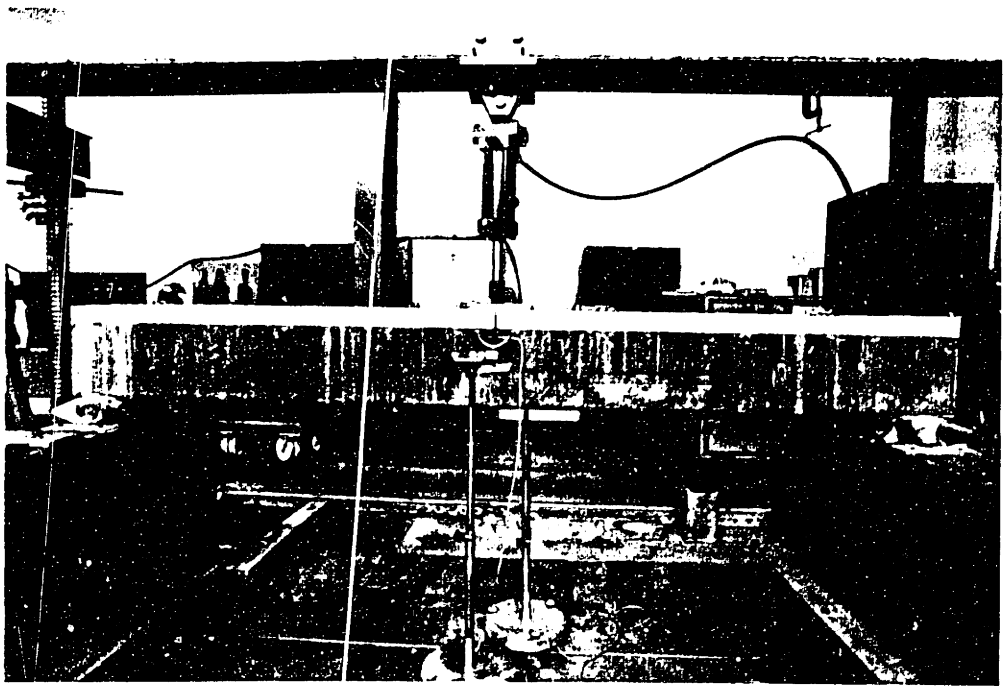

Figure 5.31 Hybrid beam static three point bending test setup.

The deformmeter readings were obtained to verify the accuracy of the strain gauges, but this was only possible in the elastic response regime since prolonged testing time would require that creep effects be taken into account. Also, at higher load levels the access to the beams becames risky due to the danger of a premature failure.

5.4 Creep Test Setup

The creep tests performed in this work can be subdivided into two groups. The first includes 24 hour tests carried out on Beams 5 and 6, performed with a loading frame which applied the loads through hydraulic jacks. The data were retrieved from strain gauges, pressure cells and LVDTs and stored on a DAS. The test setup was analogous to the one described in Section 5.3.2.2 except for the applied loads. A four point bending pattern was implemented such that a shear force free middle region was obtained, and the load was kept constant at 20 kN at each load point. Also, the location of the sections at which the strain profiles were measured was changed. The test geometry and strain gauge layout is given in the Figure 5.32.

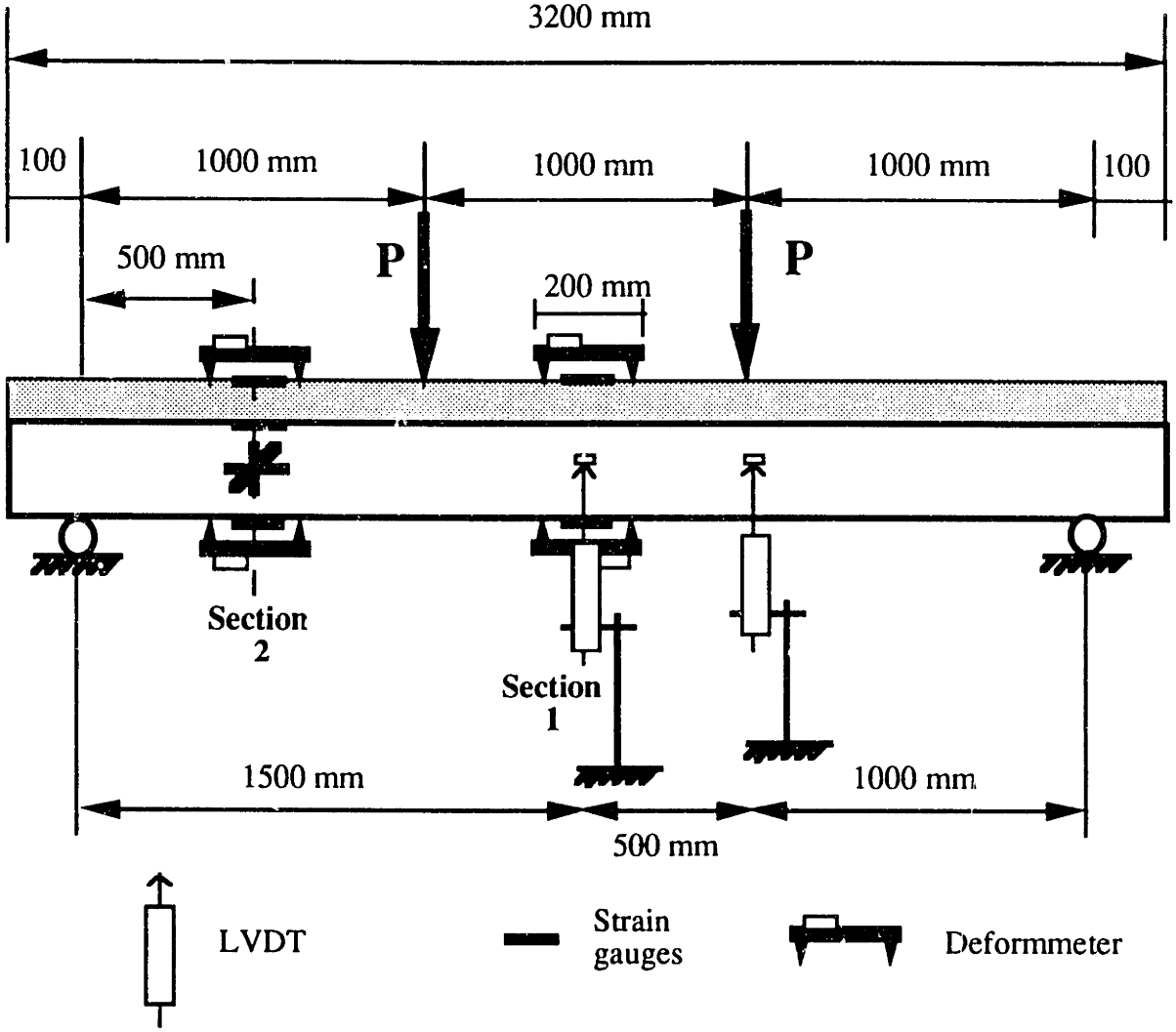

Figure 5.32 24 hour creep test setup.

The purpose of these tests was to determine the initial portion of the creep behavior of the hybrid beams. The room temperature during testing was monitored with a linear voltage thermometer and recorded with the DAS. Parallel to this, dummy strain gauges were applied to GFRP and concrete to obtain correction values taking temperature oscillations into account. In addition to the data recorded by the DAS, strain values were also measured with the deformmeter.

The other group of creep tests carried out includes tests on Beams 2 and 7 which are planned to be conducted for several years. The loads were applied with gravitational blocks appended on the hybrid beams. Beam 2 was installed as shown in Figure 5.33 in a laboratory with almost constant temperature and humidity. On the other hand, Beam 7 was exposed to weathering and environmental impact and was deployed outdoors. Figure

5.34 illustrates the test setup. The strains and deflections are still monitored with deformmeter and dial gauge readings, respectively. The total load applied to Beam 2 amounts to 42.68 kN, while Beam 7 supports a load of 39.18 kN in dry condition. Note that the load on Beam 7 might increase if the concrete blocks are saturated with water from weathering. The geometry of the tests is given in Figure 5.35. The strains in the bottom flange are measured at three points of each section: one on the GFRP and one on each of the CFRP sheets. The temperature is monitored through thermometers and recorded with all the other data during each measurement sequence.

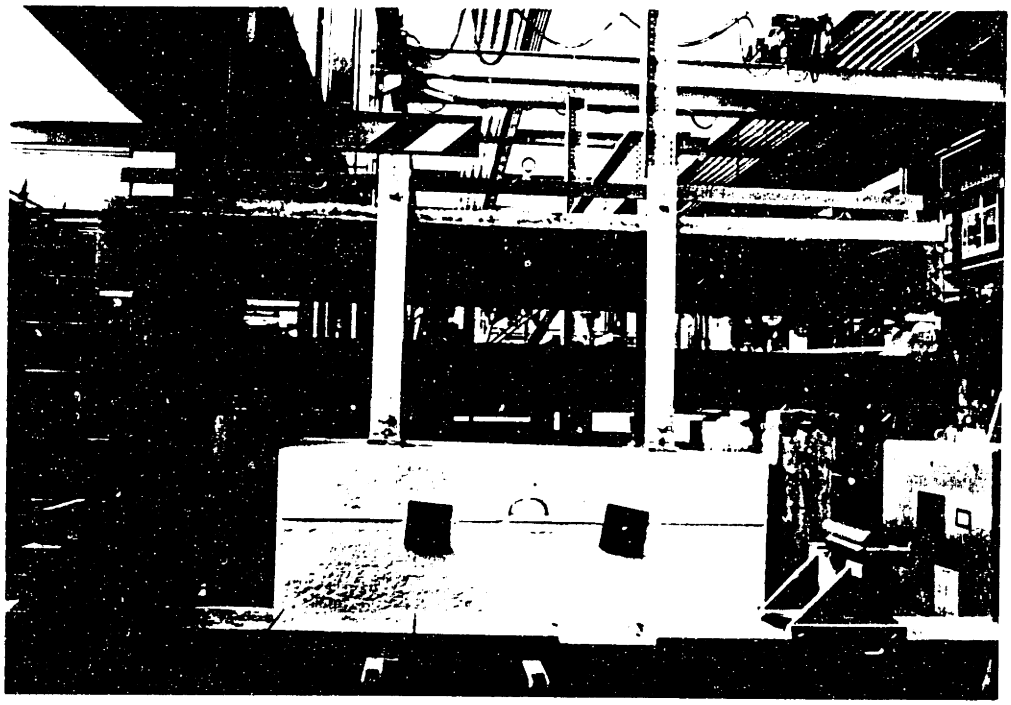

Figure 5.33 Indoor creep test layout.

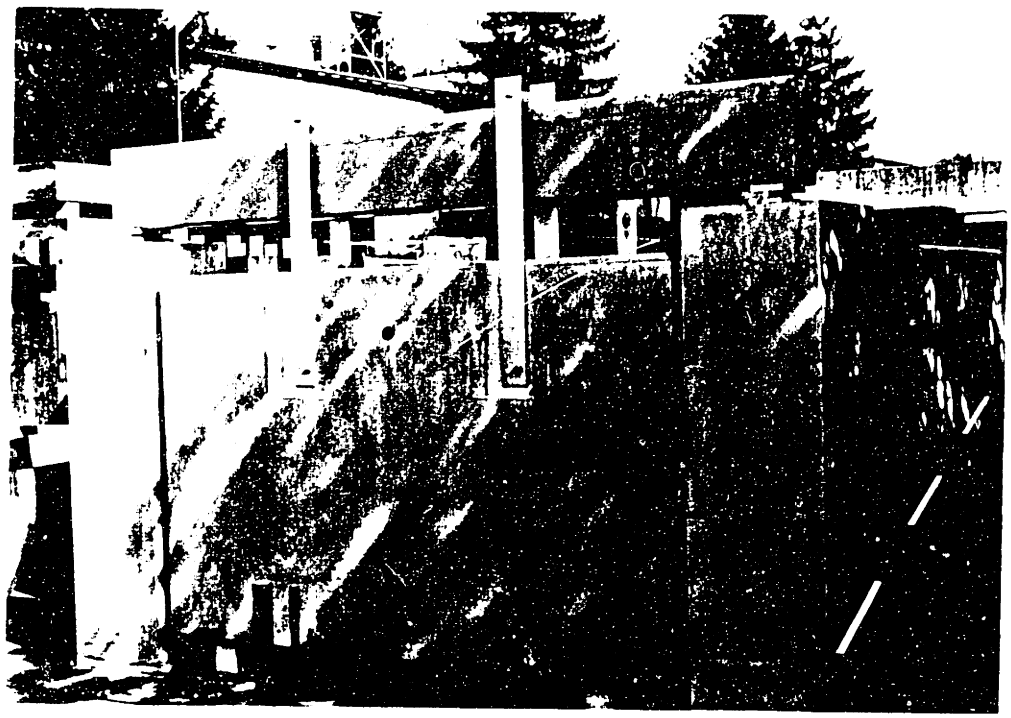

Figure 5.34 Outdoor creep test layout.

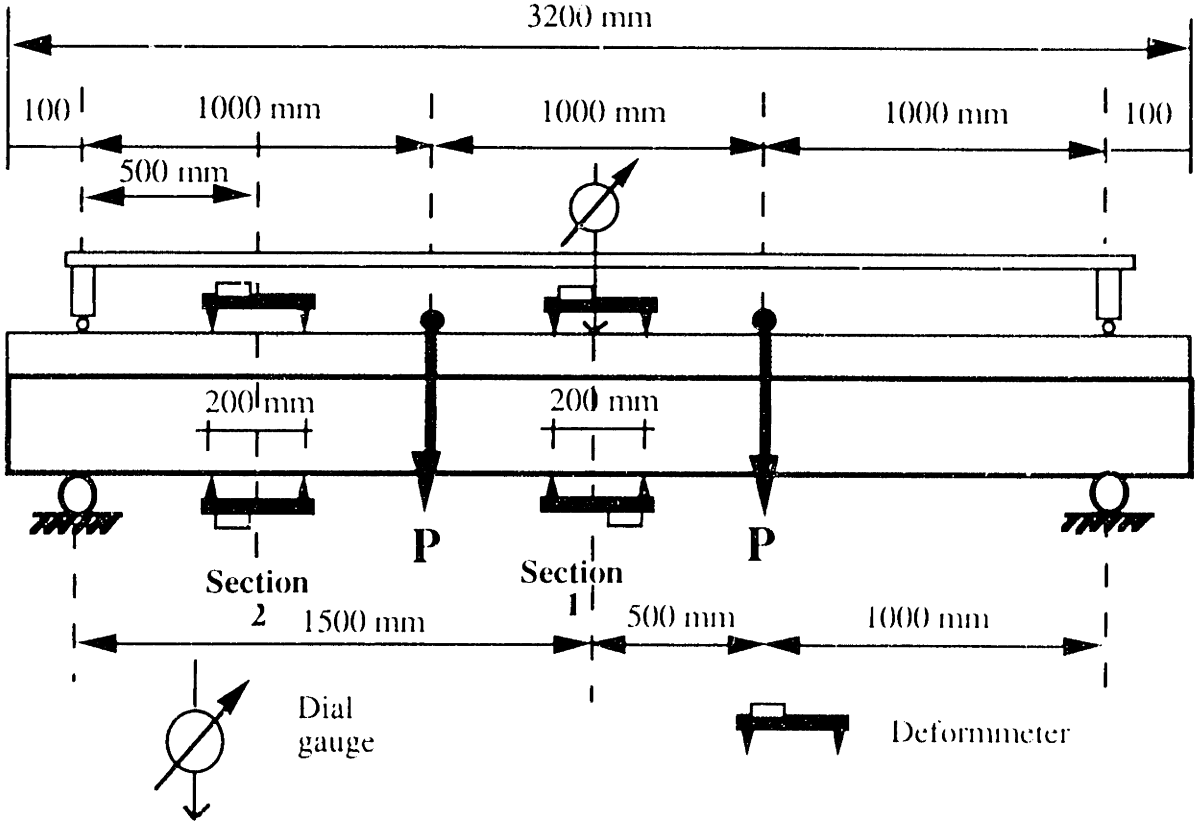

Figure 5.35 Creep test setup.

5.5 Fatigue Test Setup

The analysis developed for fatigue in Chapter 4 was validated through four point bending tests on Beams 5 and 6. The test setup was similar to the one described for 24 hour creep tests in the previous section, but with cycling loading. Figure 5.36 shows the test setup. Each of the two hydraulic jacks had a capacity of 140 kN, while the powering machine was a swing compressor with a total capacity of 110 kN. For residual strength tests (static loading) a 200 kN compressor was added. The test was load controlled; and different maximum load levels were applied with a constant frequency range of 4.2 Hz.

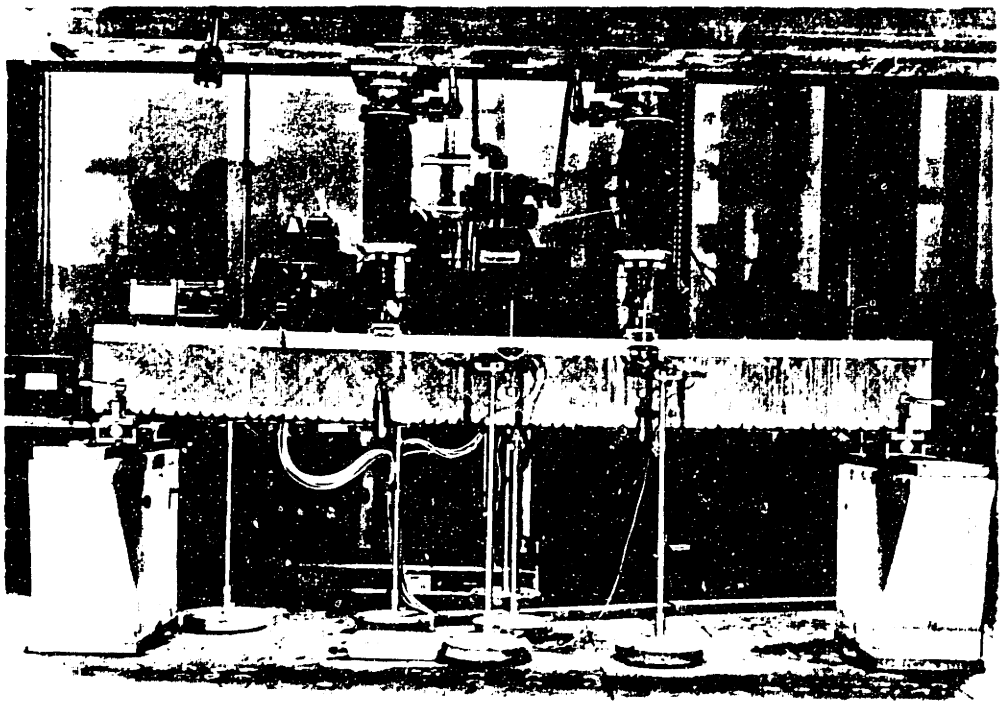

Figure 5.36 Fatigue test setup.

Figure 5.37 shows the sinusoidal loading pattern implemented, indicating maximum and minimum load ranges. Beams 5 and 6 were cycled with 60 and 80 kN (total magnitude for both load points) maximum load, respectively, and had a corresponding minimum load magnitude of 20 and 40 kN. Special attention was devoted to the support and load application points. The steel plates used at these locations were bonded with a two component epoxy based spackle in order to avoid friction and local wear of the specimens due to load cycling. Steel rollers were used to allow for free rotation and movement. Figure 5.38 shows the support in detail.

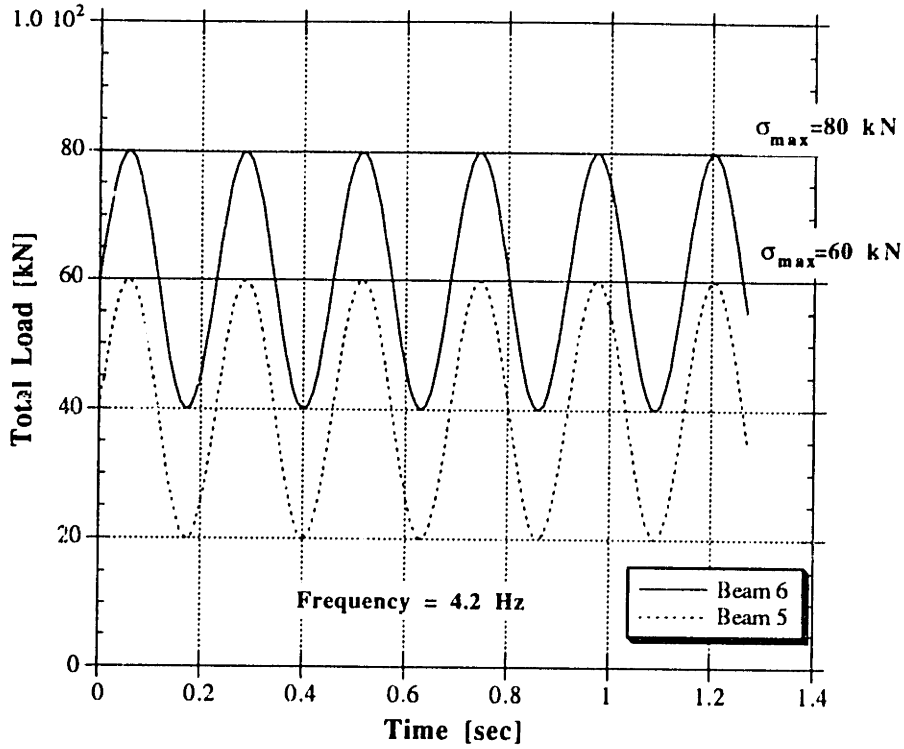

Figure 5.37 Dynamic loading configurations.

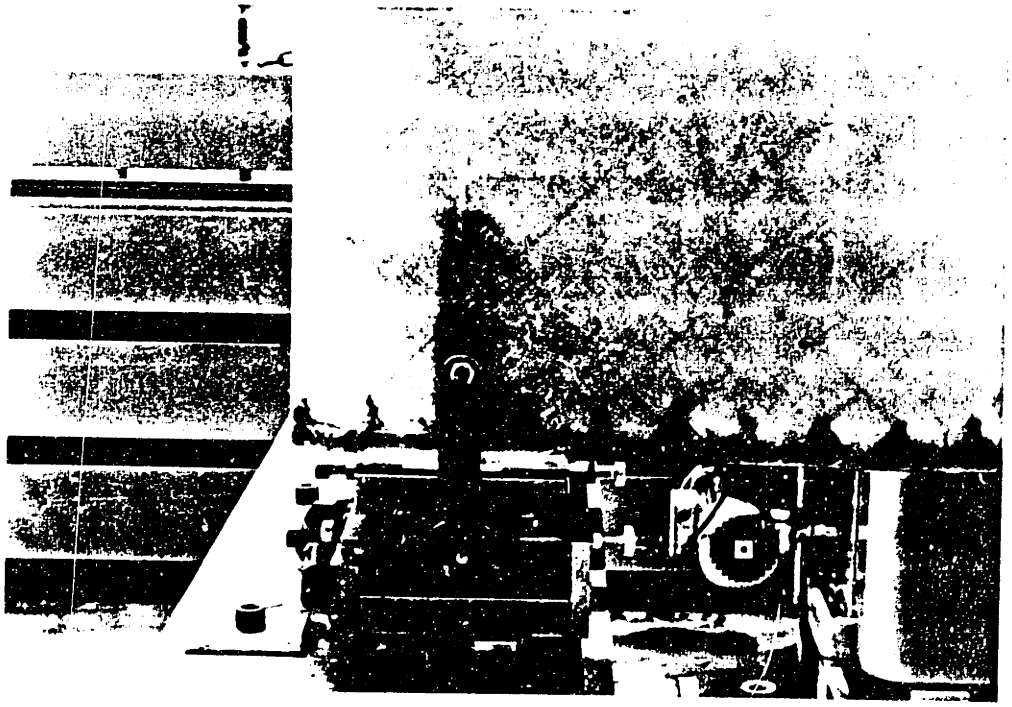

Figure 5.38 Support detail in fatigue.

The beams were loaded first with a constant load corresponding to the lower load magnitude provided with a static compressor. This value was then incremented with a dynamic load ranging between zero and the amplitude, P_{max} - P_{min}, which was achieved with a swing compressor. The effects of combined fatigue and creep were measured after each decade of cycles (1,10,100,...) until failure. At these instances, the beam was unloaded first, and then, while the loading was increased statically from zero to the maximum load level, continuous measurements were conducted (with a 1 second frequency). The load incremetation speed was 70kN/min. The data were retrieved and stored using a static data acquisition system. Two locations were used to monitor the strains with strain gauges. Deformmeter bolts were added and deformmeter readings taken to supplement the data from strain gauges. At several instances, due to microcracking of the matrix, strain gauges at the GFRP surface malfunctioned. If a matrix crack occurred beneath the strain gauge area, the gauge's resistance increased drastically. In this case, either a new strain gauge was attached and zeroed according to the value obtained from the deformmeter reading at the same location, or, if the cracks became too large and too distributed, a LVDT was attached to the surface and used with appropriate correction factors. This was necessary for Beam 6 in the last measurement after the CFRP had already failed. Figure 5.39 shows the strain gauges and deformmeter bolts used at one cross section in the bottom flange.

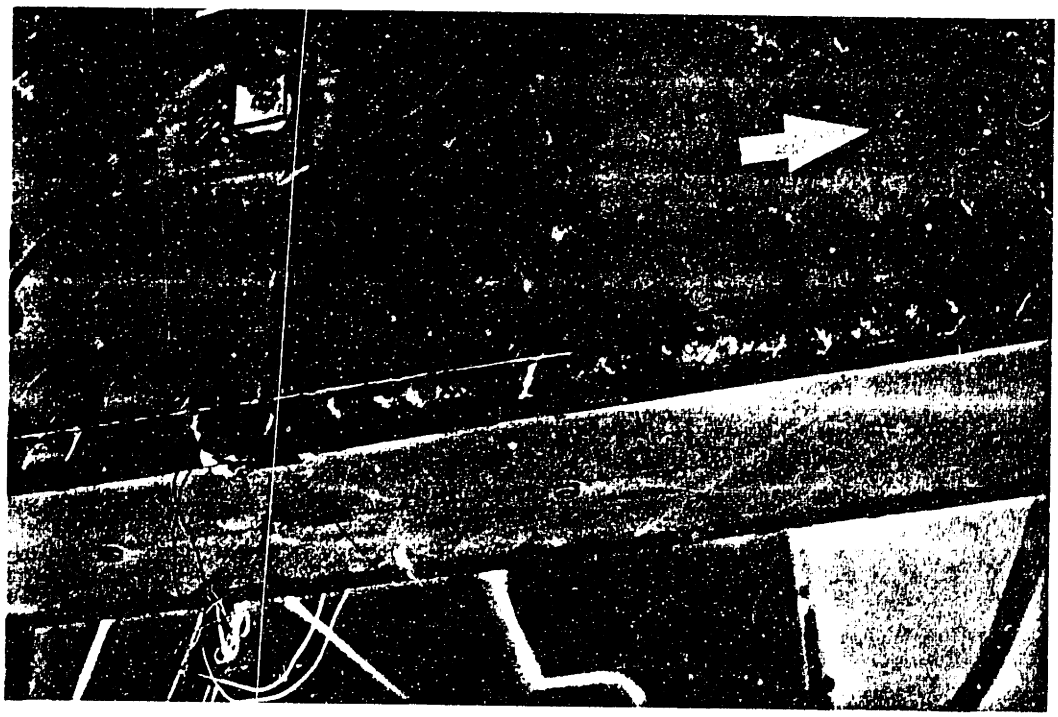

Figure 5.39 Bottom flange strain measurement equipment.

The layout of the fatigue tests with geometry and schematic strain gauge locations was given earlier in Figure 5.32. A total of 14 channels were used for the DAS.

5.6 Synopsis

This chapter gave an overview of the experimental program including the beam design procedure, test setups and details for both large and small scale beam construction. The subject presented here is needed for a better understanding of the results obtained from the experiments conducted on the hybrid beams which will be presented in Chapter 7.

Chapter 6

EXPERIMENTAL PROCEDURE FOR MODEL CALIBRATION

6.1 Introduction

The analysis described in Chapters 3 and 4 introduced several models for the characterization of the short term, shrinkage, creep and fatigue response of the three materials used for the manufacturing of the hybrid beams, that is concrete, glass and carbon fiber reinforced plastics. It was mentioned earlier that the parameters defining each particular model were obtained experimentally. In this chapter we describe the experimental procedure employed to calibrate the analytical models.

6.2 Experimental Characterization of Concrete Properties

Three different concrete types were used in the experimental program. The first two, comprising a normal strength (NS) and a high strength carbon fiber reinforced concrete (HS-FRC) containing silica fume, were used for the concrete layer of the small scale beams, while the concrete used in the large scale experiments was a standard high strength concrete (HS). The short term properties were evaluated for all three types of concrete using 50 mm diameter cylinders or 40x40x80 mm prisms. The short term stress-strain curves were evaluated and appropriate models adopted, and the elastic modulus and ultimate strength were defined. The shrinkage and creep properties for the concrete used in the large scale experiments were evaluated and the model parameters described in Chapter 4 were calibrated. Isochronic curves, defining the stress-strain response for equal times of applied load were also determined. In addition, the adopted fatigue model was presented and its effect on the stress-strain diagram was described.

6.2.1 Short Term Properties of Concrete

The short term properties of the concrete used in the small and large scale beams were determined in three groups of tests. The first were carried out in order to obtain the initial elastic modulus by measurements from compression tests on cylindrical specimens subjected to three loading-unloading cycles up to stress levels of 5, 10 and 15 MPa. The second group included a compression crushing test up to failure where the ultimate strength was recorded. The third test series was performed in order to obtain the stress-strain relationships. While all other tests were carried out on 50x150 mm cylindrical specimens, 40x40x80 mm prisms were used for the evaluation of the stress-strain relationship of the small scale beam specimens, . In both cases the aspect ratio of 2:1 or more for the length and width of specimens was maintained in order to eliminate frictional and confinement effects at the support locations. A specimen during a compression test is shown in Figure 6.1.

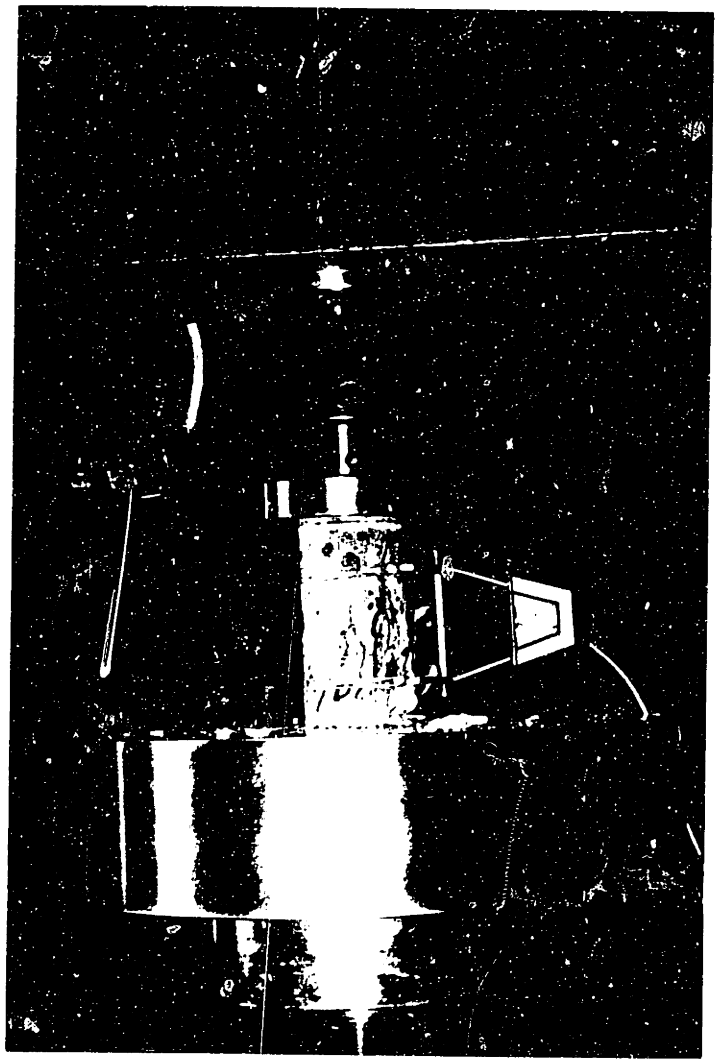

Figure 6.1 Test setup for concrete compression tests.

The tests were conducted with a computer guided hydraulic press and experimental data were recorded through a data acquisition system. The DAS had the capability of storing readings with the frequency of 120 Hz, which allowed the softening portion of the stress strain curve to be recorded. Deformations were measured using a clip gauge attached onto the specimen surface, while loads were recorded by means of a load cell built into the cross head. The model adopted for the HS concrete was described in Section 3.2.2, while for the concrete of the small scale beams an idealized bilinear model was adopted.

6.2.1.1 Material Properties of Concrete Mixes Used for the Small Scale Beams

The first series of small scale beams was cast using a normal strength concrete mix corresponding to the standard EMPA A/B aggregate curve (Beton Kalender 1987). The water to cement ratio was 0.5 and the maximum aggregate size was 16 mm. The exact weight proportions of the concrete mix employed are given in Table 6.1.

Table 6.1 Normal strength concrete mix for 40 liters of concrete.

Constituent	Weight (kg)
0-1 mm aggr.	18.82
1-4 mm aggr.	18.82
4-8 mm aggr.	15.84
8-16 mm aggr.	21.89
Cement	13.73
Water	6.89

The second series of small scale beams was cast using a high strength fiber reinforced concrete mix. From preliminary analyses it was anticipated that HS-FRC could enhance the structural behavior of the hybrid beams. FRC in general has a higher toughness and a higher strain at failure when subjected to compression. Moreover, the short fibers in the concrete mix would result in a much better control of shrinkage cracking. Common fibers used in concrete are made of steel, glass, polypropylene, aramid and carbon, the latter being the ones adopted in this study because of their superior properties. A series of different concrete mixes with different fiber types and fiber lengths were

produced and their material properties were determined from compression tests on 16x4x4cm prisms. Silica fume was also employed in order to increase the compressive strength. It was found that short fibers (length<6 mm) were more suitable for microconcretes while for normal aggregate concrete longer fibers were needed (length>10 mm). Table 6.2 gives the constituents of the mix employed (in weight percentages) for the second series of small scale hybrid beams, which resulted in increased strength and crushing strain. The mix contained 4 mm long carbon fibers and a superplastisizer to reduce the water content. The silica fume had an average particle size of 0.15 μm and a specific gravity of 2.10. It should be mentioned that regardless of the concrete mix composition, the workability of the fresh concrete is crucial for the properties of the hardened concrete. A careful compacting procedure was necessary for good concrete properties and therefore a hand vibrator was employed.

Table 6.2 Constituents of HS-FRC concrete by weight.

Water	16.91 %
Cement	56.46 %
Silica Fume	22.54 %
Super-plastisizer	3.38 %
Carbon Fibers	0.80 %

The stress-strain relationships of the two concretes used in the small scale beams were characterized from uniaxial compression tests on 40x40x80 mm prisms at the age of 28 days. These prisms were selected as more representative of the behavior of the thin top layer of the hybrid beams. Three displacement-controlled tests were run for each concrete type, recording the data up to a strain of 1.4%. The results obtained are given in Figures 6.2 and 6.3 for the HS-FRC and the NS concrete, respectively, along with the idealized stress-strain curves adopted later in the analysis of the beam test results. The idealized relationships are also summarized in Table 6.3. Note that in Figures 6.2 and 6.3 some of the curves are displaced deliberately, to allow better visualization of all the test results. The resulting elastic moduli are given in Table 6.4.

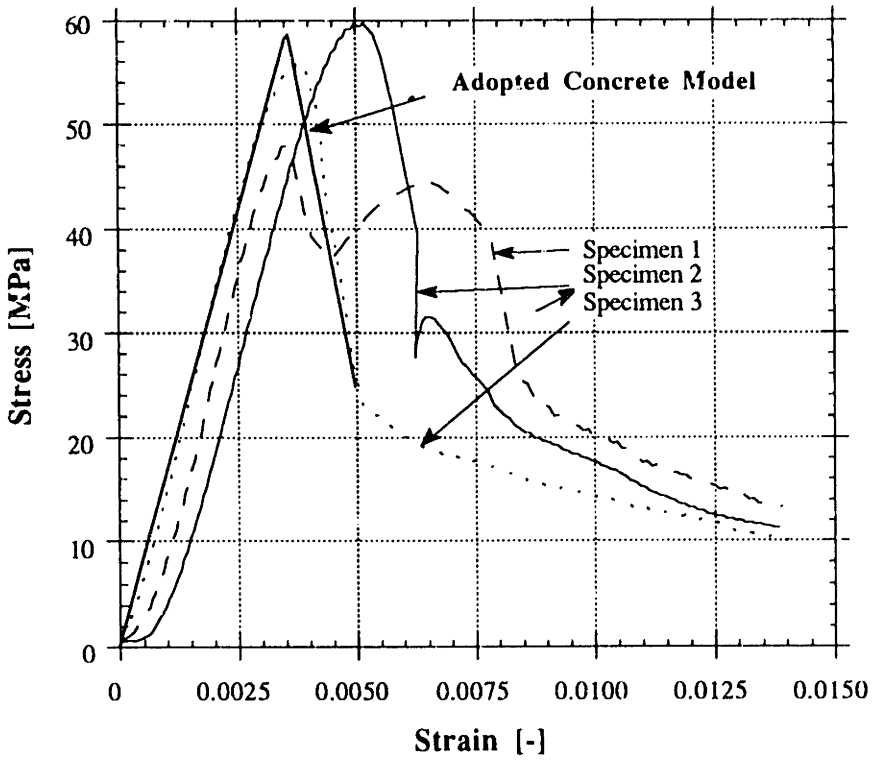

Figure 6.2 Stress-strain relationships for HS-FRC.

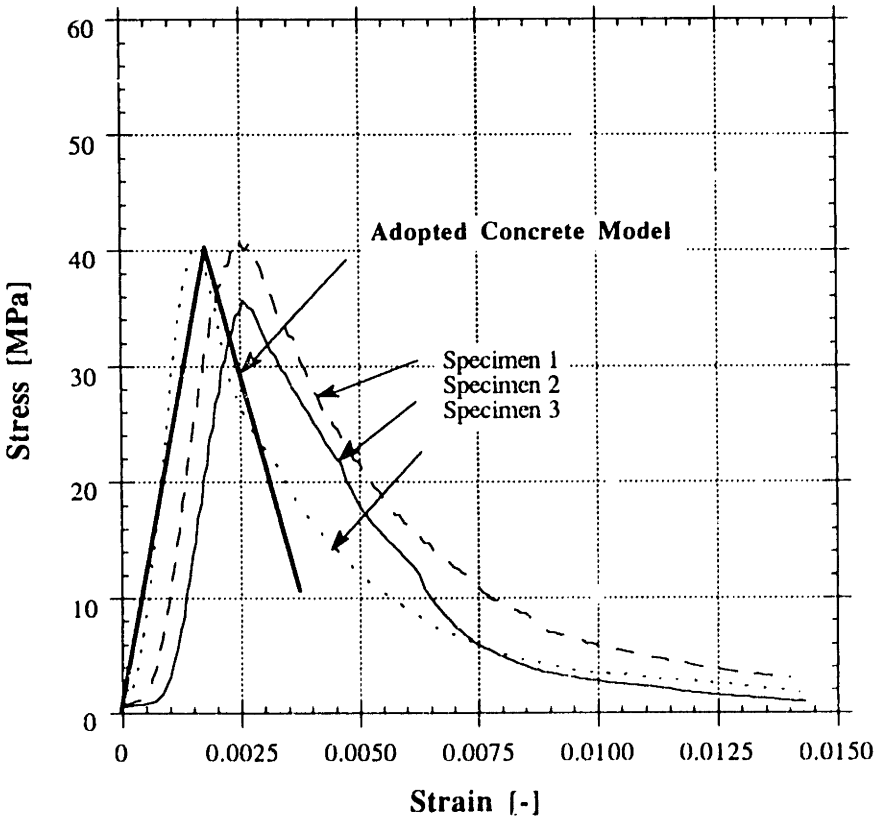

Figure 6.3 Stress-strain relationships for normal strength concrete.

Table 6.3 Material properties characterizing the idealized concrete models.

Concrete Type	Stress at Failure [MPa]	Strain at Failure [%]	Ultimate Stress [MPa]	Ultimate Strain [%]
Normal Strength	40	0.19	10	0.38
HS-FRC	58	0.35	25	0.50

Table 6.4 Elastic moduli of normal strength concrete and HS-FRC.

Specimen	Stress Range [MPa]	Elastic Modulus [MPa]
Normal Strength A	0 - 5	33641
	0 - 10	32978
	0 - 15	32567
Normal Strength B	0 - 5	34676
	0 - 10	34356
	0 - 15	34097
HS-FRC A	0 - 5	19160
	0 - 10	19408
	0 - 15	19297
HS-FRC B	0 - 5	19443
	0 - 10	19590
	0 - 15	19453

The average initial elastic moduli for the normal strength concrete and the HS-FRC were adopted at 33400 and 19400 MPa, respectively. It is seen that the fiber reinforced concrete has a considerably lower stiffness, which is attributed to the lack of coarse aggregates and, may be, to poor compacting; the fibers made the mix less workable and a higher air content may have resulted in decreased stiffness.

6.2.1.2 Material Properties of Concrete Mix Used for the Large Scale Beams

All the large scale beams were cast using a high strength concrete mix developed at the EMPA. The water to cement ratio was 0.4 and the maximum aggregate size was 16 mm. The exact weight proportions of the concrete mix employed are given in Table 6.5. The high strength was achieved by adding the superplastisizer Rheobuild 2000.

Table 6.5 High strength concrete mix for 50 liters of concrete.

Constituent	Weight (kg)
0-1 mm aggr.	21.45
1-4 mm aggr.	24.37
4-8 mm aggr.	22.42
8-16 mm aggr.	29.25
Cement PC	17.50
Water	7.0
Superplastisizer	0.350

Parallel to each beam a series of three 200x200x200 mm concrete cubes were cast. After the concrete had cured cylindrical specimens were drilled out and cut to the appropriate shape for further testing. Results from the elastic moduli and strength tests for the seven beams are given in Table 6.6.

Table 6.6 Elastic moduli of normal strength concrete and HS-FRC.

Specimen	Strength f_c' [MPa]	Elastic Modulus E_c [MPa]
Beam 1	46.5	41640
Beam 2	45.0	38656
Beam 3	43.0	38190
Beam 4	47.0	39678
Beam 5	48.6	42134
Beam 6	53.5	43597
Beam 7	47.5	39160

The reported values are an average of 5 tests. Each elastic modulus test had three load increments and a measurement was recorded for each of them. The compression tests were conducted within two days after the associated beam test in order to eliminate the aging effect of concrete as much as possible. This partially explains the variation of material properties although always the same concrete mix was used. As described in Chapter 3, the experimental values were used to model the concrete stress-strain relationship in the form of a fourth order polynomial. A comparison of the adopted model and results obtained from compression tests is depicted in Figure 6.4. It is seen that the model complies well with experimental results, particularly in the region before the concrete strength, f_c', is reached. Also the softening branch of the stress-strain curve is modeled with sufficient accuracy.

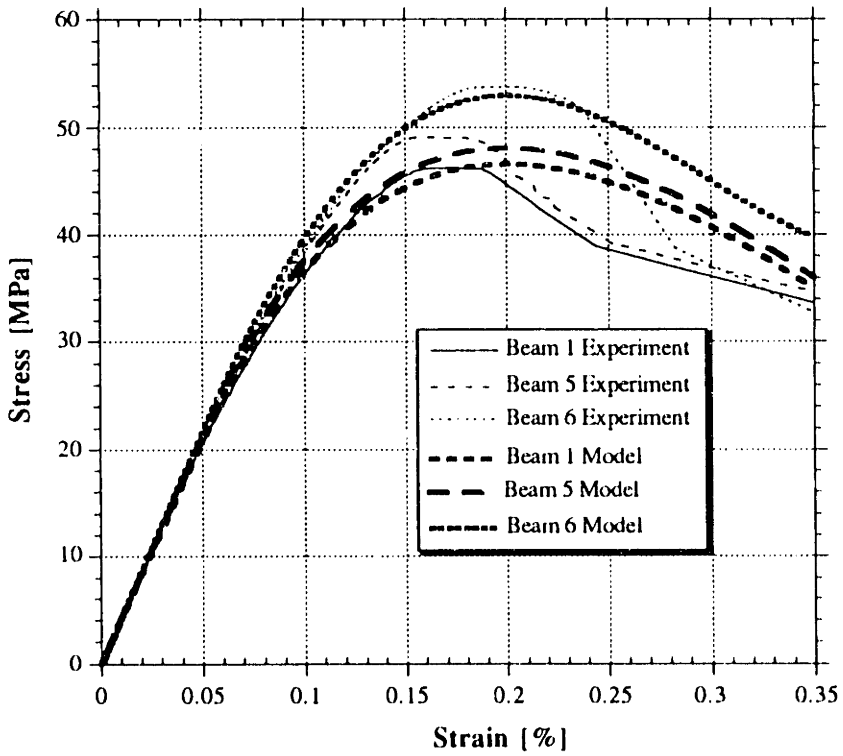

Figure 6.4 Comparison of concrete stress-strain model and experiment.

6.2.2 Shrinkage of Concrete

The concrete shrinkage model used in this work was adopted from the ACI Committee 209 (1971) and the empirical values defining the model were obtained from tests conducted on concrete specimens. Parallel to the manufacturing process of the concrete layer of the hybrid beams a set of three prisms 40x40x160 mm was produced with the same concrete mix. A pair of corrosion resistant deformmeter bolts was bonded onto the fresh concrete surface. The specimens were cured in water with the same schedule as the hybrid beams. After seven days the specimens were left at 70% relative humidity and 20°C for further curing. It was assumed that no shrinkage had occurred up to this time, and the concrete strains induced were measured using a deformmeter at daily intervals. The resulting shrinkage strain versus time data are given in Figure 6.5. ACI (1971) specifies the ultimate value of shrinkage strain dependent on several factors as described in Section 4.2.2. Using the empirical tables given by ACI the value of the ultimate shrinkage strain, ε_{shu}, was computed to be 0.8‰. Using this result and the experimental data a least squares curve fit to equation (4.3) was performed. The resulting parameters and the comparison of the model with experimental results are given in Figure 6.5.

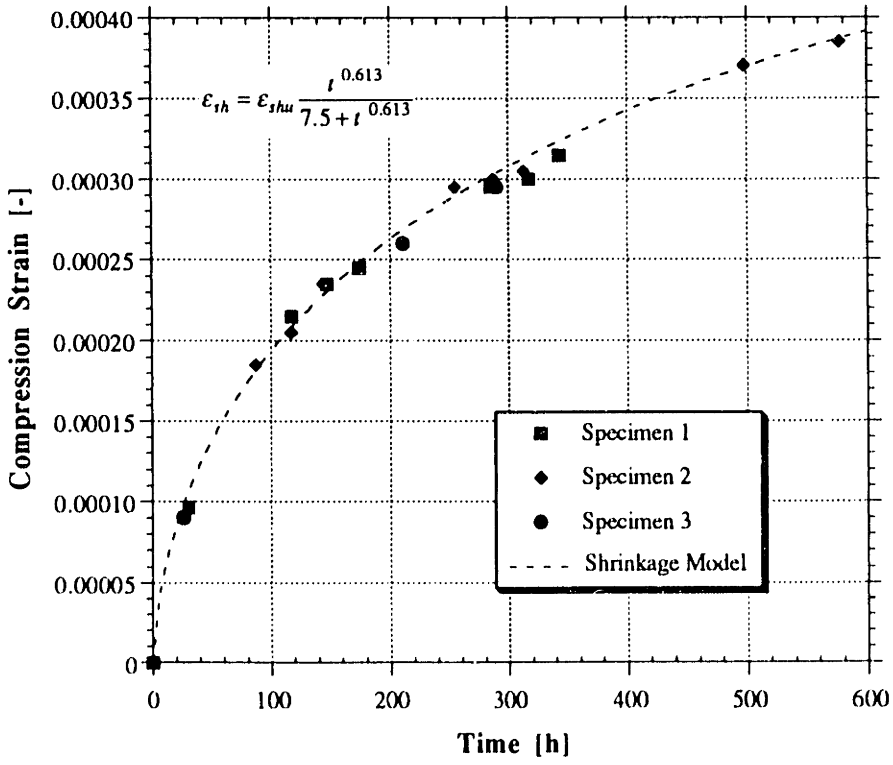

Figure 6.5 Concrete shrinkage model calibration.

The curve fit has a 1.5 % error, which is quite acceptable for the analysis. It is seen that the exponent, α, lies below the ACI recommended range of 0.9 to 1.1, but this can be explained with the fact that a low W/C ratio was used for the mix and hence the shrinkage is manifested to a lesser extent than predicted by ACI. It is seen that the test data from different specimens follow the same pattern and that the model represents the behavior to a satisfactory extent.

6.2.3 Creep of Concrete

The creep properties of the concrete used for the large scale hybrid beams were experimentally evaluated on two concrete cylinders. In order to save on time and instrumentation, the specimens were loaded in compression in a serial setup, that is one specimen on top of the other. A hydraulic press, where the pressure was adjusted through an electrically powered compressor, was used to apply a constant load of 39.4 kN. The load corresponding to an applied pressure was calibrated prior to the actual experiments. The dimensions of the specimens were 50x150 mm for the top and 100x300 mm for the bottom specimen. This gave a stress level of 20 and 5 MPa for the top and bottom specimen, respectively. A 20 mm thick steel plate was used between the two cylinders to provide a uniform load distribution, offsetting the different cylinder diameters. Two pairs of deformmeter bolts were bonded on opposite sides in the longitudinal direction onto the surface of each specimen, and using a digital deformmeter the displacement readings were recorded daily. By averaging the two readings for every measurement the corresponding strains were calculated. The resulting compressive strain versus time diagram is given in Figures 6.6 and 6.7 for the two specimens tested.

The model adopted for the concrete creep is the one proposed by ACI Committee 209 (1971); the parameters involved were calibrated using experimental results. The ultimate creep strain was calculated using empirical data from ACI (1971). A least squares curve fit of equation (4.5) to the experimental data was performed and the parameters ψ and d were calibrated. Since the same equation has to apply to the results of both specimens (assuming linear viscoelasticity), but at the same time the stresses and strains were different for each of them, the strain data of the bottom specimen were multiplied by the ratio of the initial strains of top and bottom specimens. This data were then added to the data obtained from the top specimen and the curve fit was conducted over the new data base comprising data from both specimens. The result is given in Figures 6.6 and 6.7.

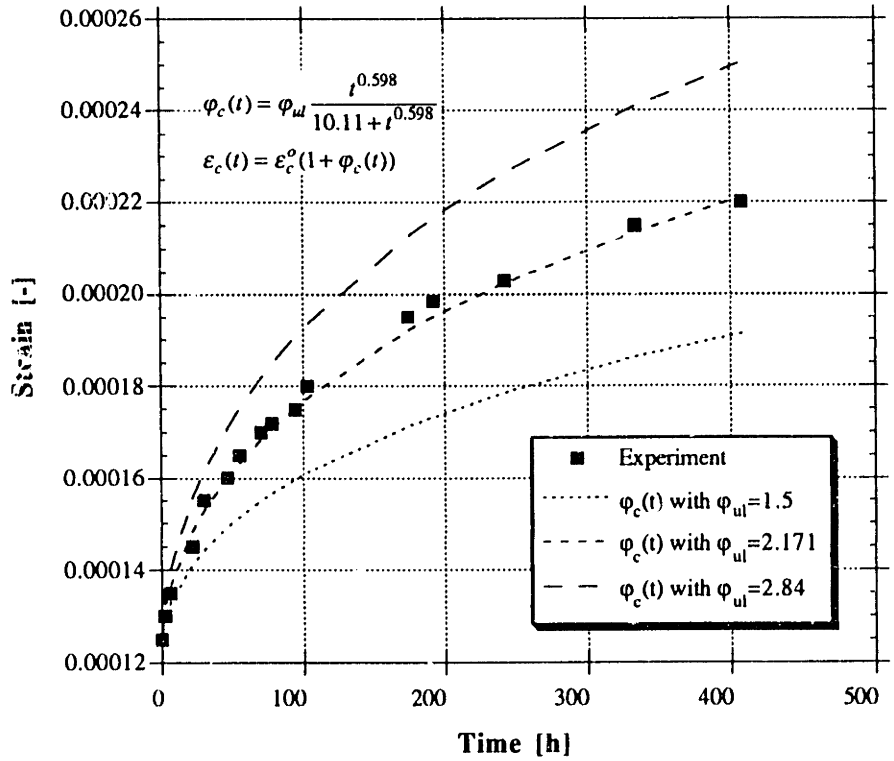

Figure 6.6 Creep response comparison of experiment with model, Stress = 20 MPa.

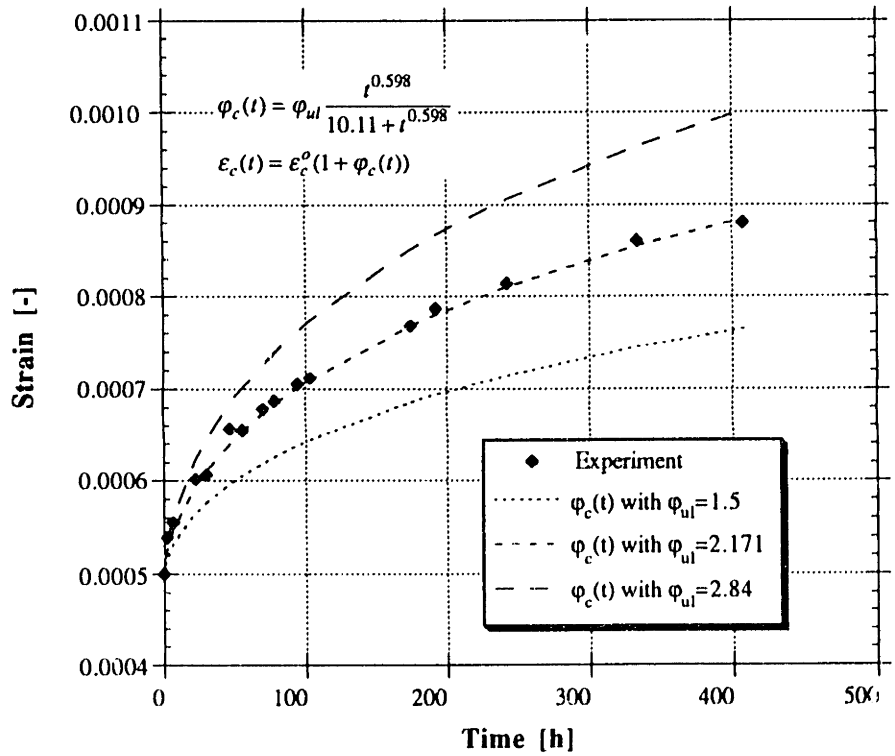

Figure 6.7 Creep response comparison of experiment with model, Stress = 5 MPa.

It is seen that the ultimate concrete strain lies within the ACI recommended parameter range. Also the curve fit was achieved with less than 1% error which justifies the usage of the adopted creep model.

Using the creep model, isochronic curves for concrete can be determined. In Figure 6.8 the fourth order polynomial model described in Chapter 3 was used for the short term stress-strain relationship description, while equation (4.7) was used for the time dependent strain calculation as given in Chapter 4. Isochronic stress-strain curves for different duration of sustained load applied are plotted. The concrete parameters used for this figure were E_c = 42000 MPa and f_c' = 50 MPa, which also corresponds to the short term properties of the concrete used for the creep specimens. A horizontal section of the diagram for a stress equal to 20 and 5 MPa would give the diagrams from Figures 6.6 and 6.7, respectively.

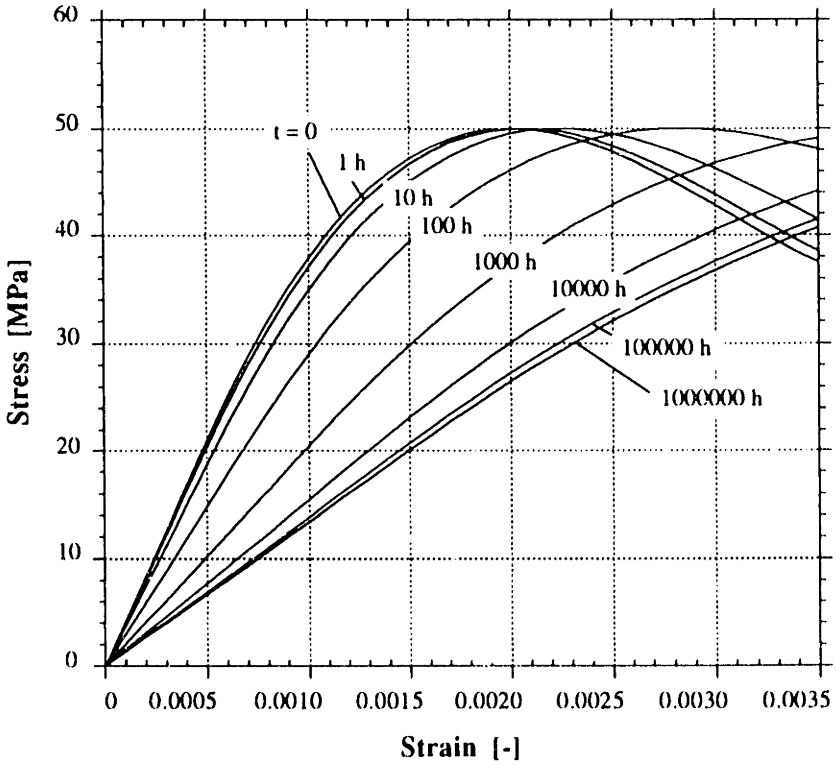

Figure 6.8 Isochronic stress-strain relationship for concrete.

It is seen that the nonlinearity of the concrete response vanishes with the increase of the duration of sustained load. Also, assuming that the ultimate strain of concrete at crushing is constant regardless of the load history, it has to be pointed out that the strength of concrete due to creep effects is reduced. Further it can be concluded that for short load

duration the integral of the stress-strain relationship does not change significantly, which implies that a concrete element loaded in creep with a non-constant strain profile (e.g., compression zone in flexure) will not loose on carrying capacity. Also it can be noted that the gradient of the creep strain, that is the creep strain increase with time, is large in the first 1000 hours after which it decreases and reduces to insignificant values (see 100000 hours curve).

The two specimens tested under sustained load were tested up to failure in compression in order to investigate the residual strength of concrete. A third specimen, a cylinder with dimensions 50x150 mm obtained from the same mix as the creep specimens, was tested simultaneously giving the short term response. The stress-strain curve of all three cylinders was recorded during the compression tests and is shown in Figure 6.9. The creep specimens were tested immediately after the creep test was concluded and thus, it is assumed that no time for recovery was allowed. The creep strain accumulated during sustained loading was later added to the actual residual strain. Figure 6.9 shows that the assumptions made in Chapter 4 on residual response and strength hold. The strength of concrete remained virtually unchanged, the stress-strain curves are almost parallel and the ultimate strain at failure is maintained.

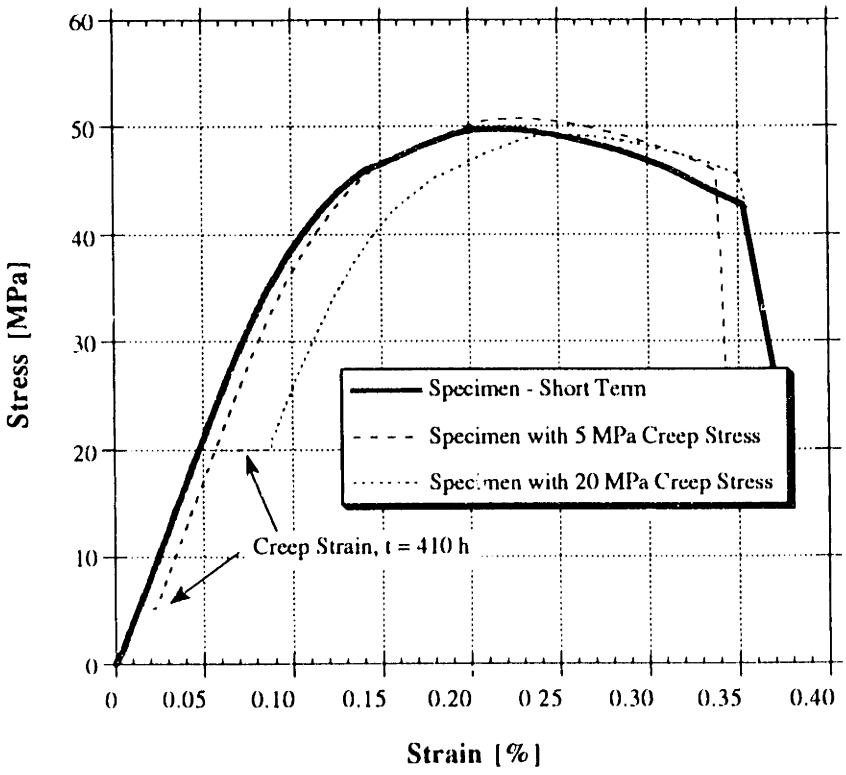

Figure 6.9 Residual response of concrete.

6.2.4 Fatigue of Concrete

The fatigue response of concrete was modeled using the model proposed by Holmen (1982) as described in detail in Chapter 4. Since the empirical equations proposed by Holmen were obtained for a concrete with almost the same strength as the one used for the hybrid beams (45 versus 50 MPa) and for similar frequency levels (5.0 versus 4.2 Hz), it was assumed that the same relations can be applied here and hence, they were implemented in the fatigue analysis of concrete. In order to gain better understanding of the model proposed by Holmen, the dependence of the total strain (including initial short term strain), creep strain and fatigue strain, to the number of cycles, elapsed time and stress level was investigated. Figure 6.10 gives a graphical interpretation of the fatigue model used, which was applied onto the same concrete properties as used earlier for the concrete is Section 6.2.3. For this plot it was assumed that the frequency of cycling is constant and equal to 5.0 Hz, giving a linear relationship between time and number of cycles. First, it has to be noted that in equation (4.51) the stress level mainly influences the magnitude of the number of cycles to failure, N_F, while the probability of failure, P, plays a negligible role. In fact, the stress level to the third power is inversely proportional to N_F, implying that only for concrete stress levels exceeding 55% of the ultimate (S_{max}=0.55) there will be an effect of fatigue. For lower stress levels the creep strains become governing and the long term effects are almost fully represented by time dependent strain increases only. It is also seen that equation (4.52) will be governing in most cases of practical applications, since it is valid for low stress levels. Figure 6.10 shows that equation (4.53) is activated only at $S_{max} = 0.7$ or higher, and it can be noted that a fatigue induced strain increase is generated for $S_{max} > 0.6$. For higher stress levels the effect of concrete fatigue to the total strain increases in an accelerated manner, where for example at $S_{max} = 0.75$ critical values of strain are reached after a few thousand cycles only. Here the creep effect is negligible. Therefore it can be concluded that the effect of fatigue loading to concrete is significant only at high stress levels, while, generally, for lower values the influence of creep is dominant and fatigue represents only a smaller portion of the total strain increase.

The model discussed above was further explored by determining the stress-strain relationship of concrete subjected to a different number of loading cycles. Again it was assumed that the frequency (= 5 Hz) is constant, the minimum stress level is zero, and that the cycle number, N, is proportional to the elapsed time, that is $N = 18000\, t$, where the time, t, is in hours. Figure 6.11 shows these stress-strain curves (called isocyclic), where each point on one of them was obtained using the algorithm given in Figure 4.16.

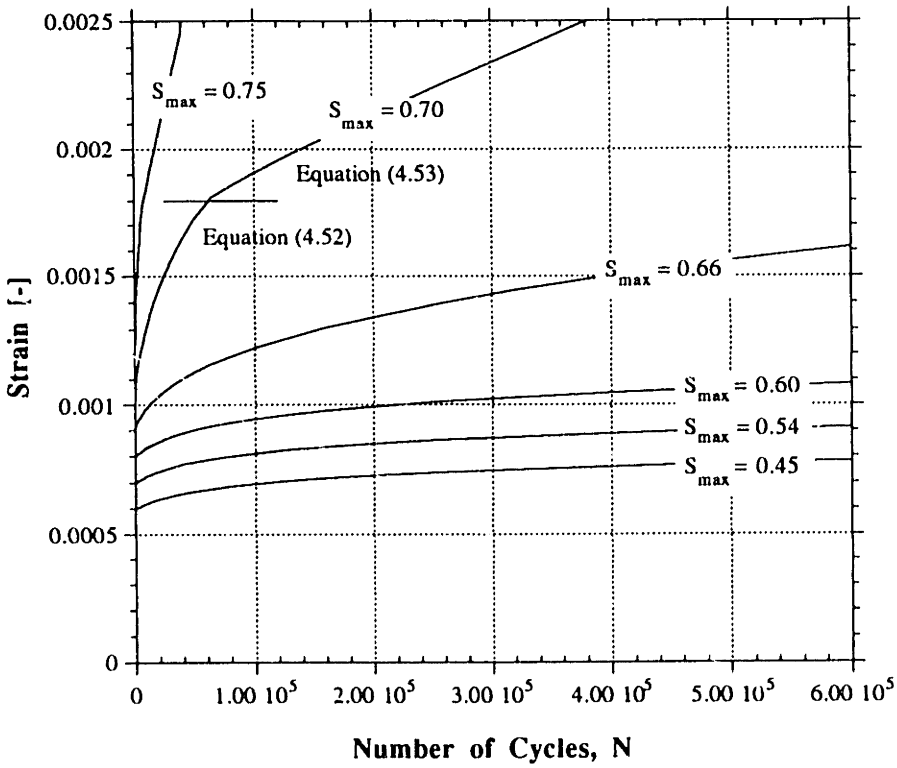

Figure 6.10 Concrete fatigue model.

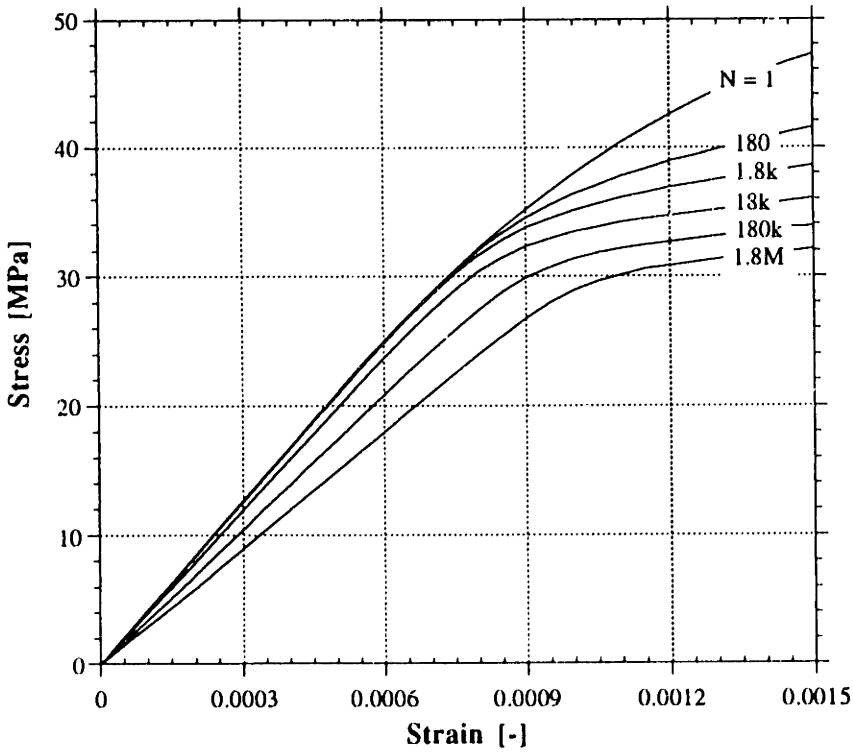

Figure 6.11 Isocyclic stress-strain relationship for concrete.

The same concrete properties and model for the short term behavior as defined in Section 6.2.3 were used. As it was pointed out earlier, it is apparent that the effect of fatigue influences the response at stress levels of 60% of the ultimate or more. For lower stress levels, the fatigue effect is negligible and the strain increase is solely due to creep effects. This is also confirmed when comparing Figures 6.8 and 6.11 where it is seen that for stress levels of 40% of ultimate or less the stress-strain curves are almost identical (note: 18000 cycles correspond to 1h of creep time). It has to be noted that each curve from Figure 6.10 represents a horizontal section in Figure 6.11 at the associated stress level.

6.3 Experimental Characterization of GFRP Properties

Two types of GFRP were used in the experimental program. The first, used for the small scale beams, constituted a pultruded profile consisting of several layers of various glass fiber types and layouts embedded in a polyester matrix. The second, used for the large scale beams, was a filament wound box beam with ±45° glass fiber orientation and an epoxy matrix. The short term properties were evaluated for both GFRP types using uniaxial tension coupon tests and full GFRP beam bending tests. The short term stress-strain curves were evaluated and appropriate models adopted. A linear model was used for the polyester GFRP and a fourth order polynomial approximation, as described in Chapter 3, for the glass/epoxy composite. Since only the large scale beams were subjected to long term loading, only the creep and fatigue properties of the epoxy GFRP were evaluated and the parameters required for the adopted models described in Chapter 4 were calibrated. Both empirical and continuum theory models were considered and the resulting response was compared to experiment. The description of the matrix properties in creep and fatigue was presented. Isochronic curves, defining the stress-strain behavior for equal times of applied load, as well as isocyclic, defining these relations for equal number of load cycles, were determined.

6.3.1 Matrix Properties

The long term behavior of GFRPs is largely dependent on the characteristics of the matrix embedding the fibers. It was seen in Chapter 4 that for the modeling of the GFRP response with the continuum theory model the matrix properties are essential. Next, the viscoelastic characteristics of the constituting matrix will be described.

The GFRP box beams used for the large scale experiments were manufactured with an epoxy based resin. Epoxy resins are synthetically produced, high polymeric duromers. They are generated through addition of reactive epoxy and OH-groups of the so called epoxy base resins with OH^-, NH_2^-- or $COOH^-$-groups of high level amides, acids and anhydrous acids of the so called hardeners (Bitterli 1987). Among the base resins two groups can be differentiated: (a) resins with a phenolic basis; and (b) nonphenolic resins. There are three groups of hardeners: (a) organic, polycarbonacid anhydrides; (b) reactive polyamides; and (c) catalytically acting alkaline and acid substances. The epoxy groups of the base resins are essential for the curing and bonding process. The high reactivity is caused by a slight opening of the epoxy chains, where through the decreased distance of the C- atoms (1.54 Å in the closed chain versus 1.47 Å in the open chain), high ring stresses as a result of large deformations are generated and an increase in the reactivity is obtained. The polymer chains bond during curing with the addition of hardeners. They react with the free epoxy- or OH^-- groups of the base resin and produce a spatial bond between the molecule chains. This polyaddition is not an equilibrium reaction, that is for the full development of the reaction an exact volume ratio is required.

The epoxy resin used for the GFRP box beam manufacturing was the Araldit® LY 556, HY 917, DY 070 system from CIBA-GEIGY AG. The short term material properties are given in Table 6.7.

Table 6.7 Epoxy matrix material properties.

Specific weight , γ_M [kg/m^3]	1.20×10^3
Tensile Strength, σ_M^* [MPa]	70.0 - 90.0
Ultimate Strain, ε_M^* [-]	3.0 -5.0
Elastic modulus, E_M [MPa]	4000
Poisson's ratio, ν_M [-]	0.35
Coefficient of thermal expansion, α_M [10^{-5}/K°]	6.8 - 7.0

The viscoelastic behavior of this epoxy resin was investigated in 10000 hour creep tests (Ciga-Geigy 1991). A series of specimens was loaded with a constant stress level of 17.9 MPa. The experimental results gave the relationship between the elastic modulus of the matrix and the time elapsed since the load was applied. Implementing a least squares curve fit these data were used to define the parameters for Findley's model described in Chapter

4. Substituting for the sustained stress into equation (4.12), the following relationship is obtained:

$$E_M(t) = \frac{\sigma_o}{a + bt^n} \tag{6.1}$$

and from the curve fit to experimental data the values for a, b and n were determined. The result is shown in Figure 6.12.

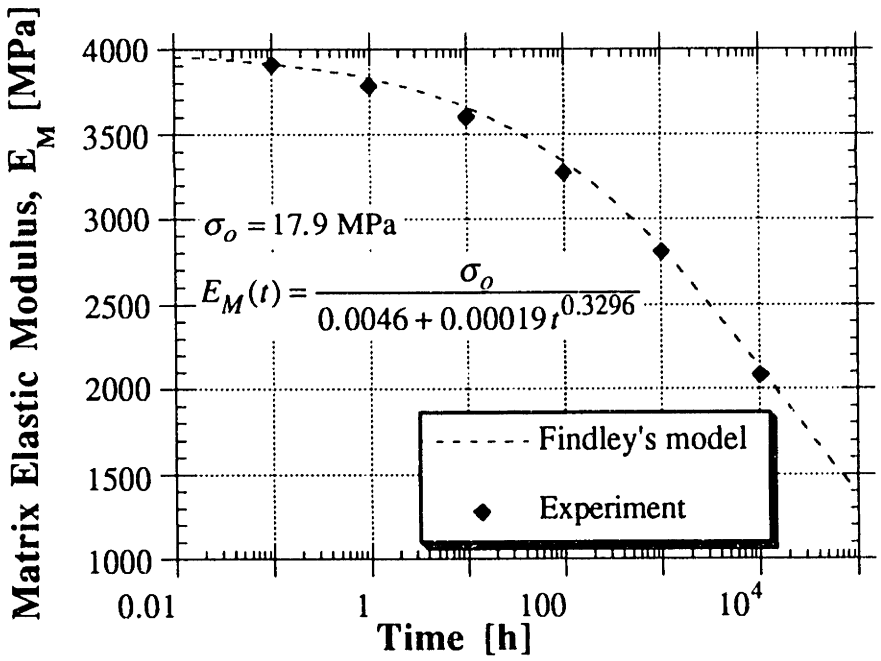

Figure 6.12 Creep model for the epoxy matrix.

It is seen that the adopted model represents the actual creep response in a satisfactory manner and was therefore used for the GFRP continuum theory creep model in the analysis of the hybrid beams.

6.3.2 Characterization of the Short Term Properties of GFRP

The short term properties of the two GFRP box beam sections were analyzed with two methods. The main goal was to define the elastic properties as well as the parameters needed for the model of the stress-strain relationship in tension. The first method was the standard experimental procedure, where coupons of GFRP were subjected to uniaxial

tension and the corresponding stress-strain curves were recorded, giving the elastic modulus, ultimate strain at failure and strength of the material. The second method involved three point bending tests which enabled the determination of an equivalent flexural and shearing stiffness for the small scale box beams and the shear modulus of the large scale beams. The test procedure differs for the two GFRP box beam sections and will be described separately next.

6.3.2.1 Small Scale GFRP Box Beam

The pultruded members consisted of various layers of glass fibers bonded together with a polyester matrix. The resin burn-off technique was applied to the GFRP walls indicating that a total of 6 different layers were used in the pultrusion process. Starting from the exterior of the cross section towards the interior, the layers were: (1) mat of randomly oriented bundled fibers; (2) two-directional 0/90° tissue; (3) unidirectional roving; (4) mat of randomly oriented fibers; (5) same as the second layer; and (6) mat of randomly oriented fibers. The volume fraction of the glass in the section was about 30%. This value had a large scatter across the section and hence the fraction of fibers in each of the four walls (see Figure 6.13) was determined. It was found that opposite walls had approximately the same fiber content per wall surface (0.24 g/cm^2 for walls 1 and 3 and 0.32 g/cm^2 and 0.24 g/cm^2 for walls 2 and 4, respectively). This corresponds to 35% more roving fibers in walls 2 and 4. In order to define the mechanical properties of the various elements of the GFRP profile, coupon specimens were tested in tension and beam specimens were tested in three point bending.

6.3.2.1.1 Tension Testing of GFRP Used in Small Scale Beams

16 dog-bone specimens cut out of 2 different locations along the GFRP profile were prepared according to the German DIN (No. 3 of DIN 53 455). The locations from where the specimens were obtained are shown in Figure 6.13, and the stress-strain relationships recorded from uniaxial tension testing of the coupons are given in Figures 6.14 through 6.17 (indicating a considerable variability in GFRP properties). The specimen dimensions and resulting material properties are summarized in Table 6.8. The adopted material properties (average of four tests) for the GFRP section are given in Figure 6.13.

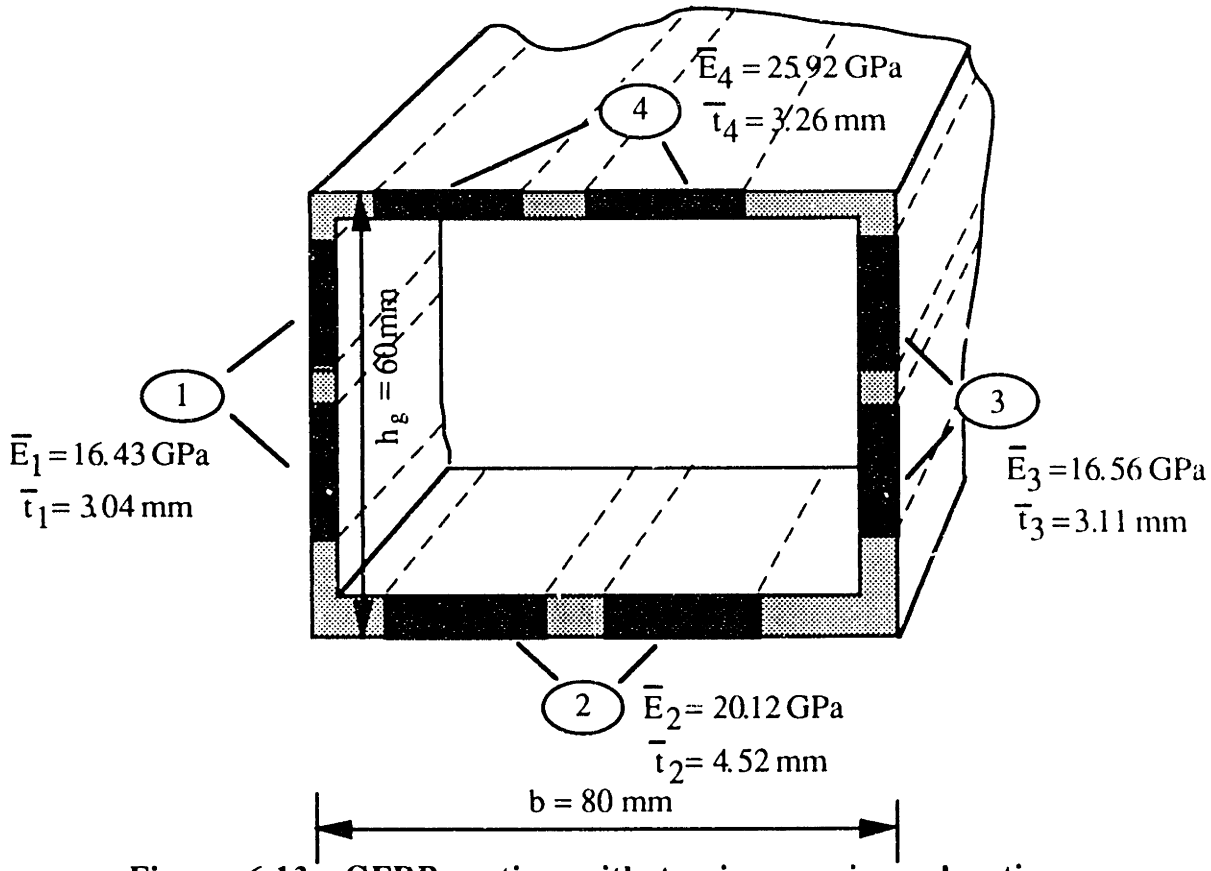

Figure 6.13 GFRP section with tension specimen locations.

Table 6.8 Tension test results.

Specimen*	Thickness [mm]	Min. Width [mm]	Elastic Modulus [MPa]	Tensile Strength [MPa]	Ultimate Strain [%]
1A	2.76	10.02	18000	376	2.05
1B	2.91	10.03	19700	360	1.83
1'A	3.33	10.04	12540	202	1.61
1'B	3.15	10.01	15500	276	1.78
2A	4.79	10.13	16170	212	2.09
2B	4.64	9.95	23390	370	2.38
2'A	4.39	10.05	16690	292	1.85
2'B	4.26	10.01	24230	437	1.80
3A	3.43	10.00	12150	120	1.99
3B	3.10	10.02	17290	287	1.77
3'A	2.89	10.01	16250	290	2.00
3'B	3.02	10.03	20570	383	1.98
4A	3.00	10.00	26000	497	2.00
4B	3.18	10.01	29000	525	1.85
4'A	3.35	9.91	24000	437	2.00
4'B	3.51	10.04	24700	463	2.03

* The ' denotes specimens obtained from a different cross section.

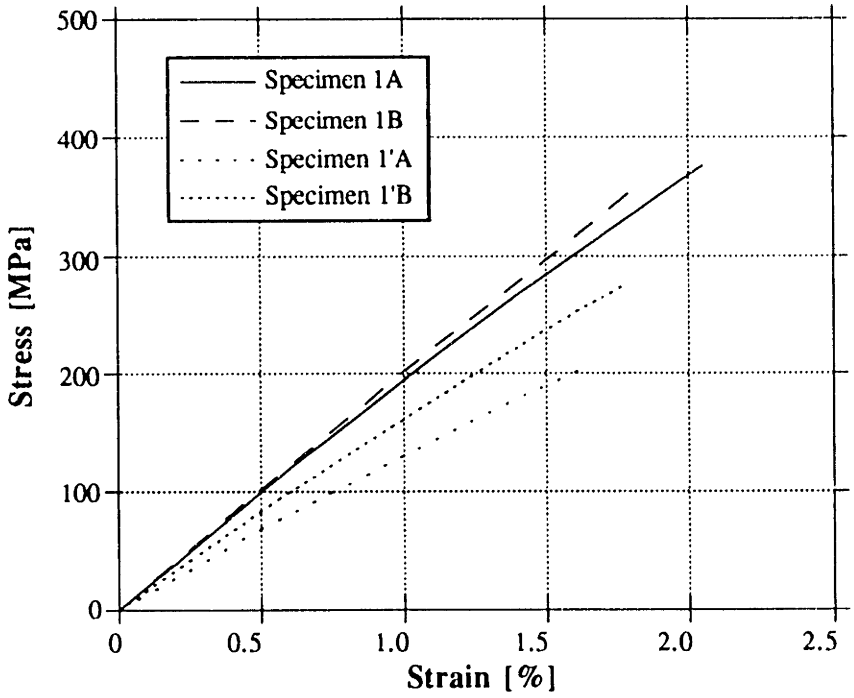

Figure 6.14 Stress-strain relationship for wall 1.

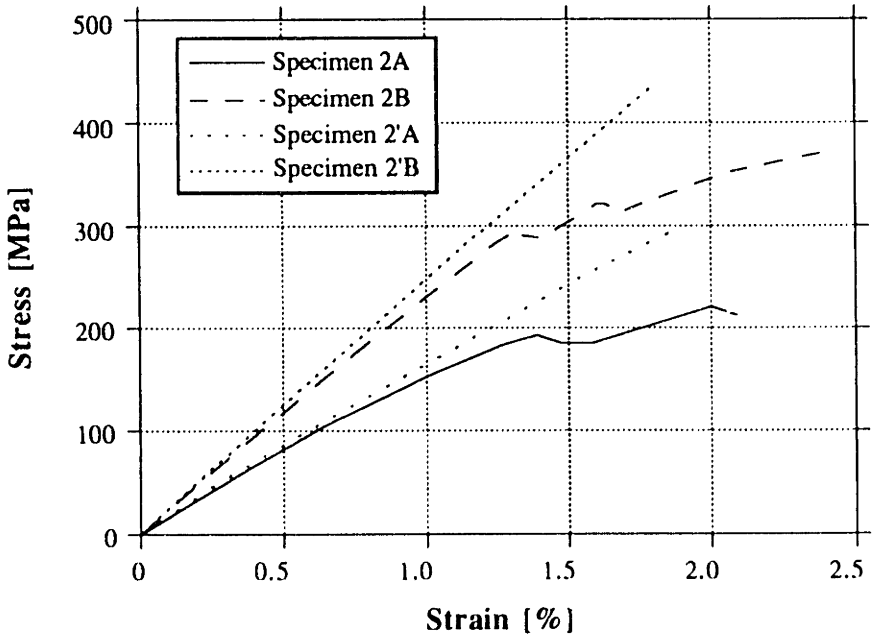

Figure 6.15 Stress-strain relationship for wall 2.

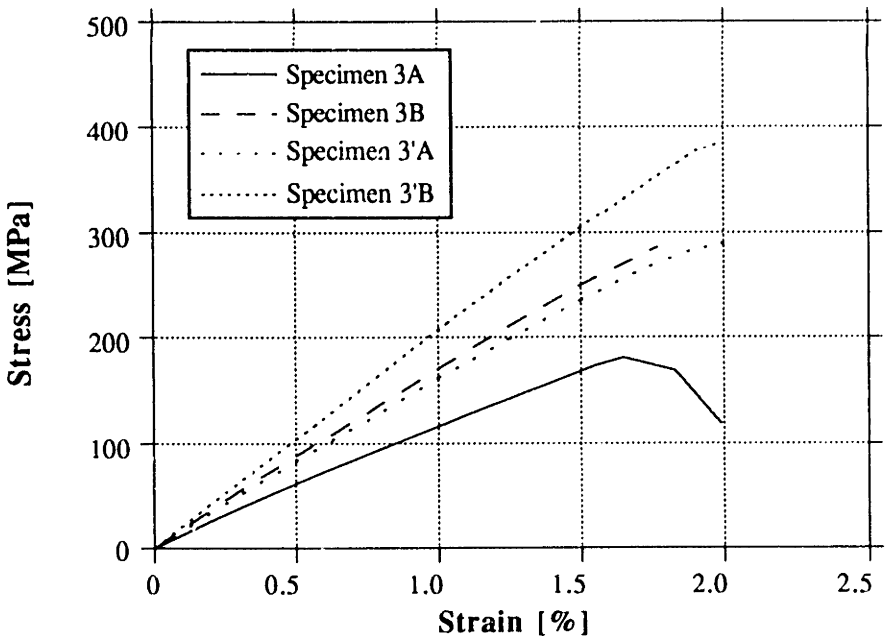

Figure 6.16 Stress-strain relationship for wall 3.

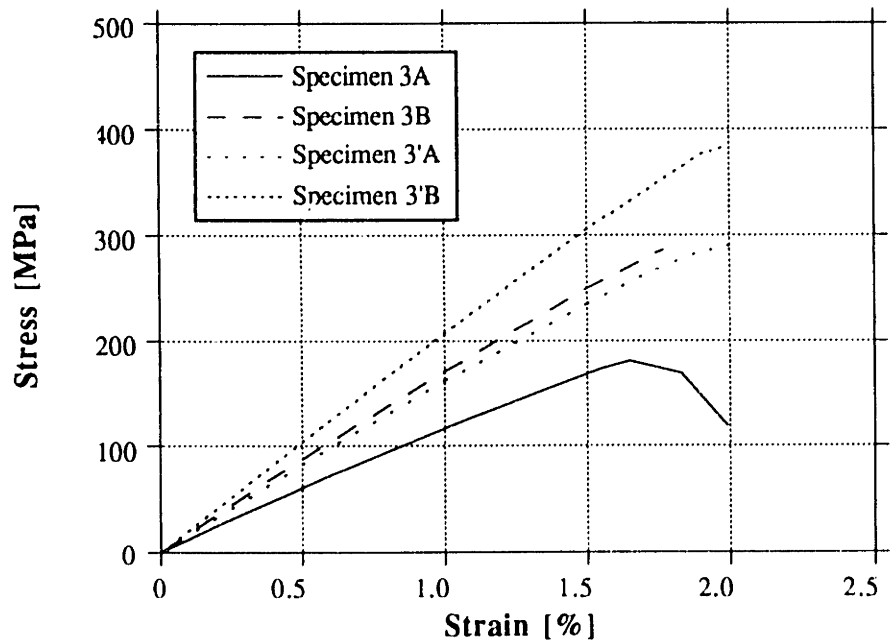

Figure 6.17 Stress-strain relationship for wall 4.

6.3.2.1.2 Equivalent Stiffness Calculation of GFRP Used in Small Scale Beams

The flexural characteristics of the polyester GFRP box beams are discussed in this section. First, the equivalent flexural and shear stiffness were determined directly from three-point bending tests at spans in the range 300 to 1000 mm. A single specimen was tested elastically at various spans, giving the load versus mid-span deflection curves shown in Figure 6.18.

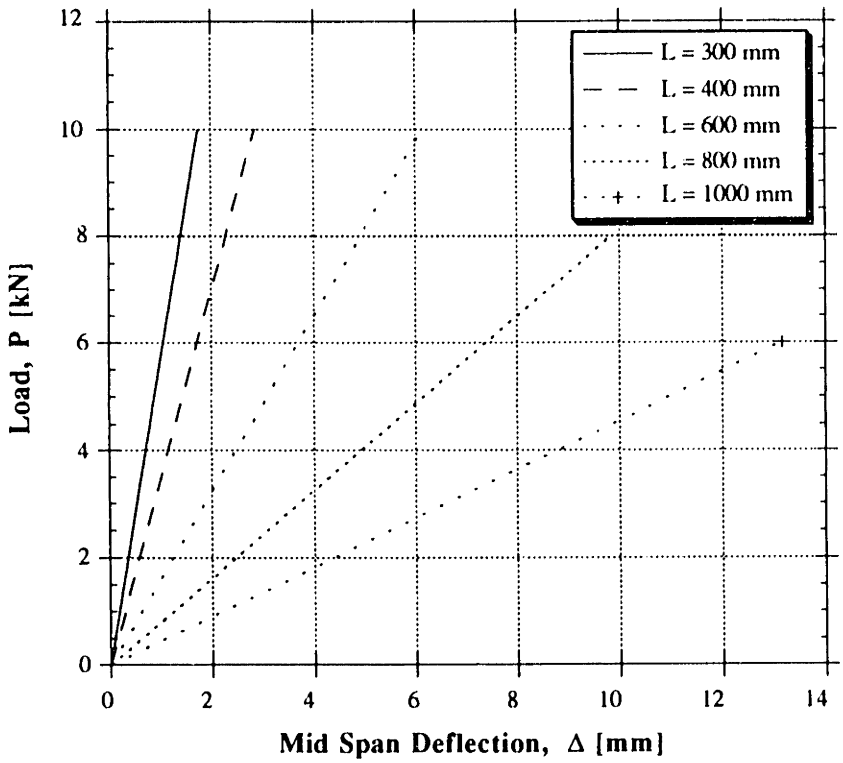

Figure 6.18 Load-deflection curves for various span lengths.

From beam theory, accounting for shear deformations the mid-span deflection in three point bending is given by:

$$\Delta = \frac{PL^3}{48D} + \frac{PL}{4Q} \tag{6.2}$$

where P is the applied load. Hence, if the measured mid-span deflections corresponding to the same load and several different spans are plotted in the form Δ/PL versus L^2 and the results are fitted by a straight line, the slope equals $1/48D$. Similarly, if Δ/PL^3 is plotted versus $1/L^2$, the slope equals $1/4Q$. Hence, the equivalent bending and shear stiffness can

be established, as shown in Figures 6.19 and 6.20, respectively. The values obtained are D=12.23 kNm^2 and Q=584 kN.

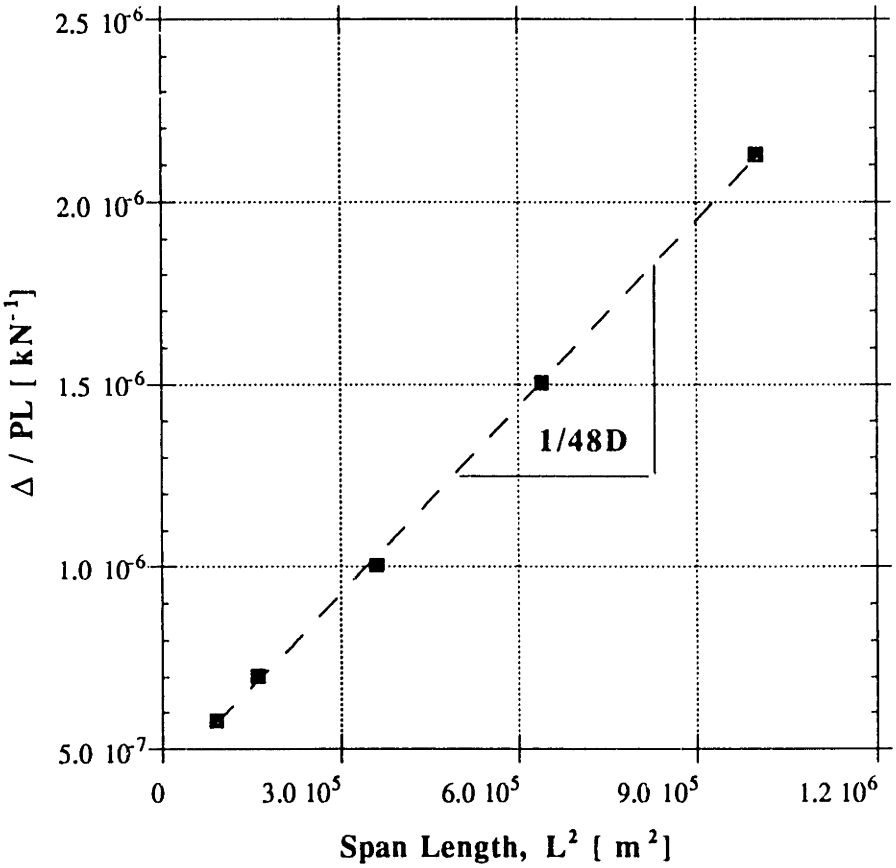

Figure 6.19 Equivalent bending stiffness calculation.

The bending stiffness can also be approximated as

$$D = \sum_i E_i I_i \tag{6.3}$$

where E_i and I_i are the Young's modulus and moment of inertia, respectively, of the i th element of the box section (discretized in four rectangular elements: 2 flanges and 2 webs). The last expression for the bending stiffness gives a value of 12.15 kNm^2, which is in a quite remarkable agreement with the experimental value. The experimental value of the shear stiffness was used to calculate the shear modulus G_w of the GFRP section using equation (6.2). An average shear modulus of approximately 2000 MPa was obtained.

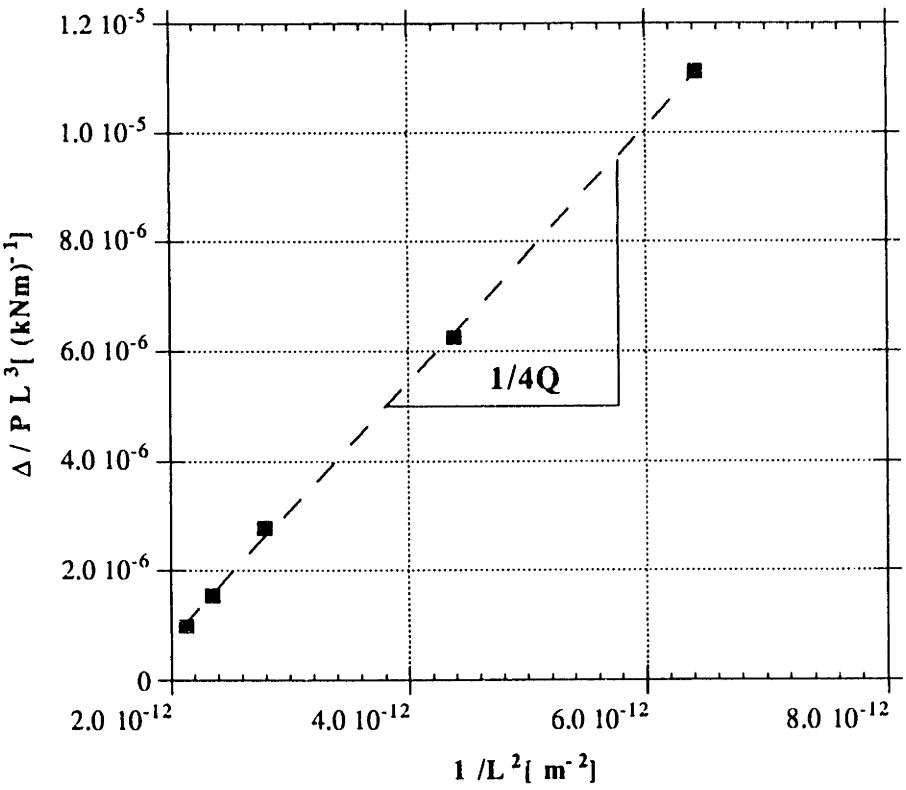

Figure 6.20 Equivalent shear stiffness calculation.

6.3.2.2 Large Scale GFRP Box Beam

The manufacturing process of the GFRP box beams was described in Chapter 5. The short term material properties were determined from uniaxial tension tests on coupons and from three point bending tests of the box beams in their elastic region. Stress-strain curves were recorded from the coupon tests and the results obtained were used in the analytical model in order to predict the beam's response in three point bending. Comparing the analytically obtained deflections to the experimental values good agreement was obtained and the adopted models verified. The fiber volume fractions of the beams were determined from 30x40 mm coupons using the resin burn-off technique. The results are summarized in Table 6.9. It is seen that an average volume fraction for the webs and flanges is 50 and 60 % respectively. The volume fractions of the glass fibers were calculated assuming the specific weight of glass to be 2.54 g/cm^3.

Table 6.9 Fiber volume fraction of filament wound box beams.

Description		Glass fiber content, by weight, W_F [%]	Glass fiber content, by volume, V_F[%]
Beam 1	Web	60	42
	Flange	66	47
Beam 2	Web	65	46
	Flange	75	60
Beam 3	Web	67	50
	Flange	75	60
Beam 4	Web	65	45
	Flange	71	55
Beam 5	Web	71	54
	Flange	70	53
Beam 6	Web	70	53
	Flange	77	62
Beam 7	Web	62	44
	Flange	76	62

6.3.2.2.1 Tension Testing of GFRP Used in Filament Wound Beams

For each beam a series of eight 25x160 mm long specimens were cut out of the flange and web at the beams' ends. Aluminum plates of 2 mm thickness were bonded at the anchorage regions as shown in Figure 6.21(a) in order to provide a better stress distribution. The specimens were tested on an INSTRON 1521 with computerized control. The displacement controlled cross head speed was 0.2 mm/min with a load range of 0-20 kN. A clip gauge was attached to the specimens recording the displacements, while a 50 kN capacity load cell, installed in the cross head, gave the associated load. From here the stresses and strains were calculated. A DAS was used to store the results. Figure 6.21(b) shows the test setup.

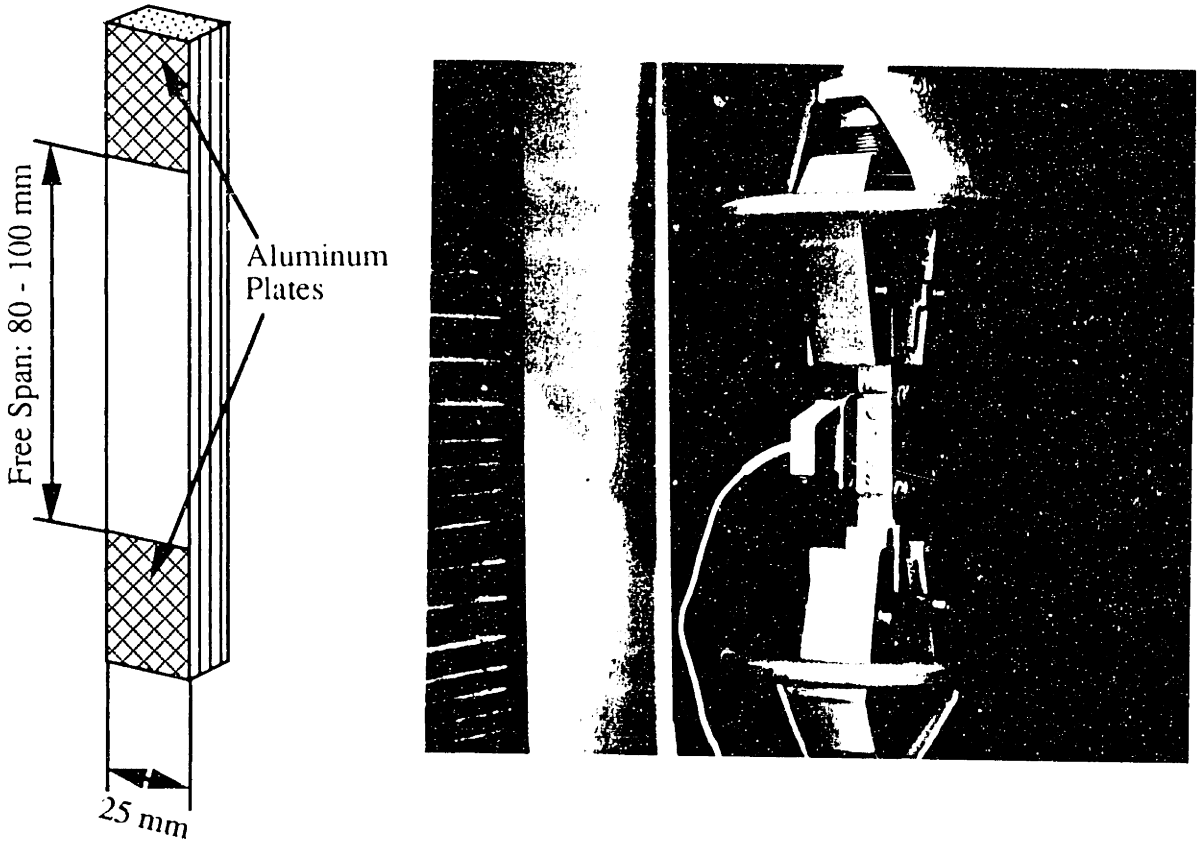

Figure 6.21 (a) Tension test specimen, (b) test setup.

Taking the average of two experimentally obtained stress-strain curves, a least squares fit to a fourth order polynomial was carried out and the parameters of the model described in Chapter 4 were derived. For each beam a separate model for the flange and the web was obtained. Figures 6.22 to 6.24 give a graphical comparison of models (polynomials) and experimental data for beams 1, 3 and 4, respectively. It is seen that a good curve fit with the fourth order polynomial can be obtained. The error is less than 1%, which gives sufficient accuracy. The analytical models are of the form:

$$f_{GFRP}(\varepsilon_g) = a_0 + a_1\varepsilon_g + a_2\varepsilon_g^2 + a_3\varepsilon_g^3 + a_4\varepsilon_g^4 \tag{6.4}$$

where the coefficients a_0 to a_4 for all seven beams are given in Table 6.10. Note that the coefficients a_0 are almost negligible and that the coefficient a_1 represents the elastic modulus of the GFRP specimen. This value was used for the definition of the elastic portion of the stress-strain curve. From the experiments performed it is seen that the ultimate strain of the GFRP web is about 2.0 2.5%, while values as high as 6% can be achieved for the GFRP flange.

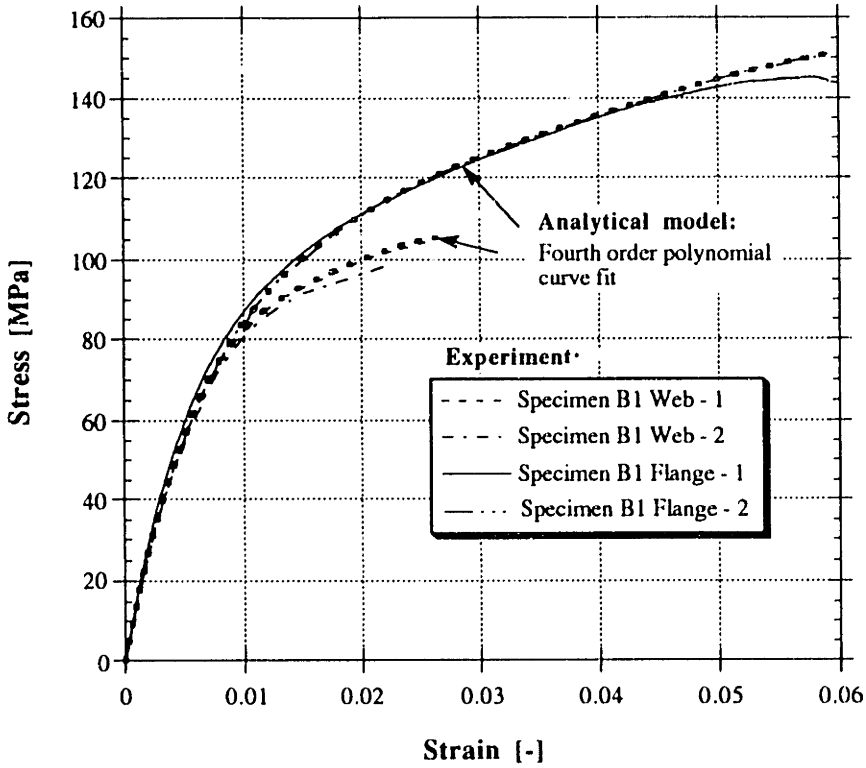

Figure 6.22 Beam 1: Stress-strain relationship, model and experiment.

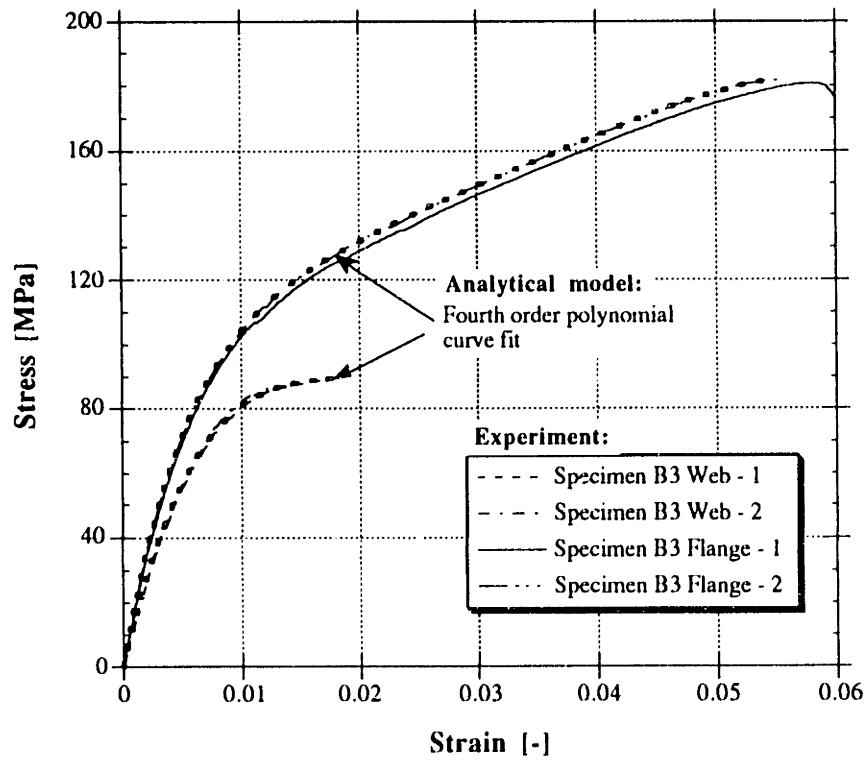

Figure 6.23 Beam 3: Stress-strain relationship, model and experiment.

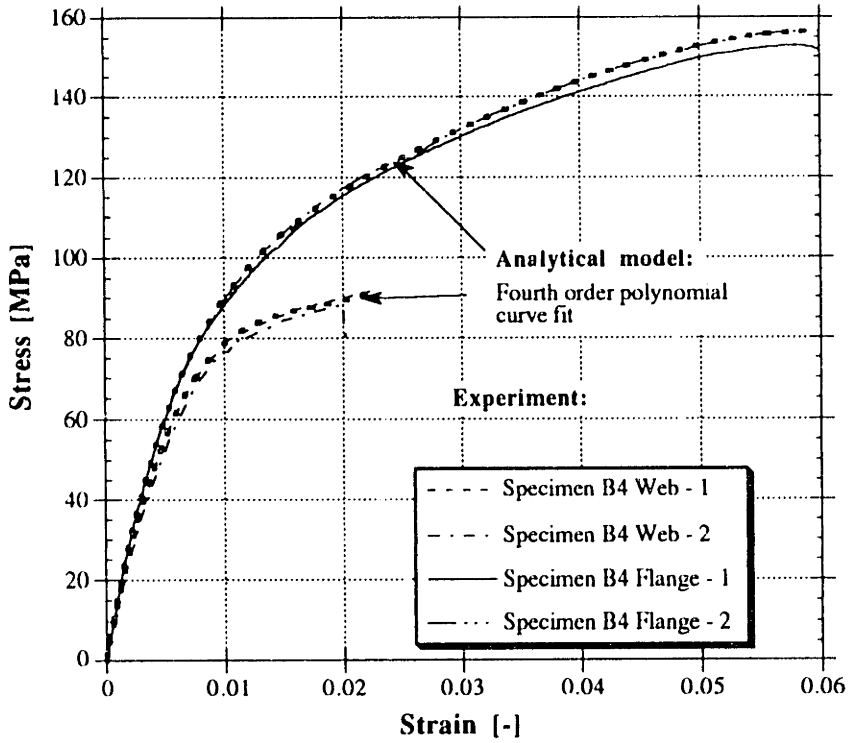

Figure 6.24 Beam 4: Stress-strain relationship, model and experiment.

Table 6.10 Coefficients for the fourth order approximation of the GFRP stress-strain curve.

Beam	a_0 [MPa]	a_1 [10^3MPa]	a_2 [10^3MPa]	a_3 [10^6MPa]	a_4 [10^6MPa]
1-Flange	2.902	13.525	-0.535	10.581	-74.278
1-Web	0.114	12.165	-1.080	36.145	463.475
2-Flange	0.064	18.400	-1.458	56.314	-837.334
2-Web	-0.983	13.130	-0.551	-26.737	1633.410
3-Flange	3.131	18.122	-0.818	18.075	-139.731
3-Web	-0.038	13.918	-1.058	30.562	-306.808
4-Flange	2.171	16.328	-0.473	8.906	-60.849
4-Web	-0.914	13.174	-1.068	32.309	-343.389
5-Flange	0.981	15.668	-0.857	21.791	-200.914
5-Web	0.187	14.890	-1.782	72.538	-1142.61
6-Flange	1.862	18.976	-0.498	13.763	-85.498
6-Web	0.346	15.512	-0.681	-22.268	1934.82
7-Flange	-0.965	18.209	-0.587	17.591	-183.892
7-Web	1.138	14.014	-0.824	21.234	-199.300

6.3.2.2.2 Three Point Bending Tests on Filament Wound GFRP Beams

The test setup for the large scale GFRP beams was described in Section 5.3.2. Here, the goal was to verify the adopted material properties for the flange and the web, and to determine the shear modulus of the webs experimentally. It is assumed that the load is low so that the materials respond within their elastic range and simple beam theory can be used. The geometry of each GFRP beam's cross section is given in Table 6.11.

Table 6.11 Geometric properties of filament wound GFRP box beams.

Thickness	Beam 1	Beam 2	Beam 3	Beam 4	Beam 5	Beam 6	Beam 7
Flange, $t_{1,3}$ [mm]	5.8	4.9	4.9	5.2	5.0	5.0	5.2
Web, t_w [mm]	3.8	2.9	3.0	2.9	3.0	2.9	3.0

Using these values and the elastic modulus from Table 6.10 (column 3) the stiffness of each beam, D, can be derived using equation (3.73). From here the top and bottom flange strains can be calculated with:

$$\varepsilon_{top,bottom} = \pm \frac{M}{D} \frac{h_g}{2} \tag{6.5}$$

where M represents the moment acting on the section and h_g is the height of the box beam. The resulting strains can be compared to experimentally obtained ones from three point bending tests. The comparison is given in Figure 6.25 for both the top and the bottom strains. It is seen that the adopted models comply well with experimental data.

The shear modulus was evaluated from strains measured with the rosette shown in Figure 5.26. The resulting shear strain, γ_{xy}, is calculated using coordinate transformation and the following relationship:

$$\gamma_{xy} = \varepsilon_x + \varepsilon_y - 2\varepsilon_{45°} \tag{6.6}$$

where the variables are explained in Figure 6.26.

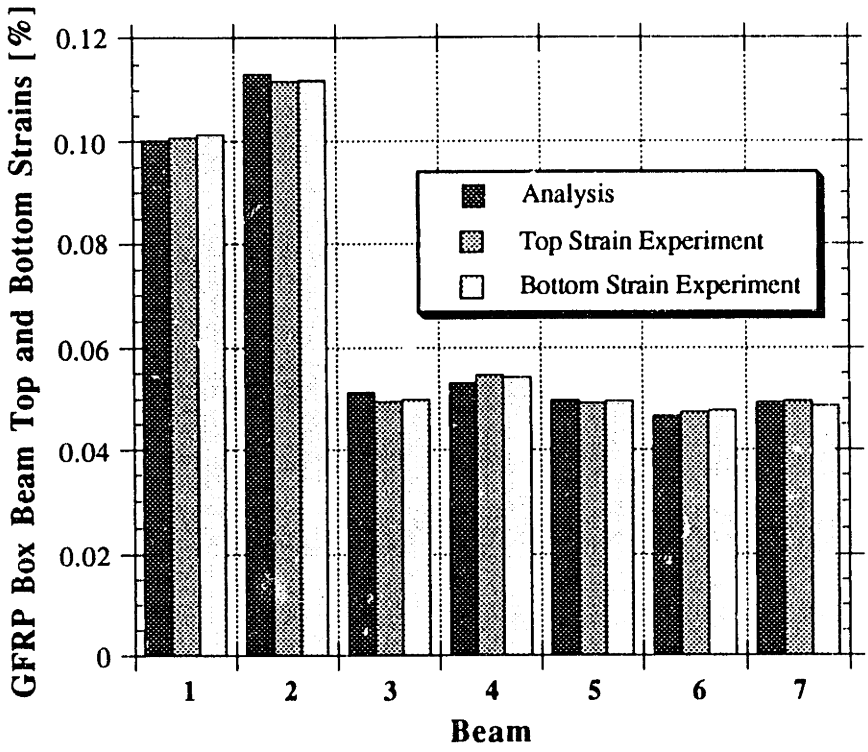

Figure 6.25 Top and bottom strains, comparison of experiment and analysis.

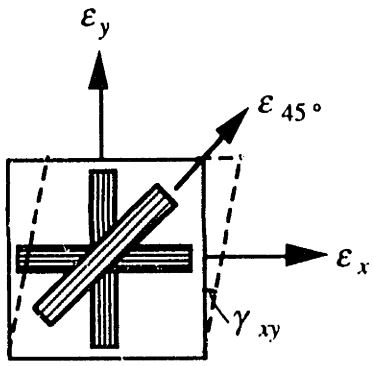

Figure 6.26 Shear strain calculation.

The shear modulus can be calculated using Hook's law for shear, where the shear stress is obtained implementing equation (3.38). The experimentally obtained shear strains at a load of 10 kN and the calculated shear modulus of the web, $G_{xy}=G_w$, are given in Table 6.12 for each beam.

Table 6.12 Shear strain and modulus of GFRP web in elastic region.

	Beam 1	Beam 2	Beam 3	Beam 4	Beam 5	Beam 6	Beam 7
Shear strain, γ_{xy} [10^{-3}]	0.170	0.172	0.160	0.164	0.147	0.150	0.171
Shear mod., G_{xy} [MPa]	10406	12203	13021	12149	14263	13797	11572

In Chapter 4 the continuum theory was presented and equations defining the elastic properties, that is the modulus of elasticity, the shear modulus and the Poisson's ratio from known properties of the constituents (glass fibers and matrix) were derived. On the other hand the experiments carried out on coupon tension tests and three point bending tests gave the same quantities experimentally. Using the fiber volume fractions given in Table 6.9 and the glass and matrix properties from Figure 5.6, the two approaches were compared and the result is shown in Figure 6.27.

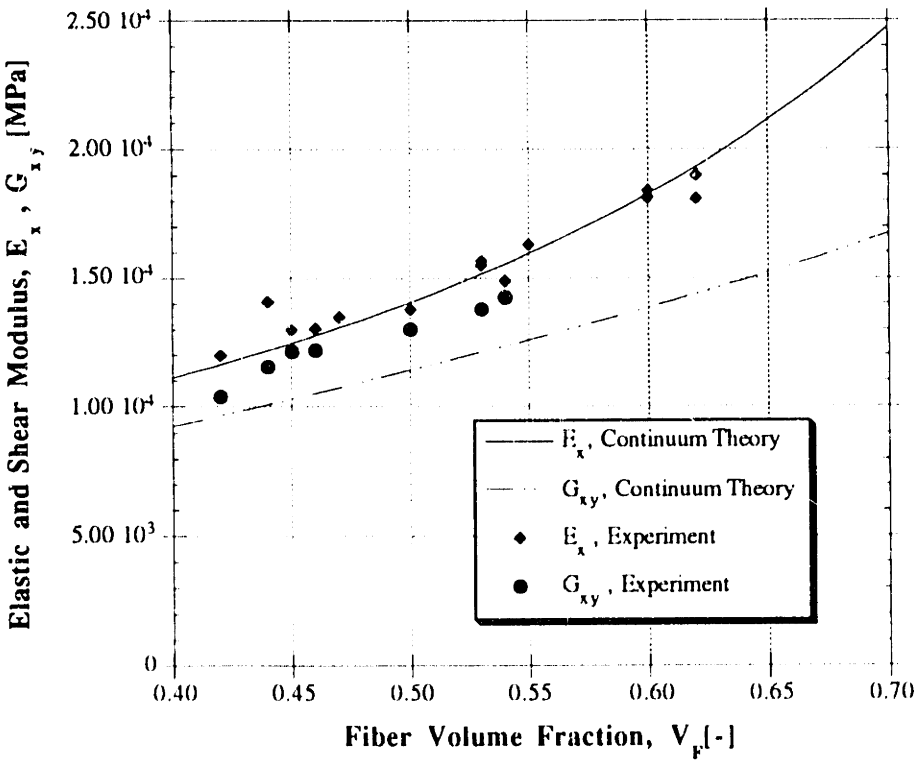

Figure 6.27 Comparison of continuum theory and experimental elastic properties.

It is seen that theory and experiment are in good agreement in defining the elastic modulus, while continuum theory gives somewhat conservative values for the shear modulus description. Further, the material properties defined above can be used in classical beam theory through equation (6.2) and the deflection of the beam can be calculated analytically. Figure 6.28 gives the comparison of the experimentally obtained and analytically calculated mid-span deflections for all GFRP beams tested in three point bending with an applied load of 10 kN. It is seen that the agreement is good and therefore it can be concluded that the material properties of the GFRP sections have been evaluated successfully; the results obtained can be used effectively for the analysis of the hybrid beams.

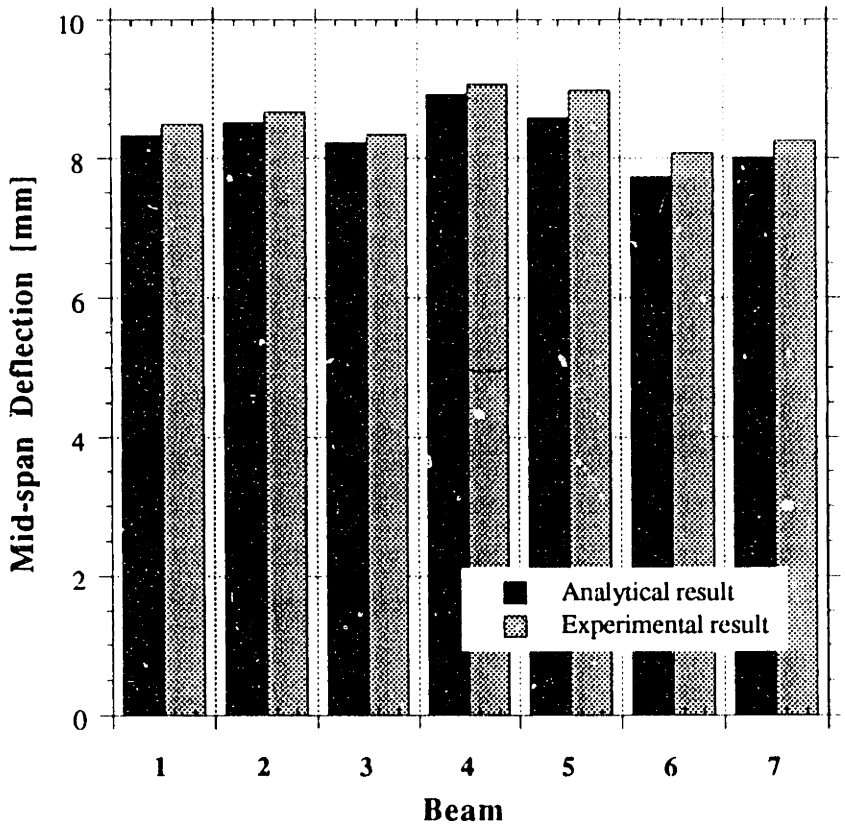

Figure 6.28 Deflection comparison of experiment with analysis.

6.3.3 Creep Properties of GFRP

The creep characteristics of GFRP used in the experiments were evaluated for the filament wound beams only. Two specimens were subjected to a sustained stress configuration and the strains recorded for a period of 32 days. The data obtained were used to calibrate the parameters of Findley's model and for comparison with the results of

the continuum theory approach. The two specimens involved were cut out from the end zones of Beam 2, which was also used for the creep test, as shown later in Chapter 7. One of the coupons was taken from the flange while the other came from the web in order to calibrate the creep response separately. The specimen dimensions and construction was shown in Figure 6.21(a). Using special wrench tightened anchorage clamps, the coupons were spanned into the tensile strut on one side of a horizontal, singly supported lever arm. The coupons were stressed with gravitational loads through lead bars appended on the other side of the lever arm which, due to antisymmetry, provided a load multiplication of roughly 10 times. Two small steel bolts were bonded onto each face of the specimens and a digital extensiometer was used to measure the strain increase at daily intervals. The average of two readings, one from each face, were used for strain calculation. The initial strain for the flange specimen was 0.195% while 0.225% strain was applied onto the web specimen.

The calibration of Findley's model parameters are given next. A least square curve fit was carried out over data from both specimens, resulting in creep models for both the GFRP flange and the web. Figure 6.29 shows the data from the creep tests and the resulting creep models. It is seen that the model complies well with experimental data and the calculated error from the least squares analysis is less than 1%. The parameters obtained for the coefficients m and n in equation (4.10) are relatively close for the flange and the web, which indicates that the same mechanism causes the viscoelastic response. This becomes even more apparent when the continuum theory model is considered. In Section 6.3.1 the creep response of the GFRP's matrix was described and modeled analytically.

Applying this model and the continuum theory approach presented in Chapter 4, the analytical prediction of the creep response of the two GFRP specimens was carried out. A fiber volume fraction of 0.6 and 0.46 was used for the flange and web coupons, respectively, which is in agreement with the data given in Table 6.9. Figure 6.30 gives the comparison of the experimental data and the analytical result from continuum theory. It is seen that the model complies well with the experiment and thus justifies the assumptions made within the continuum theory approach for the characterization of creep. It can be noted that the parameters used for Findley's creep model of the matrix and those used for Findley's creep model of GFRP are relatively close.

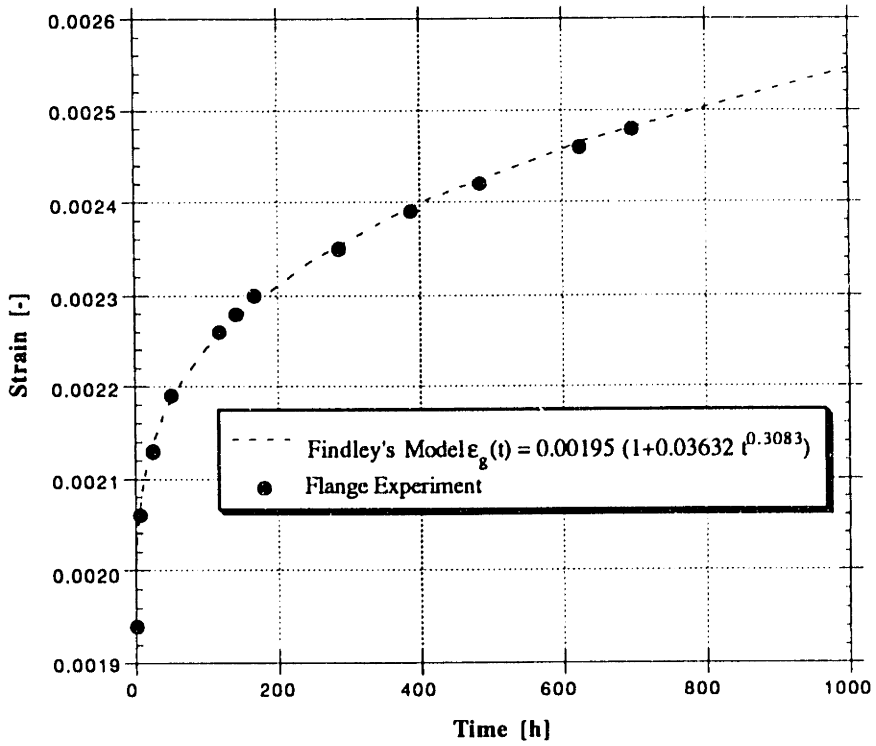

(a)

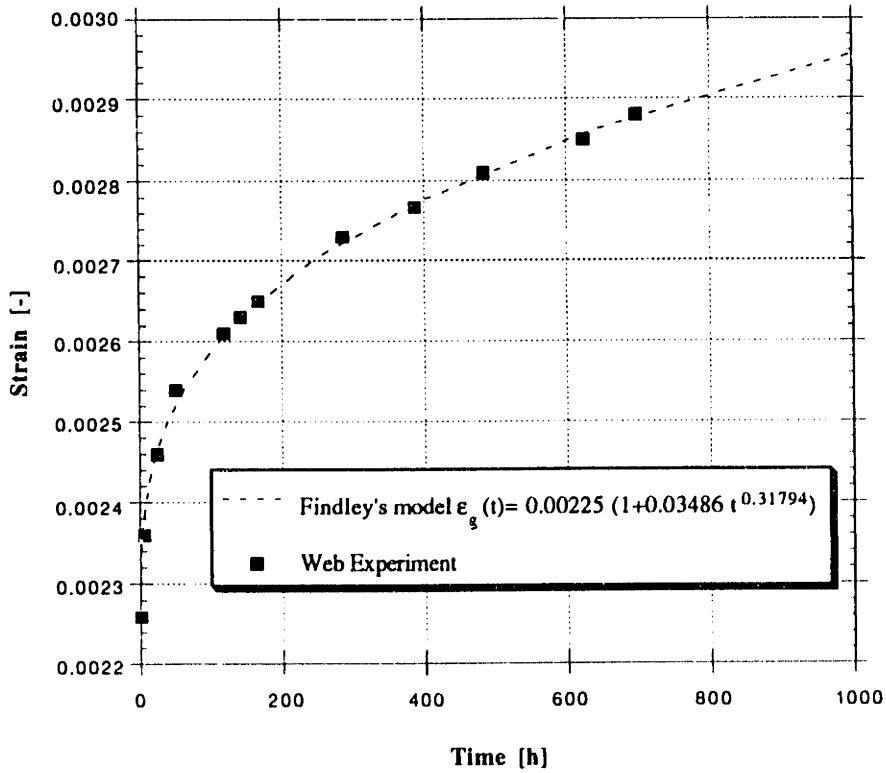

(b)

Figure 6.29 Findley's models for GFRP creep: (a) flange; (b) web.

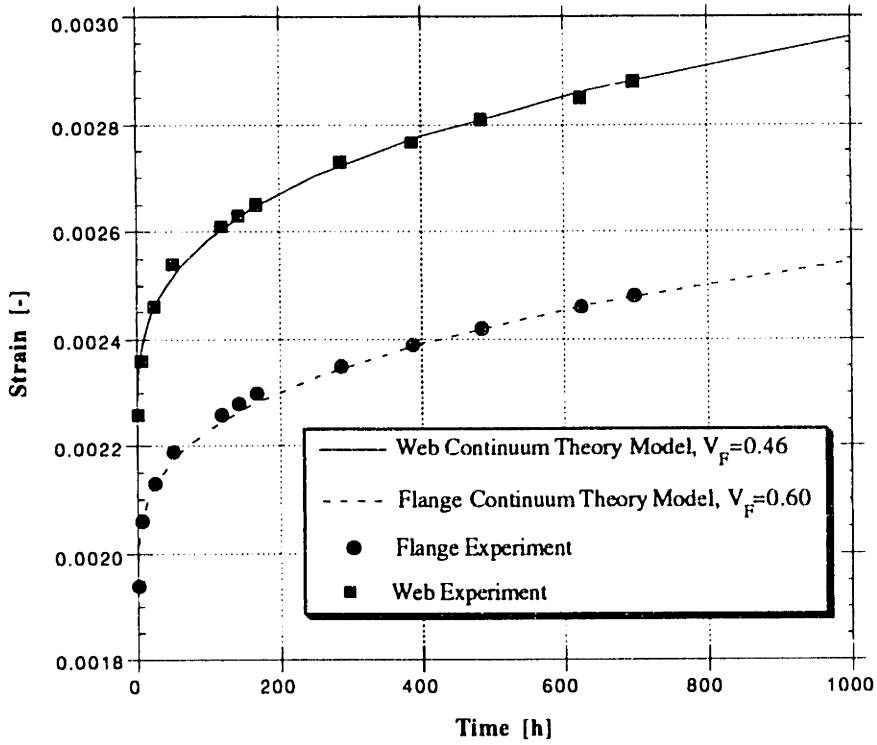

Figure 6.30 Continuum theory GFRP creep model: comparison of experiment with theory.

Using the creep models isochronic curves for GFRP can be determined. Implementing the fourth order polynomial model for the short term response of the GFRP in the flange of beam 2, which was described in Section 6.3.2.2.1 with parameters given in Table 6.10, and using equation (4.10) for the time dependent strain calculation as given in Chapter 4 with the parameters defined in Figure 6.29(a), Figure 6.31 was obtained. Isochronic stress-strain curves for different duration of sustained load are plotted. It is seen that the nonlinearity of the GFRP response vanishes with the increase of the duration of sustained load. Also, assuming that the ultimate strain of GFRP at failure is constant regardless of the load history, it has to be pointed out that the strength of GFRP due to creep effects is reduced. Further, it can be concluded that for a short creep duration the integral of the stress-strain relationship changes significantly, which implies that the viscoelastic response of the GFRP will be an important factor for the creep behavior of the hybrid beam.

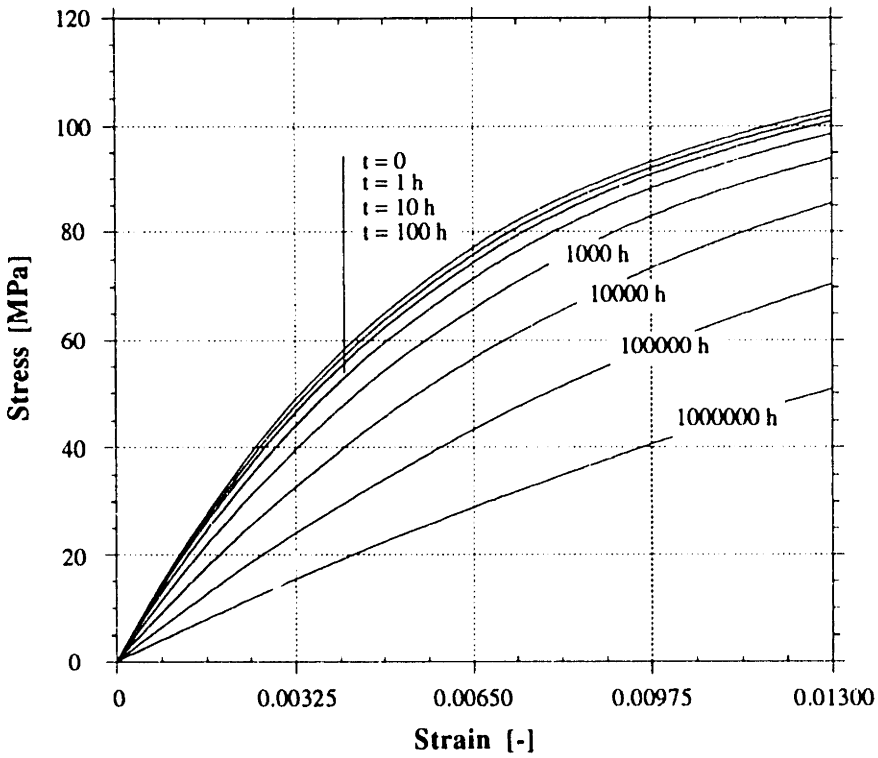

Figure 6.31 Isochronic stress-strain relationship for GFRP.

A similar result would be obtained if the continuum theory model were to be used instead of the empirical, and hence that was not specifically evaluated at this point. The web specimen described above, after being loaded in creep for 32 days along with two more specimens loaded with the same load for 14 hours and one hour, respectively, were tested up to failure in tension in order to investigate the residual strength properties of GFRP. Unlike the 32 day specimen, the other coupons were loaded directly on the INSTRON 1521 under sustained load, prior to the residual strength test. The coupon dimensions were defined in Figure 6.21(a) and were all originally cut out from GFRP box Beam 2. All three specimens were loaded in creep with a stress of approximately 30 MPa. The same test setup as described in Section 6.3.2.2.1 was implemented. Figure 6.32 shows the stress-strain diagrams of all three coupons recorded during the residual tension test, including the portion generated due to creep. The specimens were tested immediately after the creep test was concluded and thus it is assumed that no time for recovery was allowed. Figure 6.32 shows that the assumptions made in Chapter 4 on residual response hold. The stress-strain curves are almost parallel up to 70% of the ultimate strength, with a strain shift equal to the one that occurred during creep. The ultimate strain is maintained, although it can not be concluded that this verifies the assumption on constant strains at

failure, since too much scatter in GFRP data is usually expected and a more extensive test series would be required.

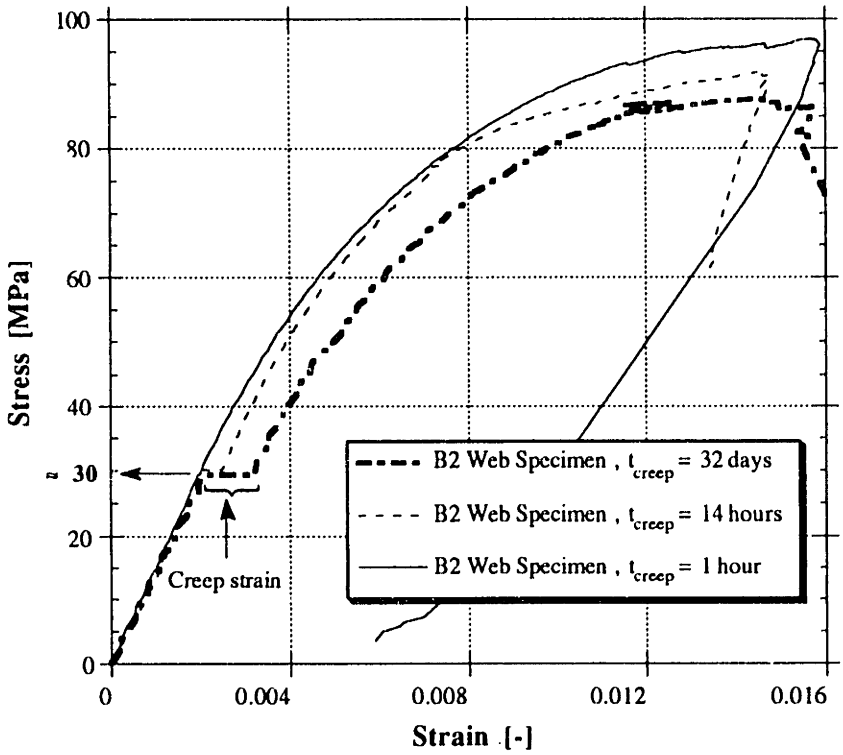

Figure 6.32 GFRP residual response.

6.3.4 Fatigue of GFRP

The fatigue response of GFRP used in the large scale beams was characterized through experiments performed on coupon specimens. Two specimens with geometry as defined in Figure 6.21(a) were subjected to cyclic loading in order to obtain experimental results. These data were then used for the calibration of parameters required for the empirical GFRP fatigue model described in Section 4.4.3.1. Also a comparison and evaluation of the continuum theory model described in Section 4.4.3.2 was carried out.

Both specimens were cut out of the bottom flange at the end zone of Beam 6, which was also used for the creep test as shown later in Chapter 7. The fatigue tests were carried out on an INSTRON 1521. Special hydraulic anchorage clamps were used for these tests, to prevent friction and anchorage slip and to provide a constant pressure at the supports. The loading was controlled by a computerized oscillator and is shown in Figure 6.33. The two coupons were loaded with a maximum stress of 75 and 50 MPa, while the minimum stress was set at one third of the maximum ($R = \sigma_{max}/\sigma_{min} = 1/3$). Note that in none of

the two models the minimum stress was defined as a parameter, and was therefore chosen to comply with the R value used in the fatigue tests of the large scale hybrid beams (see Figure 5.36). The frequency was set to 4.2 Hz. After every decade of load cycles (1, 10, 100, ...,1million) the tests were interrupted and a measurement of the short term stiffness was carried out. These short term tests were deformation controlled and were performed until the maximum fatigue stress was reached with a deformation speed of 0.4 mm per minute. The stress-strain relationship of the specimens' response was recorded. A 10 kN load cell and a 30 mm clip gauge were implemented to measure (and then to calculate) the associated stresses and strains. A dynamic data acquisition system was used to retrieve data and store them at a frequency of 120 points per second. At the beginning of every experiment the strain reading was reset to zero in order to eliminate the creep deformation. The test setup is given in Figure 6.34.

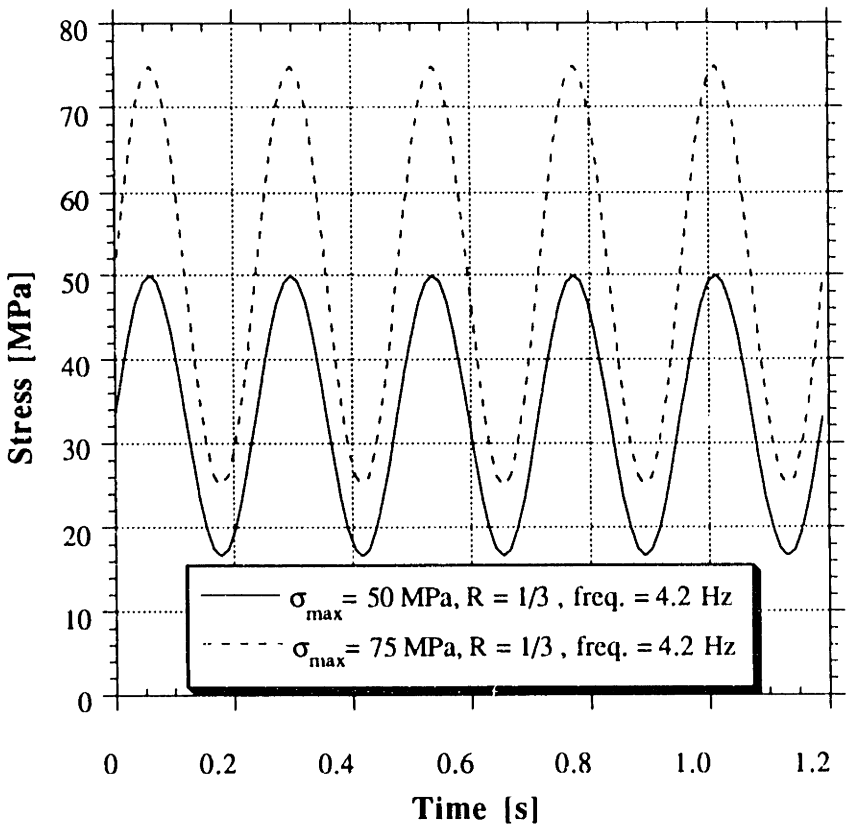

Figure 6.33 Load configuration of coupon fatigue tests.

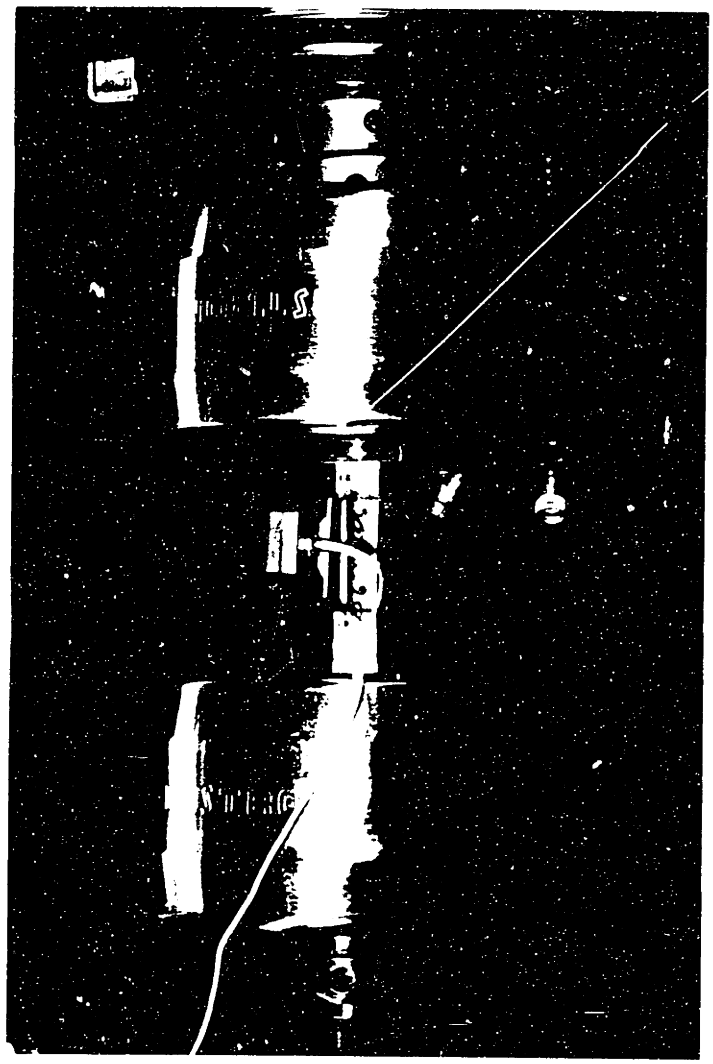

Figure 6.34 Coupon fatigue test layout.

The tests were performed with 1 million cycles for each specimen and the results obtained from the stiffness measurements are given in Figures 6.36 and 6.37 for the 75 and 50 MPa specimen, respectively. In Figure 6.35 the loading and unloading branch of the short term tension test is given, while in Figure 6.36 only the loading part is presented for better visualization. Also the diagrams for the low cycle number curves are omitted. From the diagrams obtained a secant modulus was determined at 60 and 40 MPa for the two beams, respectively, as depicted in the figures. Table 6.13 shows the calculated secant moduli obtained in the experiments. The different initial secant modulus of the two specimens, can be explained from the different stress reference (60 versus 40 MPa) and from some data scatter between the two specimens. Since the stiffness degradation was

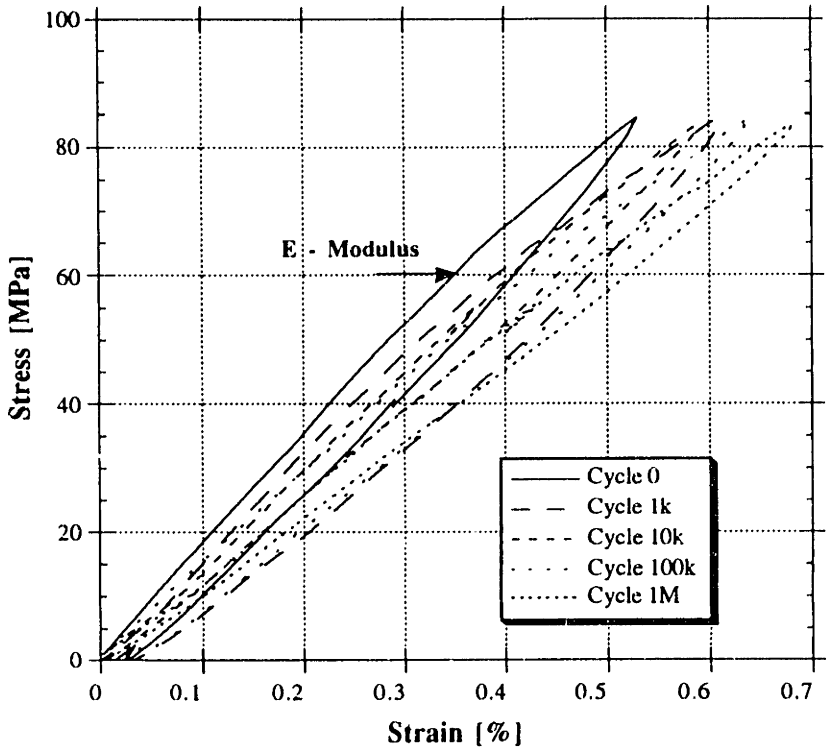

Figure 6.35 Fatigue test specimen stressed at 75 MPa.

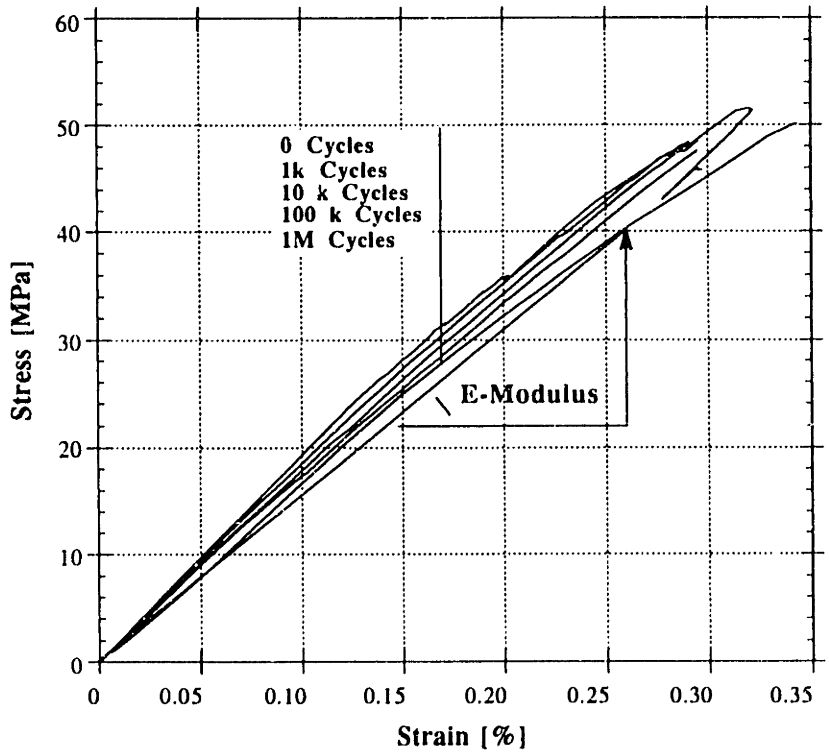

Figure 6.36 Fatigue test specimen stressed at 50 MPa.

only considered in the models as a relative value, the actual magnitude of the initial secant modulus is irrelevant.

Table 6.13 Secant modulus degradation due to fatigue.

Cycle number, N	0	1	10	100	1000	10000	100 k	1 M
E-Modulus for σ_{max} = 75 MPa	16011	15870	15750	15604	15312	14798	14171	12785
E-Modulus for σ_{max} = 50 MPa	17604	17529	17480	17405	17243	16928	16396	15484

6.3.4.1 Empirical GFRP Fatigue Model Calibration

The model chosen for the prediction of the fatigue response was proposed by Ogin et al. (1985). The basic assumptions were described in Chapter 4, where the explanation for the stiffness decrease of GFRP in fatigue is attributed to matrix cracking. The results from Table 6.13 were used to calibrate the parameters of equation (4.62).

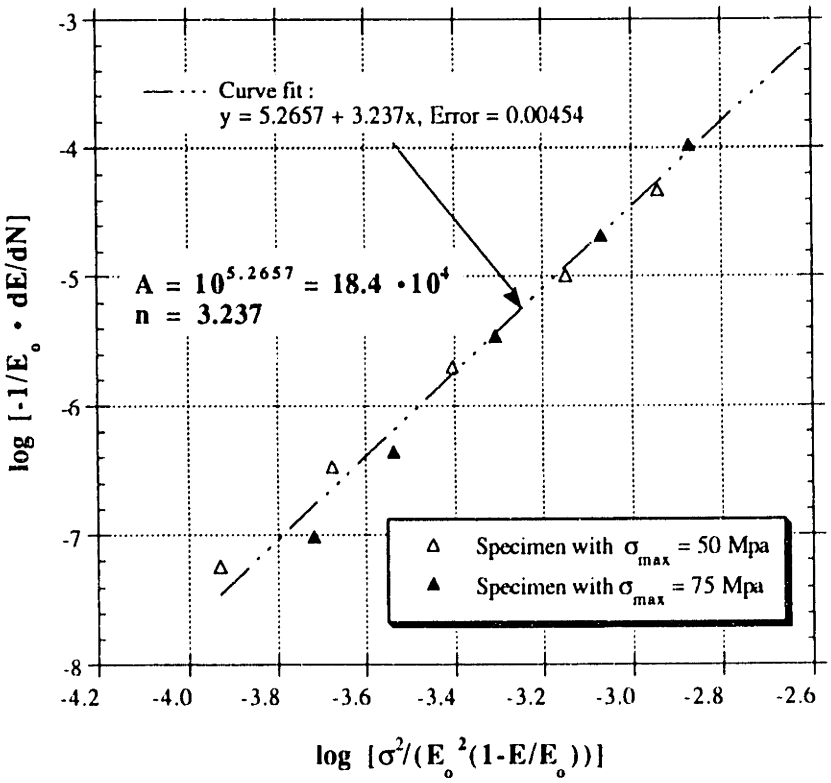

Figure 6.37 Modulus reduction rate of GFRP in log-log scale.

Figure 6.37 gives the modulus reduction rate in log-log scale and from there the constants A and n are obtained directly. Note that the error of the curve fit is less than 0.5%. Substituting these results into equation (4.63), the dependence of the elastic modulus to the number of cycles and stress level can be expressed with:

$$E(N,\sigma_{max}) = E_o\left[1 - 24.574(\frac{\sigma_{max}}{E_o})^{1.528}\, N^{0.236}\right] \tag{6.7}$$

This model for the stiffness degradation was compared to the experimentally obtained values and is given in Figure 6.38. Equation (6.7) is plotted for various values of stress level applied for each of the specimens. It is seen that the agreement between model and experiment is satisfactory, although for higher cycle numbers the model appears less conservative and gives higher elastic modulus values than the experiment.

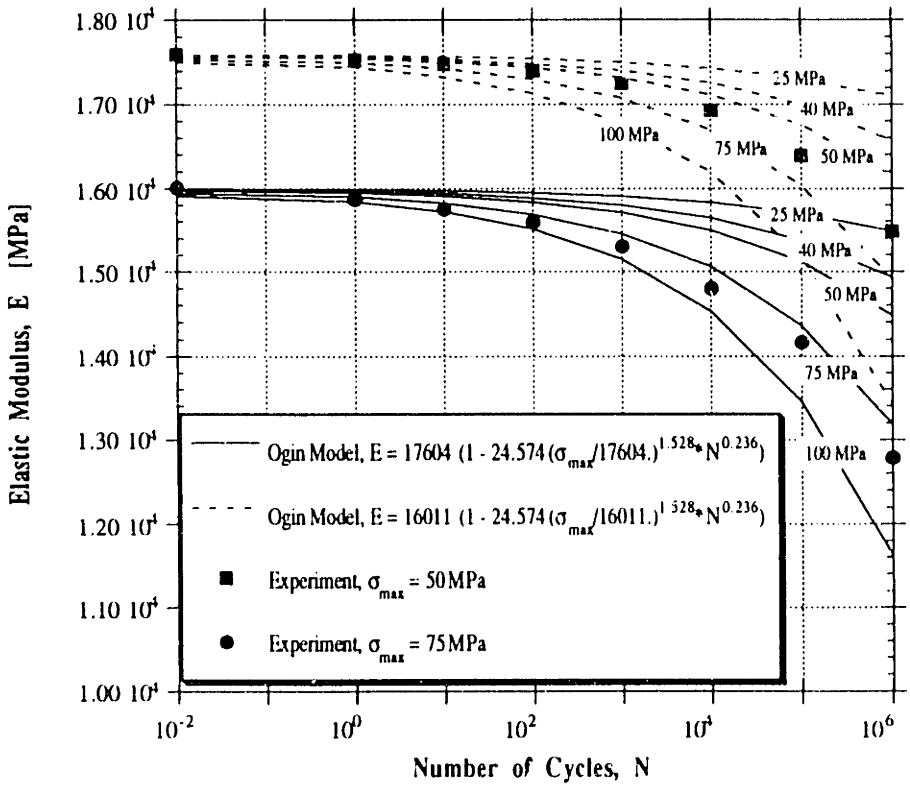

Figure 6.38 Comparison of experiment and fatigue model of GFRP.

6.3.4.2 Continuum Theory Fatigue Model of GFRP

The model implemented here was described in Section 4.4.3.2. The main idea behind this approach is to apply known fatigue properties of the unidirectional GFRP layer and obtain the response of the multilayered composite. Data from Bitterli (1987) showed that only the shear modulus, $G_{\#}$, of the unidirectional layer changes when the latter is loaded in fatigue. Under this assumption, with the continuum theory approach as described in Section 4.3.3.2 and using equation (4.70), the elastic modulus of GFRP used can be calculated as a function of the stress level applied and the number of load cycles elapsed.

Using the same material properties of fibers and matrix as defined in Figure 5.6 and implementing the above procedure, the reduction of the elastic modulus was calculated for an applied stress of 50 and 75 MPa, respectively. If these results and the data from Table 6.13 are normalized with the corresponding initial elastic modulus, E_o, Figure 6.39 is obtained. It gives the comparison of the continuum theory model and the experimental data. It is seen that the agreement between experiment and analysis is not as good as for the empirical model, but the former model compares better to the experiment for higher numbers of load cycles. In general, the continuum theory approach gives conservative results.

The proposed models are further discussed by determining the stress-strain relationship of GFRP when subjected to a different number of loading cycles. The short term stress-strain relationship of the flange coupon of beam 6 was used and both fatigue models described and calibrated above were implemented to obtain the isocyclic diagrams for GFRP. Following the iterative procedure described in Chapter 4, for a particular strain and a given cycle number the associated stress was calculated. The result of this computation is given in Figure 6.40, where the two models are compared to each other. It is seen that the continuum theory model gives more conservative results for higher stress ranges, while the empirical one shows a higher stiffness decrease at lower stress levels. Overall, it can be concluded that the fatigue models show little effect on material behavior for small stress levels, while for higher ranges this influence can be of significant importance.

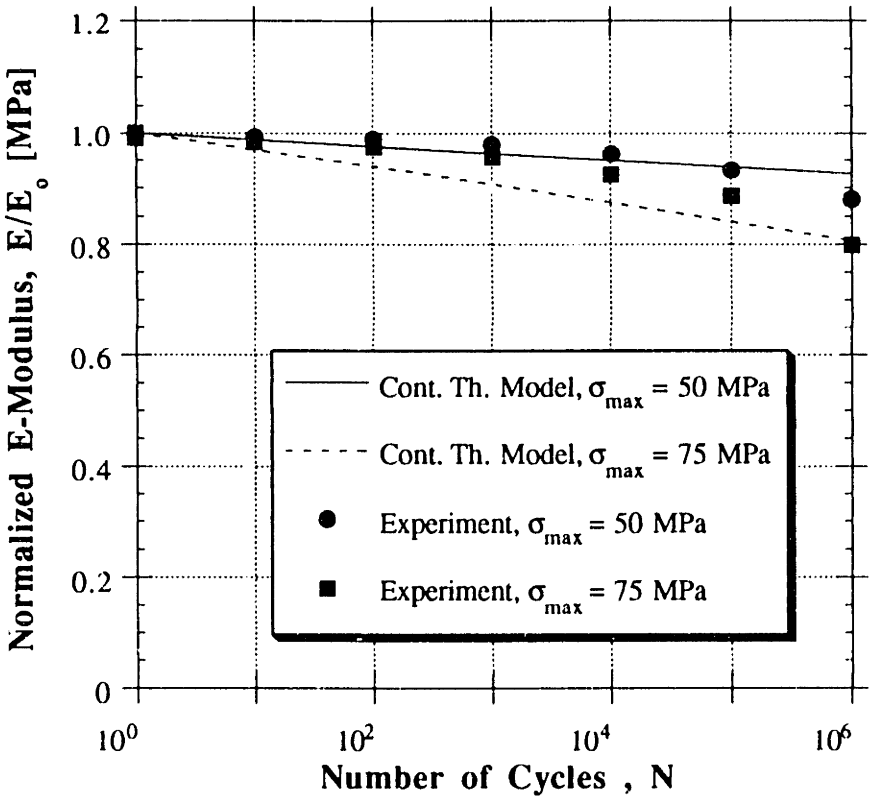

Figure 6.39 Comparison of experiment and continuum theory fatigue model for GFRP.

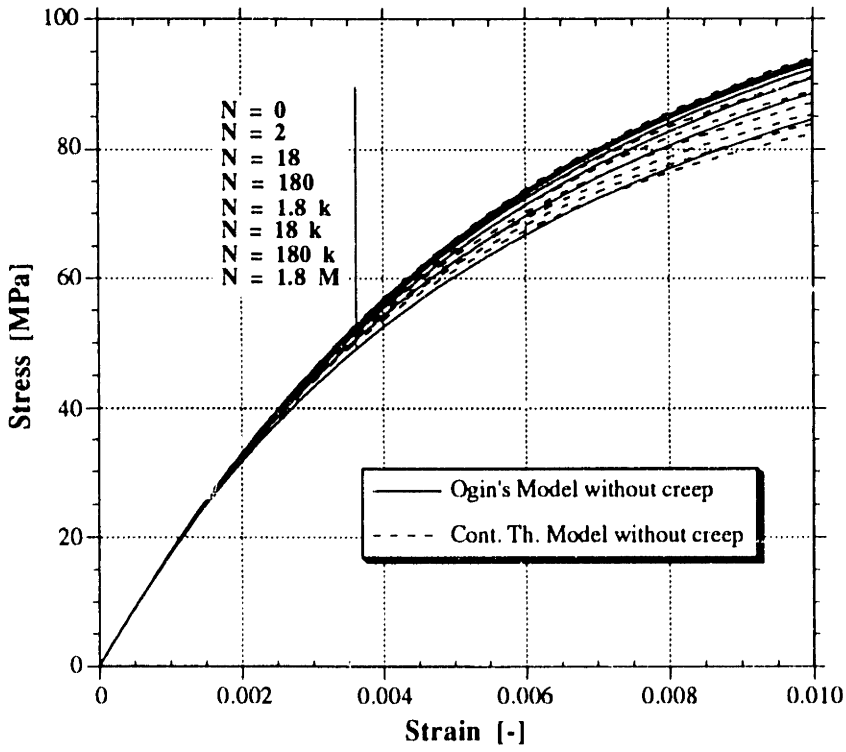

Figure 6.40 Isocyclic stress-strain relationship: comparison between continuum theory and empirical model.

Finally, combining the creep and fatigue models for GFRP, a more real-life form of the stress-strain curve can be obtained. Since physically the fatigue damage always requires some time to be conducted, it is reasonable to assume that a certain amount of creep will simultaneously be introduced in tension-tension load configurations. In order to visualize the combined effect, the empirical model was recalculated including the viscoelastic response as described in equation (4.66). Figure 6.41 shows the resulting diagrams, for the case of a constant cycle frequency of 5 Hz. Again, the creep effect is more significantly represented for lower stress ranges, while for higher stresses fatigue effects become increasingly important. Expanding this reasoning to the case of a much lower frequency (e.g., one cycle per hour) it appears that the creep effect would be dominant. On the other hand, it has to be pointed out that for lower frequencies the assumed sinusoidal load pattern would not make sense, and if it were different, the material would have time to recover and hence, creep effects would be eliminated. In practice, therefore, for design purposes of GFRPs the creep influence is not considered as a side effect of fatigue, but rather as a separate factor, which, in addition, is generated by much lower loads than those causing fatigue. It was only for the tests performed on the large scale hybrid beams, where high fatigue loads were inducing creep at the same time, that the combined effect had to be considered.

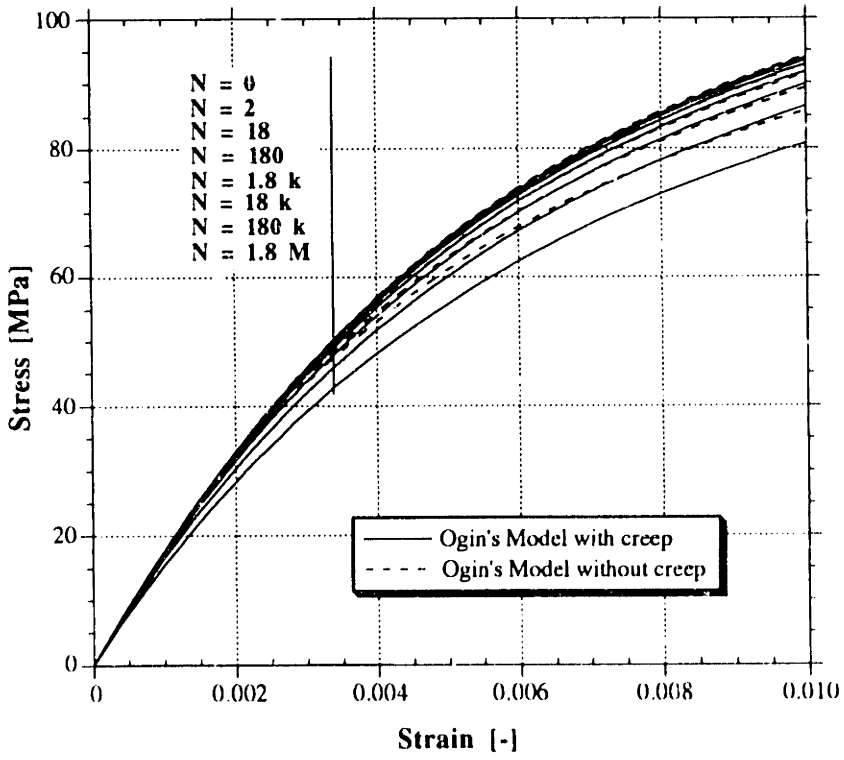

Figure 6.41 Combined effect of fatigue and creep.

6.4 Carbon Fiber Reinforced Plastic Laminate

The third material used for the hybrid beam design constitutes the thin sheet of carbon fiber reinforced plastic. The fiber orientation of the CFRP used in the experimental program is unidirectional along the hybrid beam's axis, in order to provide high strength and stiffness. If the volume fraction of fibers is relatively high, that is around 70% and considering the stiffness proportions of the fibers and the matrix, it can be concluded that their mechanical properties will strongly affect the properties of the CFRP lamina. The material properties of the fibers involved are given in Table 6.14.

Table 6.14 Mechanical properties of fibers used for the CFRP.

Fiber	Diameter, d_F [μm]	Tensile Strength, σ_F^* [MPa]	E-Modulus, E_F [GPa]	Ultimate strain, ε_F^* [%]	Density, ρ_F [g/cm^3]
Tex 1200	10	1800	76	3-4	2.52
T300	7-8	3530	230	1.5	1.76
T700	7-8	4900	230	2.1	1.80
M46J	7-8	4200	440	0.8	1.80

Three types of FRP sheets were used in the experiments, all with an epoxy matrix of the same characteristics as defined earlier in Table 6.7, but with different reinforcing fibers. The first, applied for the small scale beams, was a hybrid mix between the Tex 1200 glass and the T300 carbon fibers. The second and third were produced with the T700 and M46J carbon fibers, respectively. All laminates were produced with the pultrusion process. The mechanical properties can be determined analytically using the rule of mixtures (see equations (4.14) to (4.18)), or directly by performing tensile tests. The second method was implemented in this work.

The short term uniaxial tension properties of the three different types of unidirectional laminates used on the tension face of the hybrid FRP-concrete beams are summarized in Table 6.15 and used in the analysis of the hybrid beams.

Table 6.15 Material properties of CFRP sheets.

Laminate (Thickness)	Elastic Modulus, E_2 [MPa]	Tensile Strength, σ_2^* [MPa]	Strain at Failure, ε_2^* [%]
G/CFRP (0.3 mm)	80235	963	1.15
CFRP T700 (0.45 mm)	110000	1144	1.05
CFRP M46J (1.0 mm)	300000	2350	0.8

The long term properties of the CFRP sheets are assumed to be constant. This assumption was discussed earlier in Chapter 4. It can be concluded that any viscoelastic deformation or fatigue damage accumulated in the matrix will have such a minimal effect on the overall mechanical properties that, compared to the other materials (concrete layer and GFRP box beam), it can be neglected.

6.5 Synopsis

The calibration of the empirical parameters for the short term response of concrete and GFRP was given in this chapter. Concrete shrinkage, creep and fatigue models were elaborated and the appropriate empirical values adopted. Similarly, two models for the simulation of both creep and fatigue behavior of GFRP were defined and adjusted to experimental data. In the next chapter the results obtained are used to predict the response of the hybrid FRP/concrete beams in three and four point bending tests under both short and long term loading configurations.

Chapter 7

EXPERIMENTAL RESULTS AND COMPARISON WITH ANALYSIS

7.1 Introduction

The analysis presented in Chapters 3 and 4 for the short and long term response of the hybrid beam is evaluated and verified experimentally in this chapter. Analytical and numerical results of 18 small and 7 large scale beams in three and four point bending are compared to experimental values.

The short term behavior was investigated on the small scale beams, with the emphasis placed on the study of different failure modes. Only ultimate loads and deflections are computed here. Large scale Beams 1, 3 and 4 were subjected to three point bending tests and the results obtained were compared to the ones from analytical and numerical solutions. The full response was modeled and quantified. A finite element method model was created for the large scale beams and was validated with the experimental program.

The creep analysis was verified experimentally with 24 hour creep tests on large scale Beams 5 and 6 and with long term (still running) tests on Beams 2 and 7. Finally, Beams 5 and 6 were tested under fatigue conditions and the response was compared to the predicted behavior from analytical models.

The material models which were calibrated in Chapter 6 were implemented in the analysis and an overall satisfactory agreement between the calculated response and the experimentally obtained behavior was achieved. The three types of loading configurations, namely short term static, creep and fatigue, were examined separately, and the results are given in the following sections.

7.2 Short Term Response of Hybrid Beams

7.2.1 Three Point Bending Tests on Small Scale Beams

Eighteen small scale beams, the geometry and material properties of which were defined earlier in Table 5.1, were tested in three point bending up to failure. Different failure mechanisms were encountered and are summarized in Table 7.1. In this section the beam numbers refer to small scale beams only.

The load-displacement curves obtained from the bending tests are shown in Figures 7.1 and 7.4 to 7.6. In Figure 7.1 the flexural behavior of a plain GFRP member (Beam 18) is compared to the response of two hybrid members (Beams 13 and 14). While Beam 13 was nonprestressed, Beam 14 was prestressed with an initial strain in the CFRP sheet of 0.35% (approximately 30% of the CFRP's ultimate strain). Both beams had a 28 mm thick compression layer of HS-FRC and a 0.3 mm thick CFRP lamina. The ultimate load capacity of the hybrid beams was almost three times higher than that of the plain GFRP beam, while the stiffness was nearly four times higher. Beam 18 failed by GFRP top flange local buckling (see Figure 7.2) followed by compressive crushing. Both hybrid beams collapsed due to concrete crushing but had a substantial difference in their behavior. Beam 13 failed in a brittle manner and showed no warning prior to collapse. On the other hand, Beam 14 had a pseudo-ductile failure mechanism. The initiation of failure was announced with tensile fracture of some of the CFRP fibers, followed by complete fracture of the CFRP sheet giving a sudden drop in the load (since the test was displacement controlled). Then, both the load and the displacement increased further until the concrete crushed, but at a load level higher than that corresponding to CFRP fracture (Figure 7.3). This result indicates that the concept of pseudo-ductility described in Section 3.3.1.3 is quite valid. It should also be noted that the displacement of the two hybrid beams at failure was not much lower than that of the plain GFRP element.

In Figure 7.4 the flexural behavior of various hybrid beams is illustrated. Beams 3 and 4 had a 25 mm thick normal strength concrete layer and a 0.3 mm thick CFRP lamina. In addition, Beam 4 was pretensioned with a 0.63% initial strain in the CFRP sheet (approximately 55% of its ultimate strain). The beam displayed a higher load capacity, slightly higher stiffness and also a larger displacement at failure. In addition, a few CFRP fibers failed prior to concrete crushing, indicating that the stresses in the CFRP lamina were close to the ultimate.

Table 7.1 Failure modes recorded in three point bending tests.

Beam	Failure Mode
1	Shear failure initiation, local punching
2	Concrete crushing
3	Concrete crushing
4	Partial CFRP failure, concrete crushing
5	Concrete crushing
6	Concrete shear failure
7	Concrete crushing
8	Concrete crushing
9	Concrete crushing
10	Concrete shear failure
11	Concrete crushing
12	Concrete crushing
13	Concrete crushing
14	CFRP fracture, then concrete crushing PSEUDO-DUCTILE BEHAVIOR !
15	Concrete-GFRP interface debonding
16	GFRP shear failure initiation, then concrete crushing
17	GFRP shear failure initiation, then concrete crushing
18	Compression flange buckling, then compression flange crushing

Beams 7 and 8 had the same thickness of normal strength concrete (31 mm) and of CFRP sheet (0.3 mm) but Beam 8 had a narrower CFRP sheet than Beam 7 (70 versus 80 mm) and was pretensioned with a 0.58% initial strain in the composite sheet. The response of the two beams was similar since the pretension of beam 8 was compensated by the wider CFRP lamina of Beam 7. Both members failed in a brittle manner by crushing of the concrete layer. For the sake of comparison, the curve for Beam 11 (which had the same concrete layer but no CFRP sheet) is given, indicating reduced strength and stiffness.

In Figures 7.5 and 7.6 the flexural response of the remaining beams is shown. Beams 6 and 10 failed due to concrete shear failure and Beam 15 failed due to interface

debonding. All other beams failed by concrete crushing. It was observed that the concrete thickness contributes significantly to the stiffness of the beam (see Beams 5 and 15), while the CFRP has a less significant effect because it is quite thin (compare Beams 2 and 12). It was also observed that hybrid designs with the normal strength concrete were stiffer but weaker than those with the HS-FRC (compare Beam 9 versus Beam 16). Comparisons between the experimental results presented here and analytical predictions are given in the following section.

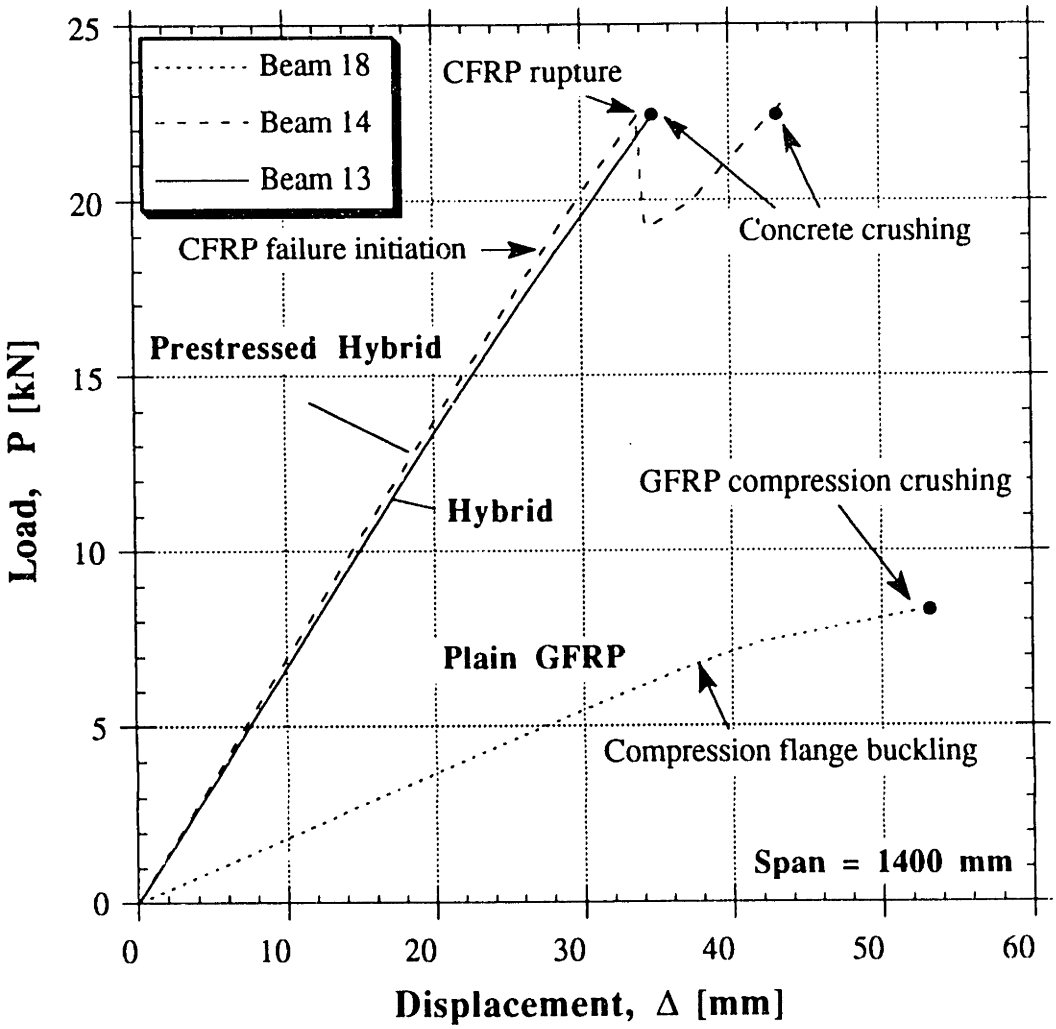

Figure 7.1 Three point bending test results, span=1400 mm.

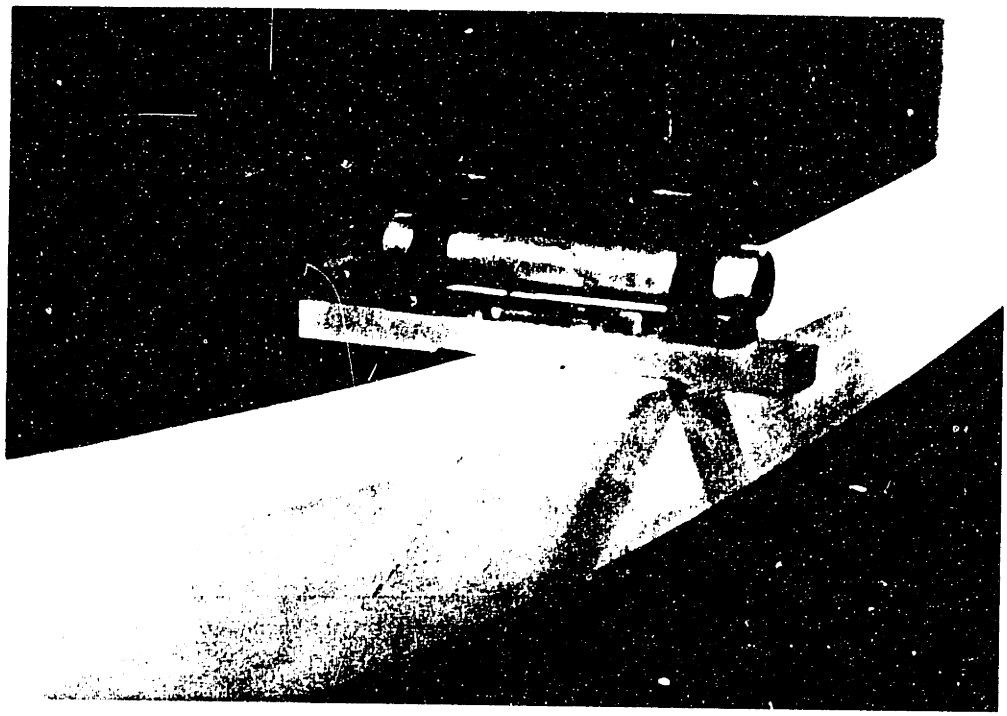

Figure 7.2 Local buckling of compressive GFRP flange.

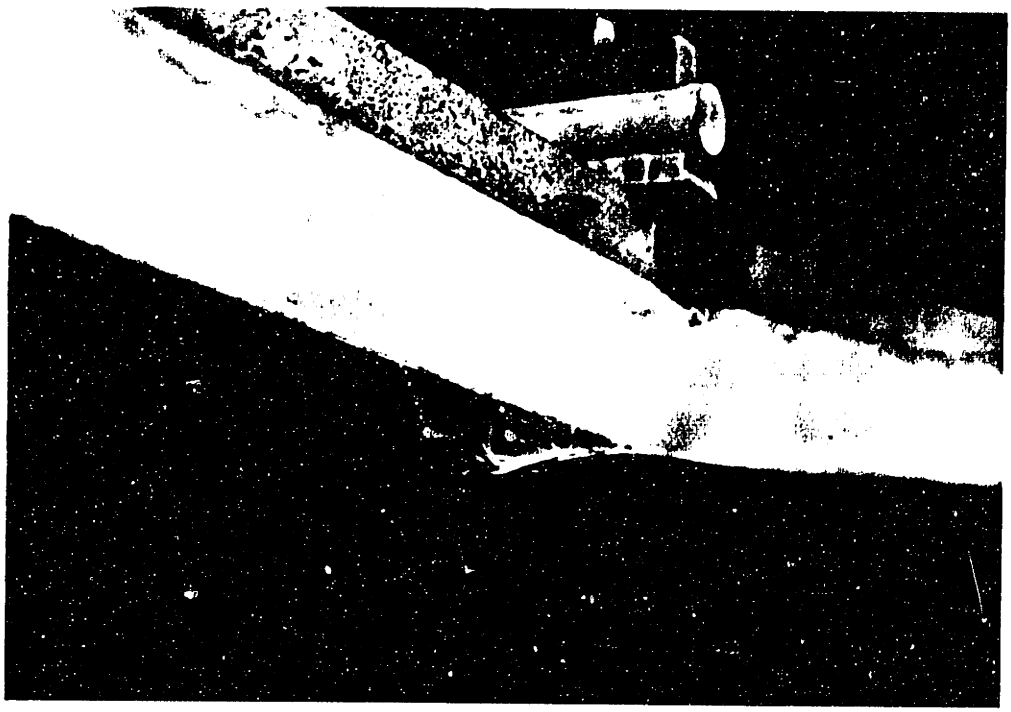

Figure 7.3 CFRP fracture followed by concrete crushing.

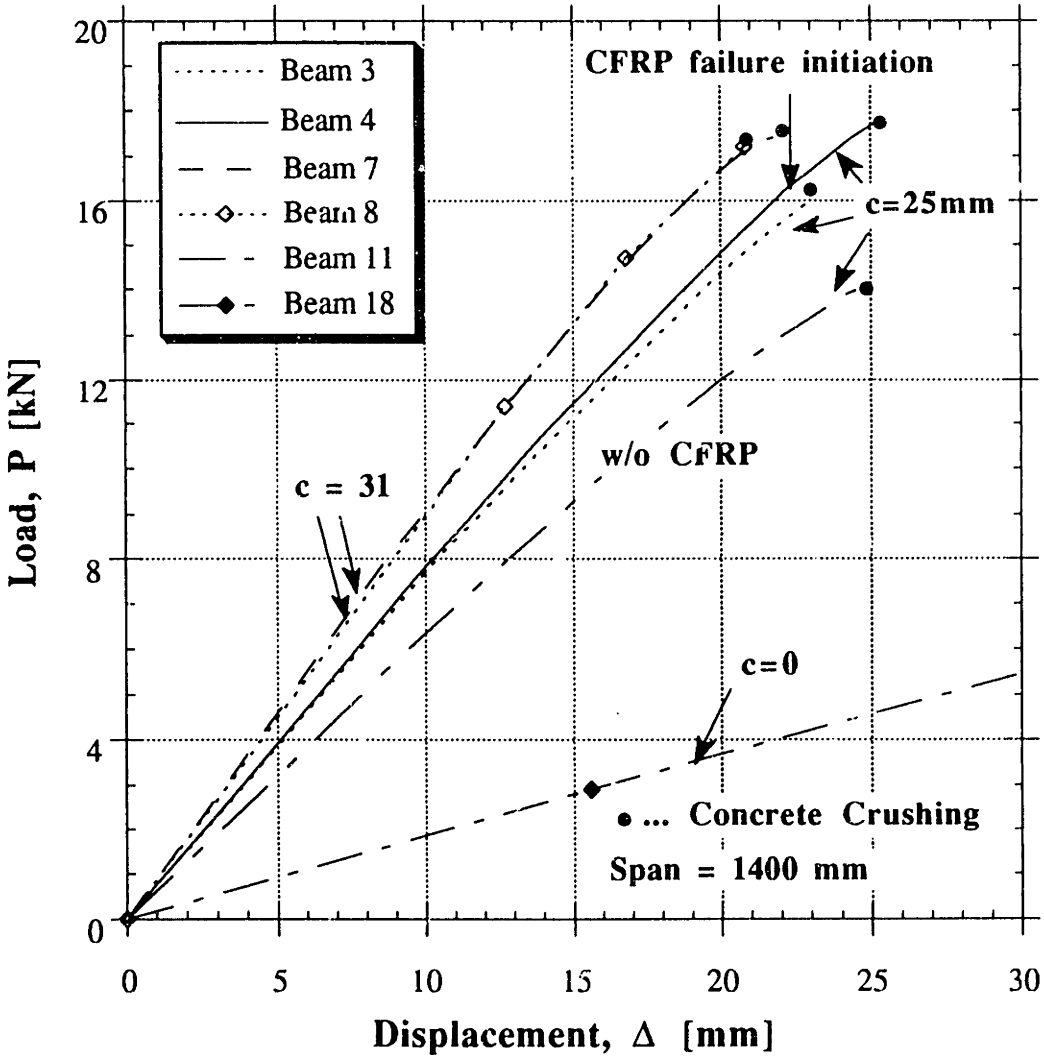

Figure 7.4 Three point bending test results, span=1400 mm.

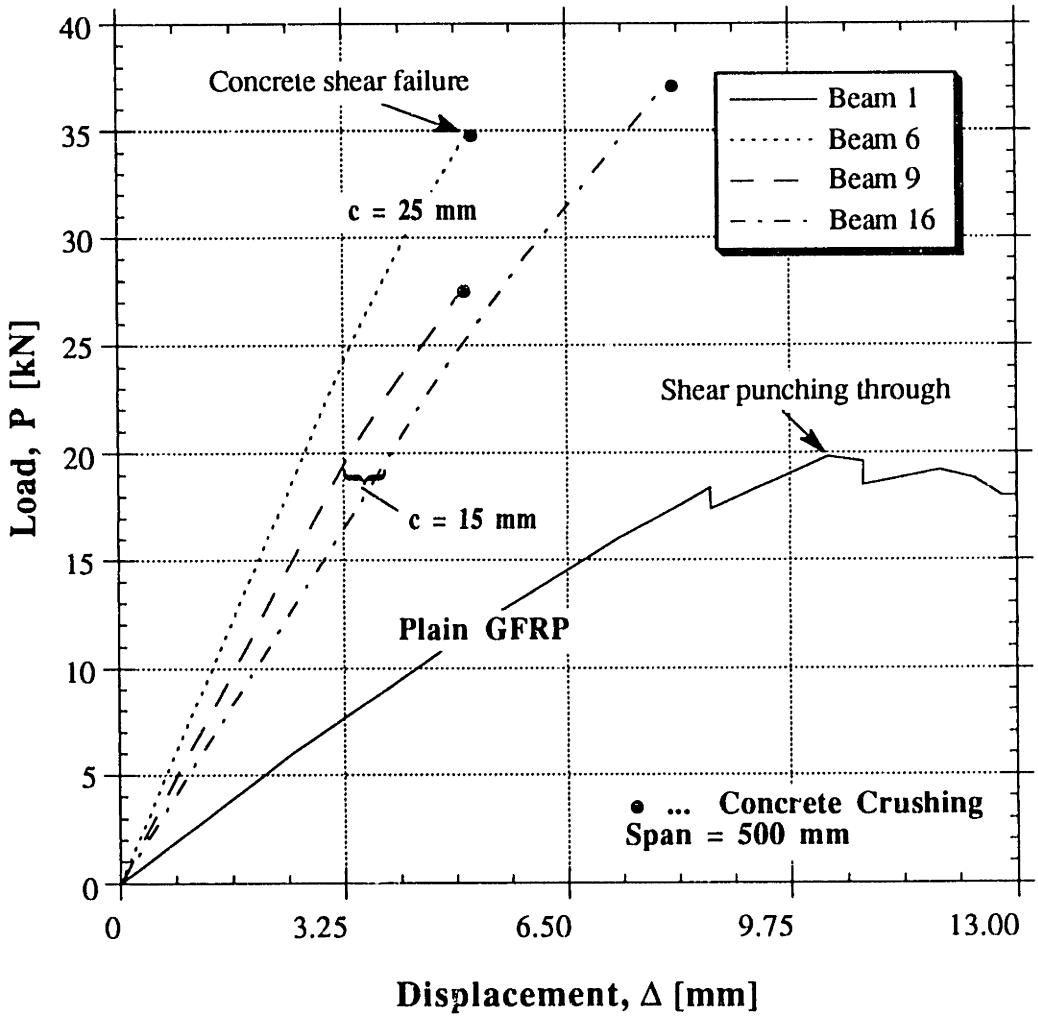

Figure 7.5 Three point bending test results, span=500 mm.

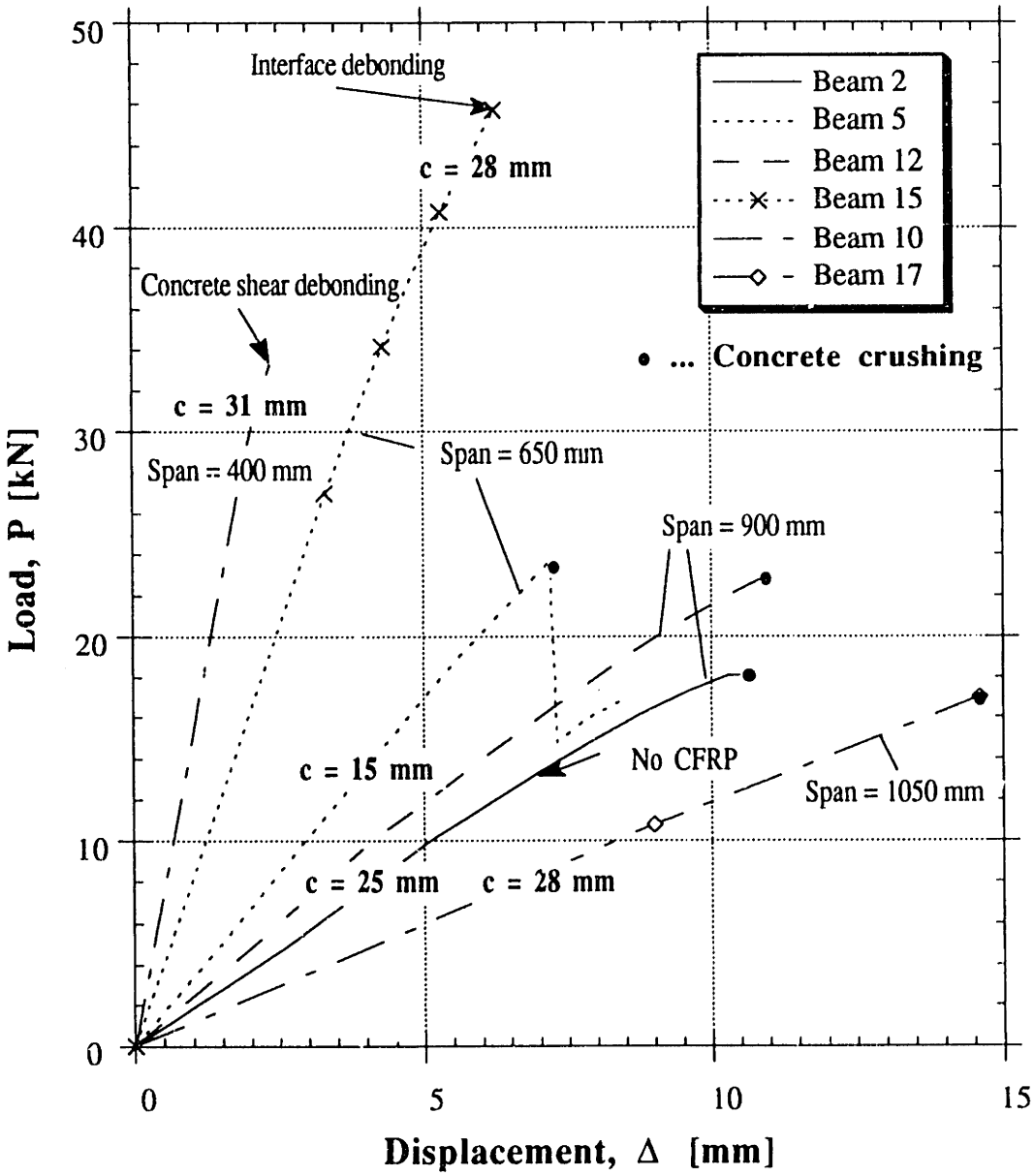

Figure 7.6 Three point bending test results, various spans.

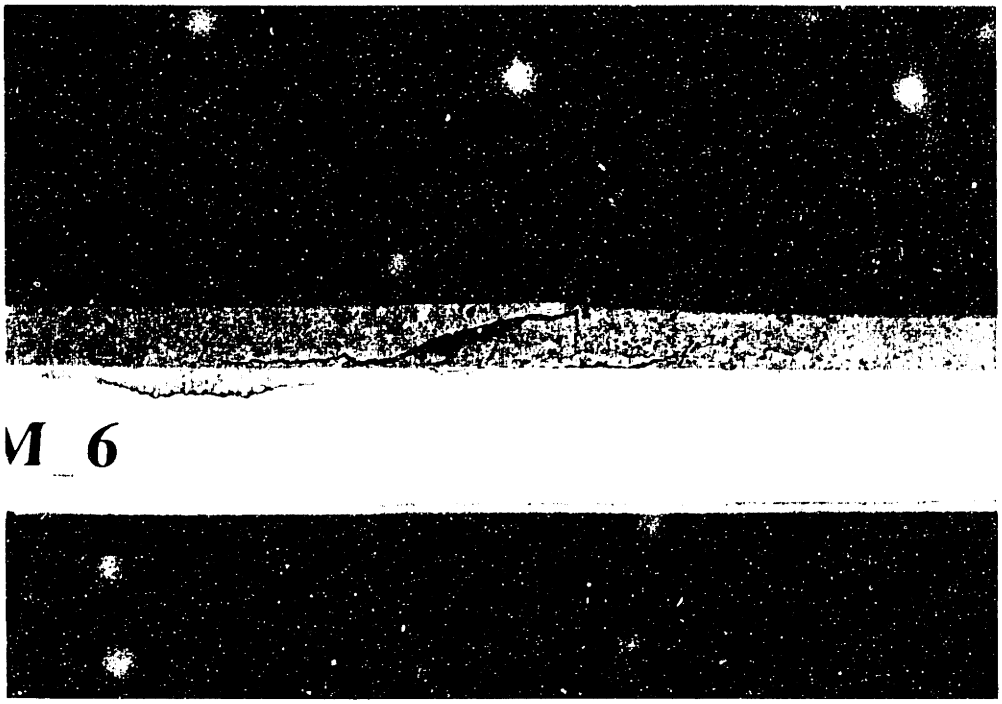

Figure 7.7 Concrete layer diagonal shear failure.

7.2.1.1 Analysis of Small Scale Beams

The analysis presented in Chapter 3 is adjusted to the specific geometry described in Table 5.1. A slight modification of the analytical approach was necessary to represent the structural behavior in a more realistic manner. The material models were adopted as defined in Section 6.2.1.1 for concrete, in Section 6.3.2.1.1 for GFRP and in Section 6.4 for the CFRP lamina. A few additional considerations were implemented in the analysis:

(a) At concrete crushing, the nonlinear concrete model was substituted with the rectangular stress block according to the ACI code specifications (ACI 1989), in order to obtain better results close to failure. Equation (3.13) giving the total compressive force carried by concrete is substituted with:

$$F_c = 0.85 f_c' c b \qquad (7.1)$$

and equation (3.19) defining the ultimate moment capacity of the section at concrete crushing becomes:

$$M_u = F_C(x_n - 0.5c) + F_{TF}\left(x_n - c - \frac{t_3}{2}\right) + F_{TW}\frac{2}{3}(x_n - c - t_3) + F_{BW}\frac{2}{3}(h_g + c - x_n - t_1) + F_{BF}\left(h_g + c - x_n - \frac{t_1}{2}\right) + F_{CC}(h_g + c - x_n + \frac{t_2}{2}) \quad (7.2)$$

(b) An average web thickness of 3.07 mm with a shear modulus, G_w, of 16500 MPa was adopted (see Figure 6.13).

(c) The effect of shrinkage and the influence of the adhesive were neglected.

(d) If the plain GFRP section is loaded in bending, failure may be governed by local buckling of the compression flange (Beam 18). The critical elastic compressive stress was given in equation (3.80) and the moment corresponding to this stress is approximately:

$$M_b = \frac{\sigma_{bf}^* D}{E_3(y + t_3)} \quad (7.3)$$

where D and y are the flexural rigidity and the position of the neutral axis, respectively, given earlier by equations (3.73) and (3.65).

(e) The effect of initial prestress (in Beams 4, 8 and 14) applied to the CFRP sheet is accounted for during the calculation of the internal CFRP force. Here equation (3.18) is transformed such that the initial prestress strain, ε_{2i}, is added to the real strain in the CFRP sheet, ε_2 , resulting in the following:

$$F_{CC} = t_2 b(\varepsilon_2 + \varepsilon_{2i}) E_2 \quad (7.4)$$

Also, in the calculation of the CFRP fracture failure mode, the ultimate strain in the bottom fiber of the beam, ε_2^*, should be reduced by the initial prestress strain, ε_{2i}, since the lamina would rupture at $\varepsilon_2 = \varepsilon_2^* - \varepsilon_{2i}$.

All the other derivations described in Chapter 3 (including shear failure) were used directly for the calculations of the load required to activate one of the failure modes.

7.2.1.2 Comparison of Analysis with Experiment

A detailed comparison between the experimental results and the analytical predictions for the failure load and initial stiffness was carried out. The analytical method followed is that described in Chapter 3 with the modifications given in the previous section, while the material models and properties were described in Chapter 6. The material properties are summarized once again in Table 7.2.

Table 7.2 Material properties used in analysis.

Property	Notation	Units	Value
Elastic modulus of concrete	E_c	MPa	Normal: 33400 HS-FRC: 19400
Compressive strength of concrete	f_c'	MPa	Normal Strength: 40 HS-FRC: 58
Tensile strength of concrete[1]	f_t'	MPa	Normal: 4.45
Ultimate concrete strain	ε_c^u	%	Normal: 0.38 HS-FRC: 0.50
Elastic modulus of CFRP	E_2	MPa	G/CFRP: 80235 CFRP: 110000
Ultimate CFRP strain	ε_2^*	%	G/CFRP: 1.15 CFRP: 1.05
Longitudinal elastic modulus of GFRP	E_3 E_1 E_w	MPa	Top: 25920 Bottom: 20120 Web: 16490
Transverse elastic modulus of GFRP top flange	E_{1T}	MPa	8000
Shear modulus of GFRP web[2]	G_w	MPa	2000
Longitudinal Poisson's ratio for top GFRP flange[3]	ν_L	-	0.33
Transverse Poisson's ratio for top GFRP flange[3]	ν_T	-	0.10

[1] Calculated as $0.664\sqrt{f_c'}$, in MPa (ACI 1989).

[2] Calculated from the response of plain GFRP beams.

[3] Estimated values based on similar GFRP material properties found in the literature.

Based on these properties, the ultimate loads were calculated using the computer programs described earlier. The results for all 18 beams are summarized in Table 7.3, along with the corresponding experimentally obtained values. For the comparison of

stiffnesses, the load over mid-span displacement ratios (P/Δ) are given at a load P=10 kN (corresponding to elastic response). It is seen that the analytical results agree quite well with the experimentally obtained ones. For the ultimate load calculations the average ratio of analytical to experimental values was 95.9%, while the standard deviation was only 0.066. The maximum deviation was found in Beam 6 with 21% discrepancy, where shear failure occurred and the analysis was based on empirical values for the tensile splitting strength of concrete. Similarly, the average ratio of analytical and experimental stiffness values was 96.5% with a standard deviation of 0.052. Here the maximum deviation was found in Beam 10 and the discrepancy was 14%. It is seen that the models employed and the assumptions regarding the behavior of the hybrid system are verified, and hence, it can be concluded that the analysis presented in Chapter 3 provides a reliable method for the design of hybrid FRP-concrete elements.

Table 7.3 Comparison of analysis with experiments.

Beam	Failure mode	Ultimate Load [N]			Stiffness [kN/mm]		
		Experiment	Analysis	A/E	Experiment	Analysis	A/E
1	Local punching	19200	-	-	2.1719	2.1700	0.999
2	Conc. crushing	18100	20141	1.113	1.9608	1.8990	0.968
3	Conc. crushing	16000	14997	0.937	0.7519	0.6968	0.927
4	Conc. crushing	17700	15740	0.889	0.7695	0.6968	0.906
5	Conc. crushing	23700	21998	0.928	3.3929	3.3967	1.001
6	Conc. shear	34800	27493	0.790	7.4627	7.3960	0.991
7	Conc. crushing	17300	16478	0.952	0.8750	0.7926	0.906
8	Conc. crushing	17200	17372	1.010	0.8976	0.7926	0.883
9	Conc. crushing	27400	26379	0.963	6.0000	5.6386	0.940
10	Conc. shear	33600	31527	0.938	15.1010	14.3971	0.860
11	Conc. crushing	14000	14271	1.019	0.6000	0.6010	1.002
12	Conc. crushing	23200	21180	0.913	2.4390	2.3468	0.962
13	Conc. crushing	22400	21434	0.957	0.6700	0.6810	1.016
14	CFRP fracture, Conc. crushing	22300 22700	21352 22126	0.957 0.975	0.6944	0.6810	0.981
15	Debonding	45700	-	-	8.1820	7.8810	0.963
16	Conc. crushing	37200	37089	0.997	5.0870	5.3467	1.051
17	Conc. crushing	30000	28946	0.965	1.2000	1.2420	1.035
18	GFRP buckling	6600	6599	0.999	0.1859	0.1821	0.980

7.2.2 Finite Element Method Analysis of Hybrid Beam

The calculations of the large scale hybrid beam response, which were based on classical beam theory as described in Chapter 3, were augmented with a finite element analysis performed through the MARC/MENTAT (1990) software package. A finite element model was created in order to simulate the response of the large scale hybrid beams. Thick shell elements were used for the discretization of the GFRP box beam and the CFRP lamina with orthotropic material properties, and eight node brick elements with isotropic material properties were used for the description of the concrete layer. The tying constraint option was also implemented to provide for compatibility at the GFRP/concrete interface. Nonlinear material behavior was introduced through the work hardening routine and an incremental formulation was adopted.

7.2.2.1 Geometry and Discretization of the Hybrid Beam

Three point bending tests on large scale hybrid beams were simulated through discretization with an appropriate finite element (FE) mesh. Due to symmetry, only one quarter of the beam needed to be analyzed. Figure 7.8 shows the geometry and spatial discretization. The model has three main components, the concrete layer, the GFRP box beam and the CFRP sheet.

Over a total axial length of 1.55 m a mesh with 994 nodes was generated. A total of 279 8-node isoparametric brick elements were used for the concrete layer. 577 4-node bilinear thick shell elements were implemented for the GFRP box beam, and 117 for the CFRP sheet. The mesh was generated through a repetitive expansion of a single stripe and a refinement of the FE mesh was carried out at the support location in order to prevent stress concentrations to cause local instabilities during the solution of equilibrium equations. The compatibility of the concrete brick elements and the GFRP shell elements was achieved through the UFORM routine, where the rotational strain components in common nodes of concrete and GFRP elements are averaged, and the tying constraint is activated.

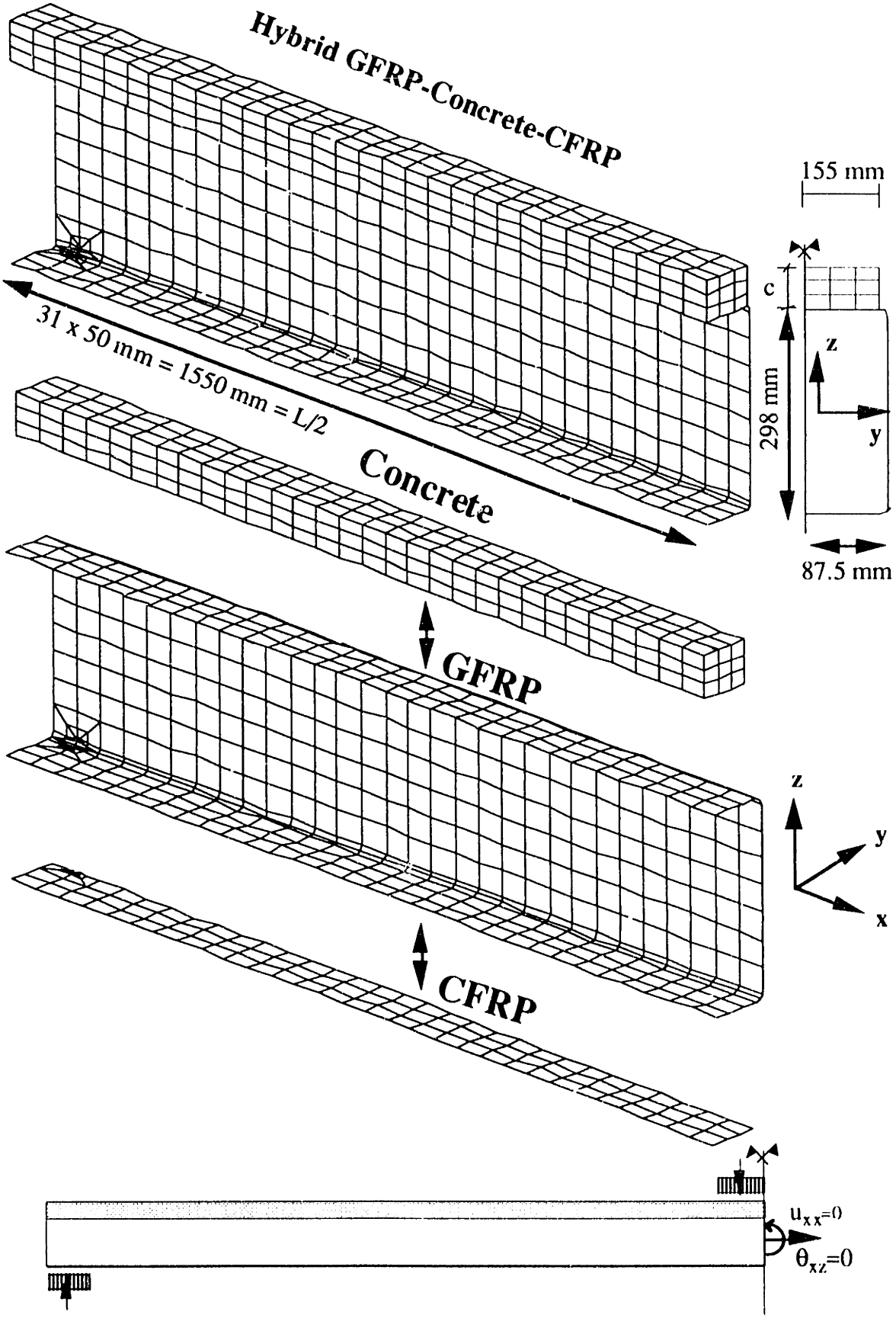

Figure 7.8 Geometry and discretization of FE model.

The boundary conditions along the symmetry planes are predefined. Out-of-plane rotations and displacements along the longitudinal centerline are fixed,that is

$$\theta_{yz} = 0 \ , \ u_{yy} = 0 \tag{7.5}$$

In addition, the in-plane rotations and translations across the mid-section of the beam are set to zero, or:

$$\theta_{xz} = 0, \ u_{xx} = 0 \tag{7.6}$$

To achieve stability of the system one node was fixed in the vertical direction ($u_{zz} = 0$). The boundary conditions are depicted in Figure 7.9. Also, in order to eliminate stress concentrations and numerical instabilities at the support, a series of nodes and thick shell elements was added to model a wooden diaphragm bonded onto the GFRP box beam walls.

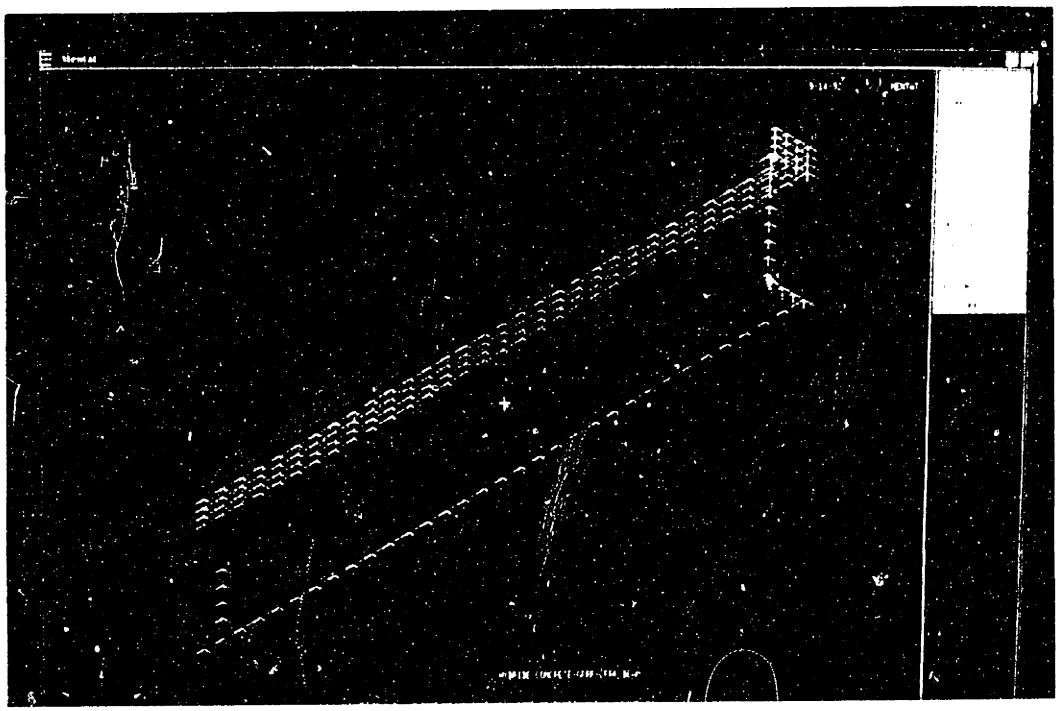

Figure 7.9 Boundary conditions layout.

7.2.2.2 Material and Geometric Models of Constituents

The finite element model simulated material nonlinearities introduced through the GFRP and the concrete. The GFRP response was described with 4-node thick shell elements with global displacements and rotations as degrees of freedom. Bilinear interpolation was used for the coordinates, displacements and rotations forming a surface of a hyperbolic paraboloid. The membrane strains were obtained from the displacement field; and the curvatures from the rotation field. The transverse shear strains were calculated at the middle of the edges and interpolated to the integration points. In this way a very efficient and simple element was obtained which exhibited correct behavior in the limiting case of thin shells. Each element had 5 stress and strain components in local coordinates and 6 displacements in global coordinates (3 translational and 3 rotational). The material nonlinearity was implemented with the "work hardening data" option and the material types were modeled for the webs and flanges separately. Ten discrete points on the stress-strain curve were picked for each wall according to values calculated from the fourth order polynomial with parameters given in Table 6.10. A schematic view of the work hardening model is given in Figure 7.10(a). The elastic portion of the stress-strain curve was assumed up to 0.0015 strain. Orthotropic material properties were adopted. The six required elastic constants (E_{11}, E_{22}, ν_{12}, G_{12}, G_{13} and G_{23}, where indices *1*, *2* and *3* denote the local coordinate system) were obtained from the continuum theory results of Chapter 6.

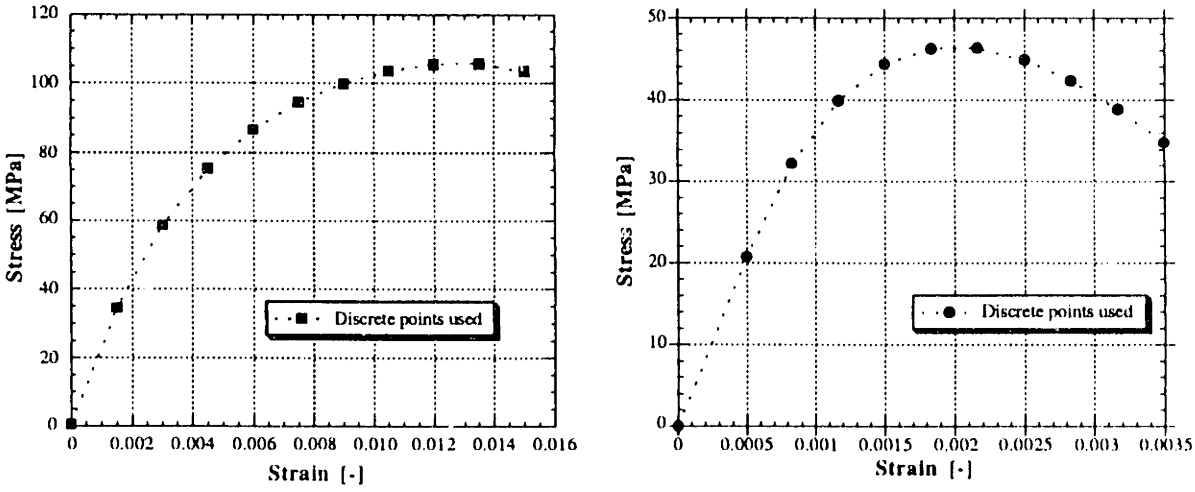

(a) (b)

Figure 7.10 Work hardening model: (a) stress-strain relationship for GFRP, (b) stress-strain relationship for concrete.

The alternative of using the composite option for the material properties definition was abandoned since experimental values for the elastic and shear modulus were already available and could be used directly. The Von Mises failure criterion was set for the GFRP material, although this state was never reached in the analysis performed. The thickness of the web and flange elements was adopted from the data given in Table 6.11.

The 8-node isoparametric brick elements which were used for the discretization of the concrete layer have six stress and strain values in global Cartesian coordinates, while each node has three displacements (in the x, y and z directions). The concrete material model is a hypoelastic model based on a uniaxial stress-strain relation that is generalized to take biaxial and triaxial stress conditions into account. The material nonlinearity was introduced through the work hardening routine with ten discrete points, and a schematic plot of the resulting stress-strain curve is given in Figure 7.10(b). The elastic portion is valid until the strain of 0.0005 is reached. The points in this stress-strain relationship were calculated for each beam according to the polynomial model with values reported in Table 6.6. The Mohr-Coulomb compressive failure envelope was adopted, where the condition of concrete crushing is defined as the function of strains, that is the stress invariants were replaced by strain. The equivalent crushing strain represents the limit compressive strain obtained by uniaxial testing, and was set equal to 0.0035. The thickness of the concrete layer, c, was adopted from Table 7.4.

The CFRP elements were modeled with the same thick shell elements as the GFRP box beam and thus no tying was required here. Orthotropic material properties were used again, taken from Tables 6.14, 6.15 and continuum theory. Only linear elastic material behavior was assumed here. Although in the experiments thin bands of CFRP were used, in the FE analysis the CFRP sheets were distributed over the whole width of the bottom flange. The corresponding thickness of the CFRP elements was calculated from the cross sectional area of the actually used CFRP bands. For this purpose the values from Table 7.4 were divided by 155 mm (width of CFRP elements in the FE model) resulting in the required dimension.

The wood diaphragm was also modeled with thick shell elements, and since in the experiment plywood was used, isotropic and linear elastic material properties were implemented. The Young's modulus of wood was taken as 18 GPa. Finally, the element thickness was defined at 20 mm.

7.2.2.3 Finite Element Analysis Procedure of the Hybrid Beam

Since material nonlinearity had to be included in the model, an incremental analysis with iterations at each load step had to be carried out to account for these effects. The load was applied to the six top concrete elements next to the midpoint of the beam (see Figure 7.8) and at the support location to eight GFRP elements in the opposite direction, each time over a surface of 100x77.5 mm^2. At both locations a uniformly distributed surface load was applied in the vertical (global z) direction. This is shown in Figures 7.8. The total load acting on the beam was hence in equilibrium, which explains why no vertical supports were used in the model.

The auto-increment option was used for the incremental analysis. The initial load level was defined at 0.32 N/mm^2, which corresponds to a total load for the whole beam of 10 kN. The maximum load level defined was 4.0 N/mm^2 (corresponding to a total load of 125 kN) which was never reached since failure occurred at lower values. The auto-increment load option was activated with a maximum step size defined at 0.1 of the maximum load, and a maximum of 30 iterations for each load step was adopted.

The analysis for each beam was performed in two parts. The first part was run with all FE elements as defined above. This analysis was carried out until the maximum strain (0.8- 0.93%, depending on the particular beam) at mid-span in the CFRP laminate was reached. After this, it was assumed that the CFRP sheet fractures and disappears from the beam. The second part of the analysis includes the same run but without the CFRP sheet elements. Here, the response of the combination of only concrete and GFRP was simulated. This analysis was performed up to the point when either concrete or GFRP failure occurred. In both cases the ultimate strain constraint was governing. Figures 7.11 to 7.14 give a typical stresses distribution which resulted from the analysis. Figure 7.11 gives the normal stresses in the concrete layer, while Figures 7.12 and 7.13 show the normal and in-plane stresses in the GFRP walls, respectively. Finally, Figure 7.14 depicts the normal stresses introduced in the CFRP sheet.

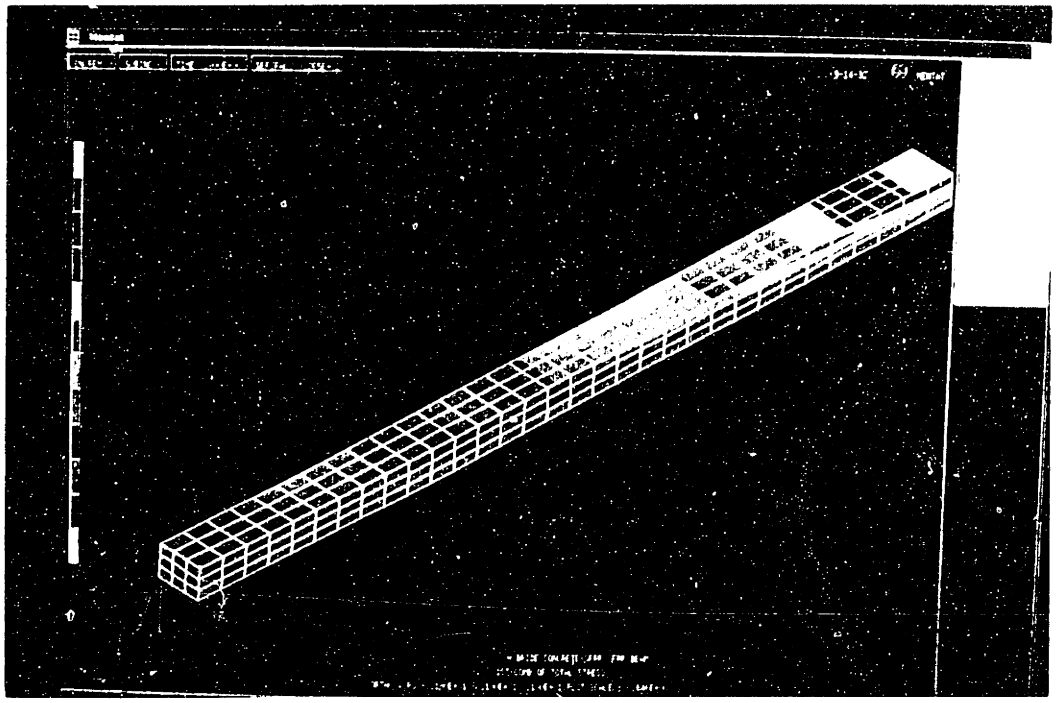

Figure 7.11 Concrete normal stress distribution.

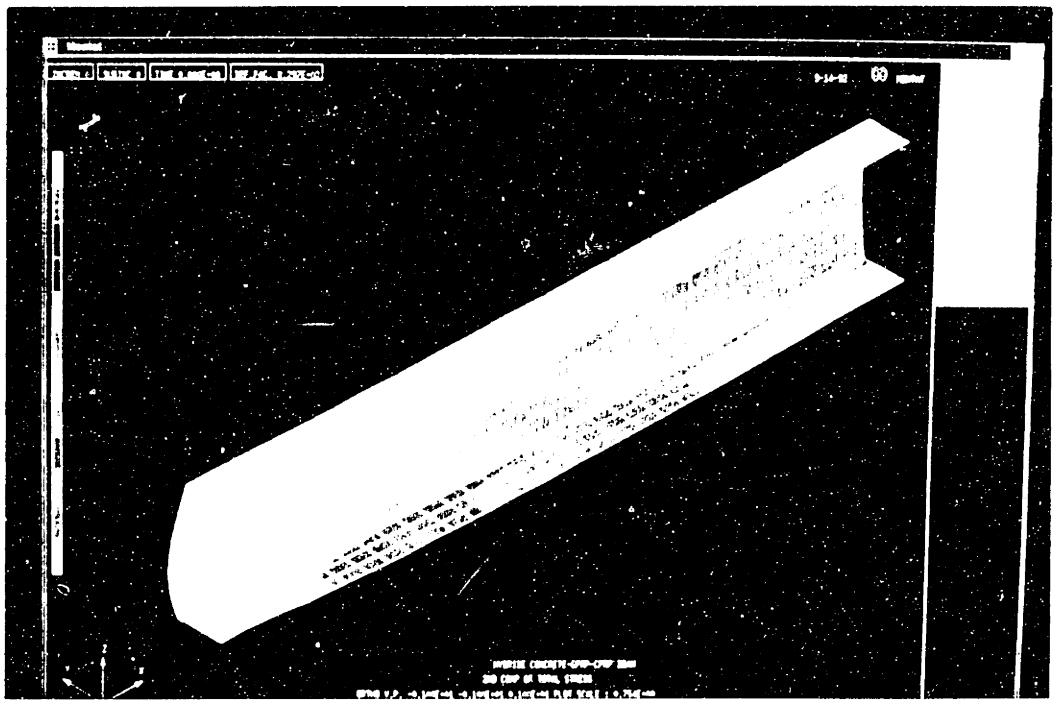

Figure 7.12 GFRP walls normal stress distribution.

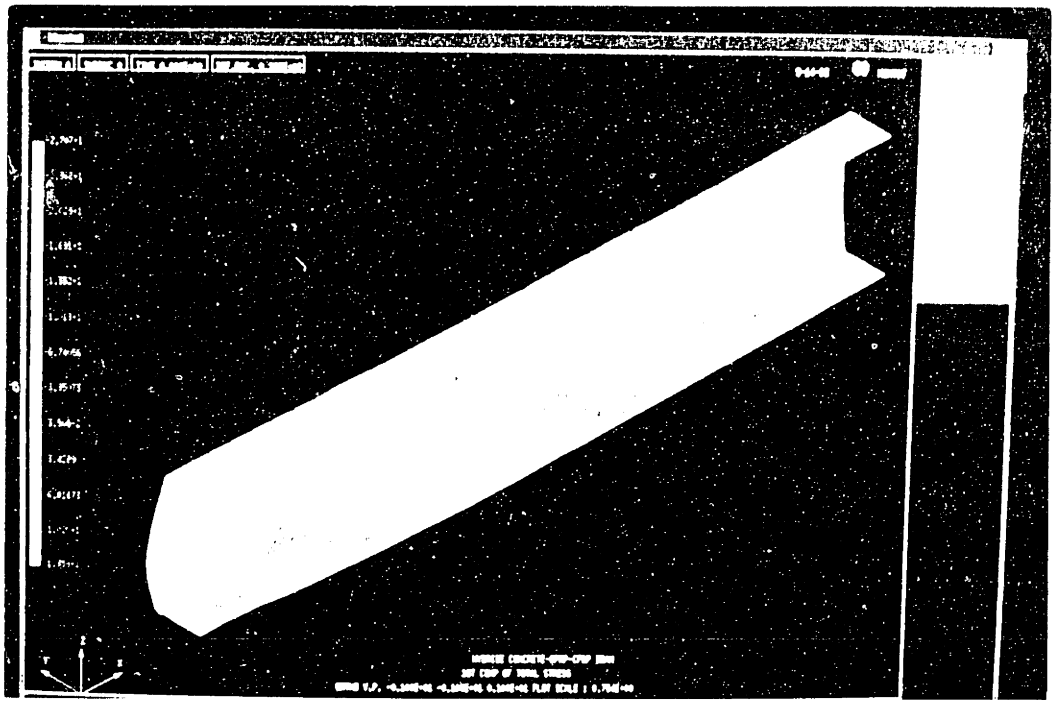

Figure 7.13 GFRP walls in-plane stress distribution.

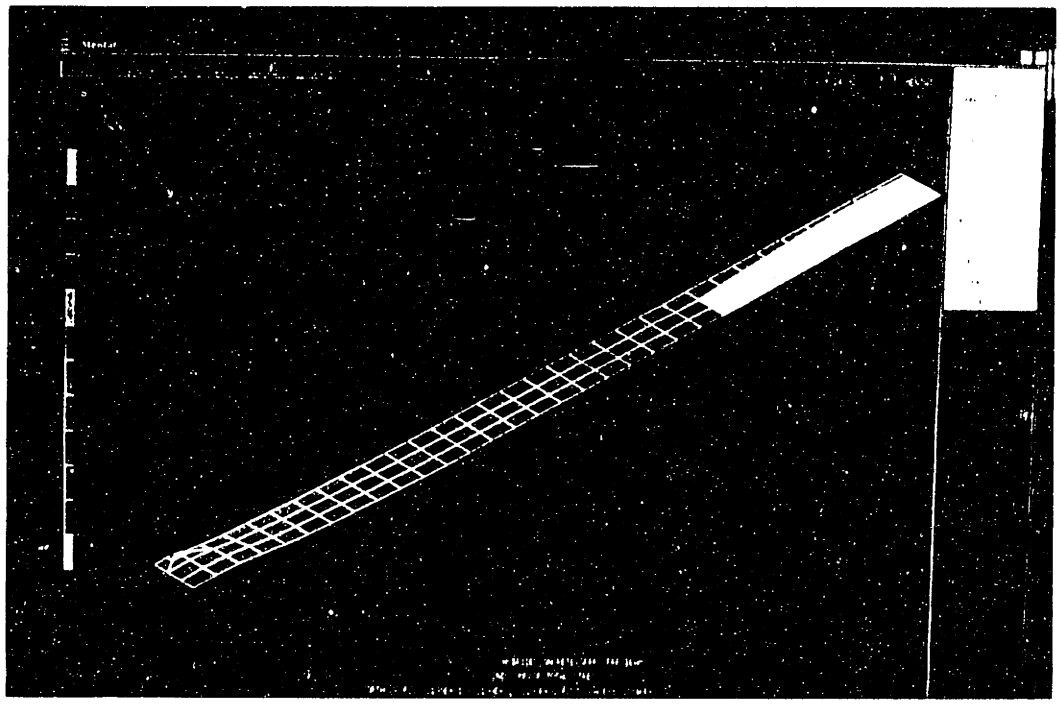

Figure 7.14 CFRP sheet normal stress distribution.

7.2.3 Three Point Bending of Large Scale Beams

Full scale Beams 1, 3 and 4 were tested in three point bending as described in Section 5.3.2.2. In parallel to the experimental program, the detailed analytical procedure developed in Chapter 3 was carried out together with the finite element analysis for each beam. The parameters used for the short term response models of the different constituent materials were extracted from results of the calibration described in Chapter 6 (see Tables 6.9, 6.10, 6.12 and 6.15). The geometric characteristics were defined earlier in Table 6.11 or are given in Table 7.4. The concrete layer thickness was obtained by averaging the measured value at 10 cross sections of each beam. The ultimate CFRP strain, although already defined earlier from uniaxial tension tests, was adjusted to the value obtained directly from the test, that is the strain measured on the CFRP at mid-span when the CFRP ruptured. The thickness of the CFRP sheet used in the analytical procedure was obtained by dividing the cross sectional area of the CFRP bands with the beam's width (b = 180 mm). The magnitude of the shrinkage strain to be used in the computations was determined from the model presented in Chapter 6.

Table 7.4 Geometric data and material properties used in the analysis.

	Beam 1	Beam 3	Beam 4
Concrete thickness, c [mm]	53.8	52.6	53.0
Total area of CFRP lamina, A_{CFRP} [mm^2]	25.04	19.89	21.02
CFRP ultimate strain, ε_2^* [-]	0.0093	0.009	0.008
Concrete shrinkage strain, ε_{sh} [-]	0.00035	0.0004	0.0004

Concrete shrinkage was not considered in the FE modeling, because it was believed that its influence on the total deflections of the hybrid beams was small, and because it was not included in the deflection measurement in the experiment. The shrinkage strain was introduced only in the analytical procedure showing the effect on the ultimate concrete strain which was accordingly increased by the same amount. Also the dead weight of the

beam was neglected in all calculations and measurements since the weight of the beams (approximately 75 - 85 kg total) was less than 1% of the ultimate load (and distributed evenly).

7.2.3.1 Experimental Response of the Beams in Three Point Bending

Beams 1, 3 and 4 were loaded in three point bending up to failure in a semi-displacement controlled test with load feed-back. In general, this is the definition of tests where there is interaction between the displacement introduced and the magnitude of the load applied. Typically a computer reads the displacement and the load level, compares the required and the actual displacement and depending on the outcome adjusts the load level. In the experiments conducted here the load was introduced by increasing the pressure in the hydraulic jack as shown in Figure 5.30, but the speed of the hydraulic jack piston movement is limited with the flow of oil in the pressure ducts. Thus, in the case that a rapid or even instantaneous displacement were to materialize, the pressure in the hydraulic jack would not be able to cause the piston to adjust immediately, and hence an immediate load drop comparable to the one in the displacement controlled tests would be generated. Therefore although the test is basically load controlled, it appears to have features of displacement controlled tests, and is referred to as semi-displacement controlled.

A pseudo-ductile response was expected in the three point bending tests, which anticipates the CFRP sheet to fail first activating the CFRP rupture mode after which the beam was supposed to sustain a load increase and fail at a higher load value due to concrete crushing or GFRP tensile failure. The experiments on Beams 3 and 4 verified this hypothesis, while in Beam 1, due to the lack of shear connectors and a weak interface bond, only the first part of the expected behavior was achieved. Here, CFRP failure occurred first but then the interface failed causing debonding of the concrete layer from the GFRP box beam resulting in premature total collapse of the member at a load lower than the one required for CFRP failure (see load displacement diagram in Figure 7.21). This means that in practice the member would collapse at the point when the CFRP sheet ruptures. Figure 7.15 shows a detail of the beam at CFRP rupture, while Figure 7.16 gives the beam configuration after the interface debonded and the concrete spalled off, releasing most of the stored strain energy. This failure mode is mostly undesirable, and due to its brittle nature has to be eliminated in design purposes. Therefore, the use of better adhesion procedures, as described in 5.2.2.3.3, or adequate shear connectors have to be implemented.

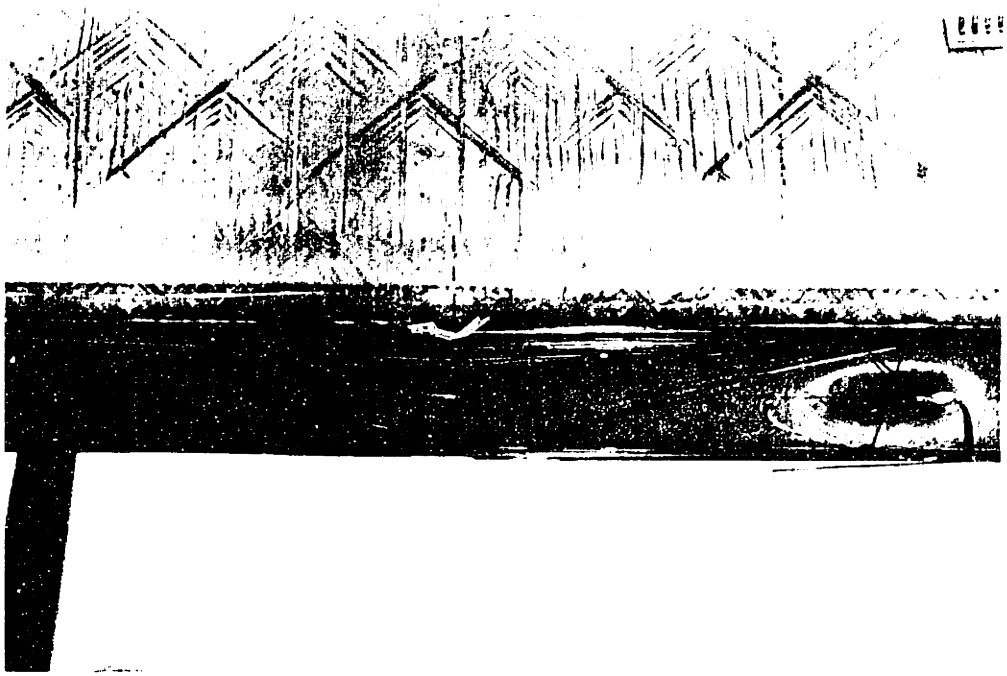

Figure 7.15 CFRP rupture in Beam 1.

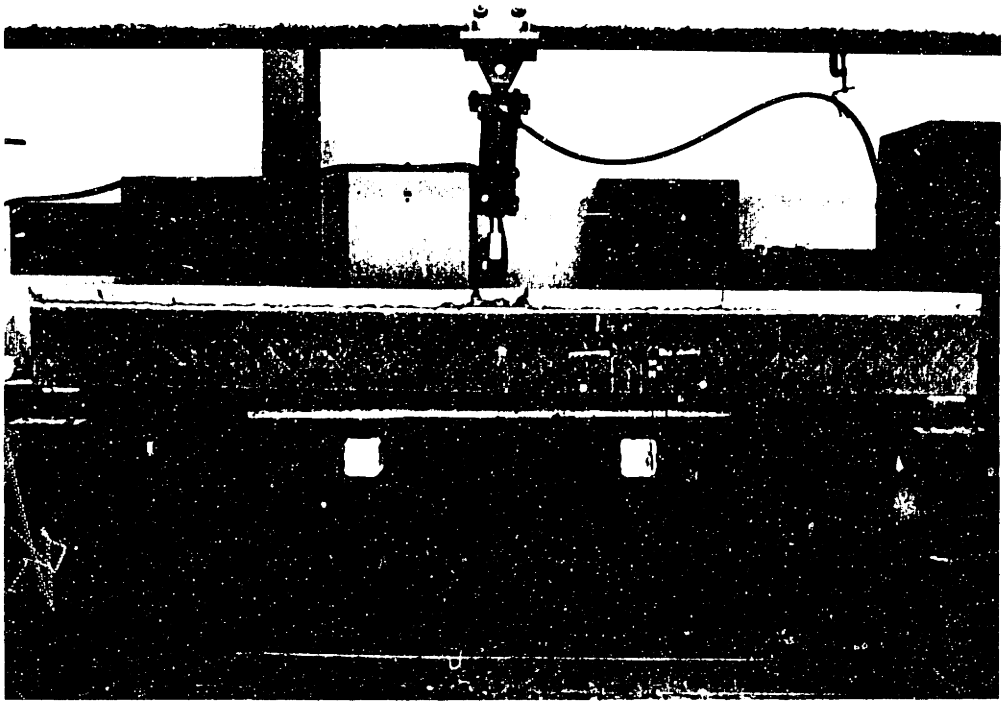

Figure 7.16 Interface debonding and concrete spalling off in Beam 1.

This was the case with Beams 3 and 4. Again the CFRP sheet failed first, then after an initial load drop (due to the semi-displacement controlled character of the test) the load increased, augmenting the displacements and ductility, until the next failure mode, concrete crushing, was reached. CFRP rupture occurred at mid-span where the moment applied to the section is highest and thus the largest stresses were induced. Concrete crushing occurred next to the steel plate supporting the forcing piston (see Figure 7.20) through which the concentrated load at mid-span was applied, and not exactly at mid-span where the moment is maximum, because a biaxial stress state was introduced in this latter region due to the confinement effect of the steel plate, and hence the concrete strength was increased. The load-displacement curve showing this desirable pseudo-ductile behavior is given in Figures 7.24 and 7.27 for Beams 3 and 4, respectively. It is seen that the corresponding ratio of ultimate to CFRP failure load, k_2, is 0.90 and 0.74. The warning produced during CFRP rupture and the large deflections generated thereafter, were impressive, as was the ability of the remaining two components, the concrete layer and the GFRP box beam, to carry an even higher load. The rupture of the CFRP occurred in an extremely brittle manner (it could be stated that it "explodes", releasing all its strain energy), but at the same time the GFRP box beam remains unharmed and continues to fulfill its load-carrying role. Figures 7.17 and 7.18 show a detail of the ruptured CFRP sheet at the bottom face of Beams 3 and 4, respectively, while Figures 7.19 and 7.20 give a zoom-in to the portion of the concrete layer which has failed under the concrete crushing mode. The shear connectors achieved their goal of producing an ideal bond between the concrete and the GFRP and did not allow for any failure mechanisms at the interface to occur.

The results obtained with Beams 3 and 4 were very encouraging and represent a viable proof to the concept of the so called "pseudo-ductile" composite structures. In addition, the anticipated behavior was very close to the analytically predicted one, the verification of which will be given in the next section.

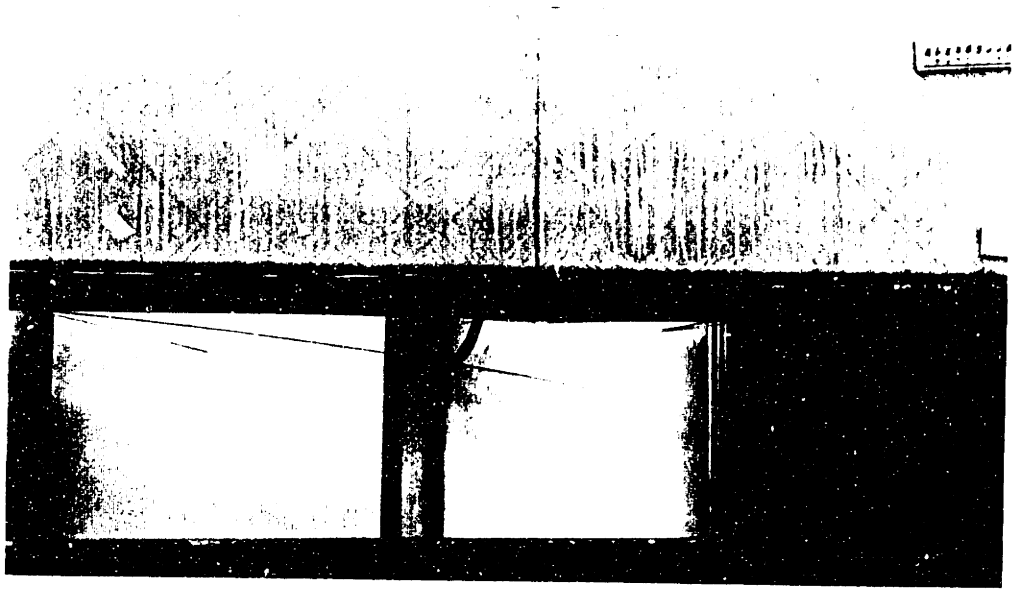

Figure 7.17 CFRP rupture at the bottom face of Beam 3.

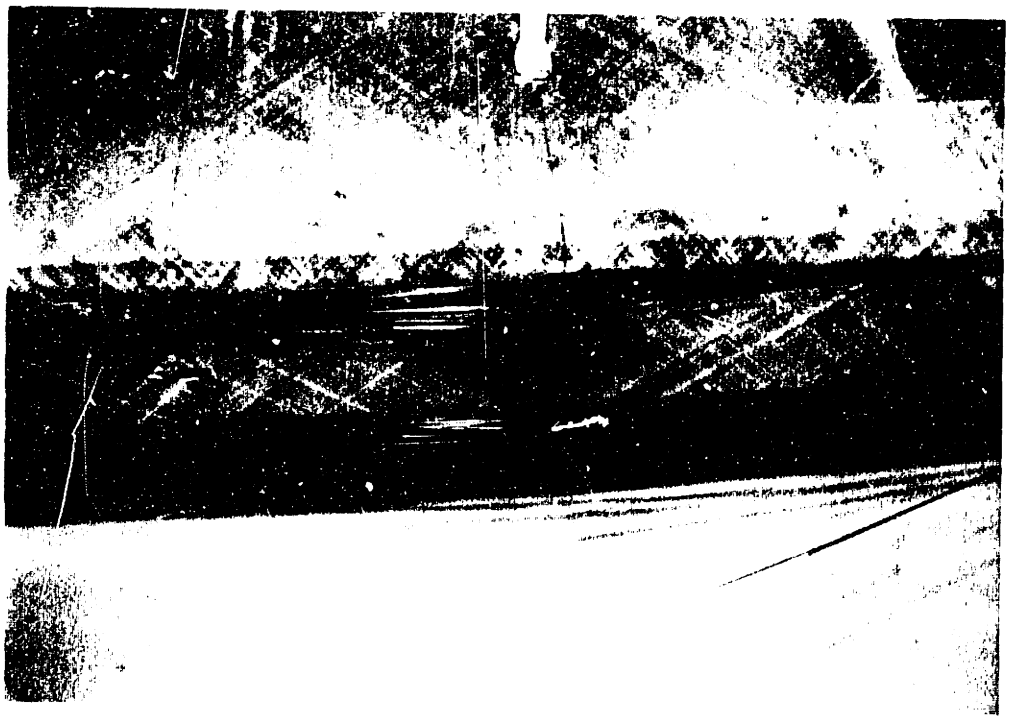

Figure 7.18 CFRP rupture at the bottom face of Beam 4.

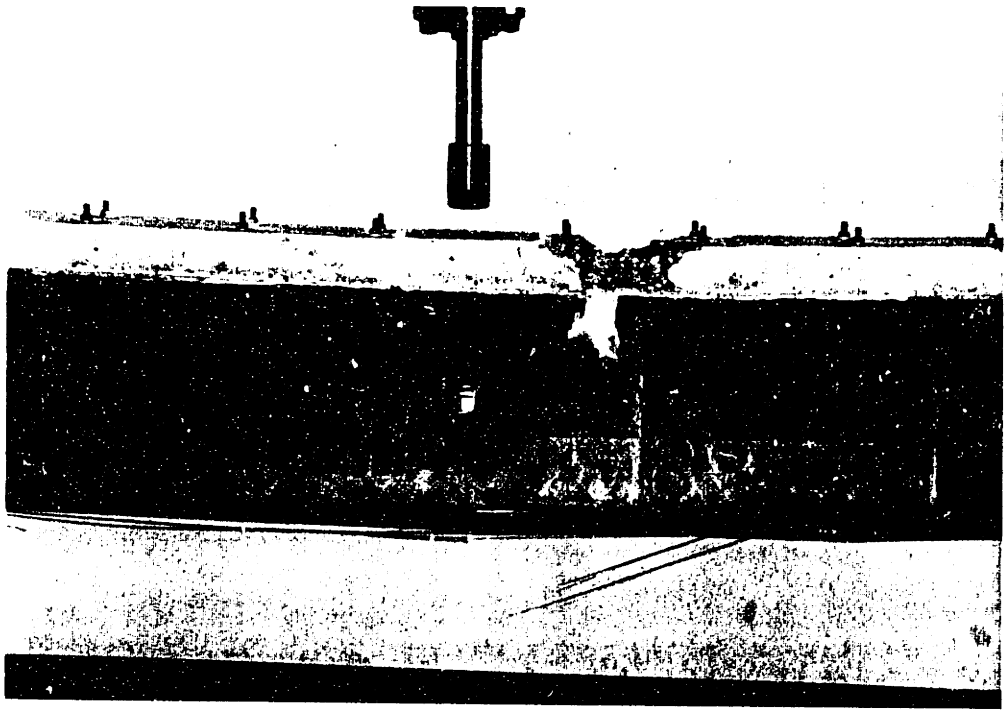

Figure 7.19 Concrete crushing close to mid-span of Beam 3.

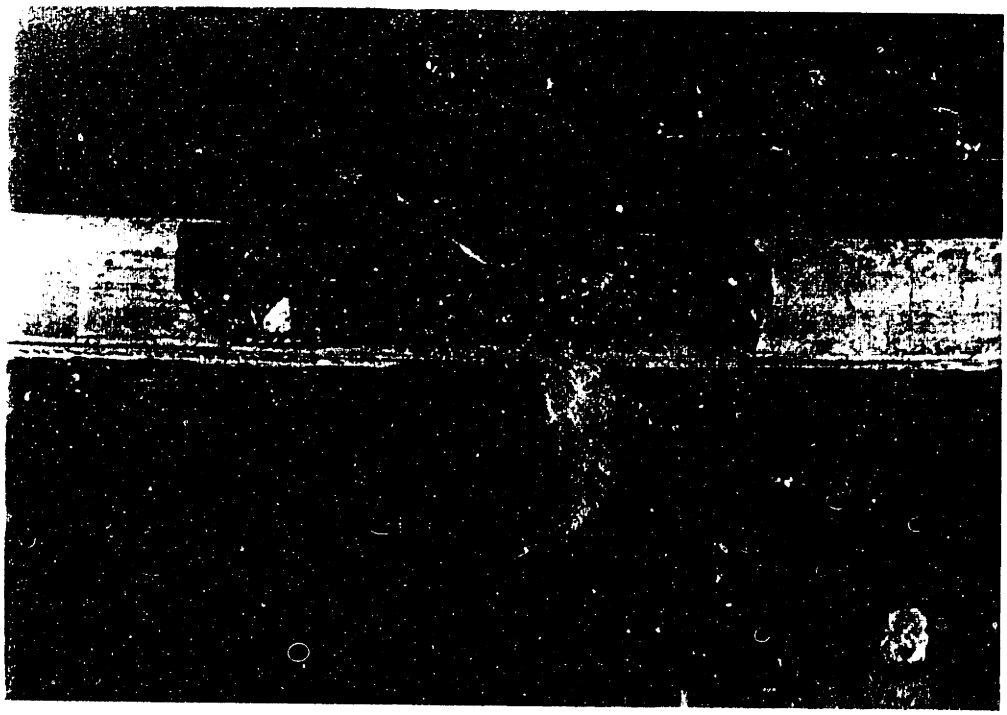

Figure 7.20 Concrete crushing close to mid-span of Beam 4.

7.2.3.2 Comparison of Experiment and Analytical Predictions

The results from the three point bending tests and the associated analysis are presented in three groups of diagrams for each beam and are shown in Figures 7.21 to 7.30. The first group gives the load versus deflection curves, while the second and third show the compressive and tensile strains of the top and bottom fibers of the hybrid beams as a function of the externally acting bending moment at two locations, respectively. The explanation of the values presented is briefly summarized next.

The deflection is considered at the mid-span and for all three approaches (experimental, analytical and FE) it is measured at the GFRP box beam's longitudinal axis, or more precisely at mid-height of the web. The compressive concrete strains are given at the top concrete fiber at cross Section 1 (see Figure 5.30). The analytical concrete strain result, ε_c, is also given for the mid-section, since this value was already used in the calculations. For neither the FE analysis nor the experiment would it make sense to retrieve data from the mid-span location since concrete is in a biaxial stress state there and the normal strains, ε_{xx}, being also affected, would be inappropriate for the comparison to the analytical predictions. The bottom fiber strains were considered for all three approaches at mid-span. In the analytical result the bottom fiber strain, ε_2, is given. From the FE analysis the average normal strain, ε_{xx}, along the CFRP edge and at mid-span of the beam is calculated from the extrapolated integration point strains at each node. The experimental strain is obtained through measurements with strain gauges attached to the GFRP and CFRP surface at mid-span as shown in Figure 5.30.

Figures 7.21 through 7.23 give the response of Beam 1 according to all three methods. The deflection comparison in Figure 7.21 shows reasonably good agreement between experiment and analysis in the initial region up to CFRP rupture and further until the interface damage occurred. The FE model gives somewhat more conservative results; the stiffness obtained here is reduced and the deflections are increased. In Table 7.5 the important points on the load-deflection curve are compared. It can be concluded that both analytical and FE models give acceptable predictions of the true behavior, and that the simple analytical model can substitute sophisticated finite element method models giving more than satisfactory results.

Table 7.5 Comparison of analysis and experiment for Beam 1.

	Load at CFRP rupture, P [kNm]	Deflection at CFRP rupture [mm]	Ultimate Load, P_u [kNm]	Deflection at ultimate load [mm]
Analysis	104.00	23.0	111.30	42.5
FEM	96.66	22.0	107.33	45.2
Experiment	98.00	22.5	Interface failed	-
Anal./Exp.	1.061	1.022	-	-
FEM/Exp.	0.986	0.978	-	-

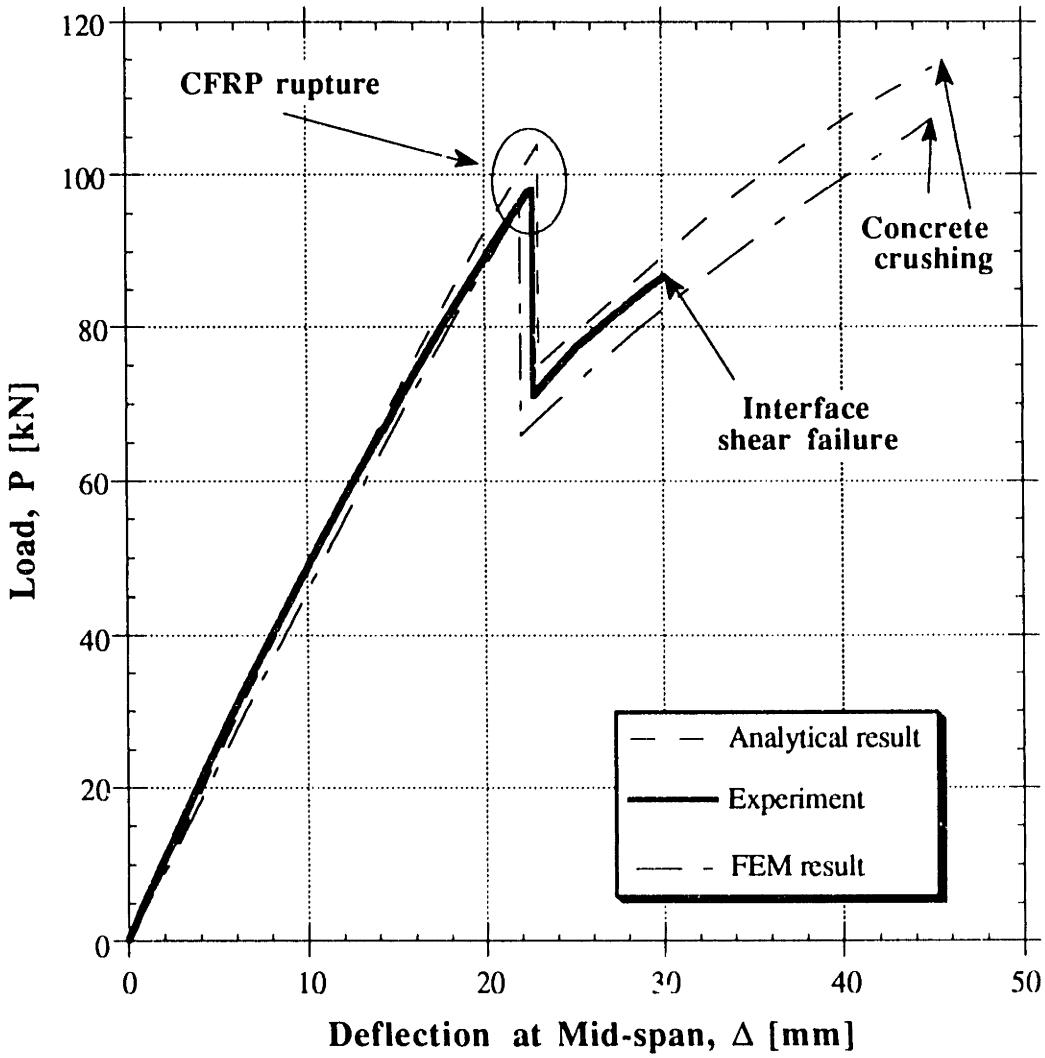

Figure 7.21 Load deflection curve comparison for Beam 1.

Figure 7.22 depicts the bottom fiber strain comparison of the results for each method. It is seen that the CFRP ultimate strain constraint is fully accounted for and that CFRP rupture occurs at this strain level. The analytical model gives slightly smaller strain magnitudes than the experimentally obtained result, while the FEM model produces slightly higher strains. The experimental curve is interrupted when interface failure occurred, while the FEM and analytical curves are shown up to the point when failure of the beam due to concrete crushing occurred.

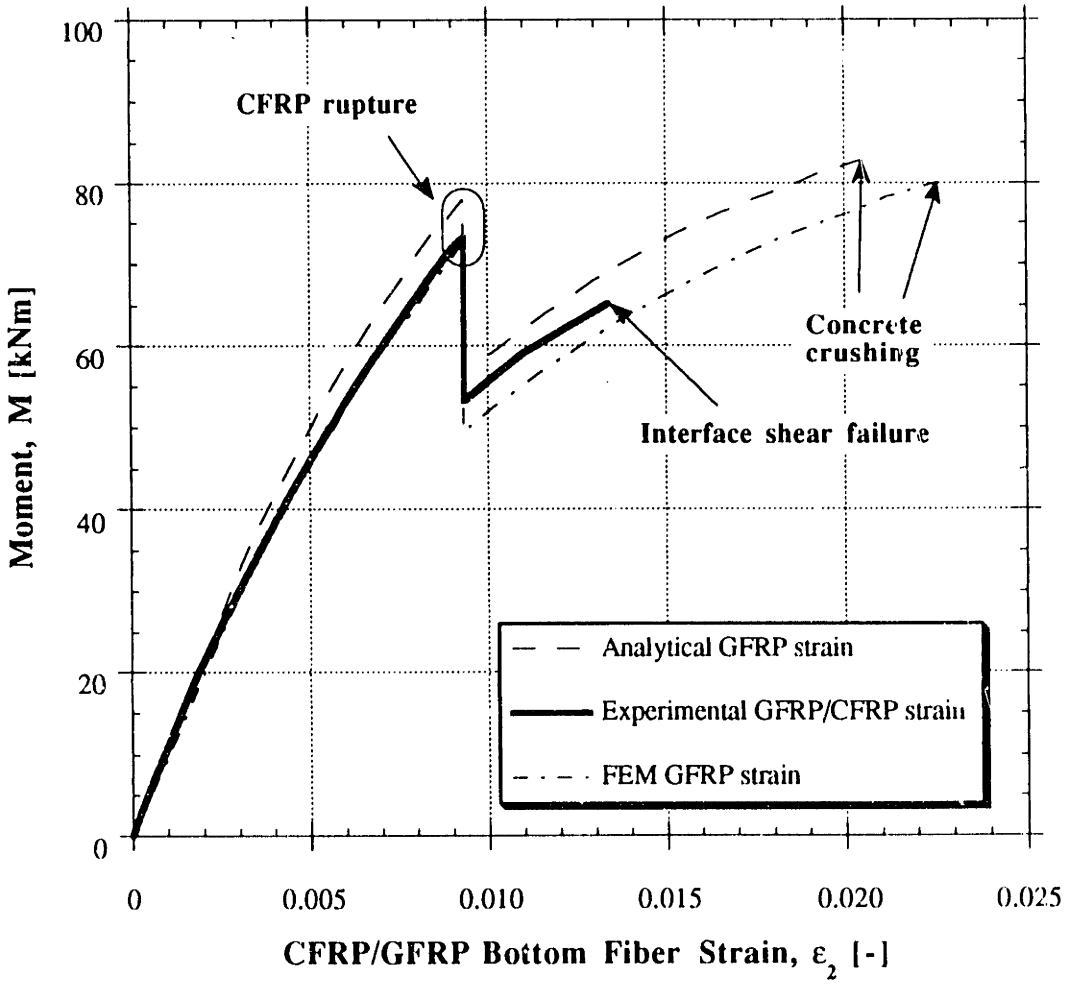

Figure 7.22 Bottom fiber strain curve comparison for Beam 1.

The top fiber concrete compression strains are compared in Figure 7.23, where the analytical response is also given for the mid-span cross section. All response curves consist of two parts: one which displays the response with CFRP in place (prior to

rupture) and the other without CFRP (after rupture). When CFRP failure at a specific section occurs, a vertical jump from curve of part one to curve of part two takes place. Note that although actual failure of the CFRP occurs initially only at mid-span, this is followed by immediate debonding all along the whole beam length. The analytical curve for the mid-span section shows the behavior up to failure of concrete, which here really takes place since the curve is given for the strains at mid-span. It is seen that the concrete strain at failure is equal to the ultimate one, ε_c^u , summed with the shrinkage strain, ε_{sh} , which complies with the assumptions made in the analysis. The experimental curve, on the other hand, stops at interface rupture, while the analytical curve for Section 1 and the FEM curve are both interrupted when the load is reached which caused concrete crushing at another location, namely at mid-span.

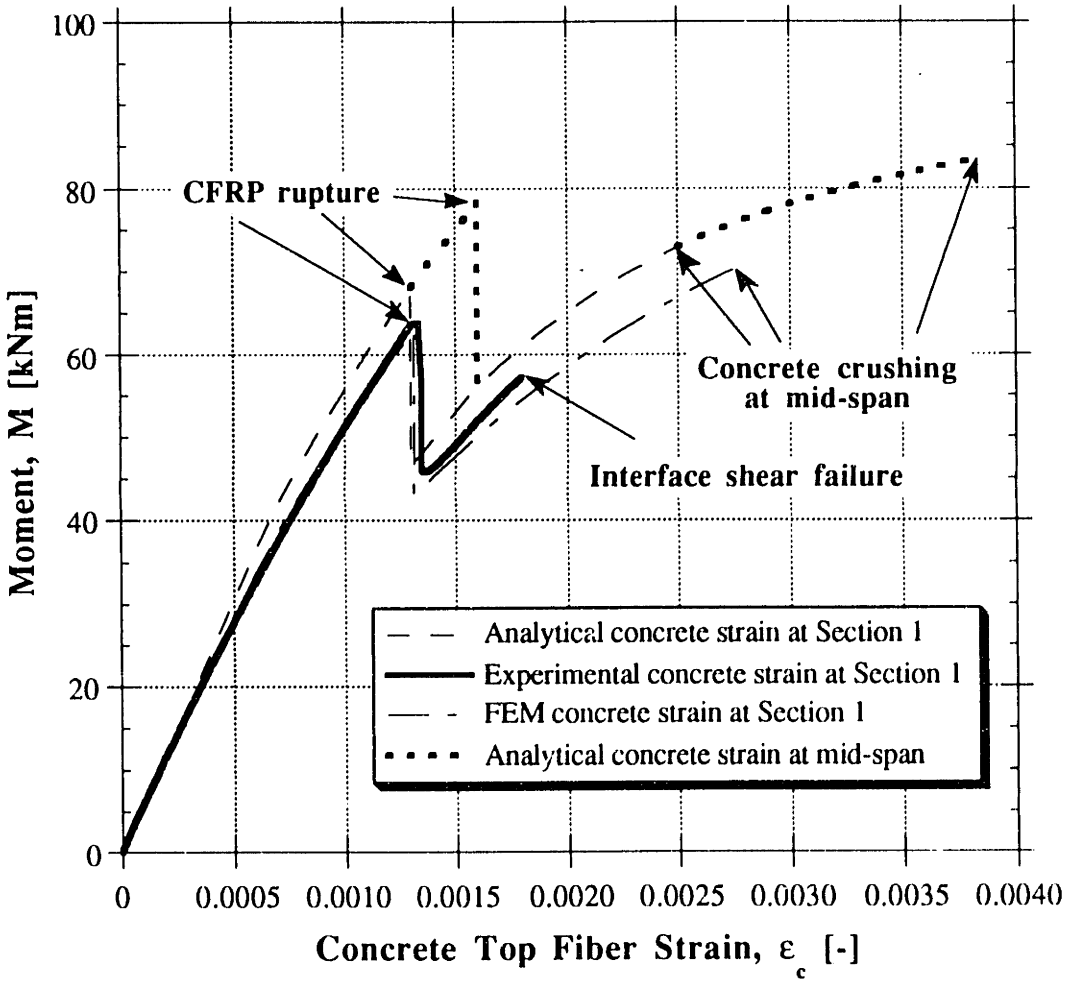

Figure 7.23 Top fiber strain curve comparison for Beam 1.

For both the top and bottom strains it can be concluded that relatively good agreement

between experiment and analysis is obtained and that sufficient accuracy is achieved.

The comparison of the response of Beam 3 with all three methods considered here is given in Figures 7.24 to 7.26. All the considerations described during the evaluation of Beam 1, given above, apply here as well and will not be stressed again. The load-deflection curves are given in Figure 7.24. The analytical model gives again a somewhat stiffer response than the experimental result, while the FEM analysis appears to produce a more compliant behavior. Nevertheless, the overall comparison is quite satisfactory. The important points on the load-displacement curve are given in Table 7.6.

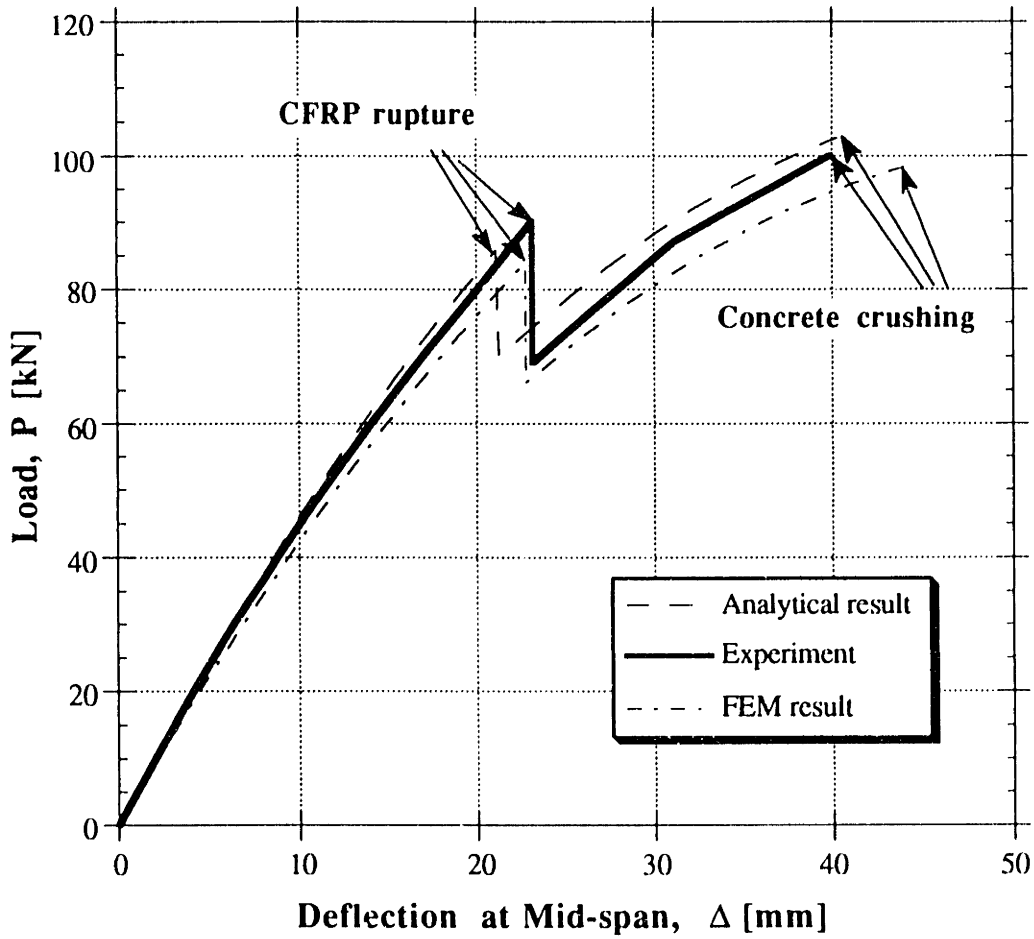

Figure 7.24 Load deflection curve comparison for Beam 3.

The largest discrepancy (about 10%) is obtained for the deflection at failure of the FEM model, which is still acceptable considering the high level of nonlinearities involved. The bottom and top fiber strain comparisons are given in Figures 7.25 and 7.26, respectively. It is seen that the agreement between experiment and both models is very good and hence

the analytical approach is verified once again.

Table 7.6 Comparison of analysis and experiment for Beam 3.

	Load at CFRP rupture, P [kNm]	Deflection at CFRP rupture [mm]	Ultimate load, P_u [kNm]	Deflection at ultimate load [mm]
Analysis	85.78	21.13	102.67	40.29
FEM	84.04	22.00	98.80	44.7
Experiment	89.96	22.8	100.17	39.93
Anal./Exp.	0.954	0.927	1.025	1.009
FEM/Exp.	0.934	0.965	0.986	1.119

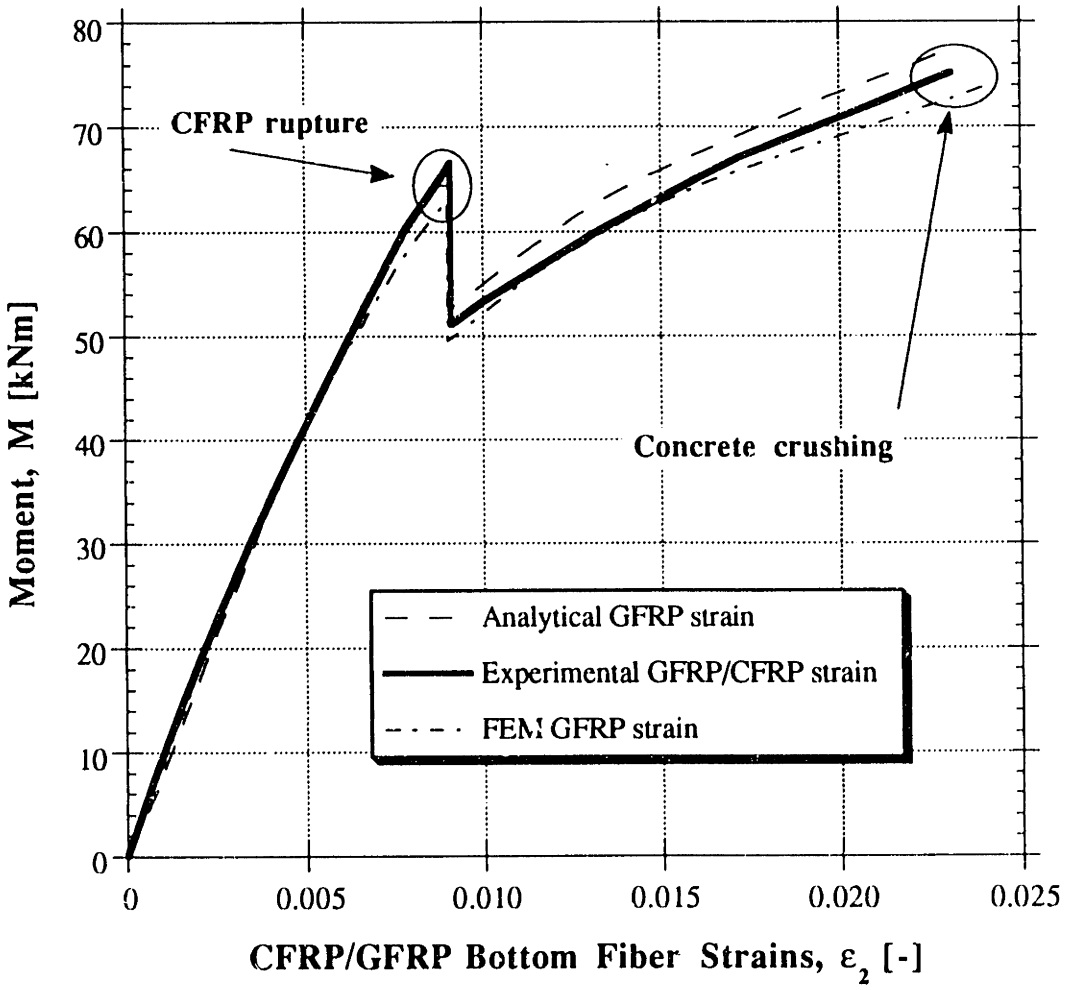

Figure 7.25 Bottom fiber strain curve comparison for Beam 3.

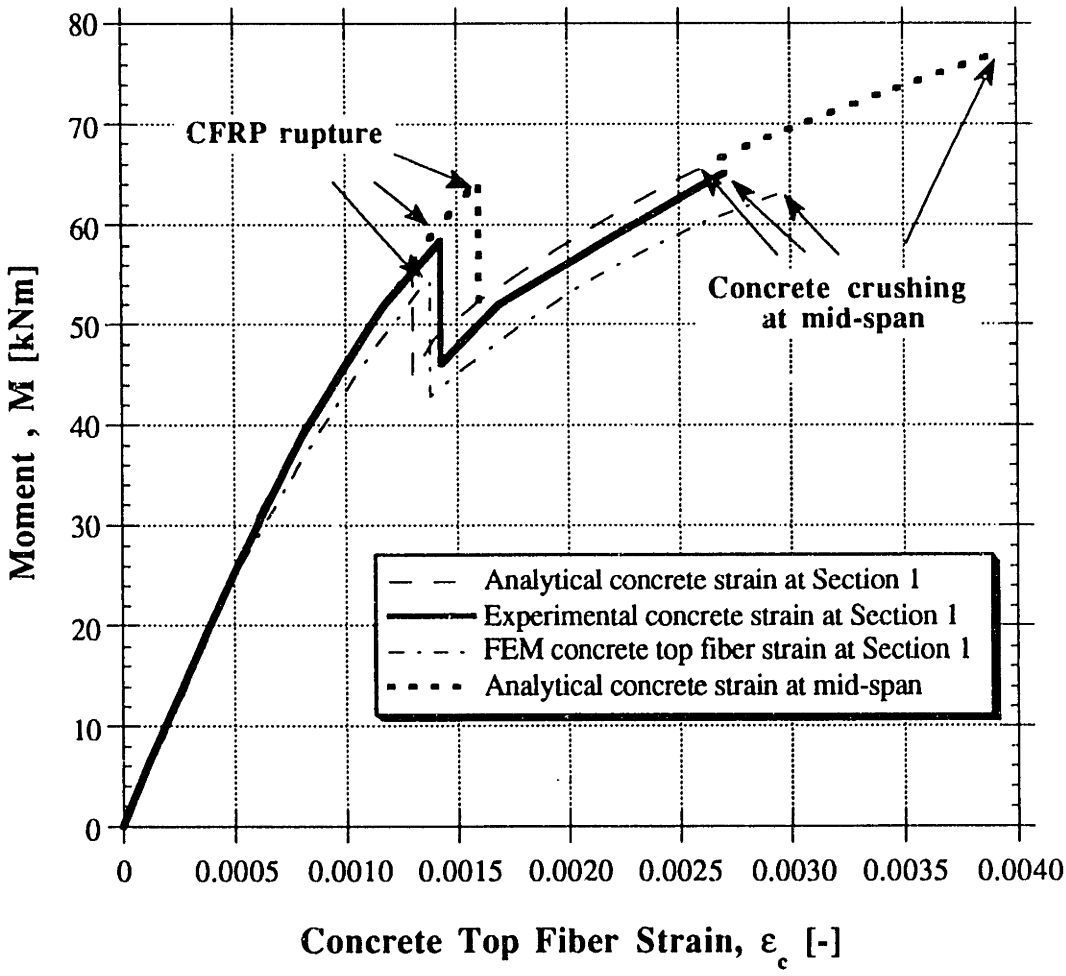

Figure 7.26 Top fiber strain curve comparison for Beam 3.

The comparison of the response of Beam 4 with all three methods investigated here is given in Figures 7.27 to 7.29. All the considerations described during the evaluation of Beam 1, given above, apply here as well and will not be repeated. The load-deflection curves are given in Figure 7.27. The analytical model appears to result in a stiffer response than the experimental one, while the FEM analysis produces more conservative deflection values. Overall the agreement is satisfactory and can be used to justify the assumptions and simplifications used in the analysis. A comparison of important points on the load-displacement curve is given in Table 7.7. It is seen that both loads and deflections are represented in a satisfactory manner and that the largest discrepancy is obtained with the deflection of the FEM model, which at about 8% is still small taking the high level of nonlinearities into account.

Table 7.7 Comparison of analysis and experiment for Beam 4.

	Load at CFRP rupture, P [kNm]	Deflection at CFRP rupture [mm]	Ultimate load, P_u [kNm]	Deflection at ultimate load [mm]
Analysis	86.25	21.09	107.81	51.21
FEM	84.66	21.30	105.05	59.89
Experiment	80.51	21.04	109.14	55.26
Anal./Exp.	1.071	1.002	0.988	0.927
FEM/Exp.	1.052	1.012	0.963	1.084

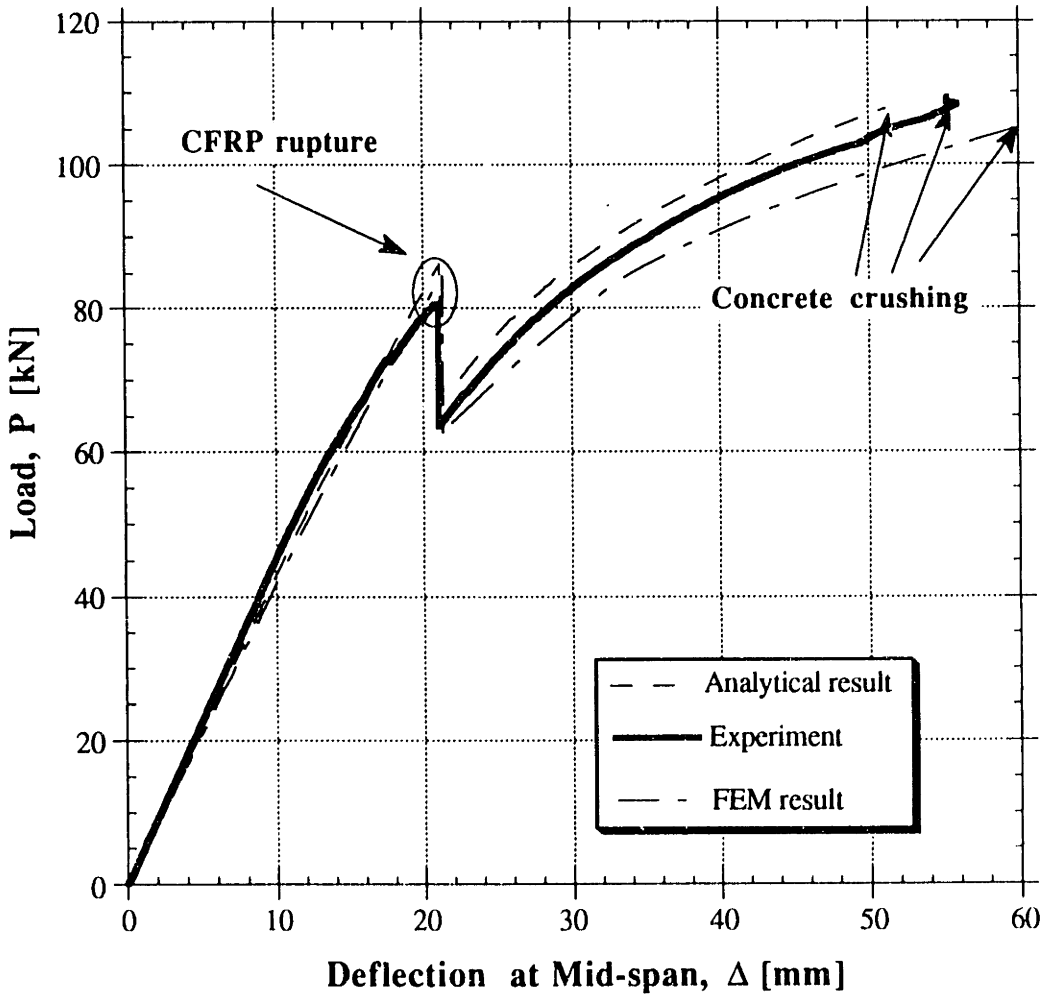

Figure 7.27 Load deflection curve comparison for Beam 4.

Figures 7.28 and 7.29 depict the bottom and top fiber strains resulting from the three approaches. Again, good agreement of experimental and analytical results can be concluded approving of the models used.

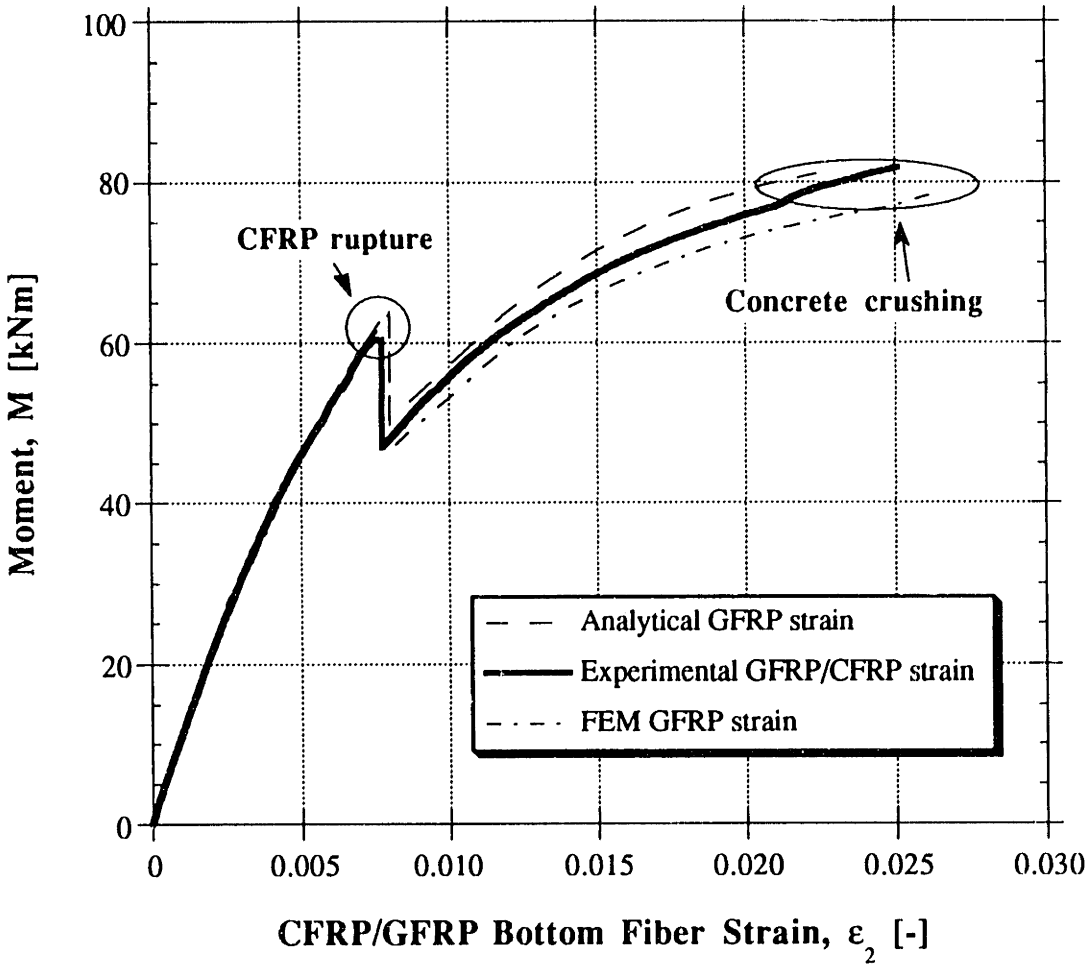

Figure 7.28 Bottom fiber strain curve comparison for Beam 4.

An additional verification of the analysis performed is related to the assumption of Saint-Venant's hypothesis of plane sections remaining plane. Here, the position of the neutral axis can be calculated from known top and bottom fiber strains of the hybrid beam. Equation (3.10) defines the position of the neutral axis measured from the top face of the concrete surface. Using this equation Figure 7.30 was created with analytical and experimental data of Beam 4 at Section 1. Here the position of the neutral axis is plotted as a function of the load applied onto the beam, *P*.

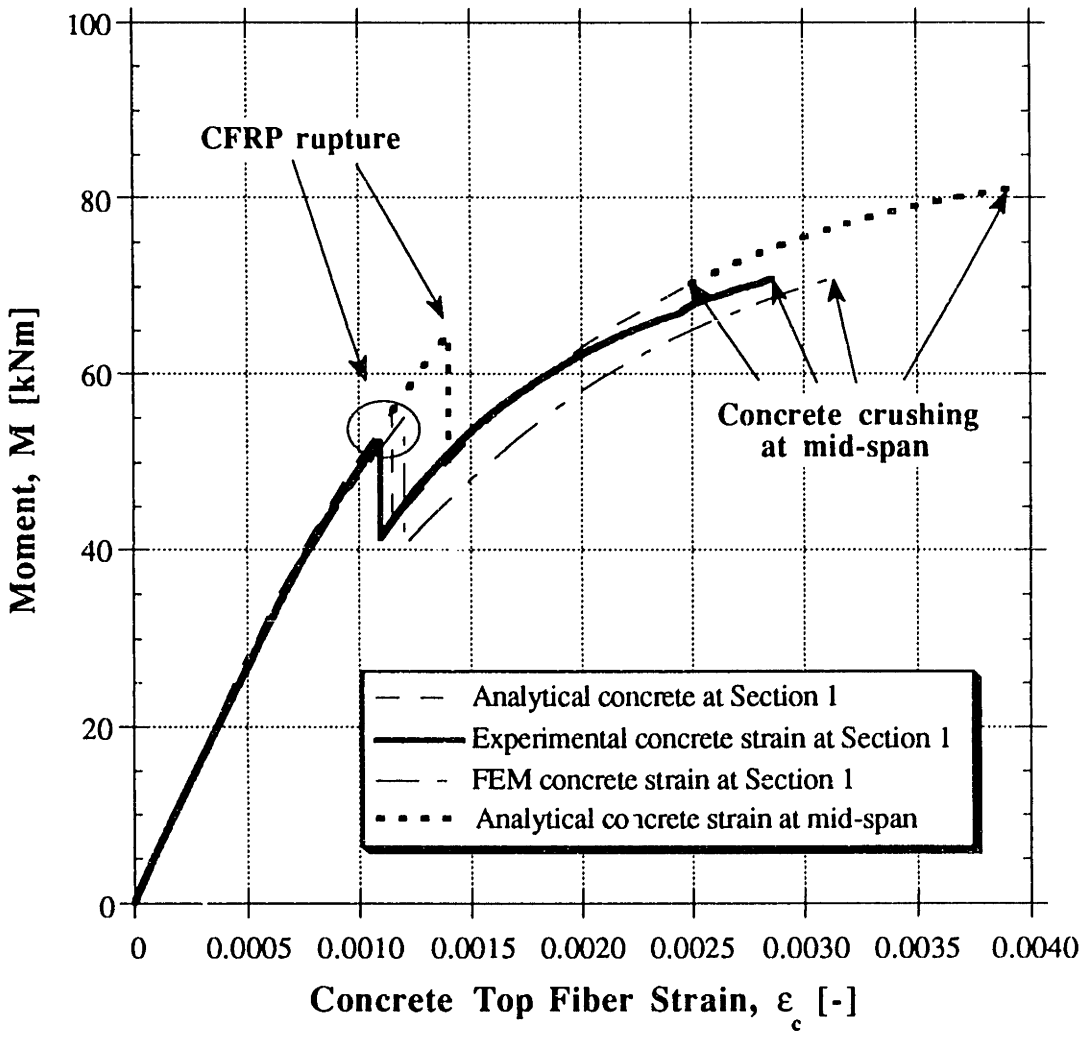

Figure 7.29 Top fiber strain curve comparison for Beam 4.

For simplicity, the position of the neutral axis is presented in reference to the interface between concrete and GFRP, x_n - c. It is seen that the neutral axis shifts towards the interface as the load increases, it exhibits a sudden jump when the CFRP sheet fails and then continues to shift upwards. In general this behavior is not desirable, since it might eventually cause the concrete to be subjected to tension (once the neutral axis penetrates the concrete layer). On the other hand, this tendency could be easily inverted if slightly different mechanical properties of the materials involved were used. The important conclusion is that the shift in the neutral axis is not very significant (here less than 1% of total member height prior to CFRP sheet failure) and that if its initial position is sufficiently far from the interface the concrete will not undergo tension before collapse of the hybrid beam occurs. This is to be considered in the design process when the material properties and geometries are chosen (see Chapter 5). Figure 7.30 shows that the neutral axis close to

the collapse load is very close to the concrete/GFRP interface. Also, it should be pointed out that the discontinuous form of the analytical results is attributed to numerical imperfections, which at this scale become visible. Overall, it is seen that good agreement of analysis and experiment is obtained.

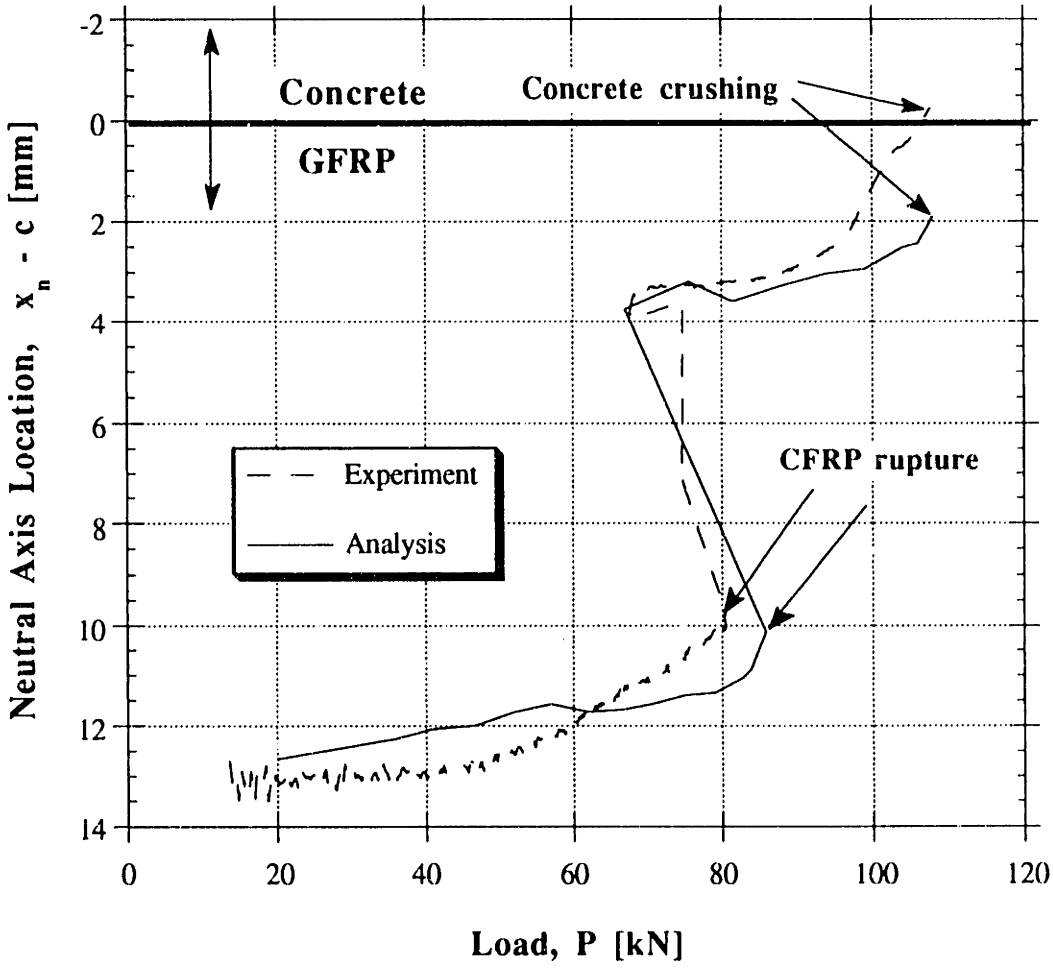

Figure 7.30 Neutral axis position of Beam 4.

7.3 Creep Response of Hybrid Beams

The creep behavior of hybrid beams was evaluated from 24 hour tests on Beams 5 and 6 as well as from 6 month tests on Beams 2 and 7. The experimental deflection data were compared to analytically predicted ones. The residual strength of the hybrid beams was calculated analytically and a parametric study giving the dependence of the ultimate moment on the sustained load applied and time elapsed was carried out. Some additional geometric characteristics of the beams involved, which were used for analytical modeling,

are given in Table 7.8.

Table 7.8 Geometric data and material properties used in the creep analysis.

	Beam 2	Beam 5	Beam 6	Beam 7
Concrete thickness, c [mm]	52.0	53.2	52.5	53.1
Total area of CFRP lamina, A_{CFRP} [mm^2]	19.82	20.14	20.36	19.98

7.3.1 24 Hour Creep Response of Hybrid Beams

The test setup for the 24 hour creep tests was described in Section 5.4. Beams 5 and 6 were loaded in four point bending. The main goal of these tests was to determine the initial portion of the creep response, which was meant to complement the analysis for the 6 month tests described later and, in addition, to give an insight in the validity of the implemented models to the initial response of the beams. The advantage here is that a DAS system could be utilized in order to have precise measurements in a relatively constant environment. For the purpose of comparison, the two models developed earlier in Sections 6.2.3 for concrete creep and 6.3.3 for GFRP creep were used to predict analytically the creep response of Beams 5 and 6. The analytical procedure was described in Chapter 4 and was adopted for the computation of deflections given here. The concrete creep model was adopted fully since it was assumed that the concrete used for these beams had equal creep behavior as the one determined in Section 6.2.3. For the GFRP creep behavior two models were used. The continuum theory model was applied directly with the appropriate fiber volume fraction percentages as defined in Table 6.9. Since there were no direct creep tests conducted on specimens from neither Beam 5 nor 6, Findley's model with the same parameters as determined for Beam 2 (see Section 6.3.3), was implemented in the empirical GFRP creep model.

Figure 7.31 shows the mid-span deflection change with time for Beam 5, including experimentally obtained data and analytically determined values. Both GFRP models are represented. The variation of the sustained load during the test is given on the right axis, where the load applied on each load point is recorded. It is seen that the results from the continuum theory model of GFRP creep comply well with the experimental ones, while the

empirical model gives poorer estimates. This was expected since the empirical GFRP creep model was taken from specimens of Beam 2, which had a quite different fiber volume fraction (see Table 6.9), and thus was not an ideal model to be used. The short term deflections complied well with the experimental (6.9 mm in the models versus 6.83 mm in the experiment). This verifies the appropriateness of the short term material models used for all the constituents implemented.

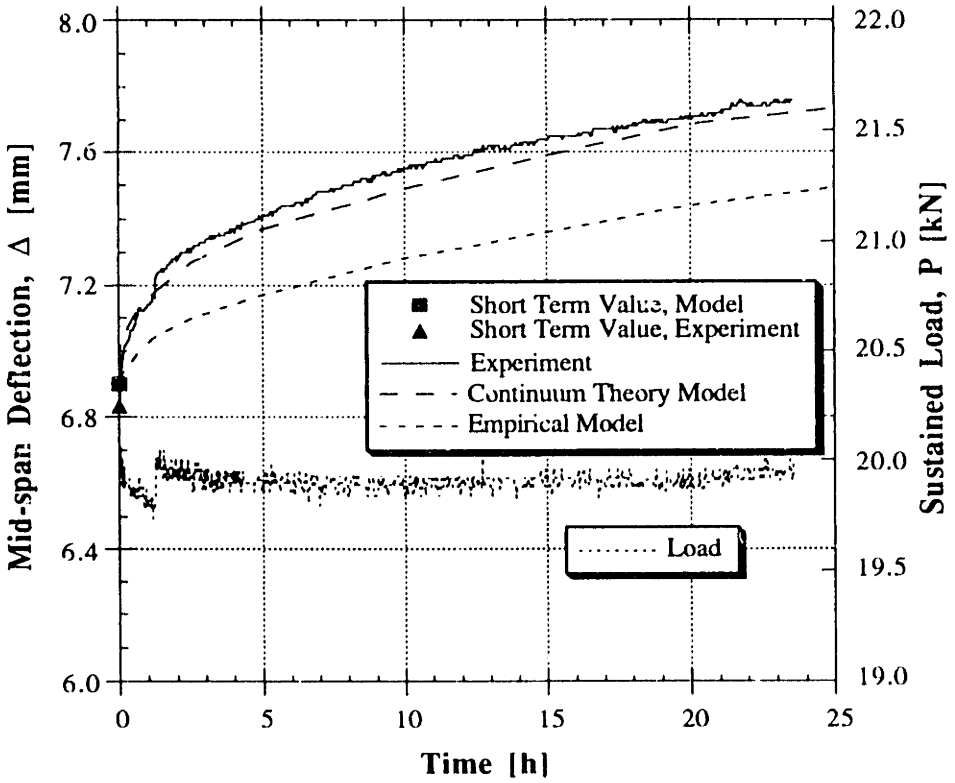

Figure 7.31 Beam 5, 24 hour creep test, comparison of experiment and analysis.

The comparison of the 24 hour creep response of Beam 6 is given in Figure 7.32. The same approach as described above for Beam 5 was implemented. The same concrete and empirical GFRP models were used, only in the continuum theory GFRP model the corresponding values for the new fiber volume fraction (form Table 6.9) were adopted. The initial (short term) deflections computed with the analytical method comply well with the experimental ones (11.1 mm in experiment versus 11.4 mm in the model). Again the continuum theory model gives better results, but this time the empirical model is closer to experimental values since the creep properties of the GFRP in Beam 6 are closer to those of Beam 2 (the empirical parameters of which were adopted). The error between analysis and

experiment is within 2-3%, which represents a very good result. The conclusion can be made that the proposed analysis for the creep response of the hybrid beams can be used effectively for the prediction of immediate creep deformations.

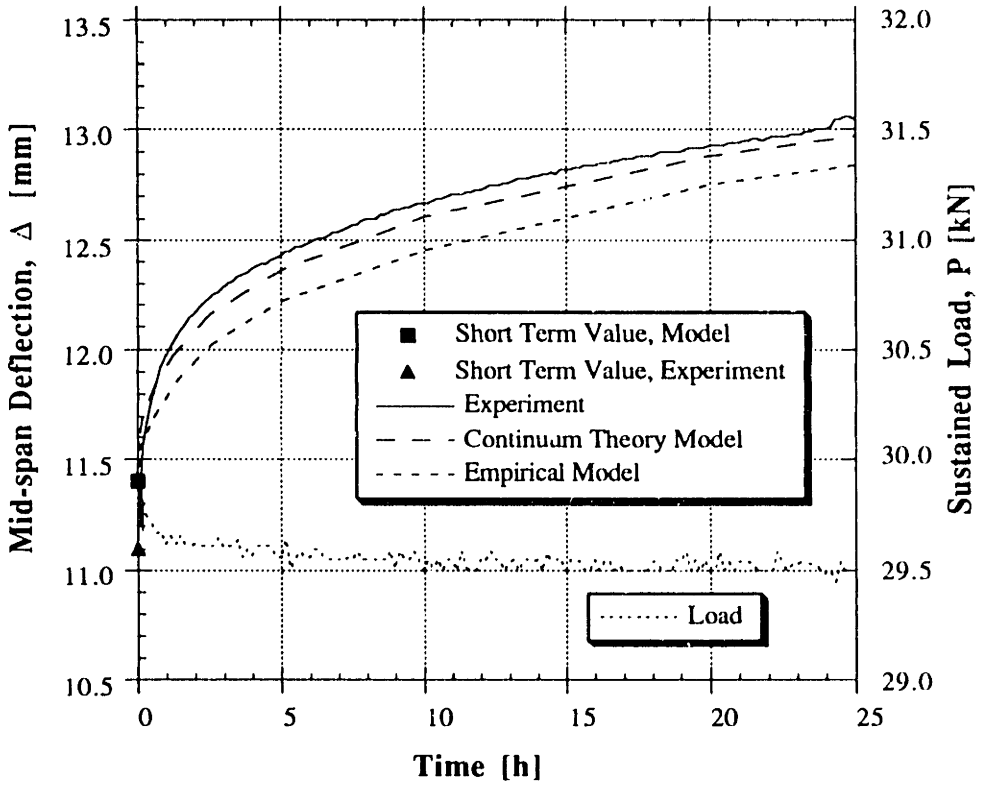

Figure 7.32 Beam 6, 24 hour creep test, comparison of experiment and analysis.

7.3.2 6 Month Creep Response of Hybrid Beams

The creep behavior of hybrid beams was further investigated with long term tests carried out on Beams 2 and 7, which were subjected to sustained gravity loads in four point bending. The test setup was given in Figure 5.35. Beam 2 was installed in a laboratory environment, while Beam 7 was exposed to weathering and environmental impact. By the time this thesis was typed, creep test data for a period of roughly six months were recorded, yet the tests are being continued thereafter. Parallel to the experimental program, the analytical procedure described in Chapter 4 was implemented and the response of the beams was predicted.

The same models, as defined earlier for the 24 hour tests but with parameters

corresponding to Beams 2 and 7 were used for the short term behavior of all constituent materials and for creep modeling of concrete and GFRP. It should be mentioned that Findley's empirical creep model used for GFRP was most appropriate for Beam 2, since the calibration of its parameters was carried out on coupon specimens of the very same GFRP box beam. Therefore, the analysis for the response of Beam 7 was conducted only with the continuum theory model since it was shown in the previous section to give more accurate results. Shrinkage and dead loads were neglected in the analysis. The ambient temperature variation for Beam 2 was relatively constant at room temperature and was, thus, not included in the analysis, while temperature osciliations for Beam 7 (being tested outdoors) showed substantial fluctuations and had to be considered. Here the temperature effect was implemented through the analytical procedure described in Chapter 4. Other factors that could have influenced the response of Beam 7, such as moisture content of the concrete blocks (used as gravitational ballast) and the associated weight change, were not examined, which partially explains deviations between experimental and analytical results. However, the behavior of Beam 7 was more of interest from the durability point of view, and the comparison of its experimental response to analytical predictions is limited. More interesting is the monitoring of its behavior in the future.

The change in deflections during creep of Beam 2 is depicted in Figures 7.33 and 7.34. The same data are given in both figures, but for better presentation the time axis in Figure 7.34 is in logarithmic scale. The experimental data are compared to the results from the analysis with the two different creep models for GFRP. It can be concluded that both models give very good results, although the continuum theory model appears to be closer to experimental values. The initial deflection of the analytical curves (as depicted on the logarithmic plot in Figure 7.34) is within one percent precision of the experimental, which verifies the short term models and parameters used. The difference in creep deformations between the two models is particularly evident for shorter times, where the empirical model lacks on performance. The empirical model gives lower deflections which can be partially attributed to the fact that shear creep deformations were neglected in it, while for the continuum theory model the latter were indirectly considered through a reduced shear modulus (see equation (4.40)). Overall the continuum theory model approximates the experimental curve with 2-3 % precision, which represents a remarkable agreement. The results from the empirical model still lie within a 5% range of the experimental and can also be used as valid approximations.

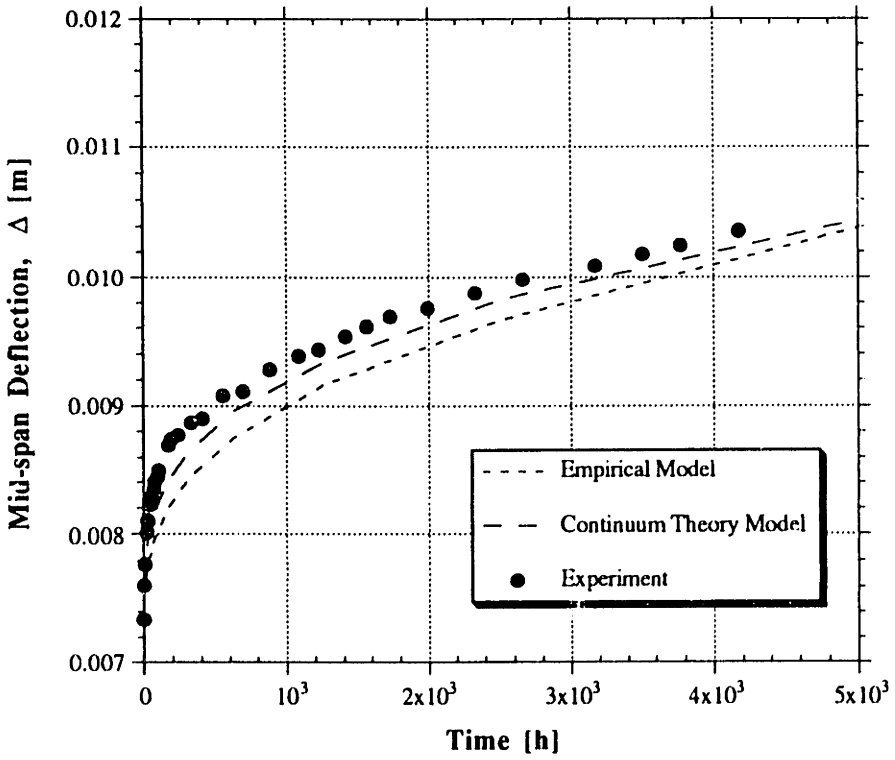

Figure 7.33 Beam 2, creep response comparison.

When plotted on a logarithmic time axis, as shown in Figure 7.34, the deflection rate of the hybrid beam is found to stabilize after approximately three months (≈2000 hours). This is concluded by the almost linear deflection increase in logarithmic time scale. In practice this means that the deflection curve will flatten out and the beam's displacements will continue to increase, but with a decreasing gradient. Analytical deflection data were calculated for a period of over 100 years (≈ 1 million hours), and it is seen that the predictions give an increase of approximately 2 mm per decade. This results in a total creep deflection (after 100 years) of roughly two times the initial short term one. Also, it is seen that the empirical GFRP model is more conservative than the continuum theory one. It has to be pointed out that the empirical model was calibrated using data of 4 weeks only (see Section 6.3.3), and hence the long term predictions might not be accurate. Controversially, the continuum theory model was calibrated with data spanning more than a year (see Section 6.3.1) and is expected to provide better estimates.

Top and bottom strain data recorded at Section 1 (beam's mid-span) and Section 2, are compared to analytically obtained results in Figures 7.35 and 7.36. It is seen that the agreement between experiment and analysis is satisfactory, which verifies the analysis and models implemented. Again the continuum theory model gives better results, but the

empirical model (Findley's model) produces also acceptable estimates.

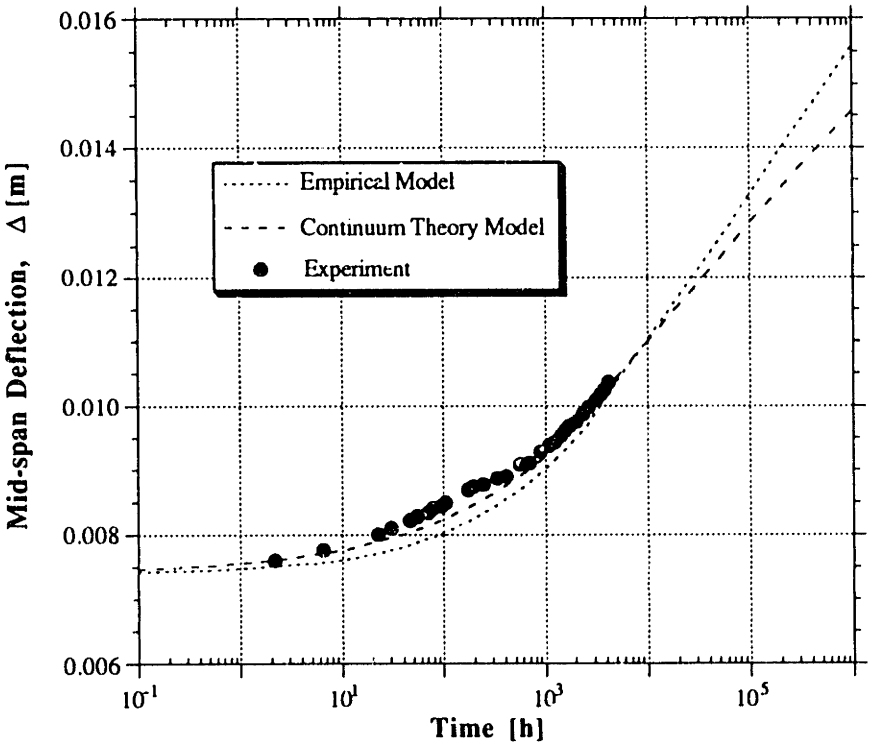

Figure 7.34 Beam 2, creep response comparison, log. scale.

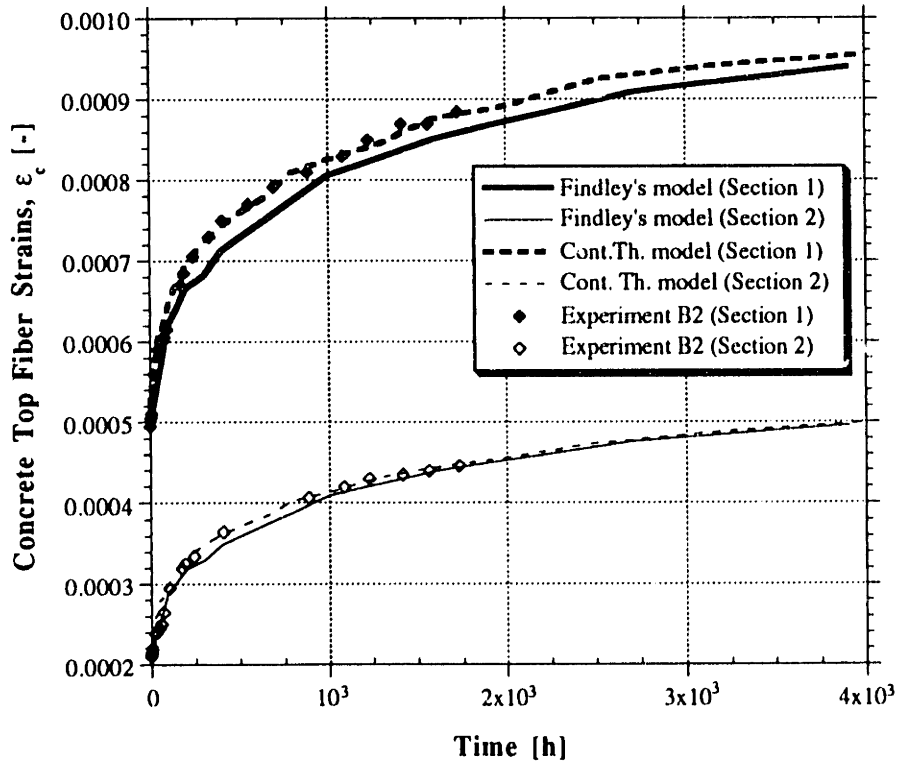

Figure 7.35 Beam 2, top fiber strain comparison at two cross sections.

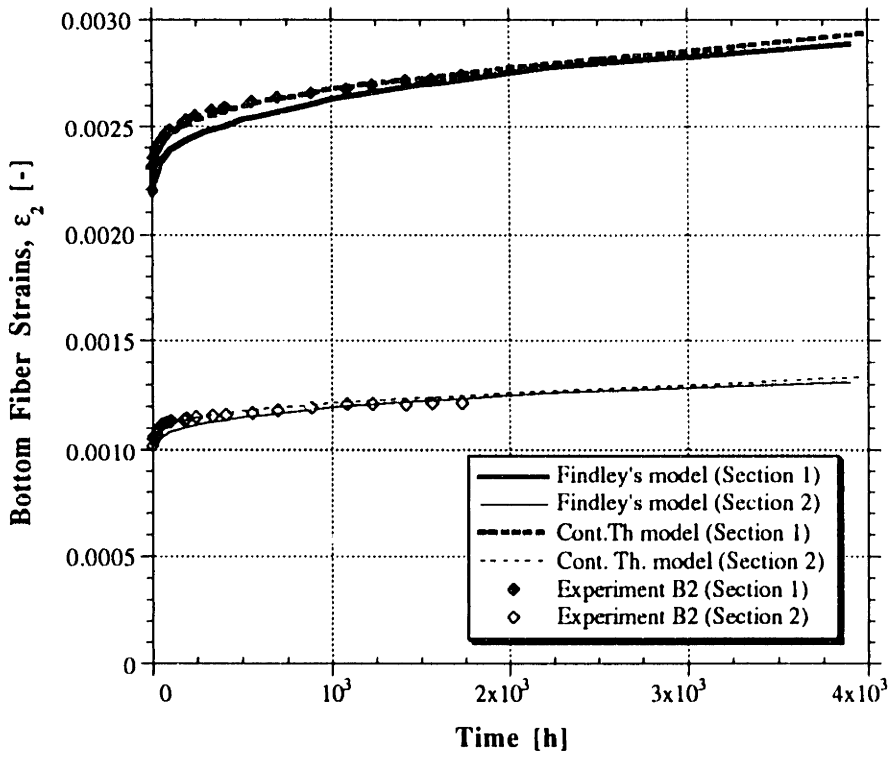

Figure 7.36 Beam 2, bottom fiber strain comparison at two cross sections.

Beam 7 was subjected to four point bending in outdoor conditions and its behavior is described next. Unlike for the analysis of Beam 2, the response of Beam 7 was monitored under varying atmospheric conditions and hence the effect of temperature had to be considered. Although temperature affects the magnitude of creep in most materials (especially in epoxies), this effect was not considered here (as explained in Chapter 4); the temperature ranges, which the test beam was subjected to, were considered too low to produce substantial changes in the creep models. Instead, only the impact of temperature on the beam's deformations was implemented through thermal expansion coefficients and the associated stress and strain redistributions. Also, since the temperature was recorded at discrete time points only, the exact temperature history of the beam's environment, which would be necessary to predict changes in creep behavior, was not known.

The analysis was carried out according to the approach described in Chapter 4. The thermal expansion coefficients were adopted as given in Table 4.3. The reference temperature was adopted at 22°C, which corresponds to the one during beam manufacturing. Figure 7.37 shows the results from the experiment and the analysis.

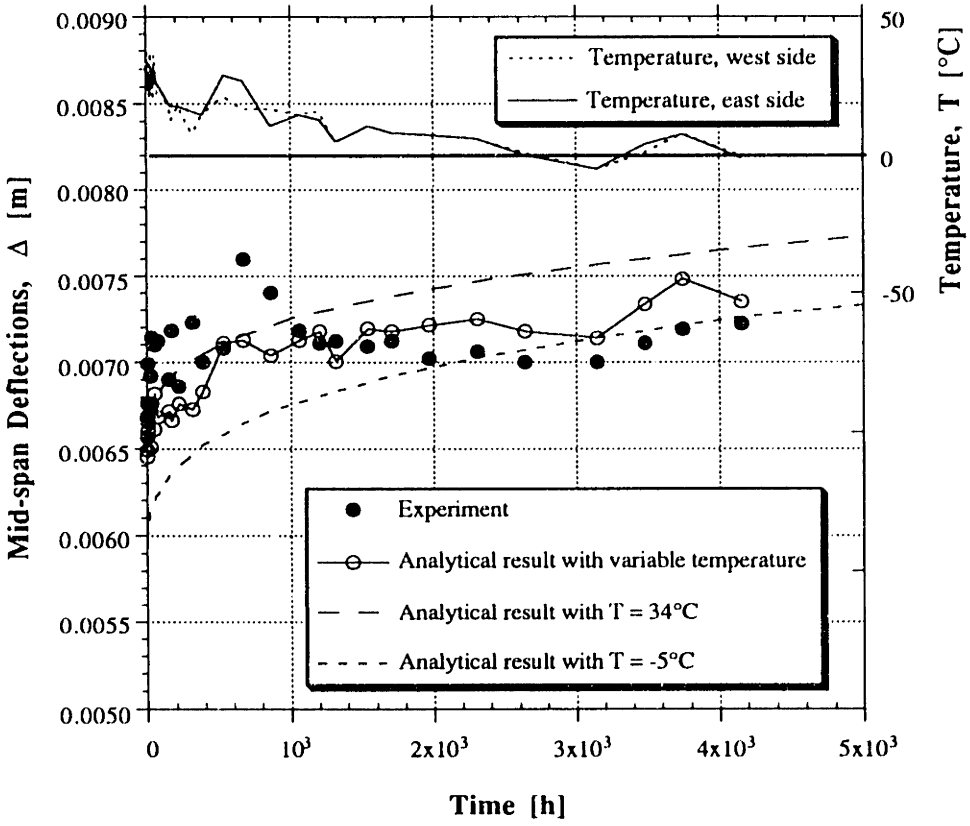

Figure 7.37 Beam 7, mid-span deflection comparison.

The temperature readings for two sides of the beam are given on the right hand side axis. It is seen that the average maximum and minimum temperatures encountered were 34 and -5 °C, respectively. Three curves were calculated and plotted. One of them included variable temperature, that is at each time the deflection was calculated, the temperature measured in the experiment was employed. The other two were calculated for constant temperature corresponding to the maximum and minimum encountered. Considering all the uncertainties involved in outdoor tests, the comparison of results obtained analytically with experimental data is quite satisfactory. In the first few months larger deviations can be observed, which can be attributed to the fact that these data were recorded on sunny days and temperatures on localized beam parts might have been higher than those recorded on the thermometers. This disturbance is not encountered on cloudy days (lower temperatures), and better agreement is achieved. Nevertheless, predictions follow overall the same pattern as experiments and are in very good agreement. Comparing the maximum and minimum temperature curves with $\Delta T \approx 40°C$, it can be concluded that the effect of temperature on bending deflections is approximately 0.5 mm in absolute value. This

verifies the expectation that temperature impact has small influence on the hybrid beam's response, which is related to the fact that GFRP and concrete have a relatively small differnce in the thermal expansion coefficient.

7.3.3 Parametric Study on Residual Response of Hybrid Beams

The analysis related to the prediction of the residual response of hybrid beams was presented in Section 4.3.5. No experiments were performed to verify this analysis, since the behavior of the two beams (Beams 2 and 7) is intended to be monitored over a period of several years in creep only, after which residual strength tests are expected to be conducted. An additional argument, which will be explained in this section, lies in the fact that the influence of sustained loading of the magnitude used here will have a substantial effect only after acting for a longer period of time (estimate 1-2 years), and hence testing at earlier stages would not be useful. Therefore, only analytical results in the form of a parametric study will be presented here, which are supposed to give an insight into the performance of the hybrid beams loaded in long term conditions.

For this purpose, the material properties and creep models of Beam 2 described in the previous section were adopted, and the residual response was analytically determined using the procedures developed earlier in Chapter 4. Concrete creep was modeled according to the proposed ACI creep model, while only the continuum theory model for the description of GFRP creep was implemented. Neither concrete shrinkage nor temperature effects were considered in this part.

The influence of two main parameters, namely the magnitude of the sustained load applied, M_o, and the time elapsed since it was applied, t_o, in residual response, was investigated. In practice these two parameters represent the level of dead load acting on the structure and its age. The main objective is, under the assumptions defined in Section 4.3.5, to define the residual strength of the member and to elaborate on its pseudo-ductile performance as a function of time and applied load.

The study was carried out over a range of possible values of parameters and the space covered is schematically summarized in Figure 7.38. It should be noted that the outmost left and bottom point corresponds to the short term static response case. The ultimate GFRP strain was defined at 2% in the analysis, which was not necessarily obtained in the GFRP coupon tests nor in the hybrid beam three point bending tests, but represents a reasonable value justified due to the approximate character of the parametric study. The ultimate concrete strain was adopted at 0.35%.

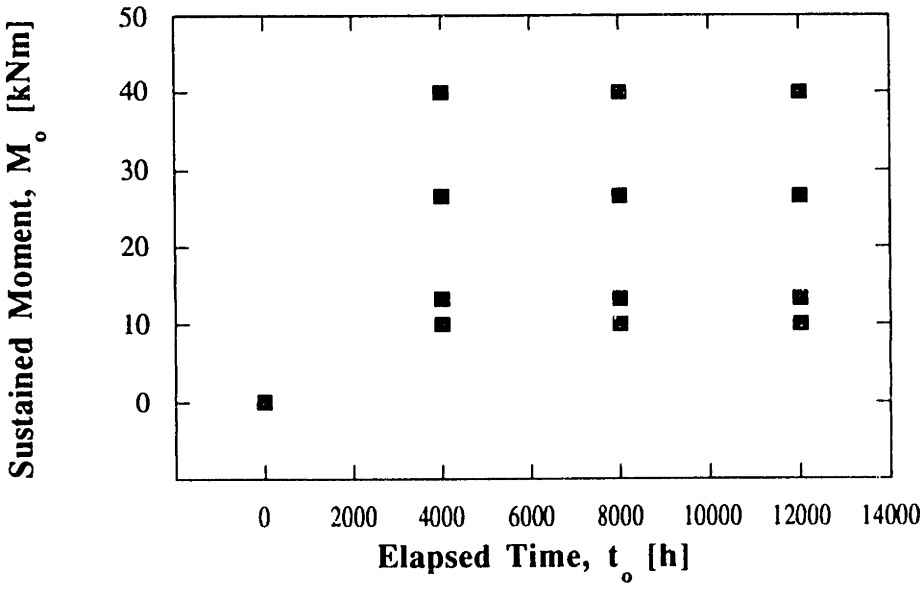

Figure 7.38 Parameter range considered.

Figures 7.39 to 7.40 show the resulting bottom and top fiber strains of a hybrid beam section, respectively, as a function of an externally acting moment M for M_o= 0, 13 and 40 kNm. Each curve corresponds to a specified combination of parameters M_o and t_o. It is seen that the concrete strain, ε_c, at CFRP fracture is augmented with increase of both M_o and t_o, and that the moment required for CFRP rupture is reduced. This implies that more creep has taken place and that the deflections of a beam would be increased, as well. Also, the effect of the sustained moment applied, M_o, appears more dominant than that of the creep time, t_o. Further, it can be noted that for M_o = 0 and 13 kNm the ultimate load is reached due to GFRP tension failure, while for higher M_o concrete crushing controls failure. This means that the beam's characteristics are such that ultimate moment capacity is achieved when both GFRP tension failure and concrete crushing modes are encountered almost simultaneously. Which of the two will govern is dependent on the sustained load applied (this basically is controlled by the relation of concrete and GFRP nonlinear short term behavior) and the creep time (thus, on the creep properties of concrete and GFRP). In addition, it is also dependent on the definition of ultimate strains of the two materials; an increase in one of the ultimate strains, ε_c^u or ε_1^*, would cause the other failure mode to dominate. For example, if the GFRP ultimate strain, ε_1^*, were to be increased, concrete crushing would always be the failure mode.

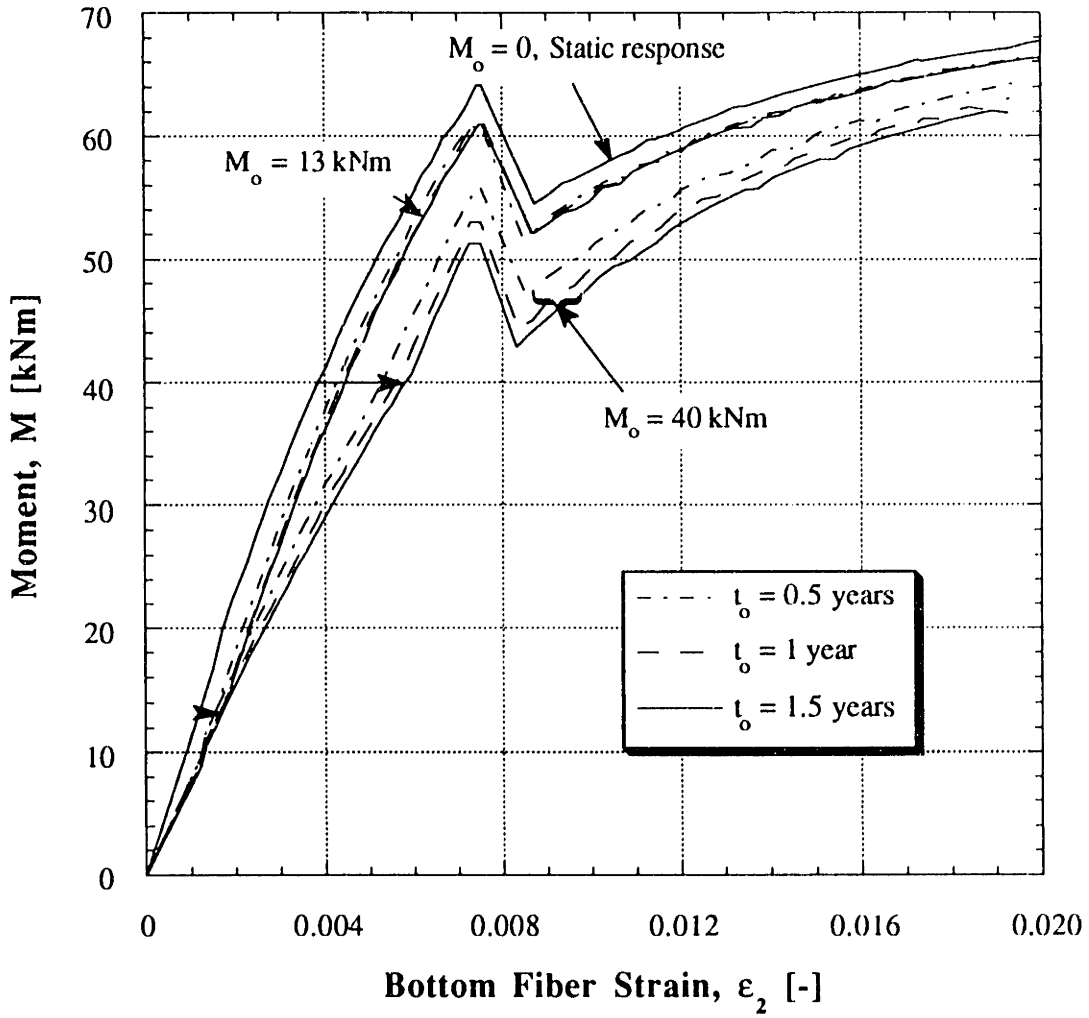

Figure 7.39 Bottom fiber strain for various residual strength responses.

The predicted load deflection curve of Beam 2 after two creep times, t_o = 1 and 5 years, is given in Figure 7.41. It is seen that the increase in ultimate deflections is in the order of 4 and 6% for 1 and 5 years, respectively. Also, the corresponding ultimate load is decreased by 3.2 and 4.6 %, respectively. It can be noted that the creep time effect is reduced with time nonlinearly, depending on the creep models used for concrete and GFRP.

Two issues regarding the residual response are important to be considered: the reduction of the ultimate moment capacity, M_{ul}, and the change of the ratio of moment capacity at CFRP rupture and ultimate moment capacity, $k_2 = M_2/M_{ul}$.

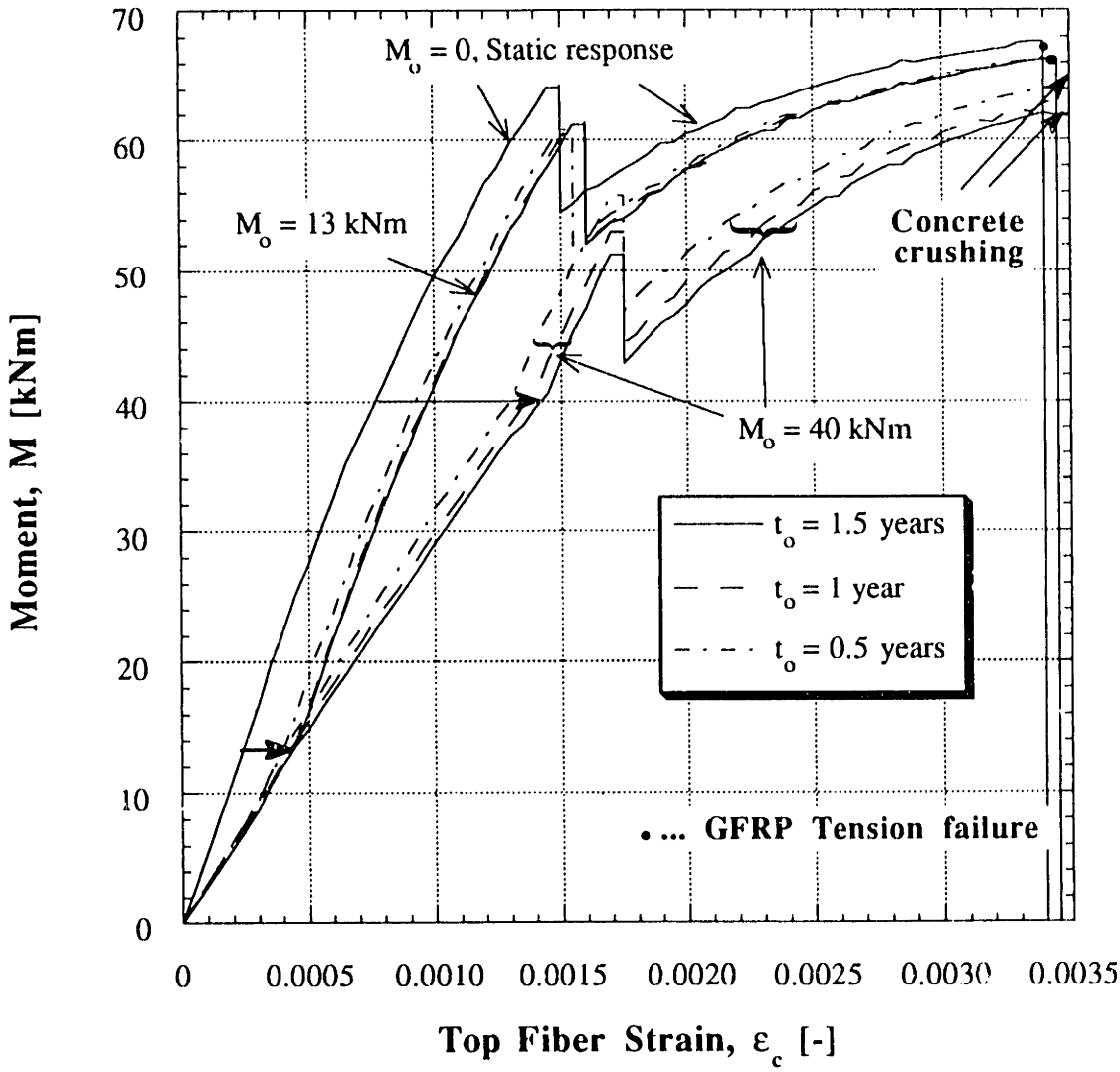

Figure 7.40 Top fiber strains for various residual strength responses.

Figures 7.42 and 7.43 show these two magnitudes as functions of creep time for different values of sustained moment. In Figure 7.42 the ultimate moment, M_{ul}, normalized with respect to the static moment capacity, M_{ul}^{st}, is plotted. It is evident that the ultimate load level decreases with both elapsed time and moment magnitude. The level of applied load is more dominant than the time elapsed. The rate of decrease of the ultimate moment capacity is descending with increasing time, but ascending with increasing load level. The decrease of ultimate strength is unfavorable for practical applications of the hybrid beam. If the deal load of the structure is assumed to be in the range of 20% of the ultimate load ($M_o \approx 13$ kNm) the decrease in the strength after 1.5 years amounts to roughly 4%, and changes only slightly thereafter. Although small, this decrement has to be

considered in the design process of the hybrid beam.

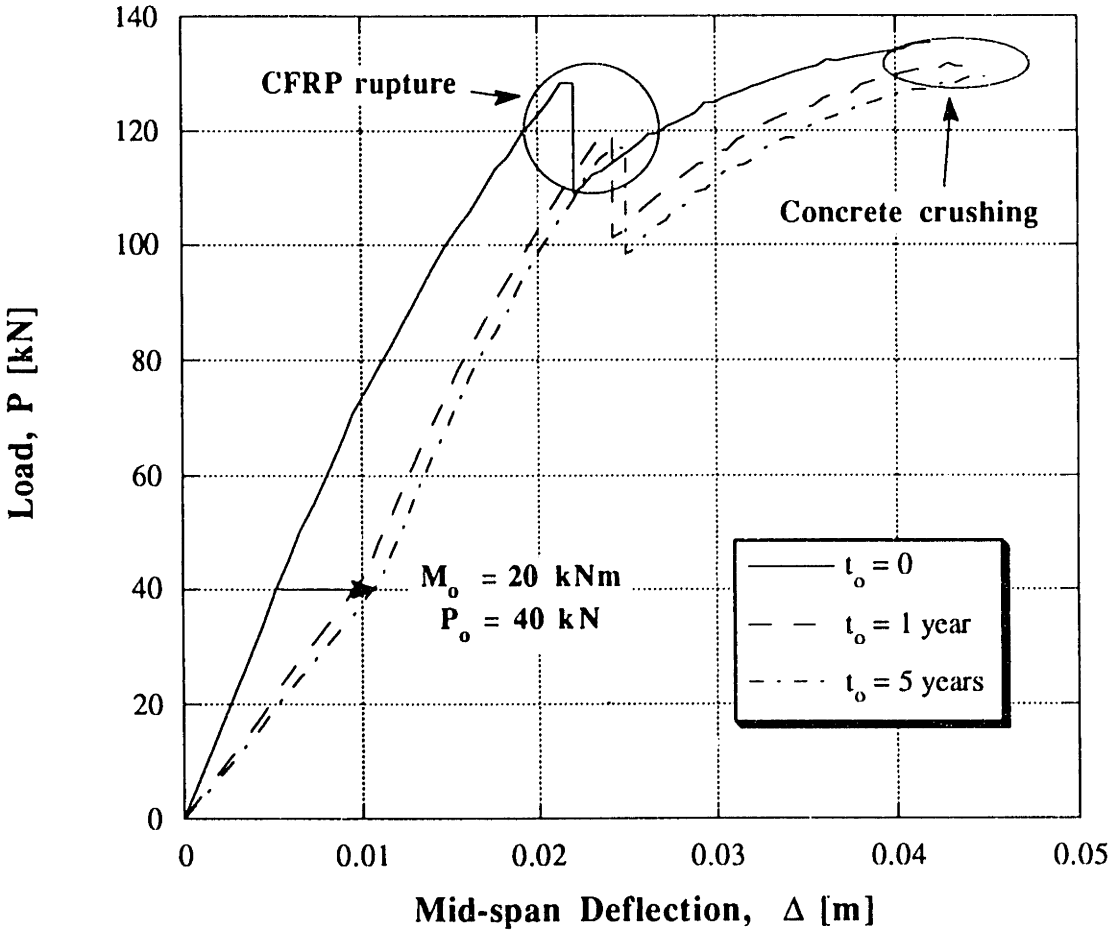

Figure 7.41 Beam 2, influence of creep time on residual response load/deflection curve.

The result from Figure 7.43 shows that the coefficient k_2 decreases with creep time and applied load level. In general this behavior is favorable, since it increases the pseudo-ductility of the member, that is the safety margin for the warning through CFRP rupture is augmented. In practice this means that as time elapses the signal for failure of the system will be given at earlier stages. On the other hand, the range up to which service loads can be applied drops, which should also be considered during the design process.

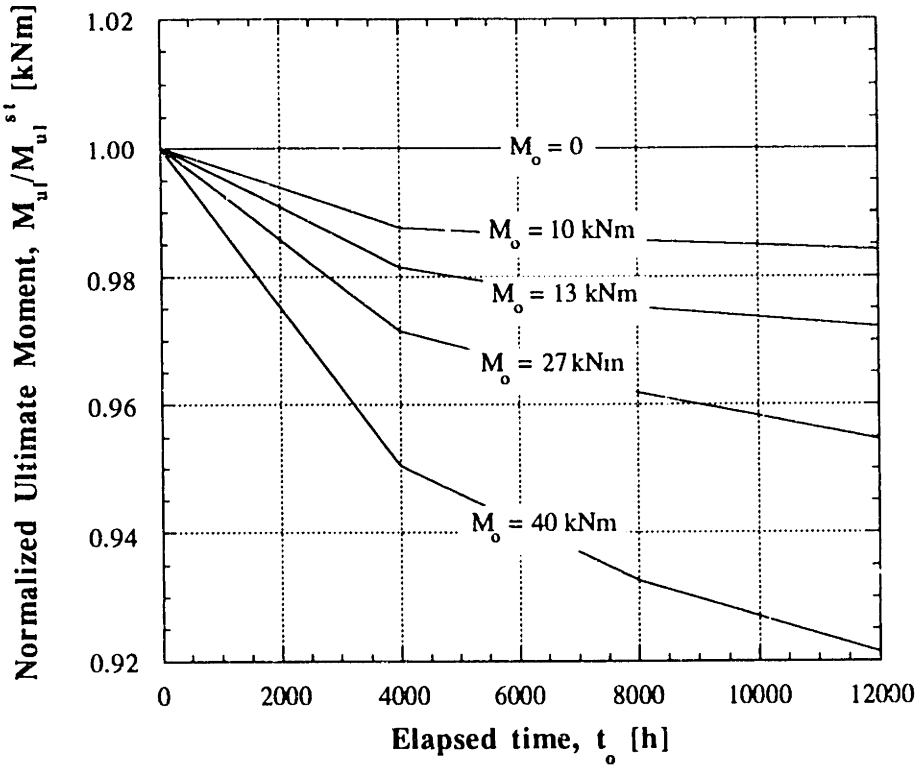

Figure 7.42 Ultimate moment reduction during residual response.

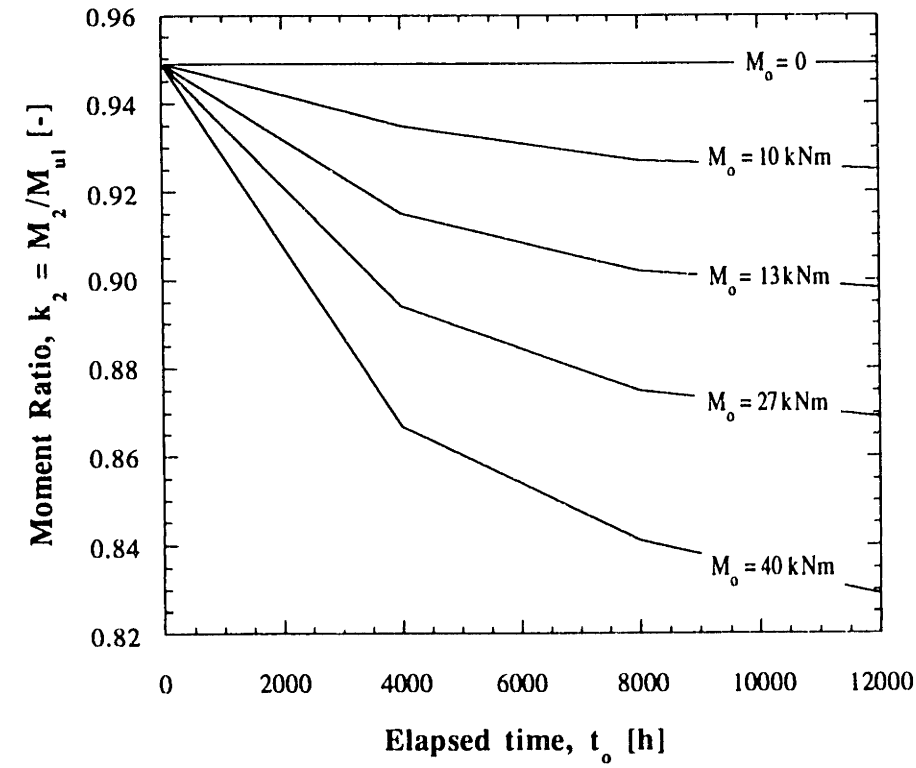

Figure 7.43 Moment ratio change during residual response.

7.4 Fatigue Response of Hybrid Beams

The fatigue response of hybrid beams was evaluated through four point bending tests on two beams subjected to cyclic loading. The experimentally obtained mid-span deflection and top and bottom fiber strain data were compared to analytically predicted ones. The effect of initial creep deformations was included. It was found that the models implemented were able to provide good predictions and hence verified the analytical approach. The residual strength response of fatigued Beam 6 was calculated and verified in the experiment.

7.4.1 Stiffness Degradation of Hybrid Beams in Fatigue

The influence of fatigue on the behavior of hybrid beams can be quantified by determining the degradation of stiffness with the number of load cycles. In order to verify the analysis developed in Chapter 4 for fatigue cyclic loading, tests were conducted on hybrid Beams 5 and 6. The test setup for the fatigue tests with the applied load levels and measurement points was described in Section 5.5. A DAS was used to record deflections and strains. The analytical procedure was described in Chapter 4 and was adopted for the computation of deflections and strains given here. The models developed earlier in Sections 6.2.4 for concrete fatigue and 6.3.4 for GFRP fatigue were used to predict analytically the fatigue response of Beams 5 and 6. The concrete fatigue model was adopted directly from Holmen (1982) and it was assumed that the concrete used for this beams had a similar fatigue behavior as the one determined in Section 6.2.4. This model also included creep effects. For the GFRP fatigue behavior two models were used. The continuum theory model was applied directly for both Beams 5 and 6, with the appropriate fiber orientation of ±45° and test results obtained from Bitterli (1987). Ogin's model was used for the empirical approach and although direct coupon tests were conducted only on specimens of Beam 6, the same parameters were implemented in the analysis of both beams. Creep of GFRP was accounted for through the already verified models given in the previous section and according to the derivations described in Chapter 4. It was further assumed that the unidirectional CFRP sheet is not affected by creep and fatigue. Also, temperature and shrinkage effects were not considered, since the tests were conducted in constant laboratory conditions, and only relative deformations were investigated.

It has to be recognized that Beams 5 and 6 were already subjected to a 24 hour

creep test prior to the fatigue test. The load applied in the creep tests corresponded to the average load level during fatigue, that is $P = (P_{max} + P_{min})/2$. This was carried out intentionally to eliminate the initially high creep deformations and create an initial deformation condition for the fatigue tests. This was important in order to distinguish between creep and fatigue influences, which at early stages are of the same order of magnitude. By preapplying a sustained load the major part of creep has already occurred by the time the fatigue test is initiated and also the creep deformations have, from then on, a much smaller gradient. On the other hand, this implies that the analysis has to be modified to account for the 24 hour creep loading. The modification due to creep was simply implemented by running the analysis (with the computer program described earlier in Chapter 4) from a -24 hour (negative time) origin and by imposing the following conditions:

- In the creep models the creep time was augmented by 24 h, that is at time -24 h the creep models predicted the behavior as at time zero.
- In the fatigue models the cycle number was set equal to zero for negative times. Hence, the fatigue effects were included only after time zero.

Further, it should be mentioned that the analysis for the first 24 hours (from time = -24 h to time = 0) is almost identical to the one given earlier for the 24 hour creep test in Section 7.3.1, and the only difference lies in the fact that the concrete creep model adopted here was defined with equations (4.52) or (4.53).

A detailed comparison of experimentally obtained and analytically calculated results of stiffness degradation is given in the following.

7.4.1.1 Fatigue Response of Beam 5

Beam 5 was subjected to a sinusoidal cyclic loading configuration given in Figure 5.37. After 3.3 millions of cycles the test was interrupted since a failure at one of the supports had occurred. A measurement of experimental data was conducted after various numbers of cycles. The resulting load displacement curves of Beam 5 are given in Figure 7.44. The deflection was measured at mid-span and the load is given per load point. It is seen that the response is almost linear and that there is an initial shift of the curve which can be attributed to the 24 hour creep deformations. The compliance (defined as the ratio of deflection to load) is increased with the number of cycles. It can be noted that apart from the decrease in stiffness, an increase in the initial displacements has occurred. The latter represents the non-recoverable (plastic) portion of the creep deformations. For better

visualization, in Figure 7.45 only the initial parts of the curves up to a load of 20 kN are given.

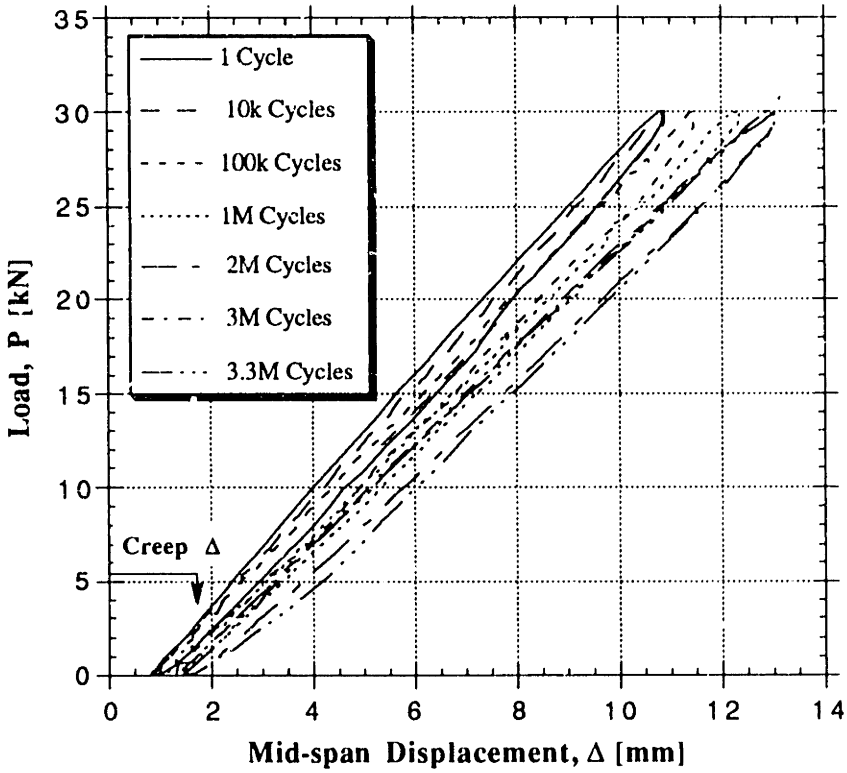

Figure 7.44 Beam 5, load deflection curves for various cycle numbers at mid-span.

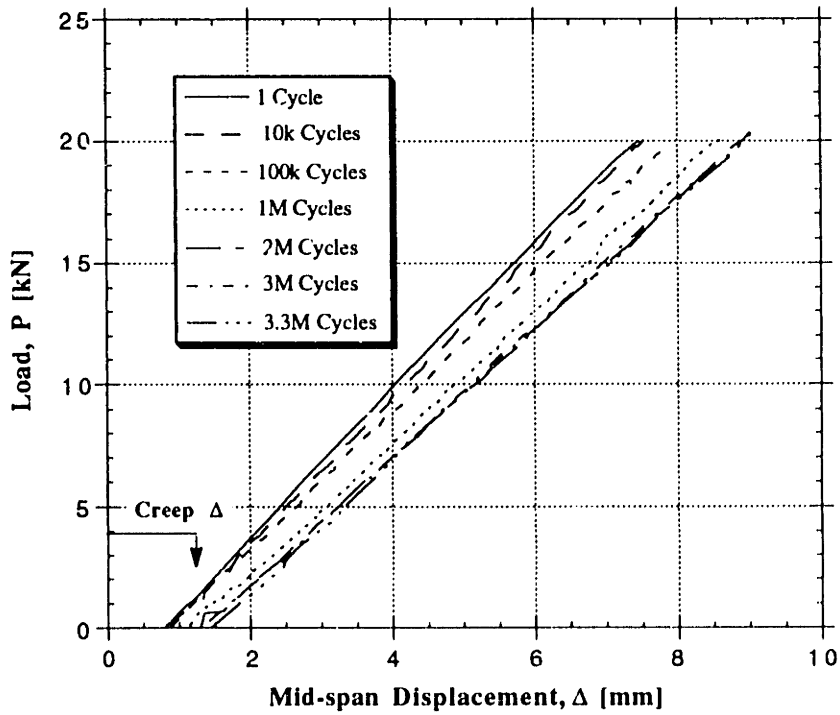

Figure 7.45 Beam 5, initial portion of load-deflection curves for various cycle numbers at mid-span.

Ignoring some experimental scatter the response complies well with the assumptions made earlier that the slope decreases with the cycle number indicating stiffness degradation. Figure 7.46 shows the comparison of experiment and analysis. Experimental deflection data at the load of 20 kN (average load level), and the corresponding analytical results using both the empirical and the continuum theory model for GFRP are given. The creep deflection portion is highlighted and the initial 24 hour creep is plotted in the negative part of the horizontal axis. As obtained earlier in Section 7.3.1 the empirical creep model somewhat underestimates the experimental results, while the continuum theory gives very good estimates. The effect of the cyclic loading is observed at $N = 0$. A sudden discontinuity point can be observed and the deflection increases with a larger gradient. Later this effect stabilizes and the slope of the deflection curve decreases.

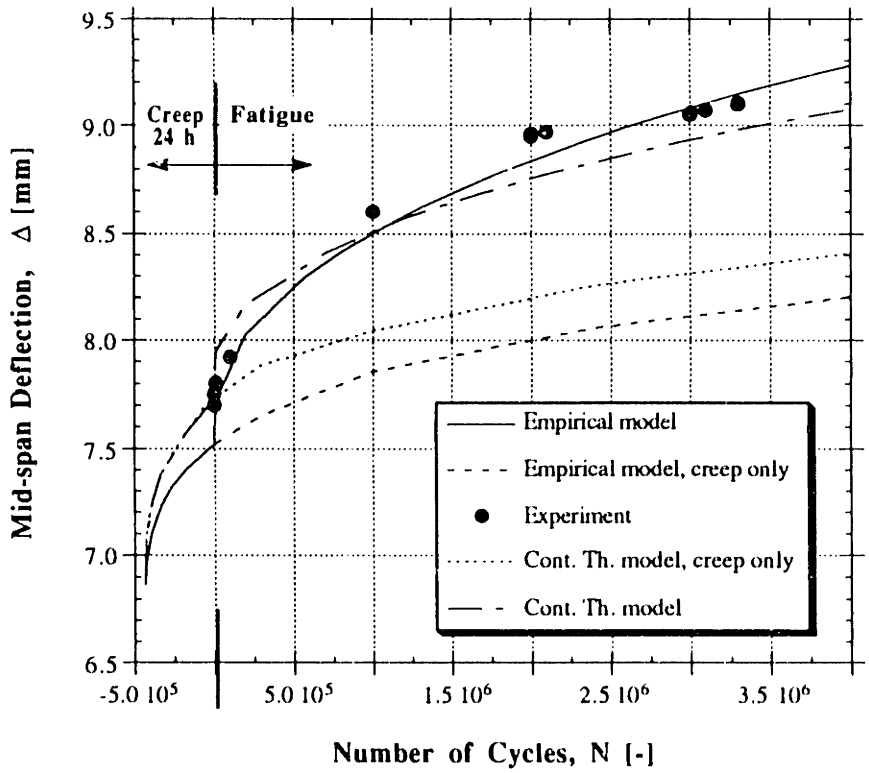

Figure 7.46 Beam 5, mid-span deflection as a function of cycle number.

The same data are given in Figure 7.47 in logarithmic scale, in order to visualize the response at low cycle numbers. It is seen that the continuum theory model gives better results for low cycle numbers while the empirical approach provides better estimates for large N. This can be explained with the fact that the continuum theory model has a better creep prediction capability and the initial deformations are closer to reality, but on the other

hand, represents a poorer fatigue model. Controversially, the empirical model starts with a less precise initial value but compares well to the experiment for larger cycle numbers. Further, it is noted that the continuum theory model gives more conservative results than the empirical one for cycle numbers less than 10^6, while for higher cycle numbers this behavior is inverted. Also, it is seen that the creep deflection (absolute increase from static value) is of the same order, if not larger, as the fatigue one. This is attributed to the sine wave loading pattern which would rarely be encountered in practice for structural elements. In practice, single load peaks would be much more apart from each other (e.g., vehicle passing over a bridge), and due to creep recovery the creep deflections would be negligible.

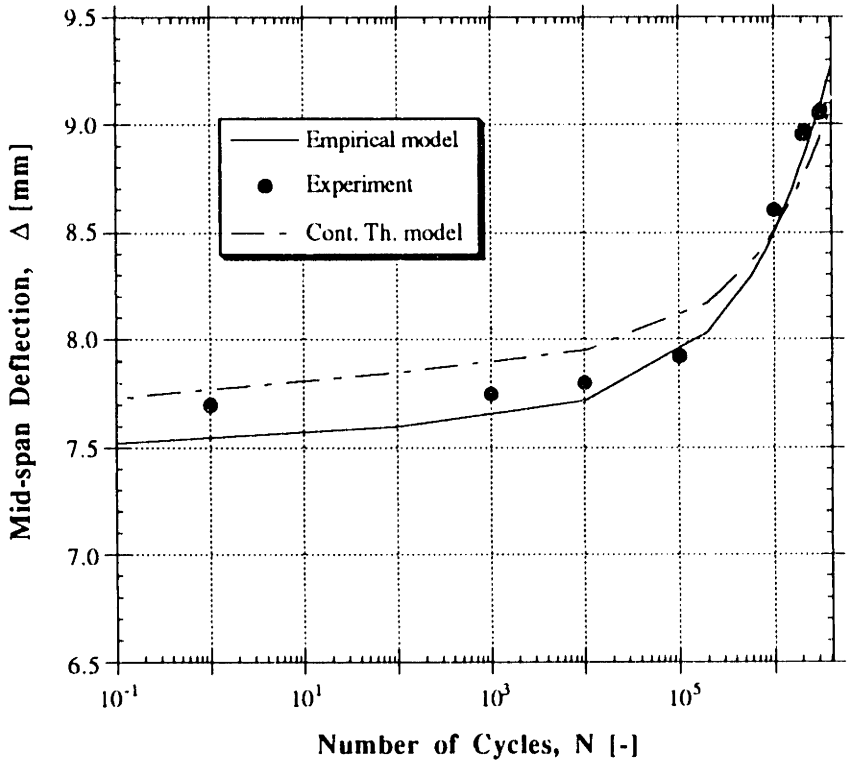

Figure 7.47 Beam 5, mid-span deflection as a function of cycle number in logarithmic scale.

The top and bottom fiber strains at Section 1 (see Figure 5.32) corresponding to the deflection curves of Beam 5 are given in Figures 7.48 and 7.49, respectively. The top fiber strains of both models comply well with the experimental values. The two models give almost the same result since the same concrete fatigue model was used for both. The difference between the two models, already observed in the deflection comparison, is

caused by the difference in the GFRP fatigue models. This is evident from the comparison of bottom fiber strains. Here the continuum theory model gives better results at initial cycling stages, but later the model underestimates the experimentally obtained results. Therefore the same behavior was observed in the deflection comparison. Overall, it can be concluded that both analytical models give very good estimates of the real behavior, although the empirical model appears to be more adequate.

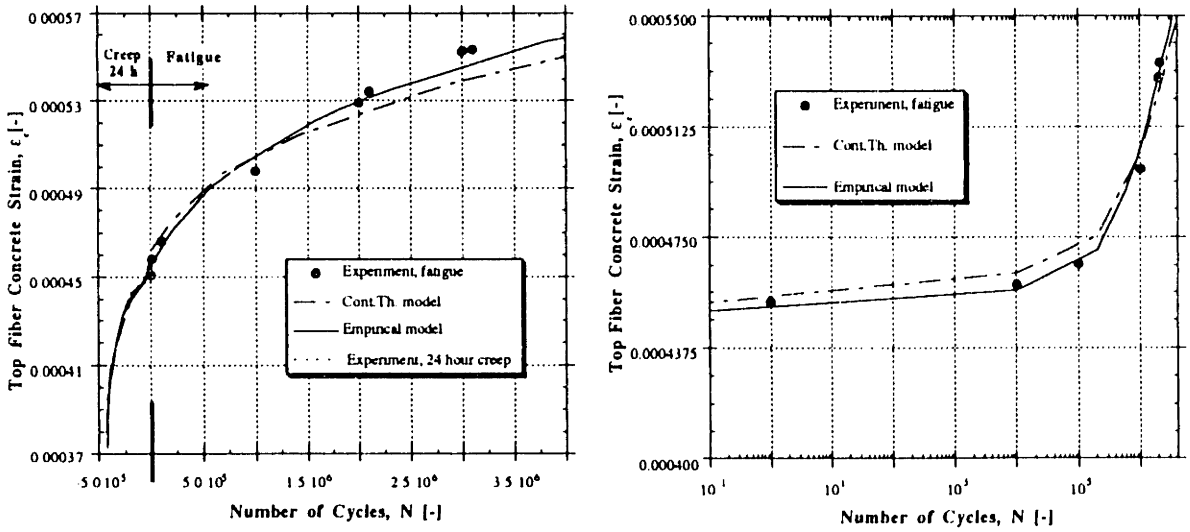

(a) (b)

Figure 7.48 Beam 5: (a) top fiber strain comparison, and (b) top fiber strain comparison in logarithmic scale.

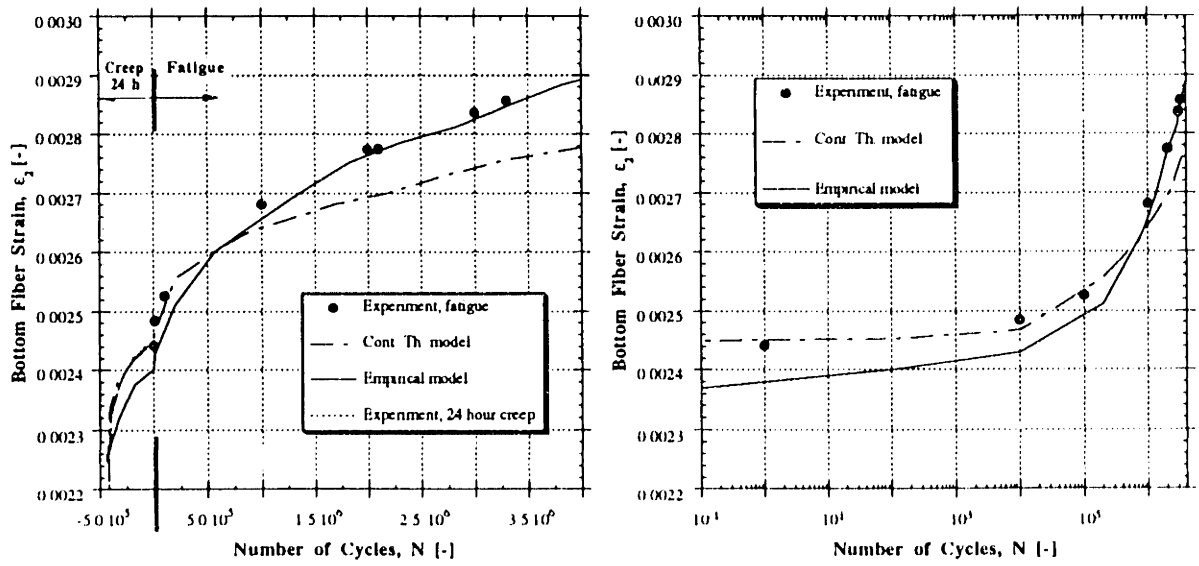

(a) (b)

Figure 7.49 Beam 5: (a) bottom fiber strain comparison, and (b) bottom fiber strain comparison in logarithmic scale.

7.4.1.2 Fatigue Response of Beam 6

The evaluation of the fatigue response of Beam 6 was analogous to the one described above for Beam 5. The same short term, creep and fatigue models (although with proper parameters) and the same analytical procedure were implemented. The detail at the support was improved to avoid premature failure of the beam. The load level was increased as given in Figure 5.37. After being loaded for 24 hours in creep and after 4,392,073 cycles (approximately 12 days) the beam failed in the desired pseudo-ductile manner. Due to stiffness reduction, the bottom fiber strains eventually reached the CFRP ultimate strain and caused both CFRP strips to rupture. Yet, at this point a collapse of the beam was not encountered and the remaining components continued to support the same load, (but with an increased deformation). The resulting load displacement curves for various cycle numbers of Beam 6 are given in Figure 7.50.

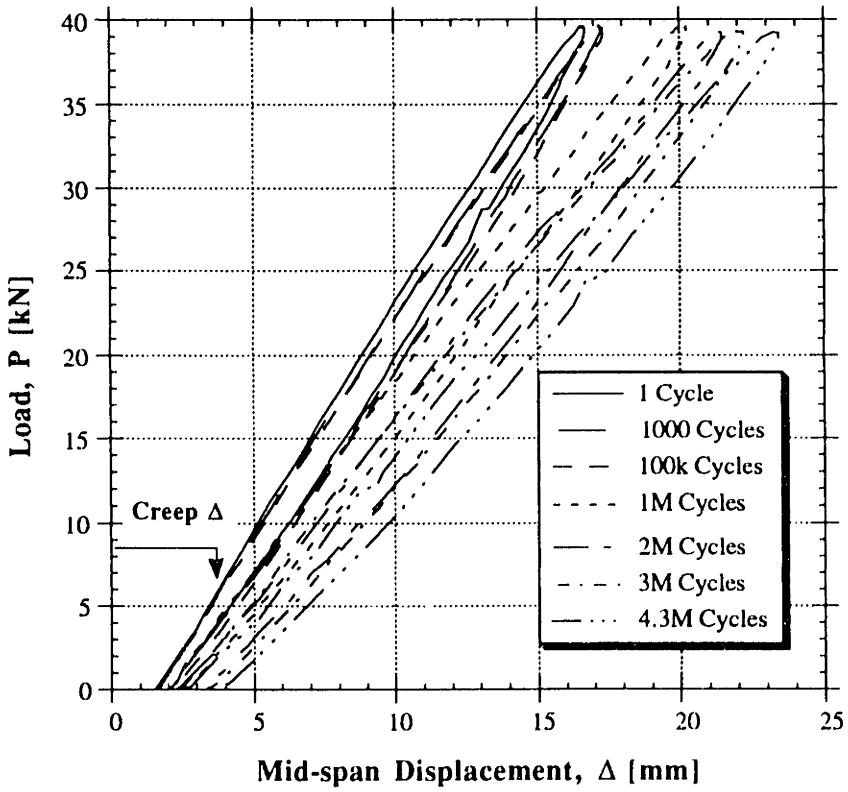

Figure 7.50 Beam 6, load deflection curves for various cycle numbers at mid-span.

The same observations listed earlier for Beam 5 apply here as well. Figures 7.51 and 7.52 compare the mid-span deflections in linear and logarithmic scale, respectively, as

a function of cycle number. Again, the 24 hour creep effect is given in the negative part of the time/cycle axis. The plot is given for a load of 30 kN acting on the beam. Since the applied load is higher than that for Beam 5, an even steeper deflection increase is obtained after initiation of load cycling. The continuum theory model gives again better results in the initial stage, but later ($N > 10^3$) the empirical model is closer to the experimental result. It is seen that the creep deflection part is substantially less than the part induced by fatigue, which verifies the dependence of the latter on the stress level applied. Controversially to Beam 5, the load applied here is higher and thus the ratio between fatigue and creep strains is increased (due to the nonlinearity between stress level and fatigue deformations).

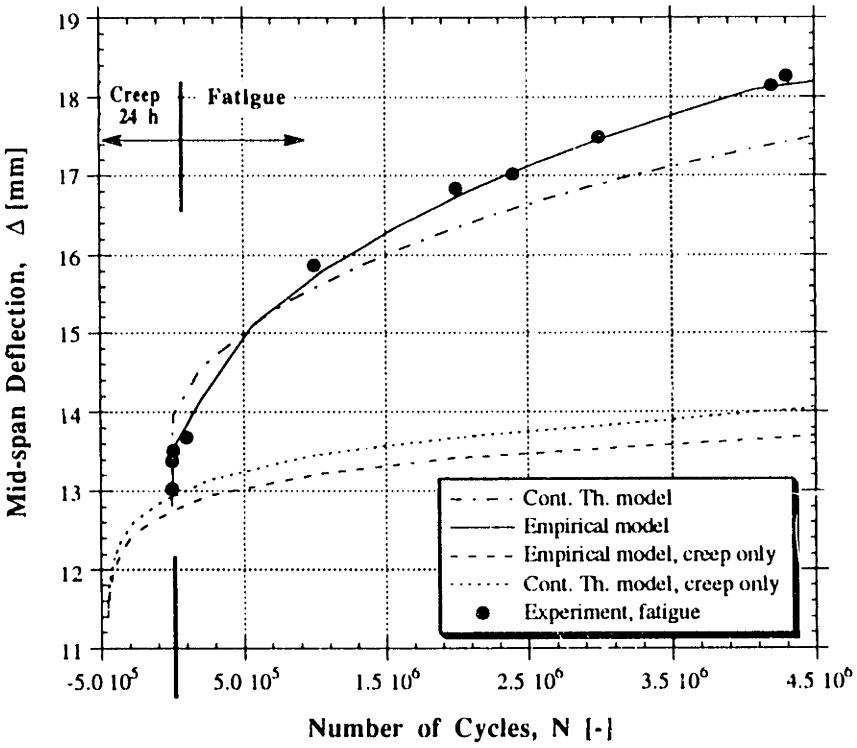

Figure 7.51 Beam 6, mid-span deflection as a function of cycle number for P = 30 kN.

Figure 7.53 compares the deflections of Beam 6 at an applied load of 40 kN (peak load during cycling). Very good agreement between experiment and both models can be observed, but it has to be stressed that the empirical model gives better approximations. The top and bottom fiber strains at Section 1 (see Figure 5.32) corresponding to the deflection curves of Beam 6 (at a load of 40 kN per load point) are given in Figures 7.54 and 7.55, respectively. It is seen that the top fiber strains are in good agreement and that

the difference between the two models is generated in the bottom fiber strain calculation. Also, it can be noted that the bottom fiber strains measured last (at 4.3M cycles) were close to the ultimate CFRP strain (≈0.85%).

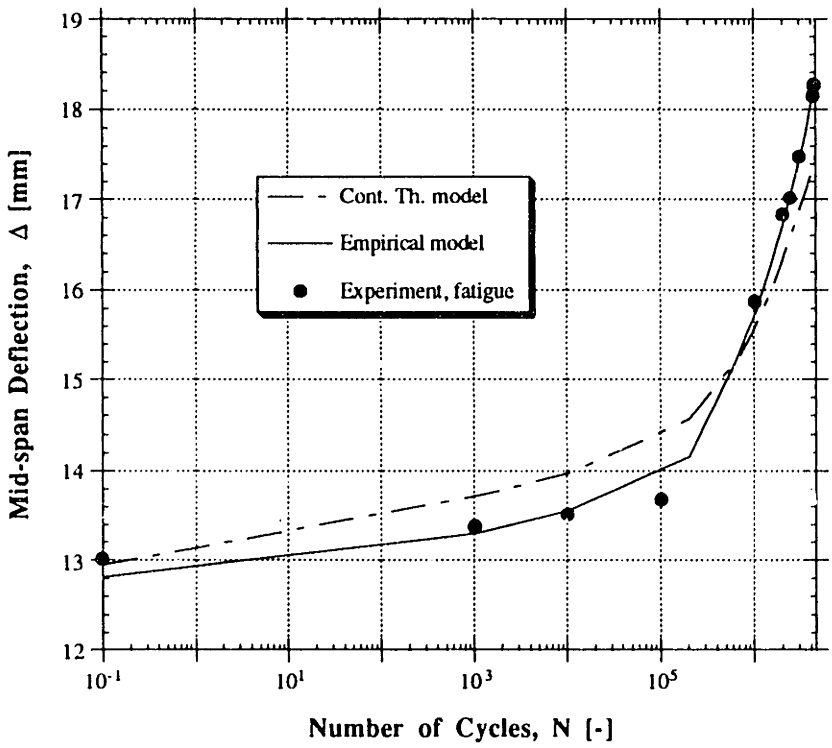

Figure 7.52 Beam 6, mid-span deflection as a function of cycle number in logarithmic scale for P = 30 kN.

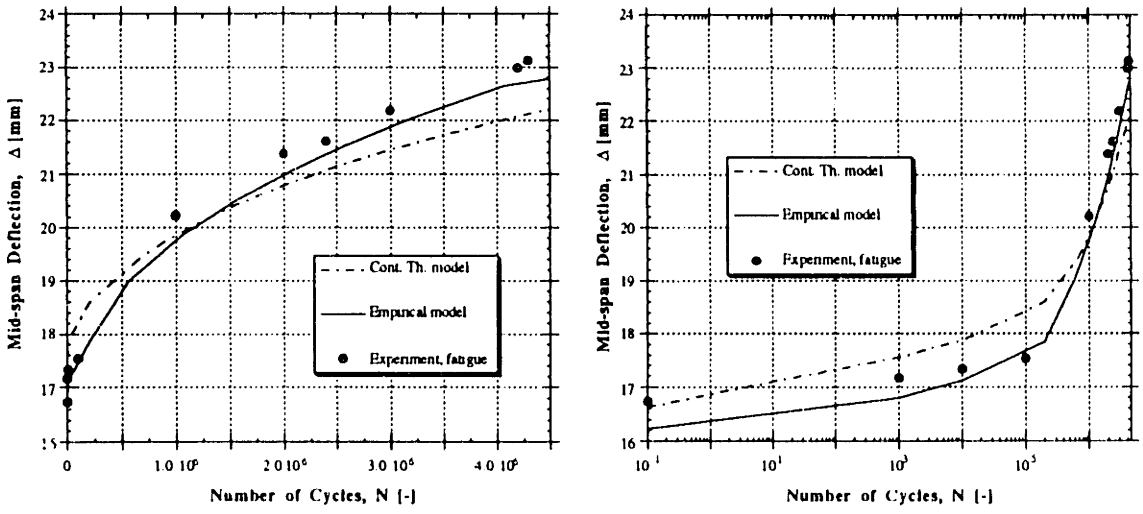

Figure 7.53 Beam 6, mid-span deflection as a function of cycle number for P = 40 kN: (a) linear scale; (b) logarithmic scale.

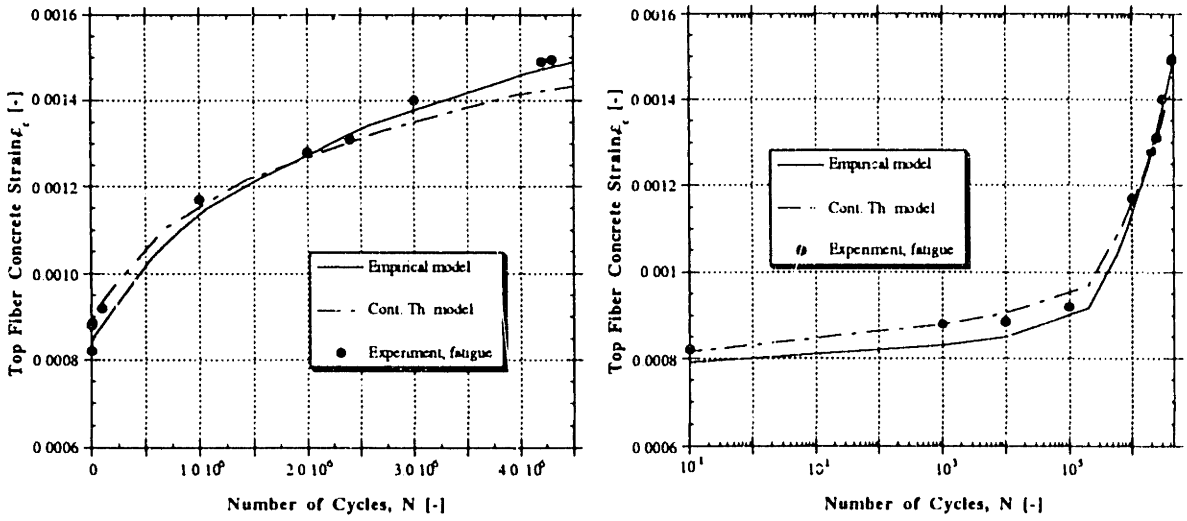

(a) (b)

Figure 7.54 Beam 6: (a) top fiber strain comparison; (b) top fiber strain comparison in logarithmic scale.

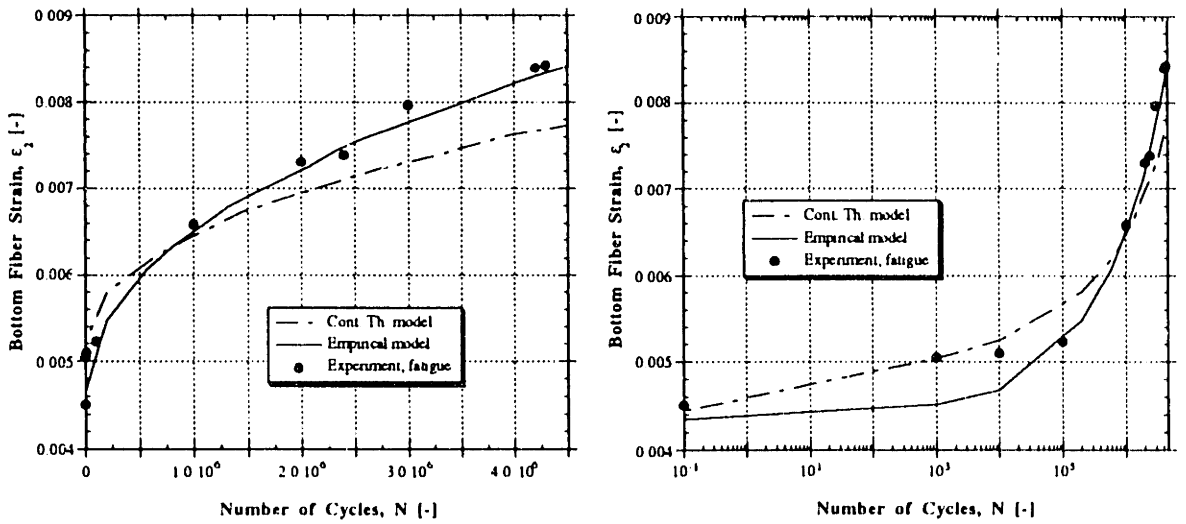

(a) (b)

Figure 7.55 Beam 6: (a) bottom fiber strain comparison; (b) bottom fiber strain comparison in logarithmic scale.

Similarly to the results obtained for Beam 5 the agreement between experiment and analysis was satisfactory. It can be concluded that the models adopted and the analytical procedure implemented represent a viable method for the prediction of the long term response of hybrid beams.

7.4.2 Residual Response of Hybrid Beam in Fatigue

The residual response of hybrid beams was studied on Beam 6. As shown in the previous section, the beam suffered damage after 4.39M cycles when the CFRP sheets ruptured. The cyclic loading caused a stiffness reduction of the hybrid beam, which induced an increase in normal strains. Eventually, the bottom fiber strains reached the CFRP ultimate strain and caused both CFRP sheets to fail. Yet, at this point a collapse of the beam was not obtained and the remaining components continued to support the same load, although, with an increased deformation. This behavior was characterized as pseudo-ductile.

The same beam was loaded statically in a short term four point bending test in order to establish the ultimate load, which the partially damaged beam is able to carry. The beam finally collapsed under a load of 113 kN which was ≈40% higher than the maximum used in fatigue (80 kN). At this point concrete crushing occurred, which then caused additional localized GFRP box beam damages and total failure. The benefit of the hybrid beam design was demonstrated, that is the beam had still a substantial safety margin in the load capacity. The additional deformations consumed additional strain energy and hence dissipated external energy. Parallel to the experimental approach the analytical model described in Section 4.4.5 was implemented in order to predict the residual response using a computer program. Having the result from the experiment, the cycle number used in the analysis was set to 4.4 million. The ultimate strain of CFRP was adopted from the experimentally obtained value at 0.0085. All the models for short term, creep and fatigue were used directly as defined in the previous section. Only the empirical model was used for the description of the GFRP response, since it was shown earlier to give best results.

The comparison of the experimentally obtained load deflection curve and the analytically calculated one is given in Figure 7.56. First, the experimental load displacement curve from the first and last cycles is plotted and then the short term curve of the hybrid beam without CFRP (since it failed at 4.39 M cycles) up to failure where the concrete crushing failure mode occurred. This was complemented with the analytical curve obtained from the computation. The analytical short term curve for a load up to 40 kN and the residual response curve up to failure are also depicted. It is seen that the predicted curve gives a good prediction of the residual strength of the hybrid beam. In the analysis, failure of the CFRP was not obtained during cycling but almost immediately after the load was increased in the residual portion of the curve (see the kink at A in the residual response curve at 40 kN). Since this depends on the precision of the fatigue model, that is the

calculated magnitude of the bottom fiber strain, it is still sufficiently close to the experimental result. At the same time, the computed stiffness is very close to the experimentally obtained one, and hence the latter verifies the assumption on the stiffness change of the member due to fatigue loading. The computed ultimate load compares well to the experimental result (58.7 kN versus 56.3 kN for the analysis and the experiment, respectively).

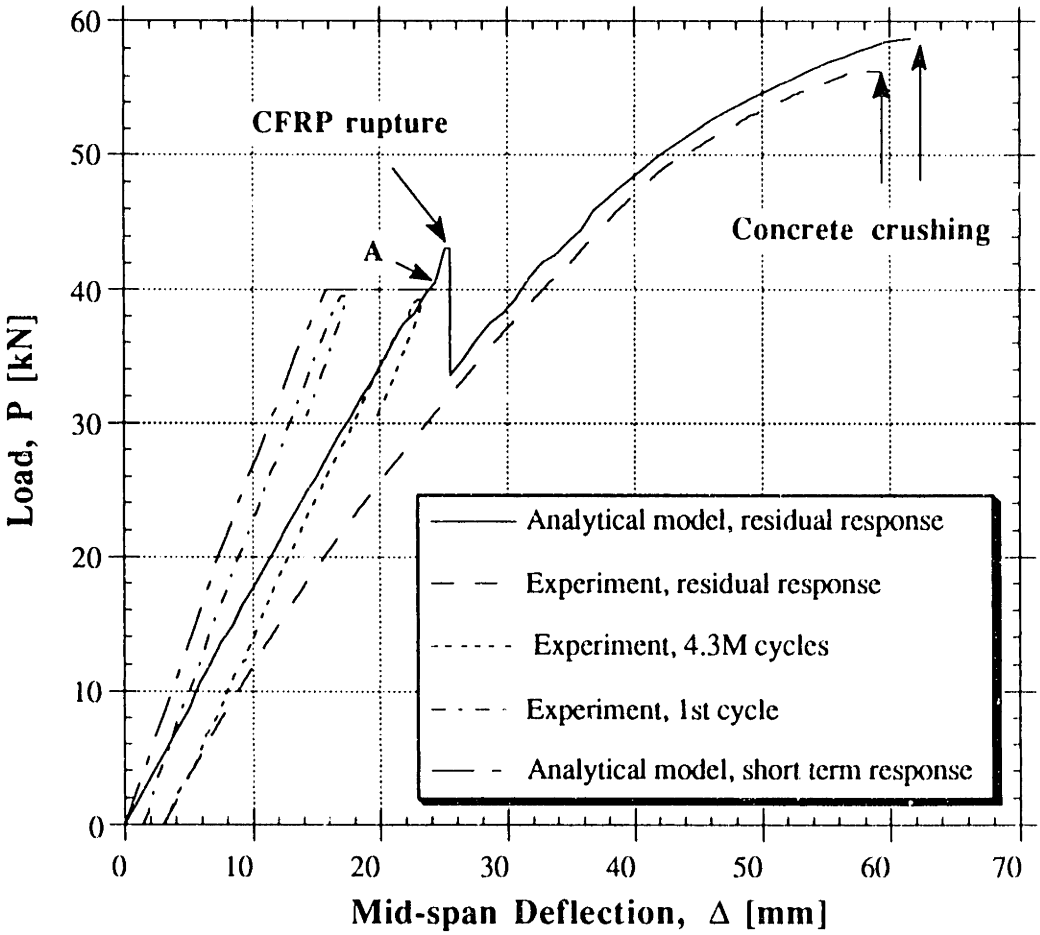

Figure 7.56 Beam 6, residual response comparison between experiment and analysis.

The conclusion can be made that the proposed models and analytical procedure can be successfully used for the prediction of the residual response of the hybrid beam.

7.5 Synopsis

This chapter presented the comparison between the results from the experimental program carried out and the models and analytical procedures developed and characterized earlier. Short term, creep, fatigue and residual response were evaluated experimentally and computed analytically and numerically. The agreement was found to be very good and the assumptions made in the definition of the models and throughout the analytical computations were verified. The software developed appears to be a viable tool for the prediction of the hybrid beam behavior in both short and long term loading conditions.

Chapter 8

SUMMARY - CONCLUSIONS - RECOMMENDATIONS

8.1 Summary

An innovative design of fiber reinforced composite members combined with concrete is presented in this work. Combining fiber reinforced plastic materials with concrete appears to be a feasible way of producing efficient and cost effective hybrid members. These members possess many desirable mechanical behavior characteristics such as ductility, high stiffness and strength, while maintaining a low weight. The main features of the new concept proposed here for hybrid sections can be summarized as follows: the concrete layer substitutes the GFRP compressive flange of traditional pultruded box sections, thus reducing the materials cost and increasing the stiffness; and the bottom flange is made by a combination of two composites (GFRP and CFRP), one failing in tension earlier than the other, serving the role of a "sensor" which indicates an imminent collapse (pseudo-ductile response). The mechanics associated with the short and long term behavior of this novel hybrid beam concept was investigated.

First, the short term analysis for the new concept of hybrid elements was developed. Using nonlinear material models several failure mechanisms were considered: a) concrete crushing, b) CFRP rupture, c) GFRP tension failure, d) beam shear failure, e) interface debonding, f) GFRP web shear buckling and g) lateral instability. In addition, stiffness and deflection response relations were derived. A computer program was developed incorporating all of the above mechanisms and used to predict the response of the hybrid beams. A FEM model was also implemented to enhance the results with numerical solutions. Two series of three point bending tests were carried out on small scale beams (cross sectional dimensions 75x80 mm to 91x80 mm and spans up to 1.4 m) and large scale beams (cross section 350x180 mm and span length 3.0 m). Comparison of the analytical solutions with both experimental data obtained from three point bending tests and numerical results verified the validity of the strain compatibility method used in the analysis. The analytical prediction of the bending behavior compared well to the

experimental results, and both deflections and bending moment predictions were within 10% when comparing analysis and experiment.

Within the description of the short term response, a simplified failure analysis was proposed and a design methodology for FRP-concrete elements was developed. A design example was given comparing the performance of a plain pultruded GFRP element to that of a hybrid member. It was found that the new design concept can reduce the material cost by 50%, although all the advantages in performance of FRP composite structures were maintained. The same design procedure was used for the design of the specimens used in the experiments. Since test results showed very good agreement with predicted values, the design methodology of FRP-concrete hybrid elements was verified. In particular, the concept of pseudo-ductile behavior was obtained experimentally, exactly in the manner as it was predicted analytically and as it was assumed in the design process. The experiments showed that the innovative design represents a viable and promising method for the improvement of today's FRP pultruded members.

Next, the long term flexural behavior of fiber reinforced composite members combined with concrete subjected to sustained load was investigated both analytically and experimentally. Creep models for concrete and GFRP were defined for the creep analysis and a computer program taking material nonlinearity and creep effects into account was developed. Two models describing the time dependent behavior of GFRP were implemented. One was developed directly from experimental results giving an empirical approach, while the other was obtained from continuum theory using experimental data for creep of the matrix only. A standard model for concrete creep was also adopted. Experiments were carried out on large scale beams loaded in four point bending under sustained loads. Two 24 hour creep tests giving data about the initial creep behavior and two 6 month tests giving the general creep response were examined. Comparing analytical and experimental data it was found that the viscoelastic response can be predicted in a reliable manner (analytical results were within 5% of experimental) and thus the model and computational procedures implemented were verified. It was noted that the creep deformations of hybrid beams for typical load ranges are of acceptable magnitudes. Further, a computer program was created in order to predict the residual strength of hybrid FRP/concrete beams. Within this description it was assumed that the beam had gone through a certain load history resulting in an initial state of deformations. The short term response at that time was computed. A parametric study was conducted in order to evaluate the influence of sustained load level and time elapsed since it was applied. It was shown that the pseudo-ductility response is maintained and that the hybrid beam design gives additional advantages with respect to long term performance.

The effects of cyclic loading were also investigated. Appropriate models for concrete and GFRP were developed and implemented in order to predict the response of the hybrid member under fatigue loads. Special emphasis was put on the stiffness reduction and its effect on the fatigue life of the beam. Two models describing the fatigue behavior of GFRP were adopted. The first is purely empirical and was calibrated from coupon tests while the other deals with the description of the fatigue response through continuum theory and known fatigue behavior of the unidirectional composite layers. The fatigue model for concrete was adopted from literature. Two large scale beams were subjected to cyclic loading, giving valuable results on the behavior of FRP-concrete hybrid elements. The comparison of experimental results and analytical prediction showed very good agreement (within 3-4% deviation). In addition, the "sensing" effect of the CFRP laminate was demonstrated. Although after a large number of cycles the CFRP sheet failed, the remaining constituents (GFRP box beam and concrete layer) were able to safely carry a load increase. The residual strength of a fatigued member was derived analytically and implemented in a computerized procedure. The computed residual response of hybrid members was compared to the experimentally obtained ones and good agreement was reached verifying the models used and the assumptions made in the analysis.

Finally, the effect of temperature on the hybrid beam was discussed and local effects at the GFRP-CFRP interface were analyzed. A method to predict temperature induced deformations of the hybrid beam was presented and its results were compared to experimental data. Satisfactory agreement was obtained when the deflection data of a beam loaded for 6 months with sustained loads in atmospheric conditions were compared to analytical results. The analytical solutions for the interface shear and normal stresses were derived. Normal stresses, resulting from a temperature change, in the lateral direction of the CFRP sheet indicate that some consideration should be given to placing some transverse fiber reinforcement.

8.2 Conclusions

The main objective in this thesis was to develop a new hybrid beam element with superior performance to existing GFRP structural members. This was achieved through an innovative design concept, where all the beneficial characteristics of GFRP (such as corrosion resistance, electromagnetic neutrality and partially lightweight construction) were maintained, and in addition improvements in stiffness, ductility (pseudo-ductile behavior) and, most important, cost were obtained. The new element is composed of a GFRP box

beam with a layer of concrete in its compression zone and a thin CFRP sheet on its tension zone. Issues regarding design as well as short and long term response were analyzed and the main findings are summarized next.

The design of hybrid FRP-concrete components is a relatively straightforward task once all the possible failure mechanisms have been identified and the design requirements and constraints have been set up. One can either employ a nonlinear optimization algorithm to minimize a certain function (e.g., materials cost) based on a certain set of constraints (e.g., stiffness, strength), or follow the simple design methodology outlined in this thesis to select the cross section dimensions. The flexural response of the resulting designs complied quite well with the desired behavior, which was demonstrated throughout the experimental program. Therefore, it can be concluded that the proposed design procedure can be successfully employed to obtain preliminary designs of hybrid FRP-concrete elements. Although the resulting designs will vary depending on the imposed requirements, in general it was found that the concrete layer will be relatively shallow, yet providing excellent stiffness improvements (by a factor of more than 3). Also good designs will have the neutral axis close to the top of the GFRP box beam resulting in mainly tensile normal stresses in the GFRP. The CFRP sheet is mainly used to provide the pseudo-ductile failure behavior and to reduce the sensitivity of the beam to creep and fatigue. The CFRP's role as a sensor is particularly important for the long term response, where its failure announces imminent collapse but yet the element is able to carry more load and hence represents a safe design. In order for the pseudo-ductile behavior to materialize the thickness of the CFRP has to be very thin, which also complies with the low cost requirement.

Once the preliminary design is carried out a more sophisticated and detailed analysis needs to be applied. Using nonlinear material models and analytical tools this goal was achieved. The results of the computer program developed agreed well with experimental data. The results verified not only the stiffness and strength calculations but also the possibility of obtaining pseudo-ductile failure mechanisms by combining materials which are essentially linear elastic to failure. The computed ultimate strength and deflections at failure were within 10% to experimental results, indicating the appropriateness of the material models and analytical procedures involved. During bending tests CFRP rupture, concrete crushing, concrete shear failure and GFRP top flange buckling (for plain GFRP beams) were obtained experimentally and thus verified the assumed failure mechanisms. It can be concluded that the analytical approach presented enables reliable designs and accurate predictions of the true response.

The long term analysis of FRP-concrete hybrid beams accounted for realistic material constitutive models calibrated from test results or derived from known properties of the constituent materials (e.g., matrix of GFRP). The viscoelastic response was described with two models for the creep behavior of GFRP and one for concrete. The assumption that all materials behave according to linear viscoelasticity was verified. It was seen that the continuum theory model for GFRP creep gives better results (2-3% deviation from experiment), and that for longer duration of sustained loading the results of both models comply well with experimental data. Considering creep deformations with typical dead load ranges (25% of ultimate load), it is found that the deformations stabilize after approximately three months and continue increasing at a rate of 20% (of the short term deflections) per decade. This gives an increase of 100% after 100 years which is an acceptable value for most structural applications.

The analysis of the hybrid beams subjected to cyclic loading is more involving than the one for creep. Here the response after a certain load history is not any more linearly proportional to the short term response (at cycle zero), but instead significant stress dependence is observed. In addition, the expected load levels in fatigue are generally higher than those in creep (e.g., a vehicle passing over a bridge, or rush hour loading), and hence stress dependence had to be included for both concrete and GFRP fatigue models. The computer program presented enables the computation of the hybrid beam response with respect to the cycle number. From the two models describing the response of GFRP in fatigue, the empirical one showed very good agreement with experimental data. Here, the deviation from experiment was found to be only 2-3%, while the continuum theory model deviated by about 5%. Overall, for the design and experiment considered here it was seen that the fatigue induced stiffness reduction was around 33% of the short term value after 1 billion cycles.

The residual strength of a member subjected to some loading history is of importance to the designer of the FRP-concrete elements. The analytical derivations and computerized procedure developed enabled the description of the residual response. The parametric study which was carried out to evaluate the influence of sustained load level and time elapsed, showed that although both factors reduce the ultimate strength, the pseudo-ductile behavior is still maintained. The effect of the applied load appears more dominant than that of the time since load application. For a typical dead load of a structure (25% of the ultimate load) the decrease in strength after 1.5 years amounts to roughly 4% and changes only slightly thereafter. This reduction has to be taken into account during the design process of the hybrid beam. At the same time the ratio between the ultimate load and the load required to rupture the CFRP sheet decreases with increasing sustained load

and loading time. Although in general this is favorable, because the pseudo-ductility of the member is increased, it reduces the allowable service load level and has to be considered in design. Comparison of the analysis for residual response after some fatigue loading history to experimental results showed good agreement. It was concluded that the residual response of the hybrid member can be predicted successfully and that the adopted models are verified.

Finally, the work presented in this thesis gives an insight into the possible advantages of the FRP-concrete hybrid beam concept. The important conclusion is that hybrid FRP-concrete members can actually be designed to possess high strength, stiffness and ductility characteristics at a cost which compares favorably with designs using pultruded members only. This is an example of maximizing system performance using materials by combination. If the design concept proposed were to be implemented in practice, the application of pultruded GFRP structural elements should be expanded. It is believed that the application of this method needs not be restricted to the improvement of existing GFRP elements and their currently very specific (limited) area of applicability only, but can also be a valid candidate for the substitution of structural elements made of conventional materials, such as steel and concrete. The high material cost can be offset by savings in transportation cost to the construction site, handling costs and, lastly, reductions in foundation related cost. For comparison an adequate reinforced concrete beam (assuming cross section 300x100 mm) to carry the same load as the large scale beam designed here would be 3.5 times heavier. Eventually, the advantages offered by the new hybrid beam concept may be explored in the future through lightweight prefabricated or in situ cast bridge and/or floor decks.

8.3 Recommendations for Future Research

As in every research project the author believes that the study described here is far from complete. Future research should address both analytically and experimentally the issue of bond between GFRP and concrete, the insulation of the top GFRP part from the alkaline environment of the concrete (e.g., via the use of an epoxy layer and/or a gelcoat at the interface), the more severe temperature impact and the reliability of the system in short and long term loading configurations.

The application of a mechanical connection between the GFRP webs and the concrete layer has to be investigated. From the experience gained through the large scale experiments it was anticipated that during construction the bond between the two materials

will not always be perfect and that an adhesive bond can not be sufficient to provide the required safety margins. Therefore, a system of mechanical connectors has to be established to augment the adhesive bond. Due to the nature of the pultrusion process (which is expected to be the primary beam manufacturing method) it is impossible to have a deformed surface along the interface. Therefore, either shear connectors have to be added afterwards on the pultruded shape by adhesion, in the form of a winding bundle of glass fibers (Figure 8.1(a)), or a system of groves and holes can be cut out of the pultruded profile to interlock with the concrete (Figure 8.1(b) and (c)). An alternative to glued-on deformations could be achieved by drilling holes into the interface area and using a combination of fiberglass and polyester (or vinylester) screws in a manner similar to classic shear studs used in traditional composite steel/concrete structures (Figure 8.1(d)).

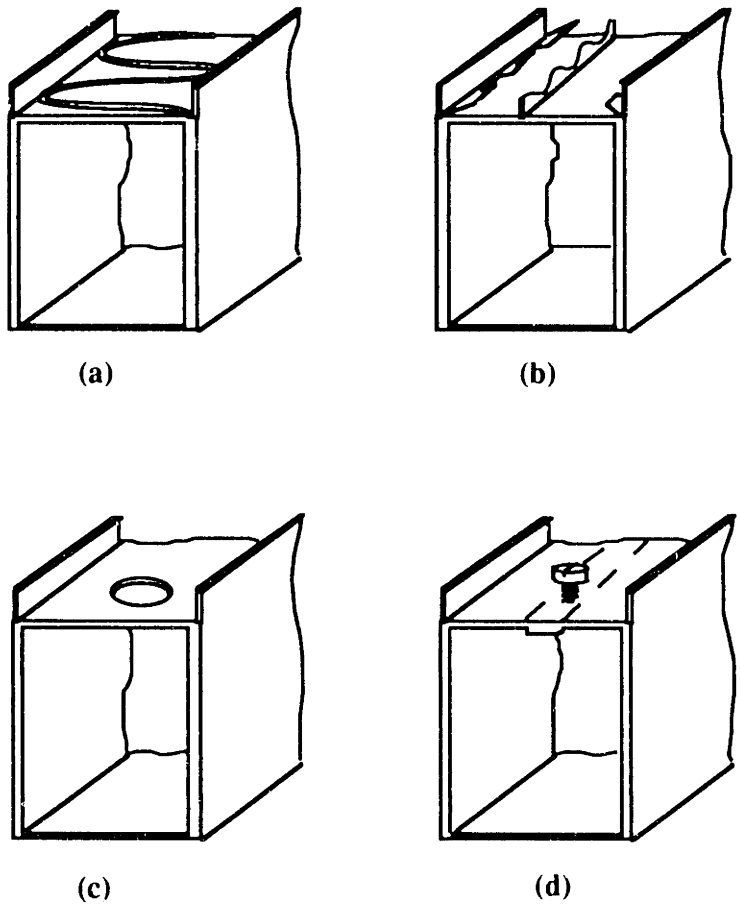

Figure 8.1 Proposed mechanical deformations at GFRP-concrete interface.

The strength of glass fibers in the polyester (or epoxy) matrix can be affected by moisture. The stacking of calcium hydroxide crystals on the fiber surface, originating from the cement matrix due to flow of ions in the moist matrix, can affect the GFRP's strength

(Meyer 91). Therefore the insulation of the top GFRP part from the alkaline environment of the concrete (e.g., via the use of an epoxy layer and/or a gelcoat at the interface) has to be investigated. The required adhesive (with an adequate diffusion coefficient and proper thickness) to prevent a significant strength decrement in the GFRP can be combined with the adhesive layer that will be used simultaneously for the shear transfer at the interface.

Further consideration should be given to temperature effects onto the behavior of the hybrid elements in severe temperature conditions (e.g., fire). Normal polyvinyl matrix pultruded sections start losing their strength at 25°C already, and reach half of their strength at about 100°C. Alternatives can be found by using phenolics, alumina trihydrates and antimony trioxide as fillers of the matrix, which maintain the strength up to 150°C and satisfy class 1 flame retardant provisions. It is also important to account for the adhesive bond between the CFRP sheet and the GFRP section, which can be damaged and lose its function at high temperatures. Hence, the carrying capacity of the hybrid section has to be evaluated taking these strength reductions into account and the fire resistance has to be predicted analytically.

An other interesting subject comprises the investigation and definition of material reduction factors for the hybrid beam design. Material reduction factors are used in design codes to account for: (i) accuracy with which various material strengths can be calculated, (ii) the importance of a particular member to the survival of the structure and (iii) the achievable quality control. In general, the randomness in the resistance of a structural element arises because of the variabilities inherent in the mechanical properties of the materials, of variations in dimensions (tolerances), and because of the uncertainties in the theory underlying the definition of member strength. This approach can be expanded and applied to the hybrid beam. Since several different materials will be involved, the overall resistance factor will depend not only on the resistance factor of each constituent but also on the geometry, loading pattern, failure mode (bending, shear) and mutual proportions of material properties.

Finally, a more thorough cost efficiency analysis needs to be carried out in order to prove and justify the method's perspective and its application potential in the construction market. Yet, it would be of interest to prove the commercial aspect of the proposed design.

References

ACI (1971). "Prediction of Creep, Shrinkage and Temperature Effects in Concrete Structures." ACI Committee 209, SP-27, Detroit, 51-93.

ACI (1974). "Considerations for for design of Concrete Structures Subjected to Fatigue Loading." *ACI Journal*, ACI Committee 215, March, 97-121.

ACI (1986). "Design Consideration for Steel Fiber Reinforced Concrete." *ACI Struct. Journal*, Committee Report 544, 4R, V. 85, No. 6, 563-580.

ACI (1989). *Building Code Requirements for Reinforced Concrete* (ACI 318-89), *and Commentary* (ACI 318-89), Detroit, Michigan.

Agarwal, B.D. and Broutman, L.J. (1980). *Analysis and Performance of Fiber Composites*, John Wiley Publishing, New York.

Aminian, P. K. and White, J. K. (1988). "A review of the properties of type F (Kevlar 29) Parafil cables with reference to the design of cable structures." *Proc. Symp. engineering applications of Parafil ropes*, Imperial College of Science and Technology, London, England, 63-71.

Anandarajah, A. and Vardy, A.E. (1985). "A theoretical investigation of the failure of open sandwich beams due to interfacial shear fracture." *Struct. Engng.*, V. 63, No. 4, 85-92.

Ashby, M. F. (1989). "On material and shape." First draft of unpublished report, Engineering Department, University of Cambridge, Cambridge, England.

Bakeri, P. A. (1989). *Analysis and design of polymer composite bridge decks*, M.Sc. Thesis, MIT, Cambridge, Massachusetts.

Bank, L. C. and Mosallam, A. S. (1990). "Structural performance of a fiber reinforced plastic pultruded frame." *Proc., 8th Struct. Congress '90*, ASCE, 509-510.

Bank, L. C.(1987). "Shear Coefficients for Thin-Walled Composite Beams." *Comp. Struct.* , V. 8, 47-61.

Banks, W. M. and Rhodes, J. (1983). "The instability of composite channel sections." *Comp.Struct. 2, Proc., 2nd International Conference on composite structures*, 443-452.

Beton Kalender (1987). *Verlag für Architektur und Technische Wissenschaften*, Ernest & Sohn, Berlin.

Bitterli, K. (1987). *Fatigue behavior of GFR Epoxies with special consideration of shear effects*, Ph.D. Thesis, ETH, Zürich, Switzerland (in German).

Brown, V. L. and Bartholomew, F. (1990). "FRP rebar in reinforced concrete members." *Proc., 8th Struct. Congress '90*, ASCE, 511-512.

Budelmann, H., Kepp, B. and Rostasy, F. S. (1990). "Fatigue behavior of bond-anchored unidirectional glass-FRP's." *Proc., First Materials Engineering Congress '90*, ASCE, 1142-1151.

Burgoyne, C. J. (1988). "Structural applications of type G Parafil." *Proc. Symp. engineering applications of Parafil ropes*, Imperial College of Science and Technology, London, England, 39-47.

Caughey, R. A. and Scott, W.B. (1929). "A practical method for the design of I-beams haunched in concrete." *Struct. Engng. 7*, No. 8, 275-293.

CEB-FIP (1970). *International Recommandations for the Design and Construction of Concrete Structures*, Paris, 88.

Ciba-Geigy Plastics Division (1991). Provisional data sheet, "Hot curing epoxy matrix systems", Matrix System: ARALDIT LY 566, Basel, Switzerland.

Deskovic, N. (1991). *Innovative method of prestressing structures with externally bonded FRP composites*, M.Sc. Thesis, MIT, Cambridge.

DIN 53 455 (1968). "Prüfung von Kunststoffen", Zugversuch, 213-218.

DIN 53 457 (1968). "Prüfung von Kunststoffen", Bestimmung des Elastizitätsmoduls im Zug-, Druck,- und Biegeversuch, 221-224.

DIN 53 454 (1977). "Prüfung von Kunststoffen", Druckversuch, 208-212.

Faza, S. S. and GangaRao, H. (1990). "Behavior of fiber reinforced plastic rebar under bending." *Proc., 8th Struct. Congress '90*, ASCE, 517-518.

Findley, W. N. and Worley, W. J. (1951). "Some static, fatigue and creep tests of a glass fabric laminated with a polyester resin." *AF, Technical Report No 6389*, Engineering Experimental Section, University of Illinois, April.

Findley, W. N. and Peterson, D.B. (1958). *ASTM Proceeedings*, V. 58, 841.

Fujisaki, T., Matsuzaki, Y., Sekijima, K. and Okamura, H. (1987). "New material for reinforced concrete in place of reinforcing steel bars." *IABSE Symp., Concrete Structures of the Future*, Paris, France, 695-696.

Gerritse, A., Maatjes, E. and Schurhoff, H. J. (1987). "Prestressed concrete structures with high strength fibers." *IABSE Symp., Concrete Structures of the Future*, Paris, France, 425-432.

Hansen, T.C. (1958) Creep of concrete - a discussion of some fundamental problems, Bul. No. 33, *Swedish cement and Concrete Research Institute*, September.

Holaway, L. (1990). "Bridging the gap." Advanced Composite Engineering, V. 6, June, 18-20.

Holmen, J. O. (1982). "Fatigue of Concrete by Constant and Variable Amplitude Loading." *ACI Publication SP-75*, Report of ACI Committee 215, 71-110.

Holmes, M. and Just, D. J. (1983). *GRP in Structural Engineering*, Applied Science Publishers Ltd., England.

Hull, D.(1981). *An introduction to composite materials.* Cambridge University Press, Cambridge, England.

Iyer, S. L. and Anigol, M. (1991). "Testing and evaluating fiberglass, graphite, and steel prestressing cables for pretensioned beams." *Proc. Spec. Conf., Advanced Composites Materials in Civil Engineering Structures*, ASCE, 44-56.

Jones, R. M. (1975). *Mechanics of Composite Materials*, McGraw-Hill Publishing, New York.

Kaifasz, S. (1960). "Some tests on beams prestressed by fibre-glass cords." *Mag. Concr. Res.*, V. 12, No. 35, 91-98.

Kaiser, H. (1989). *Strengthening of reinforced concrete with epoxy-bonded carbon-fiber plastics* , Ph.D. Thesis, ETH, Zürich, Switzerland (in German).

Kakihara, R., Kamiyoshi, M., Kumagai, S. and Noritake, K. (1991). "A new aramid rod for the reinforcement of prestressed concrete structures." *Proc. Spec. Conf., Advanced Composites Materials in Civil Engineering Structures*, ASCE, 132-142.

Kim, P. and Meier, U. (1991). "CFRP cables for large structures." *Proc. Spec. Conf., Advanced Composites Materials in Civil Engineering Structures*, ASCE, 233-244.

Knott, J.F. (1973). *Fundamentals of Fracture Mechanics*, Butterworths, London.

MARC/MENTAT (1990). *Finite element software package*, User's manual.

McCormick, F. C. (1978). "Laboratory and field studies of a pedestrian bridge composed of glass reinforcement plastic." *Transportation Research Record 665*, National Research Council, Washington, DC., 99-107.

Mallison, J.M. (1974). "Chemical plants - Engineering applications of composites." *Composite Materials 3*, Academic Press New York, 303-362.

Meier, U. (1987a). "Proposal for a carbon fibre reinforced composite bridge across the Strait of Gibraltar at its narrowest site." *Proc. Inst. Mech. Engrs.*, 201(B2), 73-78.

Meier, U. (1987b). "Bridge repair with high performance composite materials." *Material and Technik*, 4, 125-128 (in German).

Meier, U. (1990). *Grundlagen zum Bemessen von Kunststoffenbauteilen*, Textbook, ETH Zürich, Division for Civil Engineering, Switzerland (in German).

Meier, U. (1991). "Case histories." *Advanced composite materials with application to bridges* , State-of-the-art report, CSCE, 274-284.

Meier, U. and Deuring, M. (1991). "The application of composites in bridge repair", Strasse und Verkehr, No. 9.

Meier, U. and Kaiser, H. (1991) "Strengthening of structures with CFRP laminates." *Proc. Spec. Conf., Advanced Composites Materials in Civil Engineering Structures*, ASCE, 224-232.

Meier, U., Deuring, M. and Schwegler, G. (1992). "Strengthening of structures with CFRP Laminates: Research and applications in Switzerland." *Advanced composite*

materials in bridges and structures, 1st International Conference, CSCE, Sherbrooke, 243-252.

Meyer, L. (1991). "Glassfaserbeton Baustoff der Zukunft." *Beton* , June, 277-281.

Neville, A.M. (1971). *Properties of Concrete*, London, Pitman Publishing.

Ogin, S. L., Smith, P. A. and Beaumont, P. W. R. (1985). *Composite Science and Technology*, 24-47.

Park, R. and Paulay, T. (1975). *Reinforced concrete structures*, John Wiley & Sons, New York.

Phillips, L.N. (1989). *Design with Advanced Composite Materials*, Springer-Verlag. London.

Plecnik, J. M., Hamoud, A. S., Ballinger, C. and Plecnik, J. M. (1989). "Development of high strength composite cables." *Proc. sessions related to structural materials at Structures Congress '89*, ASCE, 514-525.

Plecnik, J. M., Azar, W. and Kabbara, B. (1990). "Composite applications in highway bridges." *Proc., First Materials Engineering Congress '90*, ASCE, 986-995.

Pleimann, L. G. (1991). "Strength, modulus of elasticity, and bond of deformed FRP rods." *Proc. Spec. Conf., Advanced Composites Materials in Civil Engineering Structures*, ASCE, 99-110.

Plevris, N. and Triantafillou, T. C. (1992). "FRP-reinforced wood as structural material." *J. Mat. Civ. Engrg.*, ASCE, V. 4, No. 3, August, 300-319.

Poursartip, A., Ashby, M.F. and Beaumont, P.W.R. (1982). *Proceedings of 3rd. Riso International Symposium Metall. and Mater. Sci.*, Riso Press, p. 279.

Preis, L. and Bell, T. A. (1986). "Fiberglass tendons for posttensioning concrete bridges." *Transportation Research Record 1118*, National Research Council, Washington, D.C., 77-82.

Puck, A. (1967). "Zur Berechnung und Vervormung von Mehrschichtenverbund-Bauelementen." *Kunststoffe*, V. 57, 284-294 (in German).

Rehm, G. and Franke, L. (1974). "Synthetic-resin reinforced bundled glass fiber rods as reinforcement in concrete construction." *Die Bautechnik*, V. 4, 115-120 (in German).

Rubinsky, I. A. and Rubinsky, A. (1954). "A preliminary investigation of the use of fibre-glass for prestressed concrete." *Mag. Concr. Res.*, 6(17), 71-78.

Schneider, W. (1971). "Thermal expansion coefficients and thermal stresses in unidirectional GFRP layers." *Kunststoffe*, V. 61, No. 4, 273-277.

Schwegler, G. (1992). Personal communication at EMPA, Dübendorf, Switzerland.

Sims, G. D., Johnson, A. F. and Hill, R. D. (1987). "Mechanical and structural properties of a GRP pultruded section." *Composite Structures 8*, 173-187.

Somes, N. F. (1963). "Resin-bonded glass-fibre tendons for prestressed concrete." *Mag. Concr. Res.*, V. 15, No. 45, 151-158.

Starr, T. F. (1983). "Structural applications for pultruded profiles." *Comp. Sruct. 2, Proc., 2nd International Conference on composite structures*, 193-213.

Tanigaki, M., Okamoto, T., Tamura, T., Matsubara, S. and Nomura, S. (1988). "Study of braided aramid fiber rods for reinforcing concrete." *IABSE 13th Congress Report*, Helsinki, Finland, 15-20.

Timoshenko, S. P. and Gere, J. M. (1961). *Theory of elastic stability*. McGraw-Hill Co., New York.

Triantafillou, T. C. and Deskovic, N. (1991). "Innovative prestressing with FRP sheets: mechanics of short-term behavior." *J. Engrg. Mech.*, ASCE, V. 117, No. 7, 1652-1672.

Triantafillou, T. C. and Deskovic, N. (1992). "Prestressed FRP sheets as external reinforcement of wood members." *J.Struct. Engrg.*, V. 118, No.5, 1270-1284.

Triantafillou, T. C., Deskovic, N. and Deuring, M. (1992). "Strengthening of concrete structures with prestressed FRP sheets." *ACI Structural Journal*, V. 89, No. 3, 235-244.

Triantafillou, T. C. and Meier, U. (1992). "Innovative design of FRP combined with concrete." *Advanced composite materials in bridges and structures*, 1st International Conference, CSCE, Sherbrooke, 491-500.

Triantafillou, T. C. and Fardis, M. (1993). "Advanced composites as strengthening materials of historic structures." To be presented at *IABSE Symp., Structural Preservation of Architectural Heritage*, Rome, September 13-15.

Triantafillou, T. C. and Gibson, L.J. (1989). "Debonding in foam-core sandwich panels", *Mater. Struct.*, V. 22, 64-69.

Triantafillou, T. C. and Plevris, N. (1991). "Post-strengthening of r/c beams with epoxy-bonded fiber composite materials." *Proc. Spec. Conf., Advanced Composites Materials in Civil Engineering Structures*, ASCE, 245-256.

Waaser, E. and Wolff, R. (1986). "A new material for prestressed concrete-HLV high-performance glass fiber connecting rods." *Beton*, V. 36, No.7, 245-250 (in German).

Zoch, P., Kimura, H., Iwasaki, T. and Heym, M. (1991). "Carbon fiber composite cables-a new class of prestressing members." *70th Transportation Research Board.Annual Meeting*, Washington D.C.